Oxidation Catalysis on Metal Particles: A Theoretical Study

Liam Thomas

PhD Thesis, Cardiff University 2016

Man must rise above the Earth—to the top of the atmosphere and beyond—for only thus will he fully understand the world in which he lives.

— *Socrates*

Acknowledgements

I would like to express my gratitude to my supervisor Dr David J. Willock. Through our many work related discussions I developed the skills required to perform research effectively and develop as a scientist. I would like to thank my other two academic supervisors Professor Adam F. Lee and Professor Karen Wilson with whom I had the pleasure of collaborating with themselves and members of their research group during my time at Cardiff University. I would like to thank my mentors Professor Peter J. Knowles and Professor Damien Murphy for their advice and guidance throughout this project

I express my gratitude to Professor Graham Hutchings, Dr Sarwat Iqbal, Dr Jonathan Bartley, Dan Jones and Dr Satoshi Ishikawa for valuable discussion and support with the joint theoretical and experimental NOVACAM project.

I wish to thank all members of the theoretical chemistry group at Cardiff University who I had the pleasure of working with over the past few years. Dr Jamie A. Platts, Dr Constantinos Zeinalipour, Dr Soon Wen Hoh and Dr Adam Thetford all provided substantial support in the field of computational chemistry.

Along with work related support I would like to thank Carlo Buono, Christian Reece, Matthew Turner, Dr Sean Mutter, Dr Christopher Lee and Joshua Black for providing engaging discussion on a variety of topics whilst working at 55 Park Place.

I express gratitude to my parents for their support in encouraging me to pursue research.

Finally, I would like to thank HPC Wales and Nextek for funding my PhD and allowing me the freedom to pursue additional lines of research during this project. I would like to thank HPC Wales, ARCCA and HECToR (through the Materials Chemistry Consortium) for granting me time on their supercomputers. Without this my work would not have been possible.

DECLARATION

This work has not been submitted in substance for any other degree or award at this or any other university or place of learning, nor is being submitted concurrently in candidature for any degree or other award.

Signed …… Date ……

STATEMENT 1

This thesis is being submitted in partial fulfillment of the requirements for the degree of PhD.

Signed …… Date ……

STATEMENT 2

This thesis is the result of my own independent work/investigation, except where otherwise stated.

Other sources are acknowledged by explicit references. The views expressed are my own.

Signed …… Date ……

STATEMENT 3

I hereby give consent for my thesis, if accepted, to be available online in the University's Open Access repository and for inter-library loan, and for the title and summary to be made available to outside organisations.

Signed …… Date ……

Contents

List of Papers

Chapter 6: The Interaction of Biomass Derived Molecules with Metal Particles

- An effect of Ni addition into Cu-ZrO_2 catalysts for the hydrogenation of levulinic acid. *In preparation*

Chapter 7: Oxygen Vacancy Defects on Metal Particle Supported Fe_2O_3

- A density functional study of oxygen vacancy formation on α-Fe_2O_3(0001) surface and the effect of supported Au nanoparticles. *Res Chem Intermed,* **41,** 9587 (2015)

- Gold Cluster Flexibility: A Molecular Dynamics Investigation. *In Preparation*

Summary

Oxygen adsorption and subsequent activation on unsupported gold, palladium and gold / palladium particles were investigated using computational methods.

For all particles studied the route to dissociation is via adsorption on (100) facets followed by dissociation into adjacent (111) facets, this indicates particle morphology plays a significant role in the activity of the particles towards oxygen. Calculated reaction barriers confirm 0.40 eV ,0.04 eV and 0.12 eV is required to dissociate O_2 on Au_{38}, Pd_{38} and Au_6Pd_{32} respectively. Further studies conclude it is not feasible to dissociate more than one molecular oxygen on Au_{38} – this is due to a calculated secondary adsorption energy being significantly weaker than the 0.5 eV required to dissociate the second species (the secondary adsorption energy is the calculated adsorption energy of the second O_2 molecule on a cluster with a pre-adsorbed species) This result is in sharp contrast to Pd_{38} and Au_6Pd_{32} where full adsorption and dissociation of O_2 occurs until particle saturation.

Hydroxymethylfurfural – metal particle interaction is found to occur via the furan ring – (100) / (111) junction. Adsorption energies are found to be greatest on sub nanometre Au_{13} and Pd_{13}. For larger nanometre sized particles (Au_{38}, Pd_{38} & Au_6Pd_{32}) the interaction with hydroxymethylfurfural can be up to 75 kJ mol^{-1} weaker than sub nanometre counterparts. Nudged elastic band calculations indicate a barrier to O-H activation in hydroxymethylfurfural to be 106 kJ mol^{-1} and 137 kJ mol^{-1} for Pd_{13} and Au_{13} respectively. The presence of pre adsorbed and dissociated oxygen destabilises the interaction with HMF however it can lower O-H activation barriers in the case of Pd_{13}.

The presence of a Pd_{10} particle on the surface of (0001) Fe_2O_3 was found to lower surface oxygen vacancy defect energies by as much as 1.12 eV. This defect energy can be reduced further by substituting the Pd atoms with Au. If Au_{10} is supported the oxygen vacancy defect energies are dramatically reduced (1.44 eV) even at defect site distances greater than 3 Å from the particle.

Chapter 1

General Introduction

The work presented in this thesis focuses on the adsorption and activation of molecular oxygen with gold, palladium and gold / palladium bimetallic particles. The motivation of this work is the need to understand the fundamental chemistry underpinning oxidation catalysis. The interaction of hydroxymethylfurfural with these particles is presented along with a discussion of surface oxygen vacancy defects on Fe_2O_3 and the implications for catalysis. In sections 1.1, 1.2 and 1.3 we will provide a brief overview of these fields, which is followed by a discussion of the scope of the thesis and questions it will address. This chapter is concluded with an overview of the contents of this thesis.

1.1 Gold, Palladium and Gold / Palladium Alloy Catalysis

Gold has always been considered an inert metal, its desirability for use in jewellery is attributed to this property explaining why approximately 52% of all gold mined is used for this purpose. Gold finds other uses within electronics due to its conductivity and inability to degrade. Colloidal gold has emerging use as a vessel to deliver medicines to target sites within the body. With regards to applications of catalysis gold was overlooked due to its inert nature.

The view gold was of little use within catalysis changed significantly due to work by Graham Hutchings who demonstrated gold supported on carbon could catalyse the hydrochlorination of acetylene. This process traditionally uses mercury containing catalysts therefore gold provided an exciting opportunity to replace dependence on toxic and environmentally detrimental industrial processes.

Subsequent work by Masatake Haruta proved gold was not limited to hydrochlorination catalysis. In this ground breaking work, it is determined gold nanoparticles can catalyse the low temperature oxidation of CO to CO_2 at temperatures as low as -70 ^oC.

This breakthrough opened the door to other work and initiated further studies into gold catalysis. To date it is found gold can catalyse various oxidation reactions at low temperatures providing a greener alternative to the often environmentally detrimental traditional industrial oxidation catalysis.

Oxidation catalysis is not limited to gold. Palladium nanoparticles are demonstrated to have lower light off temperatures than platinum when used in vehicle exhaust catalysts. The light off temperature is defined as the temperature in which the catalytic converter operates efficiently. The alloys of gold and palladium are also reported to efficiently catalyse hydrogen peroxide synthesis raising exciting possibilities of further catalytic applications.

It is likely gold and its alloys will find further use in catalysis. Due to cost it is unlikely gold will replace other precious metals however due to their lower temperature operating range in comparison to platinum their use will undoubtedly increase. Recent commercialisation by Johnson Matthey of PVC monomer production using gold catalysts demonstrates the increasing use of this once considered inert metal.

1.2 Hydroxymethylfurfural Conversion

Currently 99% of all plastics produced utilize fossil fuels as a feedstock. The global dependency on fossil fuels is problematic due to the finite nature of this resource. Due to this a significant amount of emerging research is being performed to find alternatives.

Food and drinks packaging is a major component of overall global plastic production. Approximately 30% of all plastics produced in the UK are for this purpose. Success has been achieved in using biomass derived chemicals as precursors to packaging material with the corn derived polylactic acid increasingly being used as a packaging material. Polylactic acid, however has been demonstrated to exhibit a low barrier to both CO_2 and H_2O diffusion which unfortunately makes it unsuitable for use for carbonated drinks packaging.

Hydroxymethylfurfural is obtained from the dehydration of sugars. It has attracted significant attention due to the recent label as a top ten molecule by the United States department for energy. This label is due to the versatility in the molecules which can be obtained by using HMF as a starting material. With regards to the packaging industry it is the conversion of HMF to FDCA which is of interest as FDCA can be polymerised in a similar way to terethphalic acid forming biomass derived polymers which demonstrate an improved barrier to CO_2 and H_2O diffusion compared to PLA.

This process is very much in its infancy however experimental work by Taarning confirm gold nanoparticles can catalyse the oxidation of HMF to FDCA at room temperature using 10 bar

air pressure. This relatively benign oxidation route is currently undergoing significant investigation to improve yield and selectivity with the overall goal of industrial scale up.

It is expected biomass derived packaging materials will represent a greater share of overall packaging material production globally over the next 10 years.

1.3 Catalysis Facilitated by Support Materials

The majority of catalysis by metal particles performed industrially employs a support material. It is increasingly accepted these materials do not solely act as support but may facilitate the catalysed mechanism through a variety of means. The Mars van Krevelen mechanism is one in which the support itself is a constituent of the reaction scheme and therefore will influence the rate. This type of mechanism was first proposed by Mars and van Krevelen in 1954 where it was reported the surface of the support can chemically bond to adsorbates and drive reactivity. Often surface vacancies on the support are the active site for reactant molecules and require replenishment by either the gas phase or bulk material.

The catalysed oxidation of CO to CO_2 has been proposed to occur via a Mars van Krevelen mechanism for reactions supported on both CeO_2 and Fe_2O_3. Understanding of reaction kinetics is vital for ensuring efficient catalytic design and therefore we believe computational modelling of support materials can be used to suggest catalyst composition and aid experimental design. This area of theoretical chemistry is increasingly used due to more computing power available and improvement of methods which are available to chemists.

1.4 Aim and Scope of the Thesis

Theoretical chemistry is becoming an increasingly powerful tool which allows researchers to understand the fundamental processes underpinning reactions which are vital for industry and biology. Theoretical chemistry by its self is not a replacement for experiment but most powerful when used to compliment an experimental investigation.

The aim of this thesis is to develop an understanding of fundamental interactions which underpin the use of metal particles as oxidation catalysts. It is widely accepted metal particles of gold, palladium and gold / palladium can catalyse oxidation reactions with CO and alcohol oxidation being examples of such a process. Whilst it is widely accepted these particles can function as oxidation catalysts the mechanism for their interaction and activation of molecular oxygen is less established. Substantial debate exits in the literature regarding the ability of gold particles to adsorb and dissociate oxygen species, this is evident as often conflicting reports exist discussing whether gold particles can dissociate multiple oxygen species.

We believe this uncertainty warrants investigation of the adsorption and activation of molecular oxygen on a variety of metal particles. This is presented through a comprehensive DFT study on O_2 activation where we report the barriers to oxygen dissociation on Au_{38} prohibit more than two species dissociating. This comprehensive study agrees with previous experimental works and provides quantitative barriers to dissociation computed through the Nudged Elastic Band (NEB) method. The NEB method is a computational method used to compute reaction barriers occurring within chemical processes. We also report the contrasting behaviour between gold and palladium particles with regards to oxygen interaction and discuss the implications towards catalysis.

Biomass derived packaging materials are becoming increasingly popular due to the need to remove dependency on non-renewable crude oil derived materials. Hydroxymethylfurfural is gaining significant attention as it can be converted into polymers (via FDCA) suitable for packaging. Experimental research confirms gold particles supported on titania catalyse this oxidation under benign reaction conditions however uncertainty exists as to the oxidation route – particularly on the order of oxidation of the side chain functional groups. There is a consensus suggesting it is the alcohol oxidation which is the rate limiting step. However, no computational evidence exists to support these experimental observations.

To our knowledge no computational investigation has been performed to deduce barriers to O-H cleavage which is the first component of an alcohol oxidation on metal particles. Here we

present a DFT study using the NEB method to confirm it is energetically difficult to cleave the O-H bond on all compositions of particle studied. An extension of our study is to ascertain the influence of oxygen (pre adsorbed on the metal particles) on these barriers and we report the surprising observation that molecular oxygen can facilitate O-H cleavage reducing barriers substantially. This work provides tantalising insight into the possibility of fine tuning metal particle composition to aid this energetically difficult step as we report a lower barrier to O-H cleavage when HMF is adsorbed on Pd_{13}.

Finally, we investigate how the presence of a supported metal particle can influence properties of the support surface. In this work we present a comprehensive DFT + U study of the oxygen vacancy defect energies on (0001) Fe_2O_3 surface. Our results confirm the presence of a supported Pd_{10} particle lowers the energy required to create a single defect at close proximity to the metal particle. A subsequent doping investigation to form Au_{10} confirm particles containing a high percentage of gold dramatically reduce defect energies, however these are still higher than oxygen activation energies on pure Au_{38} suggesting this is not an energetically favourable route. The results of our study support experimental observations which indicate the presence of a metal particle can influence surface defect energies as we present quantifiable data suggesting a dramatic reduction in defect energies in the presence of a supported particle. Our work adds to the literature discussion by indicating a Mars van Krevelen mechanism is more likely when supported metal particles containing a majority of gold are used.

The oxygen vacancy study discussed above provided an interesting observation which suggested Au particles are considerably more flexible than their palladium counterparts. As a result a comprehensive molecular dynamics study (Born Oppenheimer) has been performed in order to add to conflicting literature debate surrounding whether Au_{13} is two or three dimensional in its global minimum structure. We report from our comprehensive study Au_{13} is highly flexible in nature and it is thermodynamically favourable for Au_{13} to exist in two-dimensional form. The observation regarding Au particle flexibility does not indicate instability however it suggests particle morphology of these sub-nanometre particles is not fixed and can change with energetic ease.

1.5 Outline of Thesis

Here the aim of this study and implications of our work are presented.

In chapter two a discussion of current literature on gold particle catalysis is presented. A large section of this literature review is centred on discussion of oxygen interaction and activation with charged and neutral particles. In this section a summary of both experimental and theoretical work is presented which will address the origin of the unusual activity of gold particles in comparison to the bulk metal.

Chapter two contains an overview of the literature regarding the oxidation of HMF using gold particles. Literature covering the mechanism is presented however as this literature is not extensive a more detailed discussion regarding analogous alcohol oxidation is presented with further discussion detailing how this may apply to HMF. Chapter two concludes with a general discussion of the role of the support surface within heterogeneous catalysis and how the Mars van Krevelen mechanism may apply to CO oxidation. This section is concluded with a discussion of how metal particles may influence availability of surface oxygen in the catalytic cycle.

Chapter three contains the theoretical background which underpins computational methods used in this thesis. An introduction to density functional theory (DFT) and its implementation within the plane-wave VASP code is made. In this chapter a discussion of inclusion of dispersion interactions and special considerations required when modelling strongly correlated systems is presented along with the theory underpinning Bader analysis which is widely used in this thesis. This chapter concludes with a discussion of transition state searches and molecular dynamics calculations.

In chapter four the methodology underpinned by the theory detailed in chapter three is presented. The bulk of this chapter is focusses on discussion of how the adjustable parameters within VASP calculations have been evaluated and applied to our systems of interest. Evaluation of these parameters is the main constituent of this chapter which is concluded with a comparative study of the different methods available within VASP to determine transition states.

The next three chapters present the results of our work. In chapter five a discussion of the interaction of oxygen with Au_{38}, Pd_{38} and Au_6Pd_{32} is presented. After a brief introduction summarising literature, an overview of the methods and variables used in VASP are discussed.

This is followed by a comprehensive study of the adsorption modes of O_2 on the metal particles detailed above. Multiple oxygen adsorption on (100) facets is then investigated which is followed by a comprehensive study of the mechanistic route for dissociation of molecular oxygen on all particles studied. This comprehensive NEB study concludes with quantification of O_2 dissociation barriers as a function of number of the number of oxygen molecules adsorbed. Full reaction profiles are presented for Au_6Pd_{32} and Pd_{38}. For Au_{38}, the reaction barriers calculated conclude full oxidation is unfeasible therefore a partial reaction profiles are presented. Chapter five concludes with discussion of whether it is the global alloy composition or local distribution of atoms in bimetallic particles which influence reactivity towards oxygen along and what these results imply for H_2O_2 production.

Chapter six begins with a brief summary of HMF and why it is of significance within the packaging industry. An overview of current literature is made with discussion of the suggested mechanism for oxidation to FDCA. The introduction section concludes with discussion of the parameters used for DFT–D2 calculations. The next section in this chapter focuses on ascertaining the flexibility of the rotatable bonds in HMF which were obtained from dihedral scans using the Gaussian program. This information obtained from these scans is compiled together to obtain a reasonable minimum energy geometry which is used for all adsorption calculations. The next section of this chapter is a comparative adsorption study of HMF to Au_{13}, Pd_{13}, Au_{38}, Pd_{38}, and Au_6Pd_{32}. This is followed by a preliminary mechanistic study of the activation of the O-H bond in HMF. This study is extended by considering the effect of pre adsorbed and dissociated oxygen species on adsorption energies of HMF and activation of the O-H bond. This section is concluded with discussion as to the role of O_2 within HMF oxidation.

Chapter six concludes with a discussion of how the composition of both alloys of copper and nickel can influence electronic properties. In this section the percentage of nickel in bulk copper is adjusted to investigate the influence on the d-band centre with a discussion of the implications of this towards activation of molecular hydrogen in copper catalysts.

Chapter 7 is the final results chapter, here an investigation of oxygen vacancy defects on (0001) Fe_2O_3 is presented with and without the presence of supported Pd_{10}. This study is extended by sequential doping of Pd_{10} to form Au_{10}. A detailed discussion of the distribution of Au and Pd in each alloy composition and how this relates to the order of thermodynamic energies. At each alloy configuration oxygen vacancy defects on the (0001) Fe_2O_3 are computed and presented as a function of alloy composition. This work is followed by a discussion of the electronic and

geometric properties of the metal particles studied and how they may influence oxygen vacancy defect energies of their underlying support material.

Chapter 7 concludes with a comprehensive Born Oppenheimer molecular dynamics investigation which addresses literature debate surrounding the global minima structure of Au_{13}.

The results chapters are followed by conclusions and suggested future work which is contained in chapter 8.

Chapter 2

Literature Review

This work primarily focuses on investigating the role of heterogeneous catalysts in the oxidation of biomass derived starting materials. Additional focus is made to deduce how these catalysts interact with molecular oxygen and how supported metal particles influence surface oxygen defect energies on the support material. All three of these aspects of investigation may influence experimental design of catalysts and can aid researchers to produce heterogeneous catalyst systems to assist the growing need to replace crude oil derived resources.

2.1 The Use of Gold as a Catalyst

For a long time, gold was considered to be chemically inert. In its bulk phase gold is very stable making it desirable for use in jewellery and other long term applications. In contrast to the valency observed in the group VIII "coinage metals" gold has a fully occupied d-band which coupled with high ionisation potential explains why it is not reactive in this form[1].

DFT calculations have been performed by Sault *et al.* on the (110) surface of bulk gold, these calculations confirm gold in its bulk form does not dissociate H_2 and O_2 at temperatures below 473K[2]. These calculations support observations of inactivity in the bulk metal justifying why it was not considered for catalytic use.

This outlook however would soon change in 1989 when Haruta *et al.* determined that ultrafine gold particles with a diameter less than 10 nm deposited on metal oxide surfaces could oxidise CO to CO_2 at temperatures as low as -70 ^oC[3]. Investigation into other uses of subnanometre gold determined these particles are able to catalyse the oxidation of hydrocarbons[4], the water gas shift reaction[5], hydrochlorination of acetylene[6] therefore demonstrating the versatility of this metal.

This early research generated substantial interest in using nanometre gold in catalytic reactions, subsequent investigations were often aimed at deducing the reasons for this contrasting behaviour between bulk and nanoparticle gold.

2.1.1 The Origin of the Catalytic Behaviour of Gold Nanoparticles

In the literature there is consensus that the predominant factor governing catalytic activity of gold nanoparticles is particle size. Other factors governing activity such as morphology and the interface between the support and the metal particle will be discussed later in this chapter. For CO oxidation it is accepted the active species of gold particle are below 10 nm in diameter[3,4,7]. High activities of CO oxidation have been reported using Au particles dispersed on a variety of supports (TiO_2, Fe_2O_3 and NiO) indicating the support may influence catalytic activity through supply of oxygen from the surface to the gold particle[8] which is incorporated within CO to form CO_2.

Further proposals for the explanation of the origin of catalytic activity in gold nanoparticles is charge transfer from the support to the metal particle[9], strain within the particle which aids adsorption and dissociation of O_2[10] and low coordinate sites on Au particles which can facilitate adsorption of incoming reactant species[11].

Lopez *et al.* investigated several factors which may influence catalytic activity for CO oxidation using gold nanoparticles and have produced a hierarchy detailing how each of these factors influence CO oxidation. Their work concludes particle size has more influence on catalytic activity than any possible influence of the support material[12]. Figure 2.1 contains information on CO oxidation activity vs nanoparticle diameter on a variety of supports, it clearly confirms activity for CO oxidation dramatically increases as the particle size decreases below 5 nm. Below 5nm catalytic activity remains constant over all support materials. This confirms it is particle size which predominantly influences catalytic activity and not the support.

Confirmation that catalytic activity is primarily dependent upon particle size has generated an experimental drive to perfect techniques which can produce nanoparticles within a target size range. Considerable success has been achieved in this area using the sol immobilisation technique. This technique employs the use of a PVA coating preventing coagulation of colloidal gold (in solution) which is subsequently burned off to leave distributed Au particles on surfaces. Rogers *et al.* experimented with temperature and solvent variations during preparation of nanoparticles and confirm that altering these variables affects the TOF of the catalyst (in the case of glycerol oxidation, further discussion of alcohol oxidation is presented later in this chapter). Using this sol immobilisation method, ultra-small Au clusters were

characterised which contained 1-5 atoms as the active species[13], therefore confirming the suitability of this method for producing a required range of particle sizes.

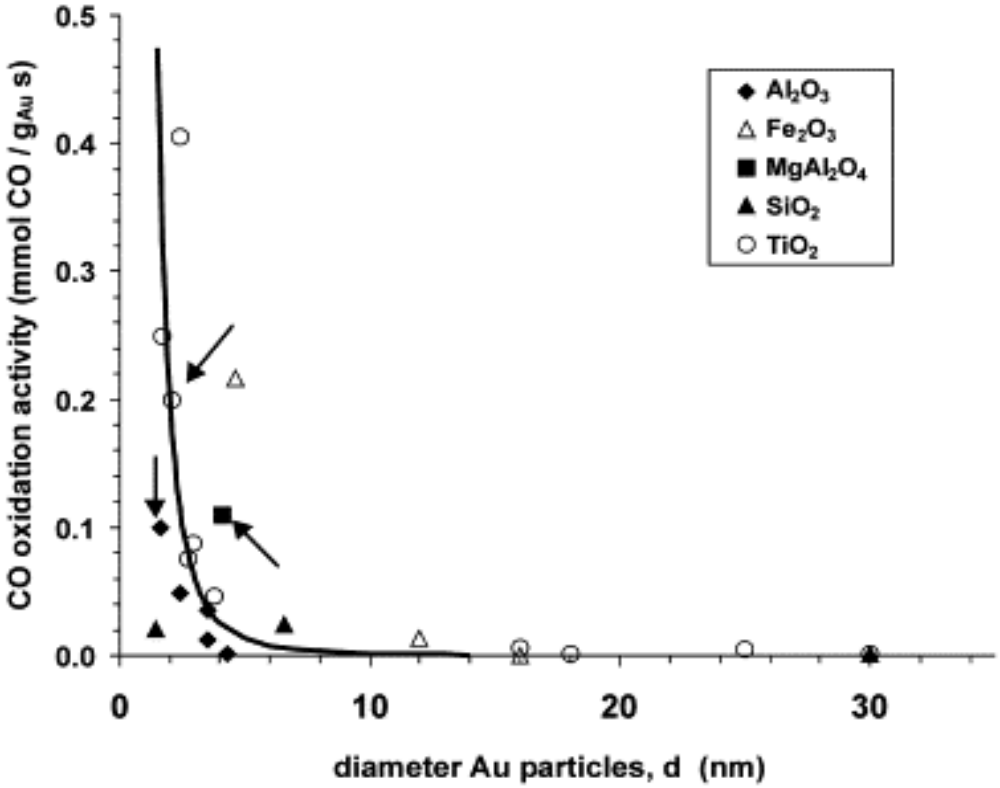

Figure 2.1: CO oxidation activity as a function of diameter of Au particles with varying support materials employed. Data compiled by Lopez *et al.* and taken from reference 11.

In bulk gold the atoms are highly coordinated with an average coordination number of 12. As nanoparticle gold forms surface exposed atoms are occurring and as the cluster diameter decreases in size these surface atoms become a major component of the overall environment of Au atoms in the particle. Low coordinate atoms are difficult to measure experimentally and due to this computational experiments have been employed to determine the relationship between low coordinate Au atoms and adsorption energies.

DFT calculations have been performed by Lopez *et al.* using the RPBE functional modelling the binding energy of O along with CO to bilayer Au_{10} and an Au (111) surface. Average coordination number of the particle is plotted with binding energy (in eV) in figure 2.2 where an inverse relationship between coordination number and binding energy is observed[11]. These calculations also confirm bulk Au (111) has a positive binding energy for all reactant species studied.

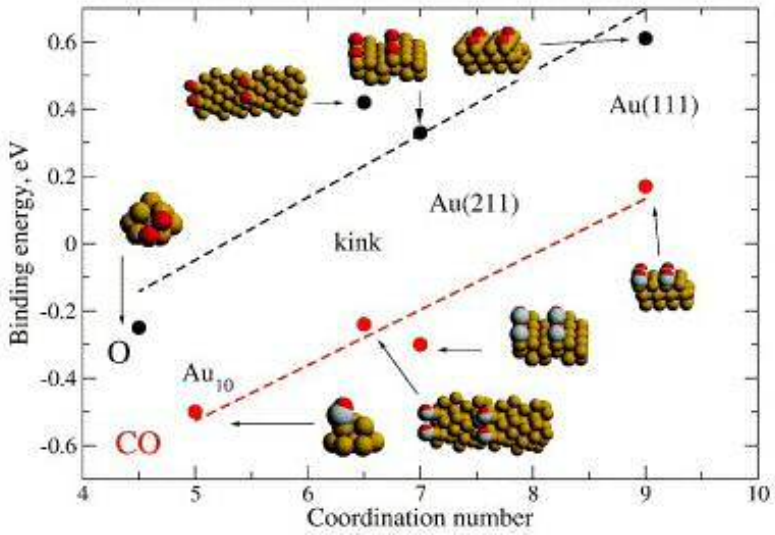

Figure 2.2: Taken from reference 11 DFT calculations performed by Lopez *et al.* confirming low coordination numbers of Au atoms enhance adsorption energies of CO and O.

As adsorption is the initial step in a catalytic cycle it is reasonable to assume a significant adsorption energy is a key requirement to drive the catalytic process. As low coordination numbers are reported to enhance adsorption it is reasonable to assume this is a contributing factor along with particle size explaining the activity of gold nanoparticles (GNP) as catalysts.

Both experimental and DFT evidence presented here indicate both low coordination numbers and particle size contribute to GNP catalytic activity. Low coordination numbers of Au atoms arise due to gold being present in a nanoparticle form. Particle size and low coordination numbers are interlinked and contribute to the overall activity.

In heterogeneous catalysis a variety of support materials are used. The role of the support in GNP catalysis is often subject to debate. It has been ascertained particle size is the predominant factor driving catalytic activity for GNP however support influences should not be overlooked as modification of support may increase activity. Sanchez *et al.* computationally investigated GNP supported on magnesia and found partial electron transfer from the surface to the cluster is essential for activation of the particle for CO oxidation[9]. Further evidence to support surface – Au particle charge transfer is from Li *et al.* who performed DFT calculations using the PBE functional on a variety of Au cluster / MgO surfaces. It is reported charge transfer between MgO (111) and the Au particle is significant whereas weak for (001) and (110)[14].

For catalytic systems requiring a transfer of electrons from the metal particle to the adsorbate to facilitate reaction, charge transfer from the support to the cluster may prove significant as

this will ensure replenishment of cluster electrons therefore ensuring continuity of the catalytic cycle. A more detailed discussion of charge transfer is contained in 2.2 and 2.4.

The final factor which is suggested to give rise to the catalytic behaviour of gold nanoparticles vs their bulk form is support induced strain. Comprehensive DFT calculations (PW91) performed by Mavrikakis *et al.* investigated three effects which may make gold surfaces more reactive towards adsorption of molecules of O_2 and CO[15]. These three effects were quantum-size effects, the effect of steps on the Au surface and the effect of strain. Their research is summarised below:

1) The number of layers of the Au (111) were varied from 1-6 with CO and O binding energies determined at each slab thickness. The results of these calculations confirm slab thicknesses of 2 layers or more produce adsorption energies of similar value therefore indicating beyond two-layer thickness quantum sized effects are not a significant contribution to adsorption energies.
2) Step sites on the particle demonstrate more activity than the flat Au (111) surface. The step density increases as particle size decreases corresponding to a diminishment of bulk metal properties. This may explain different behaviour between bulk and particle form.
3) Strain effects were elucidated by taking a four-layer slab and alternating the lattice constant parallel to the surface. It is found a 1% increase in the lattice constant increases binding energy of O_2 by 0.13 eV. Strain mismatch between the particle and the support is strongest for the smaller particle sizes and this effect diminishes as the particle becomes more bulk like.

The origin of the catalytic behaviour of GNP has been attributed to particle size effects, low coordinate sites, charge transfer and support induced strain. The factor which contributes most to this activity is particle size which has an inverse relationship to low coordinate sites. Whilst these two factors contribute most it is reasonable to assume each of the factors discussed above contributes to the overall activity of the gold nanoparticles and will be present in a variety of different catalytic systems.

2.1.2 Activity Differences Between Nanometre and Sub Nanometre Gold Particles

The origin of gold nanoparticle catalytic activity has been discussed in 2.1.1 along with a brief overview of tunable synthesis methods of such particle systems. Recent advances in the production and characterisation of gold nanoparticles however demonstrate it may be subnanometre gold as the active species as opposed to nanometre sized particles. Particle sizes of ~0.5 nm have been identified as the active species for CO oxidation using Au supported on FeO_x[16]. For propene epoxidation Au_6-Au_{10} clusters supported on Al_2O_3 have been identified as active species[17] therefore confirming these sub-nanometre particles play an active role in catalysis. Goodman *et al.* investigated the link between particle size dependence on CO oxidation rates and confirmed particle sizes around 2nm were most active[18].

Through a mixture of experimental and DFT work Boronat *et al.* investigated the electronic differences between gold particles and their subnanometre counterparts with the aim of predicting and suggesting reactivity for a range of catalytic processes[19]. Using the Gaussian09 programme along with the B3LYP/LANL2DZ hybrid functional, molecular orbital energy levels were computed and used to determine the HOMO-LUMO at each cluster size (Au_3-Au_{38}) (figure 2.3).

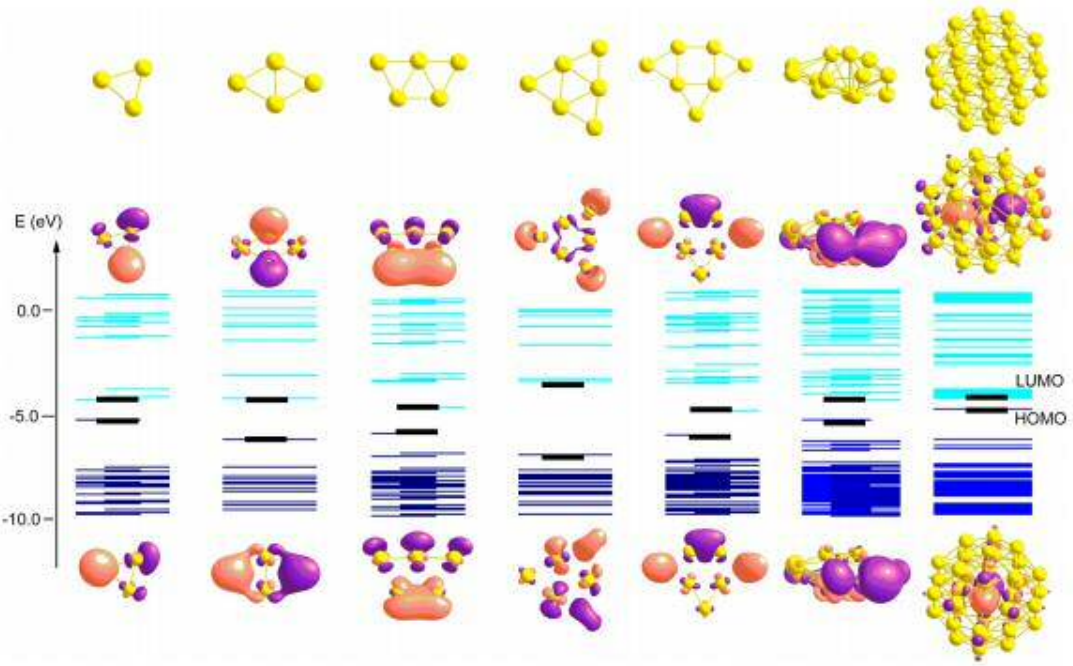

Figure 2.3: Molecular orbital energies for a range of clusters (Au_3-Au_{38}) obtained by Boronat *et al*. Figure taken from reference 19.

The HOMO – LUMO visualisations performed by Boronat *et al.* indicate for sub-nanometre clusters the frontier orbitals are exposed on the periphery of the particle whereas for Au_{38} these orbitals are encapsulated within the particle cage. These orbital differences have been proposed as an explanation for differing behaviour between particle sizes as efficient orbital overlap contributes to favourable adsorbate / metal particle interactions.

The molecular orbital energies are discrete for smaller particles and become more continuous and more towards band like separation for Au_{38}. This observation indicates electrons are more likely to be accessible for Au_{38} vs Au_3 and it would be reasonable to assume for catalytic processes requiring electron transfer to the adsorbate (as in O_2 activation) these larger particles may be preferred. Figure 2.4 details Bader charge analysis performed by Boronat *et al.* confirming larger Au particles (nanometre sized) have the highest degree of charge transfer to O_2 corresponding to an elongation of the O-O bond. Such an observation leads to the reasonable suggestion larger particles may be more suitable for reactions requiring such donation.

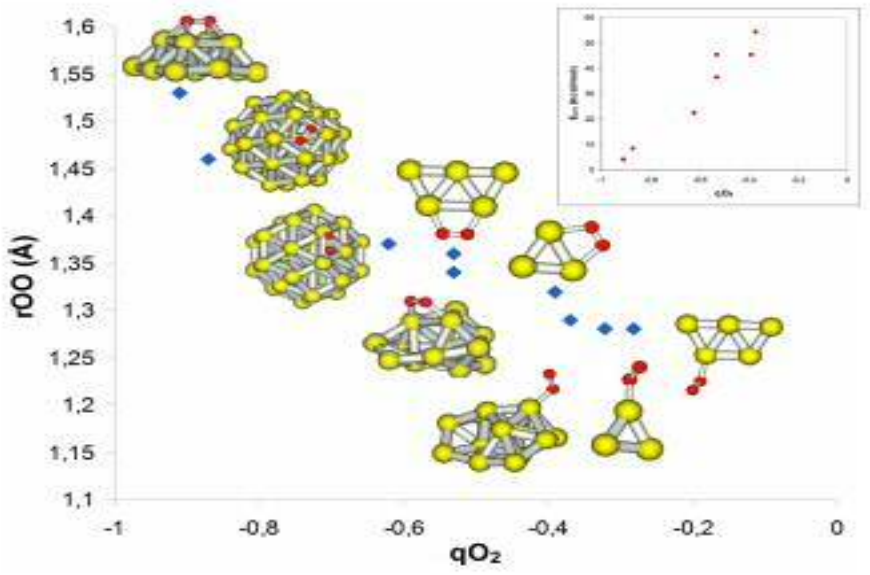

Figure 2.4: Bader charge analysis performed by Boronat *et al*. qO_2 (charge transfer to O_2 is plotted against rOO (oxygen-oxygen distance) for adsorbed oxygen species on a variety of Au particle sizes. Figure obtained from reference 19.

Data obtained by Boronat *et* al. correlate charge transfer from cluster to adsorbate and particle size. If this was the sole condition for dissociation of O_2 the calculated barrier of dissociation should decrease as particle size increases. This however does not occur as computational modelling by Roldán *et al.* confirm Au_{55} and Au_{79} have a barrier to dissociation of O_2 greater than initial adsorption energies[20] therefore requiring additional energy in order to dissociate. It can therefore be concluded that electron availability is not the governing factor in metal particle activity. Instead a balance between adsorption energies (due to efficient orbital overlap) and electron availability need to be met to obtain optimal conditions.

The work discussed above provides a fascinating insight into how subnanometre particles differ in reactivity in comparison to their nanometre sized counterparts and comparative modelling of subnanometre and nanometre interactions with HMF is presented in chapter 6.

2.1.3 Geometric Differences between Nanometre and Subnanometre Gold Particles

Particle morphology is reported to influence the interaction of gold particles with O_2[21]. Along with morphology gold particle surface roughening is also proposed to be a key factor in catalytic activity with corner sites reported to localise electron density and hence promote interaction[22].

As particle geometry influences reactivity a considerable amount of research has focussed on determining global minima structures of gold particles. Particular attention has been directed at locating the transition point between two and three dimensional clusters with neutral Au_n particles reported to adopt 3D structures at n=11[23]. MP2 methods have been employed by Garzon *et al.*[24] where suggestion the transition from 2D to 3D occurs between 6 and 7 atom neutral clusters. DFT by Xiao *et al.*[25] however predict a transition between 14 and 15 atom clusters therefore confirming there is a debate in the literature regarding the exact cross over point

Being close to the suggested 2D-3D transition region naturally there is a difference of opinion as to the exact structure of Au_{13}. Icosahedral[26], buckled biplanar (BBP)[27], cuboctahedral[28] and 2D[29] structures have all been proposed as the lowest energy for Au_{13}. With such debate surrounding the structure of Au_{13} we believe a comprehensive of geometry through molecular dynamics is necessary to provide insight into this highly flexible geometry.

2.2 The Interaction and Activation of Molecular Oxygen with Metal Particles

The ability of GNP to catalyse reactions is not solely contained to CO oxidation. GNP can catalyse the selective oxidation of alcohols[30] along with the partial oxidation of hydrocarbons[31]. In all of these instances the reaction is performed in an oxygen rich environment and therefore it is vital to understand how molecular oxygen interacts with GNP as an understanding will allow for efficient catalytic design to exploit desirable properties.

2.2.1 Molecular Oxygen and Mechanism for Dissociation

The mechanism for CO oxidation using GNP has been computationally and experimentally investigated in great detail. Despite the wide range of studies performed on this oxidation no consensus exists as to the role of molecular oxygen in the mechanism. Experimental difficulty in isolating multiple variables in this reaction such as particle size, solvent and pressure contribute to the overall difficulty in elucidating the exact role of O_2.

Molina *et al.* performed a series of theoretical investigations using Au particles which had an infinite one-dimensional direction which was used to model an extended particle (rod) / Rutile (110) interface. The results of this investigation indicated O_2 does not adsorb in an energetically

favourable configuration on the pure surface, instead the presence of the Au particle is required to aid adsorption[32]. Adsorption of O_2 has also been calculated to be favourable at the interface between particle and surface. The suggestion O_2 adsorbs at the interface of supported gold particles is one which is shared by Bond *et al.*[33] and Minico *et al.*[34]

An alternative mechanism for CO oxidation using Au / TiO_2 has been proposed by Grunwaldt. In this proposal it is oxygen vacancy sites on the TiO_2 surface which molecular oxygen irreversibly bind and spill over on the Au particle which react with CO forming CO_2[35].

Both types of mechanism above are classed as support – induced mechanisms. A further class of mechanism is a gold-only mechanism where the surface acts solely as a support. Evidence for a gold only mechanism is presented by Wallace *et al.* who performed pulsed flow reactor and mass spectroscopy methods to determine cooperative adsorption of both CO and O_2 occur on anionic Au_6[36]. Mass spectrum data indicates a loss of a CO_2 molecule leading to the conclusion the active anionic gold particle can oxidise CO at a rate 100 times that previously reported for commercial GNP catalysts.

For gold only and support induced mechanisms there is interaction between molecular oxygen and the particle. The presence of such an interaction warrants further literature investigation of the interactions and possible activation of O_2 on unsupported gold particles.

2.2.2 Interaction of Molecular Oxygen with Unsupported Gold Particles

This section of the literature review will discuss both experimental and theoretical research into the adsorption and subsequent activation of oxygen on a variety of metal particles.

Whilst it is widely accepted molecular oxygen does not adsorb favourably on flat gold surfaces at room temperature, the interaction with gold particles is subject to debate in the literature. Debate often centres on the ability of metal particle to adsorb and dissociated molecular oxygen. Evidence obtained from analysing often conflicting literature is presented below.

First principles calculations performed by Häkkinen and Landman compared the stability of various geometric isomers of Au_n ($2 < n < 10$) particles and suggested structures for each cluster type[37]. These calculations are supported by experimental observations indicating Au_{13} exists as a five sided icosahedron when prepared using citrate sols[38]. XFAS data has been obtained providing evidence for Au_6 along with a range of other gold particles of varying size[39].

Both theoretical and experimental evidence points towards the existence of stable gold particles of varying sizes. Evidence confirming existence of stable gold particles of varying sizes provides the basis for subsequent molecular oxygen – gold particle interaction studies.

Cox *et al.* performed experimental analysis of neutral, anionic and cationic gold clusters. The aim of this research was to ascertain how O_2 adsorbs on these different charged species. Observations conclusively determined O_2 only reacts with anionic gold clusters where there is an even number of atoms[40]. An even number of atoms corresponds to an odd number of electrons. It is interesting to note on Au_{10}^+ was the only cation to react with oxygen. Reactivity of gold particles towards oxygen has also been investigated using TOF mass spectroscopy. In this study even number of gold atom anionic clusters were determined to bind with molecular oxygen whereas odd numbered ones did not[41]. Whetten *et al.* used pulsed flow reactor methods at ambient temperature to probe O_2 interaction with anionic cluster containing 2-22 atoms with striking observations confirming no measurable oxygen adsorption occurred for clusters with an odd number of atoms[41]. This research also produced the striking observation no further adsorption of O_2 occurs to clusters already containing an oxygen species.

This experimental work of Whetten *et al.* however is contradicted by DFT (PW91) calculations performed by Mills and Gordon where it is reported both neutral and charged Au clusters from 2-5 atoms in size adsorb two oxygen molecules. The second oxygen molecule adsorbs with a weaker binding energy however it is reported to occur with ease in both neutral and anionic clusters[42]. The PW91 functional is known to over-bind and exaggerate adsorption energies[43] and could perhaps give rise to erroneous multiple adsorption data. The clusters used by Mills and Gordon were small and therefore higher computational cost MP2 calculations were performed and it is confirmed plane wave data using the PW91 functional is in good agreement with this higher method, validating the multiple oxygen adsorption result. Mills and Gordon do not speculate as to whether a third molecular oxygen is able to adsorb and this provides potential for a fascinating future study.

These experimental observations suggest an electron transfer is required in order to bind molecular oxygen. This is because in negatively charged gold clusters containing an even number of atoms an unpaired electron is present which is hypothesized to transfer to molecular oxygen upon adsorption.

The transfer of an electron to the O_2 molecule has been probed using DFT (GGA), where O-O bond lengths were found to elongate and vibrational frequency decrease upon adsorption to

negatively charged particles. The elongation of the bond corresponds is representative of oxygen being in a superoxo state. Subsequent dissociation energies (ΔE^{diss}) of the bond is calculated to correlate to the degree of charge transfer upon adsorption (table 2.1)[44].

Table 2.1: Charge transfer, energy of adsorption, dissociation energy and activation energies determined by Yoon *et al.* for O_2 adsorbing to a range of Au particle sizes of different charge. Taken from reference 44.

	Δq (e)	**$E_B(O_2)$ (eV)**	**ΔE^{diss} (eV)**	**ΔE^{act} (eV)**
$Au_5O_2^-$	0.588	0.61	1.42	2.02
$Au_6O_2^-$	0.745	1.06	1.27	2.33
Au_6O_2	0.321	0.24	3.10	3.34
$Au_6O_2^+$	0.143	0.46	3.15	3.61

Charge transfer from anionic gold clusters to oxygen is also proposed by Pal *et al.* who performed photoelectron spectroscopy along with DFT (PBE functional) on cluster sizes from 6-18 atoms. Two modes of chemisorption are proposed on even sized anionic clusters which are the superoxo and peroxo states. It is suggested superoxo chemisorption occurs where low binding energies exist and electron transfer occurs. For the Au_8 anion a peroxo chemisorption is reported to occur where greater degree of elongation occurs in the O-O bond and therefore proposed more likely to activate[45]. Further discussion of the activation of molecular oxygen is in 2.2.3.

The data presented in this section indicate an odd-even oscillation behaviour of adsorption of O_2 should occur which is dependent on the number of atoms in the particle. Franceschetti *et al.* performed a comprehensive DFT study on gold clusters ranging from 2-6 atoms in size and report adsorption energy oscillates as expected for negatively charged species with even number clusters having a substantially greater interaction with O_2 than odd numbered clusters[46] (figure 2.5).

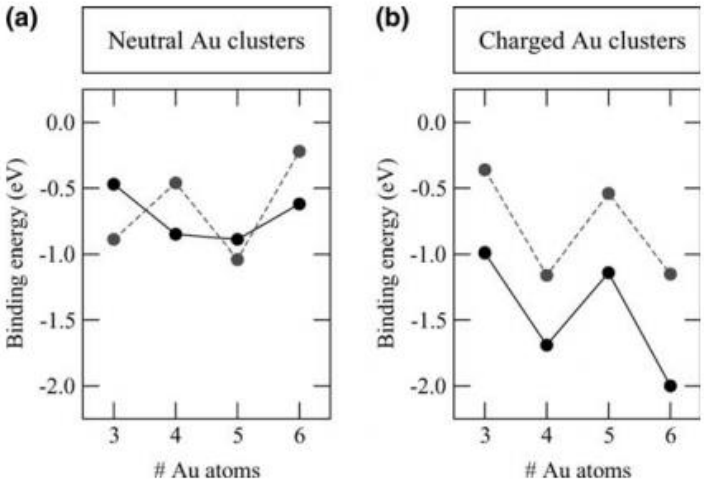

Figure 2.5: DFT binding energies for O_2 on neutral and negatively charged particles as determined by Franceschetti *et al*. Dashed lines indicate molecular chemisorption and solid lines dissociative chemisorption. Figure taken from reference 46.

Data presented in table 2.1 confirm O_2 adsorbs on neutral Au_6 with a calculated adsorption energy of 0.24 eV. Whilst this is smaller than adsorption energies calculated for negatively charged clusters it is a significant observation and contradicts earlier work by Cox who proposed neutral gold particles are inert towards molecular oxygen. Further evidence for chemisorption on neutral gold particles has been obtained by Franceschetti (figure 2.5) where favourable adsorption energies are calculated for all neutral species studied. There is clear debate as to the ease in which neutral gold particles adsorb O_2 and therefore a comprehensive study of the interaction of O_2 with gold particles is presented in chapter 5.

2.2.3 The Activation of Molecular Oxygen using Gold Particles

Literature discussed in 2.3.2 confirm molecular oxygen binds to both neutral and charged Au clusters. A smaller data set surrounding the interaction of O_2 with neutral gold species exists in comparison to charged species. The following section will discuss both experimental and computational information regarding activation of O_2 using gold nanoparticles.

2.2.4 Activation of Molecular Oxygen on Anionic Gold Particles

Adsorption of molecular oxygen literature review presented in 2.2.2 confirms interaction is strongest with anionic gold particles. Franceschetti performed a subsequent analysis to deduce whether adsorption of O_2 was dissociative or molecular. Figure 2.6 details the thermodynamically most favourable configurations for Au_nO_2 ($2 \leq n \leq 6$). Figure 2.6 demonstrates in all cases it is thermodynamically favourable to have O_2 dissociated on the metal particle as opposed to molecular adsorption. In all cases the preferred adsorption mode is in a "linear bridge" where an O-Au-O linkage occurs. If dissociated O atoms do not share a common Au atom as in the case of an Au_4O_2 system where the two atoms are on opposite sides of the cluster, total energies have been determined to be ~1.3 eV higher than the thermodynamic ground state. This clearly indicates preference for a shared gold atom.

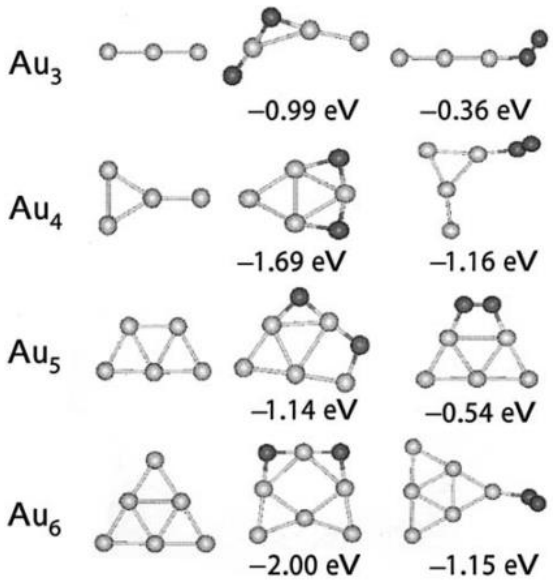

Figure 2.6: The most favourable configurations obtained by Franceschetti for anionic Au_nO_2 ($3 \leq n \leq 6$). Figure taken from reference 46.

Thermodynamic preference for dissociated oxygen is also reported by Wang and Gong through computational study of adsorption of O_2 on icosahedral Au_{32}[47]. Supporting previous theoretical

calculations, experimental confirmation of the oxidation of gold nanoparticles occurs through XANES analysis. Weiher *et al.* report a depletion of the Au d-band corresponding to chemisorption of both CO and O_2. This method could not determine whether activation of O_2 occurs at the cluster-support interface or cluster itself however this work does confirm the gold nanocluster contributes to the catalytic activity of CO conversion[48]. Whilst data here indicates thermodynamic preference for the dissociated system, this alone without kinetic information of any such barrier of dissociation makes it inconclusive to state with certainty that dissociative chemisorption occurs.

Roldan *et al.* expanded upon the limited data within the literature regarding oxygen activation. In this study an investigation was performed determining how the size of the gold particle influences the dissociation of O_2. Extensive DFT calculations on gold particles in the 1 to 2 nm range was performed. All models studied in this work included low coordinate Au atoms which are a prerequisite of reactivity. This investigation was initiated by binding molecular oxygen to an Au_{55} cluster in every possible coordination site. The geometries were optimised and energy minima isolated. Subsequent nudged elastic band calculations were performed (using the VASP program), with the starting point for these calculations the low energy minima geometry and the final point is the dissociation state (2 O atoms). The nudged elastic band calculations were used to determine reaction barriers and were corrected for zero-point energy. This investigation determined that in all cases where favourable adsorption is occurring an increase in the O-O bond of the molecular oxygen is observed compared to gas state isolated O_2. From this data it would be reasonable to assume that the elongation of the O-O bond accompanies favourable adsorption. This however is not the case as Roldan reports an elongation of the bond even in cases where the adsorption is substantially endothermic.

Similar observations are reported for analysing the vibrational frequency of the O-O bond therefore indicating the calculation of reaction barriers is required in all cases and barrier crossing feasibility cannot be measured from adsorption vs equilibrium properties of O_2. The reaction barriers obtained through this investigation are energetically higher than the energy required to desorb oxygen indicating a degree of competition between the two routes. Figure 2.7 details the energy profile for the dissociation of O_2 on gold nanoparticles of various size. It is clear Au_{55} has the highest barrier to dissociation of all clusters studied therefore indicating dissociation is most unfavourable here and desorption / adsorbed state is most likely[20].

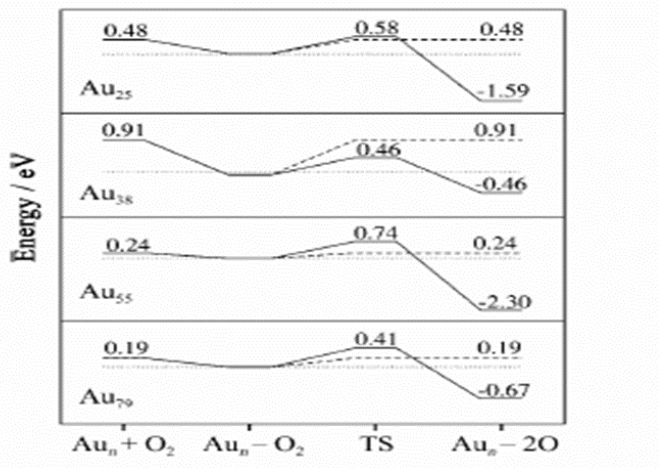

Figure 2.7: Calculated barrier of O_2 dissociation obtained by Roldan for gold particles of various size. Figure taken from reference 20.

Along with particle size morphology can influence the interaction between gold particles and O_2, this relationship has been investigated in depth by Boronat and Corma with a summary of their extensive research below[20]:

1) Adsorption of molecular oxygen was performed on Au_{13} and Au_{38} (cuboctahedral geometry) with a comparison with Au (111) and Au (100) bulk gold.

2) Different orientations of oxygen on the cluster were analysed to determine the preferential adsorption mode. These orientations were denoted end on (eo), top bridge top (tbt) and bridge-bridge (bb) (figure 2.8)

3) The hierarchy of adsorption energies is determined as: end on < bridge-bridge < top bridge top.

4) The highest degree of molecular activation occurs on bridge-bridge configurations. In these instances, calculated activation barriers (NEB) for O_2 adsorbed on Au_{38} via this site is 0.36 eV compared to 0.97 eV for tbt site.

5) Dissociation via the bridge-bridge sites require the presence of a (100) square facet and therefore particle morphology has been proposed as a key factor governing O_2 activation.

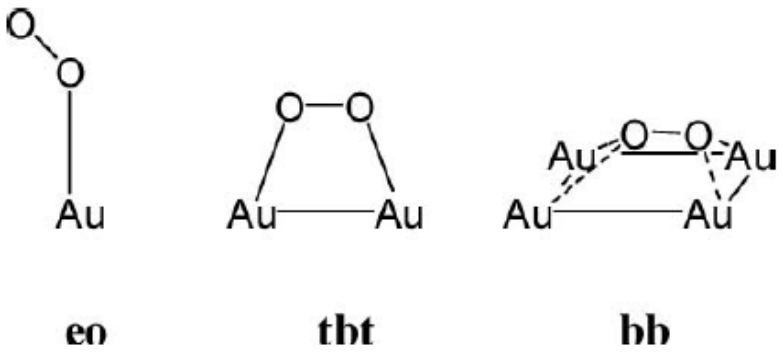

Figure 2.8: Adsorption modes of molecular oxygen studied by Corma and Boronat. Figure taken from reference 21.

Evidence in the literature through both experimental and computational methods confirm molecular oxygen adsorbs favourably on both charged and neutral gold particles. Neutral cluster interaction data is less prevalent than charged cluster data and therefore a future study investigating neutral gold particle / oxygen interactions would contribute to the literature debate.

Uncertainty exists as to the ability of gold particles to adsorb and dissociate multiple molecular oxygen species. The uncertainty stems from contradiction between experimental and computational measurement. Upon a thorough search of the literature it is clear a comprehensive study of adsorption of O_2 on gold nanoparticles is required in order to shed light and expand knowledge in this area. Calculations performed are presented in chapter 5.

Activation of molecular oxygen is experimentally and theoretically predicted. The comprehensive study of Boronat and Corma indicate particle morphology influences activation. Bridge-bridge adsorption modes will be studied in more detail in chapter 5 where this study will be extended to investigate subsequent O_2 adsorption and activation on gold particles.

2.2.5 The Interaction of Molecular Oxygen with Au / Pd Nanoparticles

Bimetallic particles often produce chemical and catalytic properties different from their component metals. Pd-Au catalysts are demonstrated to catalyse CO oxidation[49], alcohol oxidation[50] and directly synthesize hydrogen peroxide from hydrogen and oxygen[51]. As with

gold nanoparticles a detailed understanding of how molecular oxygen interacts with these particles is vital to ensure efficient catalyst design.

A comprehensive theoretical and experimental study has been performed by Yu *et al*. In this study molecular beam scattering, reflection-absorption infrared spectroscopy, and TPD have been combined with DFT modelling with the following result:

1) Contiguous Pd sites are required in the alloy in order to adsorb molecular oxygen. TPD confirms upon heating molecular oxygen desorbs with no dissociation detected.
2) DFT calculations performed using PBE functional predict an increased desorption energy as the Pd / Au (111) surface increases in size. The corresponding barrier to activation decreases as the Pd ensemble size increases indicating a large Pd ensemble is a requirement of successful activation[52].

A nanoparticle DFT study on Au / Pd bimetallic systems has been performed by Staykov *et al*. This recent work modelled 55 atom particles of the following compositions: Au_{55}, Pd_{55}, $Au_{13}Pd_{42}$ and $Au_{42}Pd_{13}$. The bimetallic systems were modelled not as a random alloy distribution but instead as a core shell with 13 Au and Pd atoms acting as the core respectively.

Nudged elastic band calculations were used to calculate barrier to O_2 dissociation on these core-shell systems with results of these presented in figure 2.9. The presence of a 13 atom palladium core produces a barrier of dissociation 0.14 eV lower than for pure Au_{55}. It is interesting to note a reverse trend occurs where the presence of a gold core increases the barrier by 0.09 eV[53]. This is an interesting observation as an Au core would produce more lattice strain on the Pd shell due to the lattice constant mismatch. This may make the cluster more active however this is not observed as the Pd cluster still exhibits the lowest barrier to dissociation.

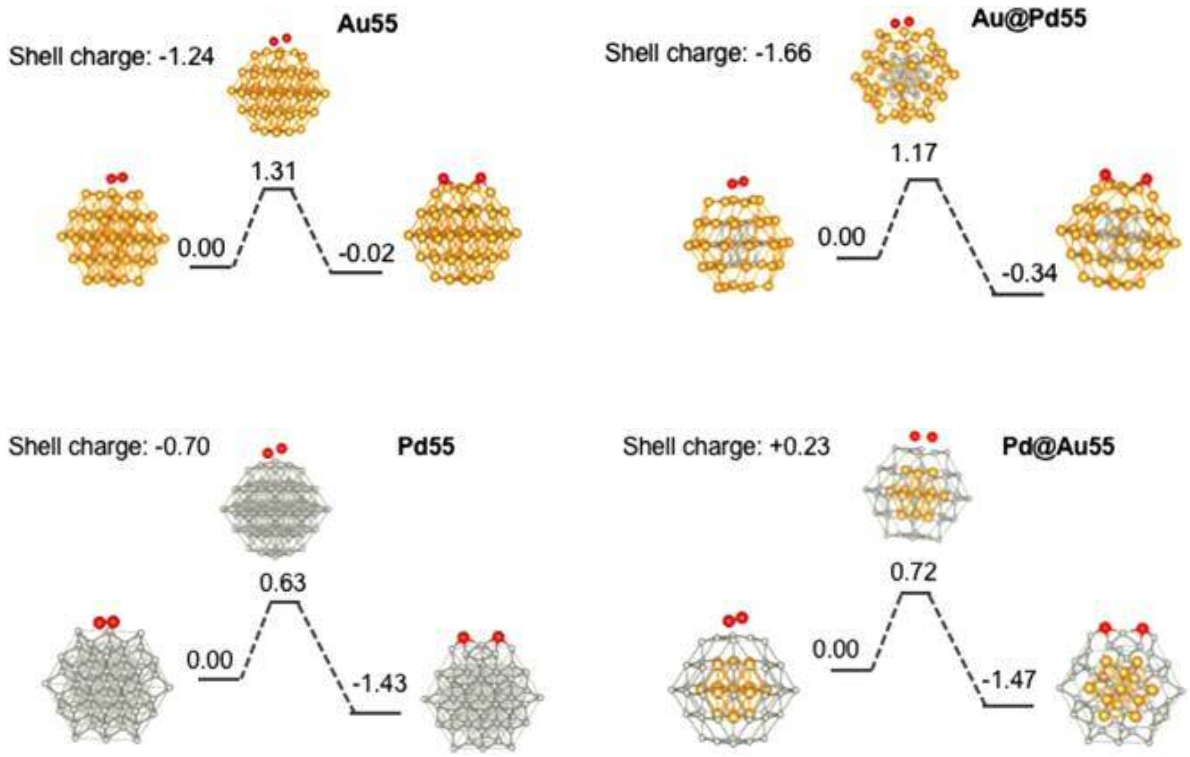

Figure 2.9: Reaction barriers calculated by Staykov *et al.* on Au / Pd core shell 55 atom particles. Figure taken from reference 53.

A lack of comprehensive literature exists describing the adsorption and activation of molecular oxygen on Au / Pd bimetallic particles. Of interest would be a comparative study of 38 atom particles (both pure and bimetallic) analogous to studies already performed by Corma *et al*. A subsequent study investigating differences in interaction behaviour between core shell and random alloy compositions will add to the limited information available within the literature and advance understanding. We believe the work presented in chapter 5 will contribute to this understanding and can aid catalysis design.

2.3 The Oxidation Biomass Derived Molecules

Approximately 5 million tonnes of plastics are produced annually in the UK[54]. Of this amount approximately 38% are used in the packaging industry. Plastic production is heavily dependent upon the crude oil derived terephthalic acid and as a result substantial attention has focussed on discovering renewable alternatives analogous to terephthalic acid which can be used as starting blocks for packaging materials.

Polylactic acid (PLA, figure 2.10) derived from corn is currently used as a biomass derived packaging material. PLA has widespread uses however gas permeability tests confirm a low barrier exists for CO_2 and H_2O permeation[55]. This low barrier renders it unsuitable for use for carbonated drinks packaging – a large component of drinks bottle production.

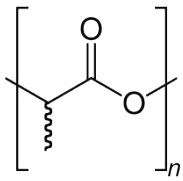

Figure 2.10: Polylactic Acid (PLA)

Hydroxymethylfurfural (figure 2.11, also called 5-hydroxymethylfurfural, HMF) is an organic molecule obtained from fructose, glucose (via isomerisation to fructose) and directly from cellulose[56]. HMF is used as an intermediate in the production of the biofuel dimethylfuran. It is possible to convert HMF into a variety of other molecules each with industrial importance (figure 2.11).

The variety of different products obtainable from HMF coupled with its renewable origin has earned it a label as a "top ten molecule" by the US Department of Energy[57]. HMF is tipped to replace traditional feedstocks used in industrial processes and as a result substantial experimental investigation has been performed in order to exploit its potential.

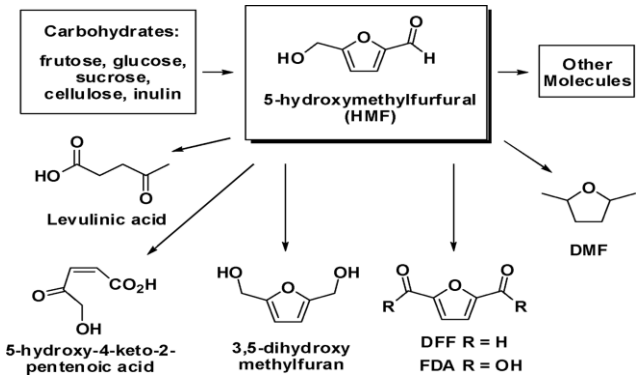

Figure 2.11: Scheme detailing variety of products obtained from HMF. (Scheme obtained from reference 47).

HMF contains an aldehyde and alcohol group attached to a furan ring. The two functional groups attached to this ring are of synthetic interest. The oxidation of alcohols and aldehydes to carboxylic acids and esters is a fundamental industrial process with uses in the food and perfume industry. With regards to the packaging industry oxidation of HMF to 2,5,furandicarxylic acid (FDCA) is of interest as FDCA can act as a replacement for terephthalate acid used in the manufacture of PET plastics[58]. The first step towards such synthesis of an industrially important chemical is the oxidation of HMF. Traditional industrial oxidation may rely on toxic chemicals with detrimental environmental effects.

A benign oxidation route using atmospheric oxygen as the stoichiometric oxidant would be highly desirable. To perform such an oxidation a catalyst will be required, in 2.3.1 a discussion of heterogeneous catalysis using gold nanoparticles to oxidise alcohols along with HMF is presented.

2.3.1 Oxidation of Alcohols using Gold Nanoparticles

Prati and Rossi first reported the ability of gold nanoparticles to catalyse the oxidation of diols using mild reaction conditions[59] (363 K and 300 kPa O_2 Pressure). Subsequent studies confirm gold nanoparticle catalysed alcohol oxidation is not limited to diols as ethanol[60] (Au/NiO) and glycerol[61] (Au/C) are examples of other alcohol group oxidation reactions.

Jorgensen *et al.* investigated oxidation of ethanol to acetic acid on spinnel ($MgAl_2O_4$) and TiO_2. Reactivity differences were observed between these support materials with the titania system producing higher yields than spinnel. Yield calculations along with ethanol conversion data indicate the presence of an intermediate proposed to be the ethanaldehyde. For this oxidation it is suggested the rate limiting step is the conversion of ethanol to ethanaldehyde[62] with subsequent oxidation oxidised to ethanoic acid reported to occur with ease (figure 2.12).

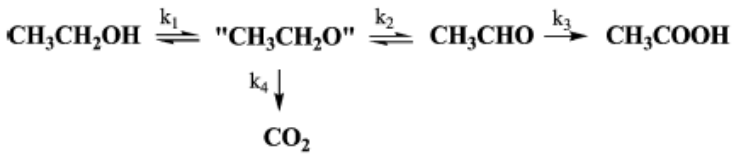

Figure 2.12: Pathway proposed by Jorgensen *et al.* for the conversion of ethanol to ethanoic acid. Reaction mechanism taken from reference 62.

Ethylethanoate is another product observed during the oxidation of ethanol therefore indicating 100% selectivity does not occur. Undesirable selectivity may prove problematic for glycerol oxidation due to the presence of three alcohol groups presenting various oxidation possibilities. This however is not the case as Hutchings *et al.* confirm 100% selectivity towards production of glyceric acid (starting from glycerol) using gold particles supported on charcoal or graphite at 60^{o}C with H_2O as solvent[63]. In this reaction it is suggested oxidation proceeds via glyceraldehyde intermediate analogous to ethanol oxidation therefore supporting previous work by Jorgensen that an aldehyde is the intermediate product.

Mechanistic understanding of alcohol oxidation using gold nanoparticles is essential for efficient catalyst design and discussion of mechanistic data is presented in 2.3.2.

2.3.2 Mechanism for Alcohol Oxidation using Gold Particles

Friend *et al.* investigated the vapour-phase gold (111) surface mediated coupling of aldehydes with methanol. It is suggested that atomic oxygen bound to a gold nanoparticle assists the reaction by producing a methoxy intermediate from the reacting methanol (through H abstraction). The introduction of an aldehyde to the reaction induces nucleophilic attack by the methoxy to the electropositive carbon of the aldehyde to produce methyl esters in a highly selective synthesis. This work confirmed cross coupling of the aldehydes was the predominant reaction as opposed to self-coupling of methoxy. This was confirmed through kinetic isotopic labelling studies[64]. Figure 2.1.3 details this process.

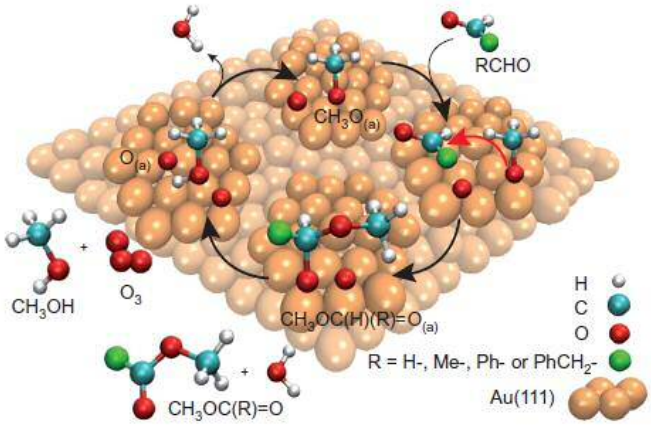

Figure 2.13: Graphic detailing proposed mechanism for cross coupling of aldehydes with methanol as obtained by Friend *et al.* Figure taken from reference 64.

It is interesting to note this work proposes the nucleophilic attack of the formaldehyde by the methoxy is preferred over the beta hydride elimination of methoxy to produce formaldehyde. This observation indicates such an elimination is energetically unfavourable under these reaction conditions. Secondary oxidation to form carboxylate species was found to be less than 5% relative to the ester production even if an excess of aldehyde is used.

To investigate the role of surface bound atomic oxygen on gold a kinetic isotope labelling study was performed by Madix and Outka where deuterated methanol (CD_3OH) was used as a test molecule. In this study H_2O was detected as opposed to any deuterated water therefore indicating the abstraction of the proton by surface bound oxygen entirely involves the hydroxy

hydrogen of an alcohol molecule[65]. By extension is therefore reasonable to assume the first step in a heterogeneous catalytic oxidation of an alcohol is the cleavage of the O-H bond.

Friend *et al.* performed another self-coupling study this time using ethanol on Au (111) surfaces. The aim of this study is to deduce the influence of surface bound oxygen on selectivity (more specifically oxygen coverage ratio). Esterification to produce ethylethanoate predominately occurs at oxygen coverages of 0.2 ML with ethanoic acid produced at higher coverages indicating high surface bound oxygen coverage is a requirement for conversion of ethanol to ethanoic acid[66]. Mechanisticly this suggests production of ethanaldehyde requires oxygen to facilitate two separate H abstractions (O-H and C-H). Once in this aldehyde form oxidation to the carboxylic acid is facile.

Experimental observations indicate the conversion of alcohol to aldehyde may be energetically unfavourable and as a result a full understanding of this conversion is required in order to design better catalysts to facilitate conversion. A detailed study by Corma *et al.* combined DFT and experimental data with results summarised below:

1) The mechanism for selective oxidation of ethanol to ethanaldehyde consists of a dehydrogenation of the hydroxyl group (to an ethoxy surface bound species) followed by a subsequent beta hydrogen transfer to the Au surface.
2) Dehydrogenation has been determined as the rate-limiting step in this reaction. Calculated reaction barriers decrease from 32.7 kcal mol^{-1} for single crystal Au (111) to 19.2 kcal mol^{-1} for the cuboctahedral Au_{38} cluster modelled. This indicates hindrance due to the rate limiting step can be mitigated through using smaller particles.
3) Strong adsorption energies are a requirement in order to overcome calculated reaction barriers with gold coordination number inversely related to adsorption energies.
4) Kinetic experiments measuring rates of benzyl alcohol oxidation were performed on Au / MgO systems where an inverse relationship between particle size (and hence coordination number) and rate supported the DFT calculations[67].

A graphical route detailing oxidation of ethanol to aldehyde is displayed in figure 2.1.4. This work has been performed using gold particles without the presence of oxygen. Future DFT studies using O to facilitate H abstraction would be of interest in quantifying reaction barrier differences with and without O and may the support the experimental observation that increased O coverage facilitates conversion of alcohol to aldehyde.

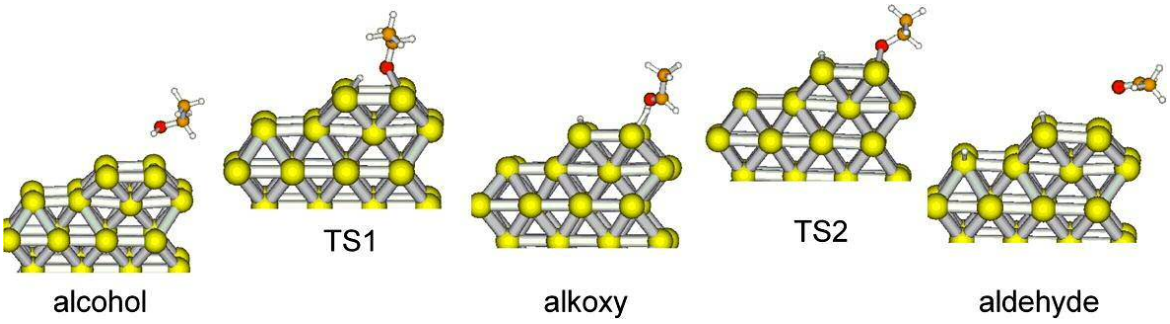

Figure 2.14: Conversion pathway for alcohol to aldehyde as proposed by Corma *et al*. TS1 is abstraction of the O-H proton whilst TS2 is secondary abstraction of C-H proton forming an aldehyde. Figure taken from reference 67.

2.3.3 Conversion of HMF to FDCA Using Gold Nanoparticles

Oxidation of HMF using gold nanoparticles is reported using a variety of supports[68–70]. Taarning *et al.* report conversion of HMF to FDCA using gold supported on titania. 8% sodium methoxide was added to enhance the reaction rate with a 98% yield reported[71]. Kinetic investigation confirms the alcohol oxidation is the rate limiting step in this reaction with the aldehyde side chain undergoing rapid oxidation by the solvent. Isotopic labelling of oxygen indicates that no atmospheric oxygen is incorporated within HMF during oxidation. Instead oxygen from the solvent water is added directly to the aldehyde intermediate forming FDCA. It is suggested hydroxide ions in water promote O-H activation in the alcohol and C-H bond forming the aldehyde intermediate. No characterisation of the size of gold nanoparticles has been performed by Taarning therefore no further discussion regarding the influence of gold nanoparticle size can be made.

Many aerobic oxidation reactions using gold nanoparticles are reported to require the use of a base. Marsden *et al.* report how the oxidative esterification of aldehydes to methyl benzoate using gold nanoparticles can be influenced by using varying amounts of NaOMe base[72]. In this study conversion rates increased if 10% NaOMe was added. The role of acids and bases in aerobic oxidation of alcohols over gold catalysts has been studied in detail by Klitgaard *et al*. Potassium titranate nanowires were used as support for gold nanoparticles and benzyl alcohol in methanol was oxidised to methyl benzoate. It was found that the presence of a catalytic amount of base promotes the reaction. The oxidation of benzyl alcohols at room temperature and 1 bar oxygen pressure is reported to produce a yield of approximately 18% after a few

days. Addition of a catalytic amount of base (KOH) is reported to dramatically increase the extent of reaction with over 99% conversion of benzyl alcohol after a day[73].

The increased operating cost incurred by using a stoichiometric or excess amount of base is problematic if industrial scale-up is to be performed on HMF conversion. As a result, numerous modifications to the metal particle / support have been performed attempting to remove the requirement of a base for this oxidation. Success has been achieved using gold palladium alloys supported on carbon nanotubes. Wan *et al.* report oxidation of HMF occurs in a three stages for Pd / CNT and Au-Pd/ CNT catalyst (figure 2.15), bypassing the degradation products observed when using Au /CNT[74].

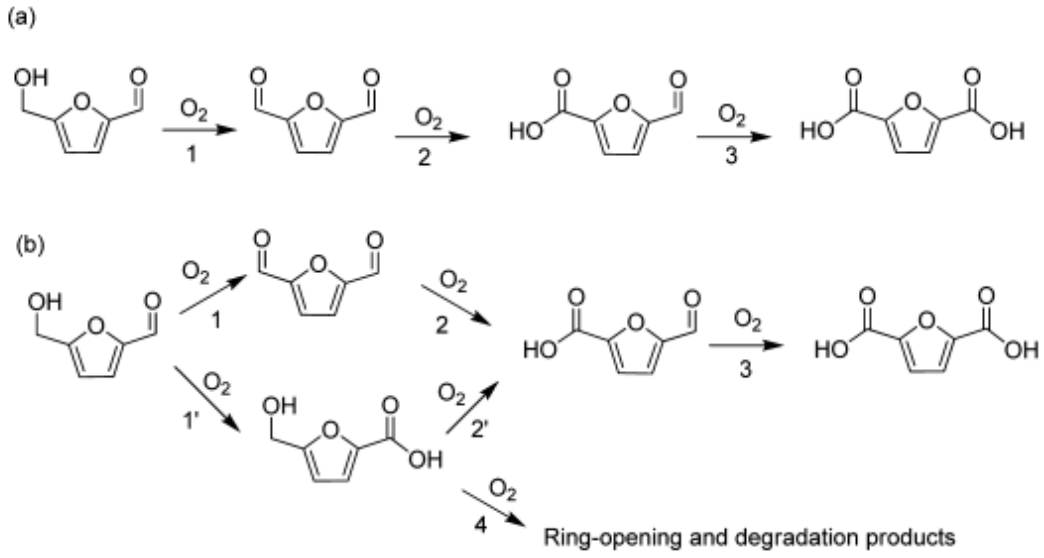

Figure 2.15: Oxidation route of HMF to FDCA using Pd/CNT and Au-Pd/CNT (a) and Au/CNT catalysts as proposed by Wan *et al*. Reaction scheme taken from reference 74.

A review of the literature indicates a clear consensus that the rate limiting step in the oxidation of alcohols and by direct extension HMF is the activation of the alcohol side chain. To the author's knowledge no DFT modelling has been performed to compute a barrier to O-H cleavage (in HMF) and therefore a comprehensive study of the interaction of HMF with metal particles is presented in chapter 6. Bimetallic particle investigation will also be performed with an emphasis on comparative adsorption / activation energies between pure and bimetallic particles performed with the aim of adding quantitative barrier data relating to O-H cleavage.

2.3.4 Levulinic Acid Conversion

As depicted in figure 2.11 levulinic acid (LA) can be obtained from HMF. LA can undergo conversion to γ-valerolactone (GVL), a promising biofuel[75] mainly due to its non-competition with food production when HMF is derived from cellulose in food production waste product streams. The conversion of LA to GVL occurs via heterogeneous catalysis with Deng *et al.* reporting TOF using an Ru / C system of 5345 h^{-1} which is substantially higher than Pd / C (68 h^{-1})[76].

The 2015 British Geological Survey risk list ranks ruthenium at 7.6[77]. This indicates a significant risk as the scale runs from 1-10 with 10 indicating the highest risk category. Several factors contribute to the overall risk rating however in the case of ruthenium total reserves coupled with supply centred in few countries warrant this high ranking.

The NOVACAM project aims to replace at risk elements used within catalysis with more abundant alternatives. The catalytic conversion of LA to GVL has been selected for investigation with success achieved using Cu-ZrO_2 under reaction conditions requiring H_2 pressure of 35 bar[75]. Conversion using Ru / C requires 5 bar H_2 therefore the industrial scale up costs accompanied by increased pressure requirements negate any benefits of using a more abundant material.

Through internal discussion along with unpublished research it is suggested that the rate limiting step in the Cu-ZrO_2 catalysed reaction and hence why 35 bar H_2 is required is the adsorption and activation of H_2 on the metal particle.

Adsorbate – metal surface interactions have been studied in depth by Norskov *et al*. In this study DFT calculations were performed investigating the interaction of H_2 with Cu, Ni, Pt and Au in order to ascertain why the interaction and barrier to dissociation of H_2 on gold are weakest. The results of this study confirm it is the electronic properties of the metal support which influence adsorbate interaction. The interaction and subsequent dissociation of H_2 is dependent upon two factors: filling of antibonding 1s orbitals and initial overlap between bonding orbitals and surface electrons[78].

Norskov *et al.* have proposed the d-band model for description of surface adsorbate interactions[79]. In this model interaction of adsorbate valence states and the s and d states of a transition metal are described. The strength of the interaction is related to the filling of the

antibonding states within the adsorbate. Correlation exists between the metal d states (relative to Fermi level) and interaction strength. The higher the d-band centre the higher the energy of the antibonding states in the adsorbate (once coupled to the metal) and therefore the less likely to be filled corresponding to a stronger bond.

Using this d-band model, DOS calculations will be performed in chapter 7 to determine whether sizeable differences exist between d-band centres of Ru and Cu bulk metals. Extension of this will be performed to investigate whether it can be altered by doping of the bulk.

2.4 Iron Oxide / Gold Nanoparticle Catalysed Systems

Iron oxides have widespread industrial usage as its ores are used to produce both iron and steel. Iron oxides are not just limited to metal production, other uses such pigmentation[80], magnetic recording[81] and uses within medicine[82] make it a vital material for industry. Iron oxides find use within catalysis as their surfaces are commonly used as supports for nanoparticles with gold particles supported onto α-Fe_2O_3 surfaces demonstrated to catalyse oxidation reactions[70]. With regards to gold particles it is widely accepted for CO oxidation a diameter of 5 nm or less is required for catalytic activity[12]. However recent characterisation has deduced that much smaller $_{\sim}Au_{10}$ particles play an active role in catalysing CO oxidation on iron oxide surfaces[83]. DFT studies have been performed on this system and demonstrate the feasibility of Au_{10} to catalyse this oxidation reaction[84], demonstrating the importance of this subnanometer sized gold particle within catalysis.

The role of the support within oxidation reactions catalysed by nanoparticles has been the subject of much discussion within the literature. Fe_2O_3 is classed as an "active support" as it has been demonstrated to adsorb large quantities of oxygen during CO oxidation reactions[85]. Surface oxygen defects within the support material have also been suggested to be nucleation sites for Au nanoparticles[86]. Mechanisms in which the surface contributes to the overall rate equation are classed as Mars van Krevelen mechanisms (MvK). MvK mechanisms have been suggested for CO hydrogenation on iron carbide surfaces[87], formaldehyde oxidation over Pt / hydrophobic supports[88] and deoxygenation of carboxylic acids to form aldehydes[89]. Figure 2.16 is a graphical representation of an MvK proposed by Hargus *et al*. In this mechanism oxygen vacancy sites on ZnO are required as they are chemisorption sites for incoming carboxylic acid molecules. The carboxylic acid deoxygenates replenishing the defected surface.

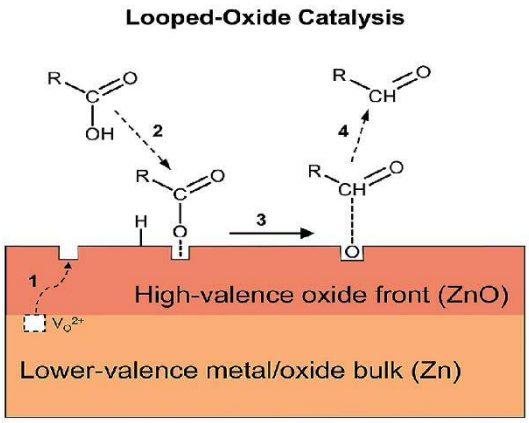

Figure 2.16: Graphical representation of MvK mechanism for deoxygenation of carboxylic acid to aldehyde as proposed by Hargus *et al.* Figure taken from reference 89.

An increasing body of evidence indicates low temperature CO oxidation catalysed by gold nanoparticles on reducible supports occurs via a MvK mechanism. Li *et al.* proposed this mechanism for Au / FeO_x reporting MvK mechanism at temperatures as low as -60°C[90]. Lattice oxygen of Fe_2O_3 is also reported to be involved in catalytic soot oxidation – a vital component of the three-way car exhaust catalyst. In this mechanism migration of oxygen from the bulk to the soot is reported to replenish surface oxygen defect sites which arise due to incorporation of O within carbon forming CO_2[91].

As surface oxygen defects are reported to be an essential component of certain catalytic cycles it is of interest to investigate how these defect energies are influenced if at all by the presence of a supported metal particle. Below is a summary of literature.

Illas *et al*. demonstrate that removal of a surface CeO_2 oxygen atom migration to the supported Pt_8 cluster is considerably easier than removal of an oxygen atom from the bare surface[92]. Elucidating the influence of the supported cluster in defect energies on Fe_2O_3 has been studied to a lesser extent therefore the authors of this work present a comprehensive study of how an Au_{10} cluster influences the oxygen defect energy on a (0001) Fe_2O_3 surface. Of particular interest is how surface oxygen defect energies are influenced by measuring proximity with the supported particle. Computational studies by Henkelman *et al.* demonstrate lattice oxygen as opposed to atmospheric oxygen at the step edge of CeO_2 oxidizes carbon monoxide bound to an Au_{12} nanocluster[93].

Of particular interest is a study by Widmann *et al.* where highly sensitive TAP measurements were performed to investigate the origin of the active oxygen species in Au/TiO_2 catalysed CO oxidation. The striking conclusion obtained through this investigation is surface oxygen on TiO_2 at the periphery of the gold particle are abstracted and incorporated within CO to form CO_2. The role of molecular oxygen in this instance is to replenish surface oxygen on TiO_2[94].

From this study it is reasonable to assume at close proximity to the gold particle surface oxygen removal is facilitated by the particle. An extension of Widmann *et al.* investigation is to quantify defect energies at a function of distance from the particle and probe the effect of a bimetallic particle on these defect energies.

References

1. Haruta, M. When Gold Is Not Noble: Catalysis by Nanoparticles. *Chem. Rec.* **3,** 75 (2003)

2. Mohr, F. & Schmidbaur, H. *Gold Chemistry: Applications and Future Directions in the Life Sciences*. (John Wiley & Sons, 2009). at <https://books.google.co.uk/books?id=eMZSOG5JJywC>

3. HARUTA, M. Gold catalysts prepared by coprecipitation for low-temperature oxidation of hydrogen and of carbon monoxide. *J. Catal.* **115,** 301 (1989)

4. Haruta, M. Size- and support-dependency in the catalysis of gold. *Catal. Today* **36,** 153 (1997)

5. Boccuzzi, F., Chiorino, A., Manzoli, M., Andreeva, D. & Tabakova, T. FTIR Study of the Low-Temperature Water–Gas Shift Reaction on Au/Fe2O3 and Au/TiO2 Catalysts. *J. Catal.* **188,** 176 (1999)

6. Hutchings, G. J. *Vapor phase hydrochlorination of acetylene: Correlation of catalytic activity of supported metal chloride catalysts*. *Journal of Catalysis* **96,** (1985)

7. Herzing, A. A., Kiely, C. J., Carley, A. F., Landon, P. & Hutchings, G. J. Identification of active gold nanoclusters on iron oxide supports for CO oxidation. *Science* **321,** 1331 (2008)

8. Schubert, M. M. *et al.* CO Oxidation over Supported Gold Catalysts—'Inert' and 'Active' Support Materials and Their Role for the Oxygen Supply during Reaction. *J. Catal.* **197,** 113 (2001)

9. Sanchez, A. *et al.* When Gold Is Not Noble: Nanoscale Gold Catalysts. *J. Phys. Chem A.* **103,** 38 (1999)

10. Xu, Y. & Mavrikakis, M. Adsorption and Dissociation of O_2 on Gold Surfaces: Effect of Steps and Strain. *J. Phys. Chem. B* **107,** 9298 (2003)

11. Lopez, N. & Nørskov, J. K. Catalytic CO Oxidation by a Gold Nanoparticle: A Density Functional Study. *J. Am. Chem. Soc.* **124,** 11262 (2002)

12. Lopez, N. On the origin of the catalytic activity of gold nanoparticles for low-temperature CO oxidation. *J. Catal.* **223,** 232 (2004)

13. Rogers, S. M. *et al.* Tailoring Gold Nanoparticle Characteristics and the Impact on Aqueous-Phase Oxidation of Glycerol. *ACS Catal.* **5,** 4377 (2015)

14. Li, Z. *et al.* Experimental and DFT studies of gold nanoparticles supported on MgO(111) nano-sheets and their catalytic activity. *Phys. Chem. Chem. Phys.* **13,** 2582 (2011)

15. Mavrikakis, M., Stoltze, P. & Nørskov, J. K. Making gold less noble. *Catal. Letters* **64,** 101 (2000)

16. Herzing, A. A., Kiely, C. J., Carley, A. F., Landon, P. & Hutchings, G. J. Identification of active gold nanoclusters on iron oxide supports for CO oxidation. *Science* **321,** 1331 (2008)

17. Lee, S. *et al.* Selective propene epoxidation on immobilized au(6-10) clusters: the effect of hydrogen and water on activity and selectivity. *Angew. Chem. Int. Ed. Engl.* **48,** 1467 (2009)

18. Valden, M., Lai, X. & Goodman, D. W. Onset of Catalytic Activity of Gold Clusters on Titania with the Appearance of Nonmetallic Properties. *Science (8).* **281,** 80 (1998)

19. Boronat, M., Leyva-Pérez, A. & Corma, A. Theoretical and experimental insights into the origin of the catalytic activity of subnanometric gold clusters: attempts to predict reactivity with clusters and nanoparticles of gold. *Acc. Chem. Res.* **47,** 834 (2014)

20. Roldán, A., González, S., Ricart, J. M. & Illas, F. Critical size for O(2) dissociation by au nanoparticles. *Chemphyschem* **10,** 348 (2009)

21. Boronat, M. & Corma, A. Oxygen activation on gold nanoparticles: separating the influence of particle size, particle shape and support interaction. *Dalton Trans.* **39,** 8538 (2010)

22. Mills, G., Gordon, M. S. & Metiu, H. Oxygen adsorption on Au clusters and a rough Au(111) surface: The role of surface flatness, electron confinement, excess electrons, and band gap. *J. Chem. Phys.* **118,** 4198 (2003)

23. Walker, A. V. Structure and energetics of small gold nanoclusters and their positive ions. *J. Chem. Phys.* **122,** 94310 (2005)

24. Bravo-Pérez, G., Garzón, I. L. & Novaro, O. Non-additive effects in small gold clusters. *Chem. Phys. Lett.* **313,** 655 (1999)

25. Xiao, L. & Wang, L. *From planar to three-dimensional structural transition in gold clusters and the spin–orbit coupling effect*. *Chemical Physics Letters* **392,** 452 (2004)

26. Erkoç, Ş. Stability of gold clusters: molecular-dynamics simulations. *Phys. E Low-dimensional Syst. Nanostructures* **8,** 210 (2000)

27. Longo, R. & Gallego, L. Structures of 13-atom clusters of fcc transition metals by ab initio and semiempirical calculations. *Phys. Rev. B* **74,** 193409 (2006)

28. Häberlen, O. D., Chung, S.-C., Stener, M. & Rösch, N. From clusters to bulk: A relativistic density functional investigation on a series of gold clusters Au[sub n], n=6,…,147. *J. Chem. Phys.* **106,** 5189 (1997)

29. Assadollahzadeh, B. & Schwerdtfeger, P. A systematic search for minimum structures of small gold clusters Au(n) (n=2-20) and their electronic properties. *J. Chem. Phys.* **131,** 64306 (2009)

30. Alhumaimess, M. *et al.* Oxidation of benzyl alcohol by using gold nanoparticles supported on ceria foam. *ChemSusChem* **5,** 125 (2012)

31. Alshammari, H. *et al.* Initiator-free hydrocarbon oxidation using supported gold nanoparticles. *Catal. Sci. Technol.* **4,** 908 (2014)

32. Molina, L. M., Rasmussen, M. D. & Hammer, B. Adsorption of O[sub 2] and oxidation of CO at Au nanoparticles supported by TiO[sub 2](110). *J. Chem. Phys.* **120,** 7673 (2004)

33. Bond, G. C. & Thompson, D. T. Gold-catalysed oxidation of carbon monoxide. *Gold Bull.* **33,** 41 (2000)

34. Minicò, S., Scirè, S., Crisafulli, C., Visco, A. M. & Galvagno, S. FT-IR study of Au/Fe2O3 catalysts for CO oxidation at low temperature. *Catal. Letters* **47,** 273 (1997)

35. Grunwaldt, J.-D. & Baiker, A. Gold/Titania Interfaces and Their Role in Carbon Monoxide Oxidation. *J. Phys. Chem. B.* **103,** 1002 (1999)

36. Wallace, W. T. & Whetten, R. L. Coadsorption of CO and O 2 on Selected Gold Clusters: Evidence for Efficient Room-Temperature CO 2 Generation. *J.Am.Chem.Soc.* **124,** 7499 (2002)

37. Häkkinen, H. & Landman, U. Gold clusters (Au N , 2 <~ N <~ 1 0) and their anions. *Phys. Rev. B* **62,** 2287 (2000)

38. Turkevich, *J. Colloidal gold*. Part I. *Gold Bull.* **18,** 86 (1985)

39. Guzman, J. & Gates, B. C. Gold Nanoclusters Supported on MgO: Synthesis, Characterization, and Evidence of Au 6.*Nano Letters.* **1,** 689 (2001)

40. Cox, D. M., Brickman, R., Creegan, K. & Kaldor, A. Gold clusters: reactions and deuterium uptake. *Zeitschrift fur Phys. D Atoms, Mol. Clust.* **19,** 353 (1991)

41. Salisbury, B. ., Wallace, W. . & Whetten, R. . Low-temperature activation of molecular oxygen by gold clusters: a stoichiometric process correlated to electron affinity. *Chem. Phys.* **262,** 131 (2000)

42. Mills, G., Gordon, M. S. & Metiu, H. The adsorption of molecular oxygen on neutral and negative Aun clusters (n=2–5). *Chem. Phys. Lett.* **359,** 493 (2002)

43. Visart de Bocarmé, T. *et al.* Oxygen adsorption on gold nanofacets and model clusters. *J. Chem. Phys.* **125,** 54703 (2006)

44. Yoon, B., Häkkinen, H. & Landman, U. Interaction of O 2 with Gold Clusters: Molecular and Dissociative Adsorption. *J. Phys. Chem. A* **107,** 4066 (2003)

45. Pal, R., Wang, L.-M., Pei, Y., Wang, L.-S. & Zeng, X. C. Unraveling the Mechanisms of O 2 Activation by Size-Selected Gold Clusters: Transition from Superoxo to Peroxo Chemisorption. *J.Am.Chem.Soc.* **134,** 9438 (2012)

46. Franceschetti, A., Pennycook, S. J. & Pantelides, S. T. *Oxygen chemisorption on Au nanoparticles*. *Chem Phys Letters* **374,** 417 (2003)

47. Wang, Y. & Gong, X. G. First-principles study of interaction of cluster Au 32 with CO, H 2 , and O 2 First-principles studies for CO and O 2 on gold nanocluster First-principles study of interaction of cluster Au 32 with CO, H 2 , and O 2. *J. Chem. Phys.* **125,** 124703 (2006)

48. Weiher, N. *et al.* Activation of Oxygen by Metallic Gold in Au/TiO $_2$ Catalysts. *J. Am. Chem. Soc.* **129,** 2240 (2007)

49. Xu, J. *et al.* Biphasic Pd−Au Alloy Catalyst for Low-Temperature CO Oxidation. *J. Am. Chem. Soc.* **132,** 10398 (2010)

50. Zhang, H., Watanabe, T., Okumura, M., Haruta, M. & Toshima, N. Catalytically highly active top gold atom on palladium nanocluster. *Nat. Mater.* **11,** 49 (2011)

51. Landon, P., Collier, P. J., Papworth, A. J., Kiely, C. J. & Hutchings, G. J. Direct formation of hydrogen peroxide from H2/O2 using a gold catalyst. *Chem. Commun.* **18,** 2058 (2002)

52. Yu, W.-Y., Zhang, L., Mullen, G. M., Henkelman, G. & Mullins, C. B. Oxygen Activation and Reaction on Pd–Au Bimetallic Surfaces. *J. Phys. Chem. C* **119,** 11754 (2015)

53. Staykov, A., Derekar, D. & Yamamura, K. Oxygen dissociation on palladium and gold core/shell nanoparticles. *Int. J. Quantum Chem.* (2016)

54. British Plastics Federation. at <www.bpf.co.uk> Last Checked July 2016

55. *Biofoams: Science and Applications of Bio-Based Cellular and Porous Materials*. (CRC Press, 2015) <https://books.google.com/books?id=AHe9CgAAQBAJ&pgis=1>

56. Rosatella, A. A., Simeonov, S. P., Frade, R. F. M. & Afonso, C. A. M. 5-Hydroxymethylfurfural (HMF) as a building block platform: Biological properties, synthesis and synthetic applications. *Green Chem.* **13,** 754 (2011)

57. Bozell, J. J. & Petersen, G. R. Technology development for the production of biobased products from biorefinery carbohydrates—the US Department of Energy's 'Top 10' revisited. *Green Chem.* **12,** 539 (2010)

58. Eerhart, A. J. J. E., Faaij, A. P. C. & Patel, M. K. Replacing fossil based PET with biobased PEF; process analysis, energy and GHG balance. *Energy Environ. Sci.* **5,** 6407 (2012)

59. Prati, L. Gold on Carbon as a New Catalyst for Selective Liquid Phase Oxidation of Diols. *J. Catal.* **176,** 552 (1998)

60. Takei, T., Suenaga, J., Ishida, T. & Haruta, M. Ethanol Oxidation in Water Catalyzed by Gold Nanoparticles Supported on NiO Doped with Cu. *Top. Catal.* **58,** 295 (2015)

61. Sankar, M. *et al.* Oxidation of glycerol to glycolate by using supported gold and palladium nanoparticles. *ChemSusChem* **2,** 1145 (2009)

62. Jørgensen, B., Egholm Christiansen, S., Dahl Thomsen, M. L. & Christensen, C. H. Aerobic oxidation of aqueous ethanol using heterogeneous gold catalysts: Efficient routes to acetic acid and ethyl acetate. *J. Catal.* **251,** 332 (2007)

63. Carrettin, S., McMorn, P., Johnston, P., Griffin, K. & Hutchings, G. J. Selective oxidation of glycerol to glyceric acid using a gold catalyst in aqueous sodium hydroxide. *Chem. Commun. (Camb).* 696–7 (2002). at <http://www.ncbi.nlm.nih.gov/pubmed/12119680>

64. Xu, B., Liu, X., Haubrich, J. & Friend, C. M. Vapour-phase gold-surface-mediated coupling of aldehydes with methanol. *Nat. Chem.* **2,** 61 (2010)

65. Outka, D. A. & Madix, R. J. Broensted basicity of atomic oxygen on the gold(110) surface: reactions with methanol, acetylene, water, and ethylene. *J. Am. Chem. Soc.* **109,** 1708 (1987)

66. Liu, X., Xu, B., Haubrich, J., Madix, R. J. & Friend, C. M. Surface-Mediated Self-Coupling of Ethanol on Gold. *J. Am. Chem. Soc.* **131,** 5757 (2009)

67. Boronat, M. *et al.* Mechanism of selective alcohol oxidation to aldehydes on gold catalysts: Influence of surface roughness on reactivity. *J. Catal.* **278,** 50 (2011)

68. Casanova, O., Iborra, S. & Corma, A. Biomass into chemicals: aerobic oxidation of 5-hydroxymethyl-2-furfural into 2,5-furandicarboxylic acid with gold nanoparticle catalysts. *ChemSusChem* **2,** 1138 (2009)

69. Gorbanev, Y. Y., Klitgaard, S. K., Woodley, J. M., Christensen, C. H. & Riisager, A. Gold-Catalyzed Aerobic Oxidation of 5-Hydroxymethylfurfural in Water at Ambient Temperature. *ChemSusChem* **2,** 672 (2009)

70. Gupta, N. M. & Tripathi, A. K. The role of nanosized gold particles in adsorption and oxidation of carbon monoxide over Au/Fe2O3 Catalyst. *Gold Bull.* **34,** 120 (2001)

71. Gupta, N. K. *et al.* Hydrotalcite-supported gold-nanoparticle-catalyzed highly efficient base-free aqueous oxidation of 5-hydroxymethylfurfural into 2,5-furandicarboxylic acid under atmospheric oxygen pressure. *Green Chem.* **13,** 824 (2011)

72. Marsden, C. *et al.* Aerobic oxidation of aldehydes under ambient conditions using supported gold nanoparticle catalysts. *Green Chem.* **10,** 168 (2008)

73. Klitgaard, S. K. *et al.* Aerobic Oxidation of Alcohols over Gold Catalysts: Role of Acid and Base. *Catal Lett.* **126,** 213 (2008)

74. Wan, X. *et al.* Base-Free Aerobic Oxidation of 5-Hydroxymethyl-furfural to 2,5-Furandicarboxylic Acid in Water Catalyzed by Functionalized Carbon Nanotube-Supported Au−Pd Alloy Nanoparticles. *ACS Catal.* **4,** 2175 (2014)

75. Jones, D. R. *et al.* The conversion of levulinic acid into γ-valerolactone using Cu–ZrO $_2$ catalysts. *Catal. Sci. Technol.* **49,** 4479 (2016)

76. Deng, L. *et al.* Conversion of Levulinic Acid and Formic Acid into γ-Valerolactone over Heterogeneous Catalysts. *ChemSusChem* **3,** 1172 (2010)

77. Risk list 2015 | Commodities & statistics | MineralsUK. at <http://www.bgs.ac.uk/mineralsuk/statistics/risklist.html> Last Checked August 2016

78. Hammer, B. & Norskov, J. K. Why gold is the noblest of all the metals. *Nature* **376,** 238 (1995)

79. Norskov, J. K., Abild-Pedersen, F., Studt, F. & Bligaard, T. Density functional theory in surface chemistry and catalysis. *Proc. Natl. Acad. Sci.* **108,** 937 (2011)

80. Gunter, Buxbaum, Gerhard, P. *Industrial Inorganic Pigments*. (2005)

81. Sugimoto, M. The Past, Present, and Future of Ferrites. *J. Am. Ceram. Soc.* **82,** 269 (2004)

82. Kim, E. C. The Oxidation of Magnetic Particles in Medicinal Ointment. *J. Magn.* **17,** 83 (2012)

83. Herzing, A. A., Kiely, C. J., Carley, A. F., Landon, P. & Hutchings, G. J. Identification of active gold nanoclusters on iron oxide supports for CO oxidation. *Science* **321,** 1331 (2008)

84. Carley, A. F. *et al.* CO bond cleavage on supported nano-gold during low temperature oxidation. *Phys. Chem. Chem. Phys.* **13,** 2528 (2011)

85. Schubert, M. CO Oxidation over Supported Gold Catalysts—'Inert' and 'Active' Support Materials and Their Role for the Oxygen Supply during Reaction. *J. Catal.* **197,** 113 (2001)

86. Wahlström, E. *et al.* Bonding of Gold Nanoclusters to Oxygen Vacancies on Rutile TiO2(110). *Phys. Rev. Lett.* **90,** 26101 (2003)

87. Gracia, J. M., Prinsloo, F. F. & Niemantsverdriet, Bullet J W. Mars-van Krevelen-like Mechanism of CO Hydrogenation on an Iron Carbide Surface. *Catal Lett.* **133,** 257 (2009)

88. Chuang, K. T., Zhou, B. & Tong, S. Kinetics and Mechanism of Catalytic Oxidation of Formaldehyde over Hydrophobic Catalysts. *Ind. Eng. Chem. Res.* **33,** 1680 (1994)

89. Hargus, C. *et al.* Looped-oxide catalysis: a solar thermal approach to bio-oil deoxygenation. *Energy Environ. Sci.* **7,** 3122 (2014)

90. Li, L. *et al.* Origin of the high activity of Au/FeOx for low-temperature CO oxidation: Direct evidence for a redox mechanism. *J. Catal.* **299,** 90 (2013)

91. Wagloehner, S. & Kureti, S. Study on the mechanism of the oxidation of soot on Fe2O3 catalyst. *Appl. Catal. B Environ.* **125,** 158 (2012)

92. Bruix, A. *et al.* Effects of deposited Pt particles on the reducibility of CeO2(111). *Phys. Chem. Chem. Phys.* **13,** 11384 (2011)

93. Kim, H. Y. & Henkelman, G. CO Oxidation at the Interface of Au Nanoclusters and the Stepped-CeO 2 (111) Surface by the Mars–van Krevelen Mechanism. *J. Phys. Chem. Lett.* **4,** 216 (2013)

94. Widmann, D. & Behm, R. J. Activation of molecular oxygen and the nature of the active oxygen species for CO oxidation on oxide supported Au catalysts. *Acc. Chem. Res.* **47,** 740 (2014)

Chapter 3

Theoretical Background

This chapter will present the theory used throughout our work. Density functional theory (DFT) underpins the following methods which are discussed in this chapter: Bader charge analysis, vibrational frequency analysis, nudged elastic band calculations (NEB) and geometry optimisation. Along with plane wave methods localised basis sets have been used for Gaussian 09 calculations and a discussion of this method is presented.

3.1 Density Functional Theory

Density functional theory is perhaps the most widely used method to computationally investigate systems containing moderate to large numbers of atoms. Its popularity stems from accuracy achieved investigating a range of systems and generally good if perhaps less certain performance at analysing transition states and transition metal complexes[1]. An historical overview of DFT is presented in 3.1.1.

Essentials of Computational Chemistry by Cramer has been used as reference for this chapter[2].

3.1.1 The Origin of DFT

The Schrödinger equation (3.1) contains the wavefunction (which is dependant upon the positions and spin of the electrons it is describing. By splitting the Hamiltonian into its components (3.2) where is the kinetic energy , is the potential energy from the external positively charged nuclei and is the interaction energy between electrons the mathematical complexity in calculating can be appreciated.

(3.1)

—

(3.2)

For one electron systems, the Schrödinger equation can be used to determine exact ground state energies. As the number of electrons in a system increases, difficulty in solving the Schrödinger equation increases exponentially making it impossible to solve for large systems. The complexity of solving this equation led to the search for a simpler alternative.

The search was aided by knowledge that the Hamiltonian (H) only depends upon the positions and atomic number of the nuclei and the total number of electrons. The total number of electrons in a system is related to measurable electron density (ρ). Integration of electron density over all space (3.3) can be performed in order to deduce number of electrons (N).

(3.3)

Atomic nuclei by their nature are positively charged and therefore are considered point charges. Surrounding these nuclei will lie the electron density with maxima corresponding to regions of higher charge density. In order to finalise computation of the Hamiltonian atomic numbers are required which are computable via the electron density at a maximum (r_A).

——— (3.4)

is the average spherical density, Z is atomic number of a nucleus A, r_A is the radial distance from nucleus A.

Equation 3.2, 3.3 and 3.4 confirm electron density can be used to first obtain the Hamiltonian operator, input the Hamiltonian to solve the Schrödinger equation and then compute energies of a system. It does not provide any simplification of the difficult nature of the equation and therefore further approximations are required in order to determine properties of a system.

3.1.2 The Hohenberg-Kohn Theorems and Kohn-Sham DFT

In 1964 two theorems were put forward by Hohenberg and Kohn. The first theorem states the ground state properties of a system which contains many electrons can be determined by the electron density. The electron density depends on 3 spatial coordinates therefore reducing 3N spatial coordinates of a many electron system to three[3]. The second principle states the

minimised density corresponds to a ground state energy, confirming the relationship between these two properties.

The above theorems of Hohenberg and Kohn indicate that the density can determine the external potential, which can determine a Hamiltonian which subsequently can determine the wavefunction. With the wavefunction and Hamiltonian in hand the energy can be determined however this provides no simplicity over molecular orbital theory as the Schrödinger equation will still need to be solved. This is problematic as electron – electron interaction is a difficult term to compute within the Hamiltonian. With this information in mind further work to find a simplification was performed.

This simplification was obtained in 1965 when Hohenberg-Kohn decided to consider the Hamiltonian as a sum of one electron operators which are a set of non-interacting electrons[4]. This fictitious treatment of the system eliminates the need to compute electron-electron interaction. By taking a starting point of this fictitious system containing non interacting electrons that have same the ground state density of a real system the following mathematic derivation takes place:

Various components sum to make the energy functional, by splitting this functional into components further analysis can take place (3.5).

(3.5)

is kinetic energy of the non-interacting electrons (fictitious system), is the attraction energy between the nucleus and electrons, is the energy corresponding to electron-electron interactions, is the kinetic energy arising from electron correlation and is the non-classical electron contribution to the energy.

The corrections to the kinetic energy and the electron-electron interaction by treating them as non-interacting can be combined into one term which is E_{xc}. This is the exchange correlation energy term. The term not only contains the exchange and correlation corrections, but also the self-interaction correction and also the correction to the kinetic energy. Put simply E_{xc} is the sum of the error in using a non-interacting kinetic energy and treating electron-electron interactions as classical.

The Kohn-Sham equations (3.6 and 3.7) are non-linear which describe the behaviour of a non-interacting set of electrons in a local potential.

(3.6)

(3.7)

Kohn-Sham density functional theory is an empirical methodology meaning the exact functional cannot be determined. Approximations are made in order to obtain energies and these are presented in 3.1.3.

3.1.3 Exchange Correlation Functional

DFT methodologies employ many varieties of functionals, the underlying difference of these functionals is the treatment of E_{xc}. One route would be to find functionals which obey certain physical constraints, another is the parametric form which optimises it by fitting E_{xc} to a set of experiments.

Local density approximation (LDA)[5] is an approximation to the exchange-correlation energy which is dependent upon the value of electron density at points in space. Local density approximations are formalised in equation 3.8 where E_{xc} is the energy of each particle in the system interacting with the uniform electron gas of density .

(3.8)

In LDA the exchange-correlation energy in an infinitesimal volume in space (dr) is considered to be the same as the value if the whole of the space were filled with the homogeneous electron gas of the same density. This approximation holds true for systems in which the density slowly varies. In reality constant local density does not exist (electron density varies greatly at close proximity to the nucleus) and therefore it is understandable why the LDA method will have limitations. The correlation functional may be improved by considering how the density is

changing at the point being sampled. Most of these gradient corrected functionals have an additional term which is added to the LDA functional.

The generalized gradient approximation (GGA) has widely used with Becke (B88)[6], Perdew and Wang (PW91)[7] and Perdew, Burke and Enzerhof (PBE)[8] being the most widely used GGA functionals. Both LDA and GGA methods perform poorly in systems where electrons are strongly correlated or localised such as transition metal oxides[2]. In 3.2 a discussion of methods to increase accuracy is presented.

3.1.4 Pseudopotentials

The wavefunction by its nature differs substantially at close proximity to the nucleus, therefore finding a function which describes it at all distances is mathematically challenging. This is due to the rapidly changing electron density which occurs at close proximity to the nucleus.

Fortunately, properties of a chemical system are often governed by the valence states and not the core. Therefore, core states can be assumed to be fixed and treated as a "pseudopotential" which take into account effects of the nucleus (core contraction) in an appropriately accurate manner.

Norm conserving pseudopotentials are commonly used within DFT calculations. An all electron DFT calculation is first performed on the atom of interest and a norm conserving pseudopotential is chosen so that outside of the core the pseudo wavefunction generates the same charge density as the real system (3.9).

(3.9)

is the all electron wavefunction (obtained from Kohn-Sham calculation containing all electrons) and is the pseudopotential.

The projector augmented wave (PAW) method[9,10] is developed to provide a more accurate method of treating electrons particularly in instances where the wave function close the nucleus is of importance.

The PAW method is based on the following concept:

All electron energy is comprised of pseudo energy minis pseudo-onsite + all electron onsite interactions.

To account for long range electrostatic interactions between the spheres a soft compensation charge is introduced. Within VASP the PAW method is recommended through use of pre supplied pseudopotentials. The PBE[8,11] functional is used alongside the PAW method for calculations within this thesis.

3.2 Inclusion of Dispersion and Modelling Strongly Correlated Systems

3.2.1 Dispersion Interactions

Traditional DFT fails to account for long range dispersion interactions. These attractive interactions are vital components to the energies of DNA systems, inert gas interactions and catalytic surface / adsorbate systems.

An interaction energy plot (Lennard-Jones) indicates dispersion energy falls off as ⁻ therefore indicating the sufficiently long range which must be modelled to account for dispersion in calculations. A common method of including dispersion energies is to add a correction (E_{disp}) to the Kohn-Sham DFT energy obtaining $E_{DFT\text{-}D}$ (3.10).

(3.10)

The popular DFT-D2 method of Grimme[12] obtains E_{disp} from semi-empirical pair wise interactions given by equation 3.11.

⁻ (3.11)

N_{at} is the number of atoms in the system being modelled, is the dispersion coefficient between pair of atoms ij, s_6 is the global damping function which is functional dependant. To avoid a singularity at small R distances between atoms a damping function is used (f_{dmp}) (equation 3.12) where R_r is the sum of atomic van der Walls radii.

⁻ (3.12)

The dispersion coefficients can be obtained from a variety of methods, one being the use of a higher accuracy method (CCSD(T)). CCSD(T) is often labelled the "gold standard" for accounting for dispersion interactions within systems[13] and as a result, calculations can be performed in order to fit parameters to cheaper dispersion corrected functionals.

3.2.2 Strongly Correlated Systems

Electrons within d or f orbitals are often localised. These localised electrons are not accurately described using LDA or GGA. On-site self-interaction due to density approximations cause the electron to experience potential due to its own contribution to the density. For localised interactions this problem is especially acute with LDA and GGA giving solutions which tend to favour a distribution rather than localisation of 1 electron orbitals. In these cases, parameters are used to describe on-site Coulomb and exchange interactions (U and J respectively).

Dudarev *et al.* introduced a method to account for U and J within calculations[14]. This is formed by adding a "penalty function" to the DFT energy (equation 3.13). U is the spherically averaged Hubbard parameter which is used to describe an energy increase for placing an electron on a particular site, J is an exchange parameter.

—— (3.13)

In strongly correlated systems electron-electron repulsion through localised orbitals such as d and f are accounted for by using this correction and provide a more accurate treatment of these systems.

3.3 Bader Charge Analysis

Atomic charges are not observable and therefore are not contained within the output of a quantum mechanical calculation. Instead charge density is presented as an output with difficulty in partitioning electrons against atoms or molecules. Mulliken analysis[15] is fast and can provide partial charges on atoms however it is basis set sensitive and plane wave calculations do not centre functions on particular atom / atoms therefore rendering it unsuitable in these cases.

The approach of Bader is to use charge density partitioned over regions[16]. Space is divided into regions by surfaces that run through minima in the charge density[17]. The advantages of a Bader charge analysis is that it is solely dependent on the charge density and as a result is insensitive to the basis set used and is applicable to planewave calculations such as VASP.

Bader analysis is performed through integration of the electronic charge contained within a specified Bader region. Typically, Bader regions contain a nucleus however this is not a requirement for analysis. If neighbouring Bader regions do not contain a nucleus the electronic density in this region accompanied by the original Bader region can be added together to determine an estimate of the charge on an atom.

Implementation of this method within the VASP programme has been developed by Henkelmen *et al.*[17–19]. In this method grid points are used (i,j,k) where a steepest ascent move is made which maximises the charge density gradient. In order to speed up the calculations movement is only allowed from one grid point to the 26 neighbouring grid points. Derivatives of the charge density is calculated for each of these 26 directions (denoted $\hat{r}$) using equation 3.14.

— (3.14)

di, dj and dk are assigned numbers (-1, 0 or 1) with (0,0,0) being disallowed. The change in charge density is evaluated using equation 3.15.

(3.15)

The distance between neighbours is determined using equation 3.16.

(3.16)

is the Cartesian vector corresponding to grid point (i,j,k) with the steepest ascent step taken which maximises the positive values of the change density. If no positive values are found (i,j,k) is determined to be at a charge density maximum.

A graphical representation of this algorithm as developed by Henkelmen is presented in figure 3.1.

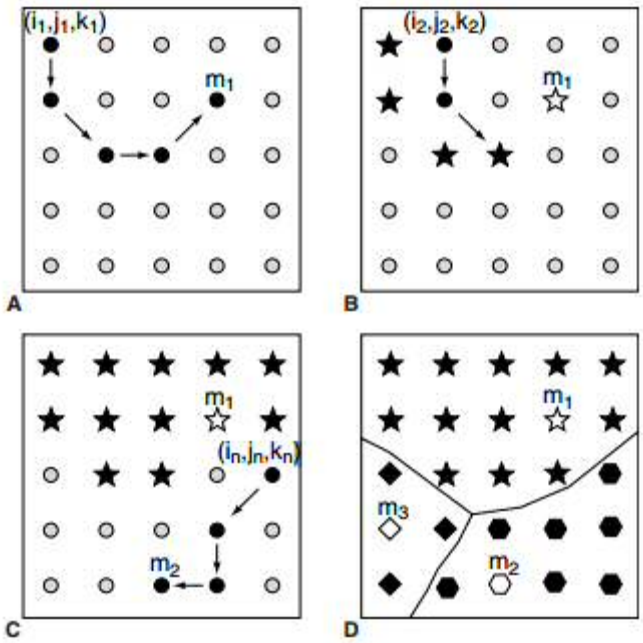

Figure 3.1: Graphical representation of equation 3.15 and 3.1 as proposed by Henkelmen *et al.* Figure taken from reference 17.

If pseudopotentials are used caution is required when analysing charge density as the core electron wavefunction will differ from the pseudopotential wavefunction. A charge density minimum may occur around the nucleus if pseudopotential is used with few valence electrons. In these instances, the core electron density can be added to the density determined at the grid points.

3.4 Vibrational Frequency Analysis

Atoms bonded together can be considered as simple harmonic oscillators where the period of oscillation (T) depends upon the reduced mass and the spring constant (k) (equation 3.17).

–
– (3.17)

VASP can compute vibrational frequencies by invoking the IBRION=5 or 6 tag within the INCAR file. For IBRION=5 displacement of all atoms in all Cartesian coordinates occurs whereas employing IBRION=6 utilizes symmetry to reduce the computational cost of calculating all elements of the Hessian matrix.

The forces are used to form the Hessian matrix (3.18). This matrix is comprised of second order differentials of the energy with respect to Cartesian coordinates of the atoms.

(3.18)

Through finite displacements (increments) of the atoms, gradients are calculated. Decrements follow with a recalculation of the gradient. The second derivative is obtained from the difference of these two derivatives along with the displacement step size (x) (3.19)

(3.19)

The Hessian can be redefined due to its symmetric nature (3.20)

(3.20)

To calculate the vibrational frequencies mass weighting of the Hessian matrix is required. This is performed through division of the elements within the matrix by the square root of the mass of the two atoms multiplied together (equation 3.21).

(3.21)

Matrix diagonalization produces eigenvalues corresponding to the square root of the spring constant over the reduced mass. These eigenvalues are then used to calculate the vibrational frequencies (equation 3.22).

(3.22)

Even with symmetry taken into consideration these calculations are often computationally expensive. Often a full analysis of each vibrational mode within a system is not required therefore by fixing all but the vibrational modes of interest the computational cost can be reduced. Within the VASP POSCAR file selective dynamics can be invoked by typing "selective dynamics" in the POSCAR file and assigning an "F" next to the coordinates of each atom to be fixed.

3.4.1 Imaginary Vibrational Frequencies

Confirmation that a valid transition state has been located is through vibrational frequency calculation as performed in 3.4. A transition state corresponds to a maximum on the PES therefore the second derivative will contain a single negative frequency corresponding to the mode which is maximised in the transition state.

3.5 Geometry Optimisers

This section is largely based on work performed by Sheppard *et al.*[20] and Wang *et al.*[21]

The Born-Oppenheimer approximation states the geometry of a molecule at absolute zero corresponds to the minimum of the total energy. Finding the positions of atoms which minimise the energy is called geometry optimisation with several methods used to locate these minima.

Geometry optimization is inherently a mathematical problem. The search for the minimum of a function requires computation of the Hessian matrix along with principle minors (reformatting of the matrix by elimination of certain rows to obtain coefficients) which are evaluated as follows:

1) If all principle minors are positive a minimum is found
2) If principle minors alternative between positive and negative a maximum is found.
3) For everything else a saddle point is found.

The VASP program utilizes various optimisation methods presented below.

3.5.1 Steepest Descent Method

The steepest descent method requires an approximate Hessian matrix. From this matrix the largest eigenvalue is taken and used to direct the algorithm to the next geometry. Steepest descent methods follow the force vector from the initial configuration to the new configuration (3.23)[20].

(3.23)

F_j is the force and is an adjustable parameter. If the adjustable parameter is chosen so it is the inverse of the curvature along the step direction the optimizer will move directly to the minimum along the F_j direction. This is repeated over all variables in the system.

The steepest descent method is regarded as a simple algorithm towards geometry optimisation however it converges at a very slow rate due to the small iteration step size[21]. This can be speeded up by increasing step size however an error may be introduced as a result. Best practise whilst using the steepest descent method is to start with geometries reasonably close to the minima to assist the algorithm.

3.5.2 Conjugate Gradient Method

The conjugate gradient method is more sophisticated than the steepest descent method. This method uses the previous step to direct the optimizer towards the next step. The first step (s_1) in this method is in the direction of the negative gradient vector (g_1) (3.24)

(3.24)

The next step uses the previous gradient and follows the new search direction (3.25)

(3.25)

s_{k-1} is the search direction from the previous step and b_k is the scaling factor which is given by:

—— (3.26)

The scaling factor multiplied by the previous step as in 3.25 removes the constraint that the new step direction should be orthogonal to the original. The removal of this requirement is reported to speed up convergence and memory requirements of calculations[22].

3.5.3 Newton-Raphson Method

The Newton-Raphson method is the most computationally demanding of the three methods presented in this chapter. To perform a Newton-Raphson minimization the 3n coordinates of the system are minimised to form vector x, an additional vector (g) is formed through derivation

of the energy with respect to the 3n coordinates[23]. Hessian matrix B is constructed comprising of the second derivatives of the energy with respect to the coordinates (3.27).

(3.27)

x_0 is the previously visited point and x_1 is the new step. Computation of the second derivatives can prove difficult due to the amount required to form the matrix coupled with storage of the matrix elements.

Figure 3.2 highlights the optimisation algorithm within VASP.

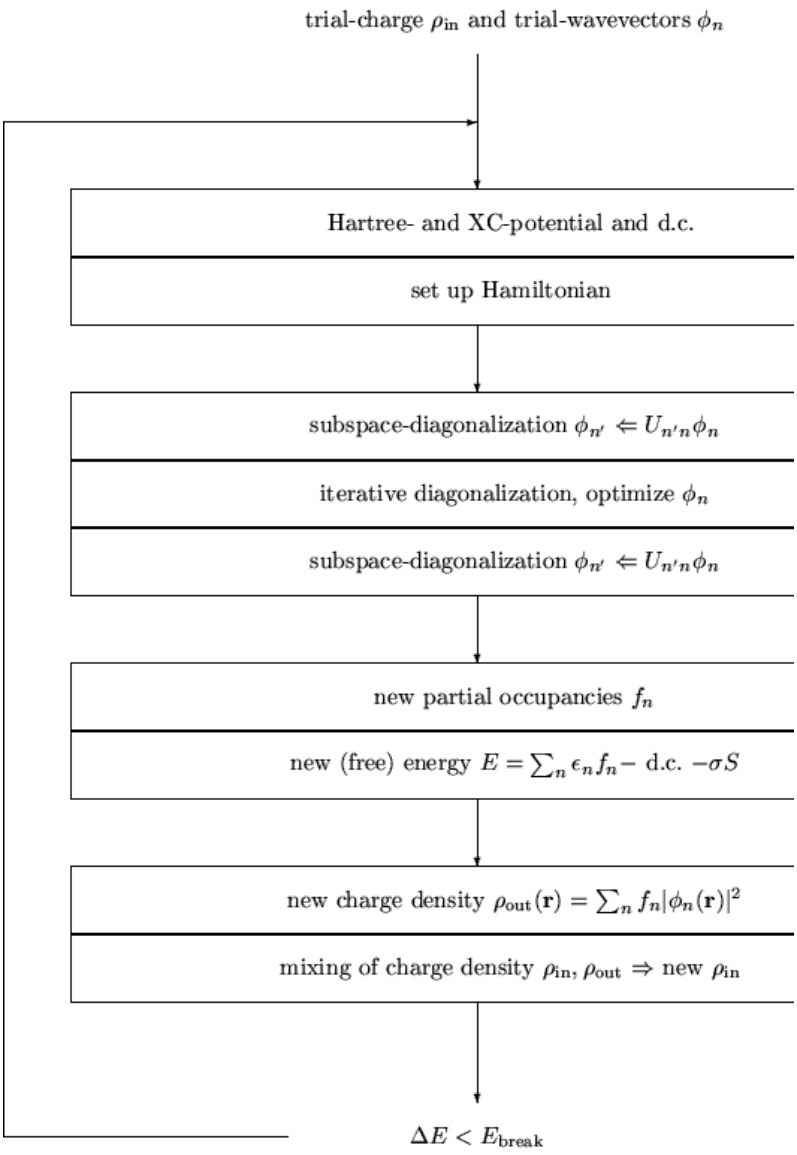

Figure 3.2: Flowchart detailing the optimisation scheme used within VASP (figure obtained from VASP manual online)

3.6 Molecular Dynamics

To simulate the motion of a system molecular dynamics is employed which uses forces to suggest suitable motion. Newton's second law of motion (3.28) states force (F) acting on an object is its mass (m) multiplied by acceleration (a). If this equation is rewritten replacing acceleration with the second derivative of atomic displacement (s) with respect to time (t) a useable version emerges (3.29).

(3.28)

— — (3.29)

To determine the dynamic behaviour of the system the second order differential must be solved for each atom. Integrating equation 3.29 with respect with time gives equation 3.3.

— — (3.30)

C_1 is the constant introduced through integration and corresponds to the velocity at time = 0. At time t the constant is replace with the initial velocity u.

Further integration of 3.30 produces equation 3.31. In this equation the constant c_2 is the current position. This equation means displacement from an initial velocity and acceleration can be determined.

– (3.31)

This derivation leads to a truncated Taylor series for displacement (3.32)

— — – (3.32)

Ignoring higher order terms inevitably introduces an error within calculations. Selecting a suitable time step is also vital for ensuring accuracy within calculations. A time step is typically chosen to be approximately the vibrational frequency of a bond stretch. Errors through truncation and choice of time step can be overcome using the Leapfrog Verlet algorithm[24]. Within VASP forces are obtained from electronic SCF optimisation and used in the Newtonian equations of motion to model atomic motion.

All calculations presented in this thesis are post equilibrium meaning the temperature has equilibrated.

3.7 Transition State Searches

This section is largely based on work by Henkelmen *et al.*[25,26]

VASP has two methods for determining the transition state of a system, these are the Nudged Elastic Band (NEB) and Improved Dimer Method (IDM).

3.7.1 Nudged Elastic Band Method

The NEB method is developed and implemented within VASP by Henkelmen *et al.*[25,26] It is a method to locate the minimum energy path (MEP) between a known start and end structure both in local minima. Any point on the MEP has a property that it is in an energy minimum in all directions perpendicular to the path. A linear interpolation is used between start and final states and the configurations corresponding to the images are connected by spring forces ensuring equal spacing along the reaction pathway.

Images along the NEB are optimised to the MEP through force projection scheme ensuring potential forces are perpendicular to the band.

The NEB force acting on image i comprised of two independent components[20] (3.33)

(3.33)

In 3.33 is the component of the force arising due to potential perpendicular to the band and is the spring force parallel to the band.

The optimiser moves the NEB along these forces to the MEP. The optimisation criteria are governed by forces dropping below a specified amount. Consideration needs to be made when choosing the constraint for the NEB step size. A step size too large risks jumping past structures of interest during the NEB run.

3.7.2 The Improved Dimer Method

The improved dimer method (IDM) is a method for optimization of a transition state[27]. This method does not require knowledge of the start or final structures however it requires a reasonable estimate of the transition state geometry[28]. Within VASP the following steps are taken through invoking the IBRION=44 tag within INCAR.

- Curvature along the dimer axis is computed using finite differences. A frequency calculation is required beforehand in order to locate the unstable direction (the dimer axis)
- Dimer is rotated such as its axis is parallel with the direction of the maximum negative curvature.
- Geometry optimization step minimises the energy in all directions except the unstable direction where it is maximised. The energy from this output is taken to be the energy of the transition state.

3.7.3 VASP

The primary software package used throughout this thesis is the Vienna *ab initio* Simulation Package (VASP)[29–32]. This package uses periodic DFT along with plane wave basis sets, projector-augmented wave (PAW)[9,33] methods or pseudopotentials within the code. Periodic DFT is able to calculate properties of extended systems and can also be used to calculate molecular properties. VASP utilizes *ab initio* methods to calculate ground state structure properties, transition states and can be used to perform Born-Oppenheimer molecular dynamics simulations.

The PAW or pseudopotential method reduces the size of the basis set with no more than 100 plane waves per atom used to describe bulk materials. This ensures suitable scaling properties which enables efficient modelling of large systems.

The electronic ground state is determined via a self-consistency model. Matrix diagonalization schemes (RMM-DISS and blocked Davidson) are reported to be the fastest schemes currently available and therefore enable efficient calculations.

3.7.4 Gaussian 09

Developed by John Pople the Gaussian program[34] is a powerful software package which can perform molecular calculations using localised basis sets. Gaussian can perform geometry optimisations, transition state searches and also various bond angle including dihedral scans. For work presented in this thesis Gaussian has been used to perform dihedral scans of isolated molecules using 6-311 g(d,p) basis set. Basis set nomenclature mean this contains 6 primitive Gaussian functions used to describe each atomic orbital, three valence orbitals including d and p electrons.

References

1. Ghosh, A. Just how good is DFT? *J. Biol. Inorg. Chem.* **11,** 671 (2006)

2. Cramer, C. J. *Essentials of Computational Chemistry: Theories and Models*. (Wiley, 2005). at <https://books.google.co.uk/books?id=BKJcbvzl0RsC>

3. Hohenberg, P. & Kohn, W. Inhomogeneous Electron Gas. *Phys. Rev.* **136,** B864–(1964)

4. Kohn, W. & Sham, L. J. Self-Consistent Equations Including Exchange and Correlation Effects. *Phys. Rev.* **140,** A1133 (1965)

5. Von Barth, U. Basic Density-Functional Theory—an Overview. (2003)

6. Becke, A. D. Density-functional exchange-energy approximation with correct asymptotic behavior. *Phys. Rev. A* **38,** 3098 (1988)

7. Perdew, J. P., Burke, K. & Wang, Y. Generalized gradient approximation for the exchange-correlation hole of a many-electron system. *Phys. Rev. B* **54,** 16533 (1996)

8. Perdew, J. P., Burke, K. & Ernzerhof, M. Generalized Gradient Approximation Made Simple. *Phys. Rev. Lett.* **77,** 3865 (1996)

9. Blöchl, P. E. Projector augmented-wave method. *Phys. Rev. B* **50,** 17953 (1994)

10. Kresse, G. From ultrasoft pseudopotentials to the projector augmented-wave method. *Phys. Rev. B* **59,** 1758 (1999)

11. Perdew, J. P., Burke, K. & Ernzerhof, M. Generalized Gradient Approximation Made Simple [Phys. Rev. Lett. 77, 3865 (1996)]. *Phys. Rev. Lett.* **78,** 1396 (1997)

12. Grimme, S. Semiempirical GGA-type density functional constructed with a long-range dispersion correction. *J. Comput. Chem.* **27,** 1787 (2006)

13. Řezáč, J., Šimová, L. & Hobza, P. CCSD[T] Describes Noncovalent Interactions Better than the CCSD(T), CCSD(TQ), and CCSDT Methods. *J. Chem. Theory Comput.* **9,** 364 (2013)

14. Dudarev, S. L., Savrasov, S. Y., Humphreys, C. J. & Sutton, A. P. Electron-energy-loss spectra and the structural stability of nickel oxide: An LSDA+U study. *Phys. Rev. B* **57,** 1505 (1998)

15. Mulliken, R. S. Electronic Population Analysis on LCAO[Single Bond]MO Molecular Wave Functions. I. *J. Chem. Phys.* **23,** 1833 (1955)

16. Bader, R. F. W. *Atoms in molecules : a quantum theory*. (Clarendon Press, 1990)

17. Henkelman, G., Arnaldsson, A. & Jónsson, H. A fast and robust algorithm for Bader decomposition of charge density. *Comput. Mater. Sci.* **36,** 354 (2006)

18. Tang, W., Sanville, E. & Henkelman, G. A grid-based Bader analysis algorithm without lattice bias. *J. Phys. Condens. Matter* **21,** 84204 (2009)

19. Sanville, E., Kenny, S. D., Smith, R. & Henkelman, G. Improved grid-based algorithm for Bader charge allocation. *J. Comput. Chem.* **28,** 899 (2007)

20. Sheppard, D., Terrell, R. & Henkelman, G. Optimization methods for finding minimum energy paths. *J. Chem. Phys.* **128,** 134106 (2008)

21. Wang, X. Method of Steepest Descent and its Applications. (2008)

22. Grant, G. H. & Richards, W. G. *Computational Chemistry*. (Oxford University Press, 1995). at <https://books.google.co.uk/books?id=IQZ4kQEACAAJ>

23. Rappé, A. K. & Casewit, C. J. *Molecular Mechanics Across Chemistry*. (University Science Books, 1997). at <https://books.google.co.uk/books?id=U0TeILEDTr0C>

24. GRUBMÜLLER, H., HELLER, H., WINDEMUTH, A. & SCHULTEN, K. Generalized Verlet algorithm for efficient molecular dynamics simulations with long-range interactions. *Mol. Simul.* **6,** 121 (1991)

25. Sheppard, D. & Henkelman, G. Paths to which the Nudged Elastic Band Converges. *J Comput Chem* **32,** 1769 (2011)

26. Sheppard, D., Xiao, P., Chemelewski, W., Johnson, D. D. & Henkelman, G. A generalized solid-state nudged elastic band method. *J. Chem. Phys.* **136,** 74103 (2012)

27. Henkelman, G. & Jónsson, H. A dimer method for finding saddle points on high dimensional potential surfaces using only first derivatives. *J. Chem. Phys.* **111,** 7010 (1999)

28. Heyden, A., Bell, A. T. & Keil, F. J. Efficient methods for finding transition states in chemical reactions: Comparison of improved dimer method and partitioned rational function optimization method. *J. Chem. Phys.* **123,** 224101 (2005)

29. Kresse, G. & Hafner, J. Ab initio molecular dynamics for liquid metals. *Phys. Rev. B* **47,** 558 (1993)

30. Kresse, G. & Hafner, J. Ab initio molecular-dynamics simulation of the liquid-metal–amorphous-semiconductor transition in germanium. *Phys. Rev. B* **49,** 14251 (1994)

31. Kresse, G. & Furthmüller, J. Efficiency of ab-initio total energy calculations for metals and semiconductors using a plane-wave basis set. *Comput. Mater. Sci.* **6,** 15 (1996)

32. Kresse, G. Efficient iterative schemes for ab initio total-energy calculations using a plane-wave basis set. *Phys. Rev. B* **54,** 11169 (1996)

33. Kresse, G. From ultrasoft pseudopotentials to the projector augmented-wave method. *Phys. Rev. B* **59,** 1758 (1999)

34. Frisch, M. J. *et al.* Gaussian 09, Revision B.01. *Gaussian 09, Revision B.01, Gaussian, Inc., Wallingford CT* (2009). at <citeulike-article-id:9096580>

Chapter 4

Methodology

The methodology used for this work will be presented in this chapter. The practical application of the theoretical details discussed in chapter 3 will be presented through a discussion of choice of potential, plane wave energy cut-off values, calculations performed with dispersion, determination of U values, transition state searches and finally appropriate treatment of surfaces.

4.1 Potentials used for Calculations

For VASP calculations several DFT functionals can be used. For all calculations presented in this thesis the PBE functional[1,2] has been used. PBE is reported to perform well for a variety of systems ranging from isolated molecules to extended transition metal surfaces. It can be considered a universal functional and therefore suitable for all systems modelled in this thesis[3]. PW91[4] is another widely used functional, however difficulty is reported when calculating adsorption properties using this functional as over-binding of adsorbate to substrate as in CO / Pd (111) surface is reported[5]. Due to reports of overbinding, calculations will be performed using the PBE functional only. Another benefit of using the PBE functional is the ease in which the D2 correction can be activated. The D2 method of Grimme[6] is available in VASP 5.2.12 and will be discussed further in this subsection.

4.1.1 Valence and Core States within Pseudopotentials

Pseudopotentials are used to describe atoms in all calculations performed in this thesis. All pseudopotentials are contained in POTCAR files obtained through VASP. Often different variants of pseudopotential are available to the user with the primary difference being the number of core and valence electrons within the potential.

An example of this variant is the potential used to describe titanium, in this instance two functionals exist with the option of including either 4 or 6 valence electrons in the calculations

In order to determine which functional is appropriate both variants were taken and bulk moduli calculated as per the method detailed in (4.14). The result of these calculations along with comparison to literature is presented in table 4.1.

Table 4.1: Bulk Modulus for Rutile and Anatase obtained through calculation according to method detailed in 4.2. Values in brackets are the experimentally determined bulk moduli[7,8].

	Rutile Bulk Modulus / GPa	Anatase Bulk Modulus / GPa
4 Valence Electrons	227.8 (210)	194.5 (178)
6 Valence Electrons	207.6 (210)	190.6 (178)

Inclusion of more valence electrons in the pseudopotential of titanium produces a calculated bulk modulus value significantly closer to the experimentally obtained value for rutile. For anatase the difference is less pronounced however inclusion of more electrons shifts the calculated value closer to the experimental value. The results of these calculations indicate the functional with more valence electrons should be used for all calculations involving titanium and where applicable other atoms in this thesis. Inclusion of a higher number of valence electrons will inevitably increase computational cost however we believe a higher degree of accuracy is possible by a larger valence region and therefore justifies the extra expense.

4.1.2 Determination of Suitable Plane Wave Cut-Off

In the VASP INCAR file plane wave cut-off energies can be modified through setting the ENCUT tag to the required value in eV. It is important to evaluate the suitability of a cut-off energy as a value too small will not accurately account for interactions in the system whilst a value unnecessarily too large will slow calculations down without adding any tangible benefits / accuracy to the calculation.

For each system modelled in this thesis an evaluation of planewave cut-off has been performed by taking a bulk material (gold, rutile etc) and performing geometry optimisations over a range of ENCUT values with a set increment value. Figure 4.1a contains absolute energies plotted against ENCUT values for Au_{38} in a 625 $Å^3$ box, figure 4.1b for Pd_{38} particles in the same box size and figure 4.1c for bulk Rutile in a box size set to the dimensions of the unit cell.

a)

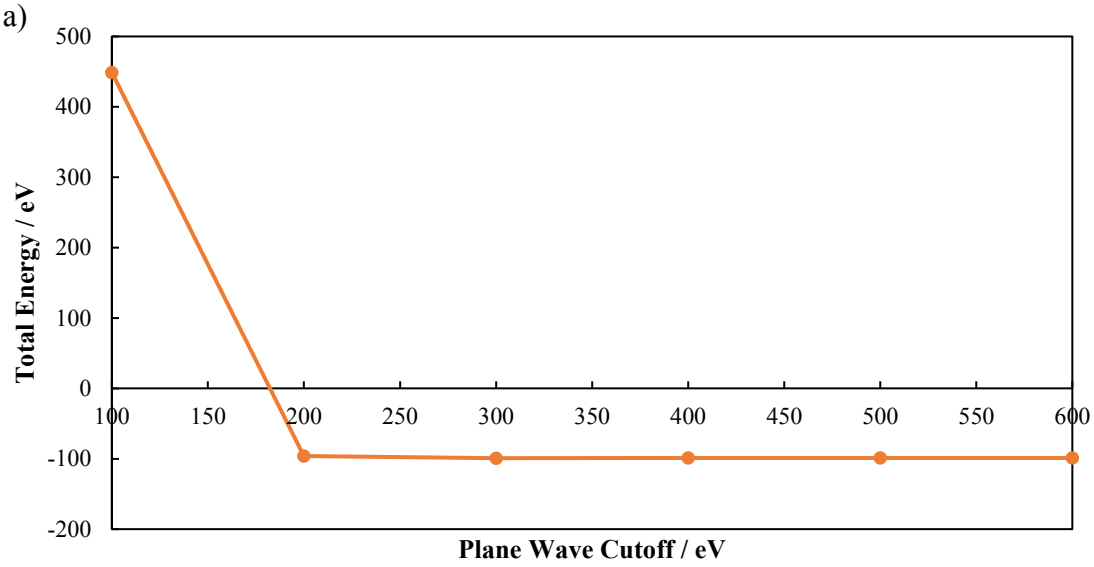
500
400
300
200
100
0
-100
-200
Total Energy / eV
100
150
200
250
300
350
400
450
500
550
600
Plane Wave Cutoff / eV

b)

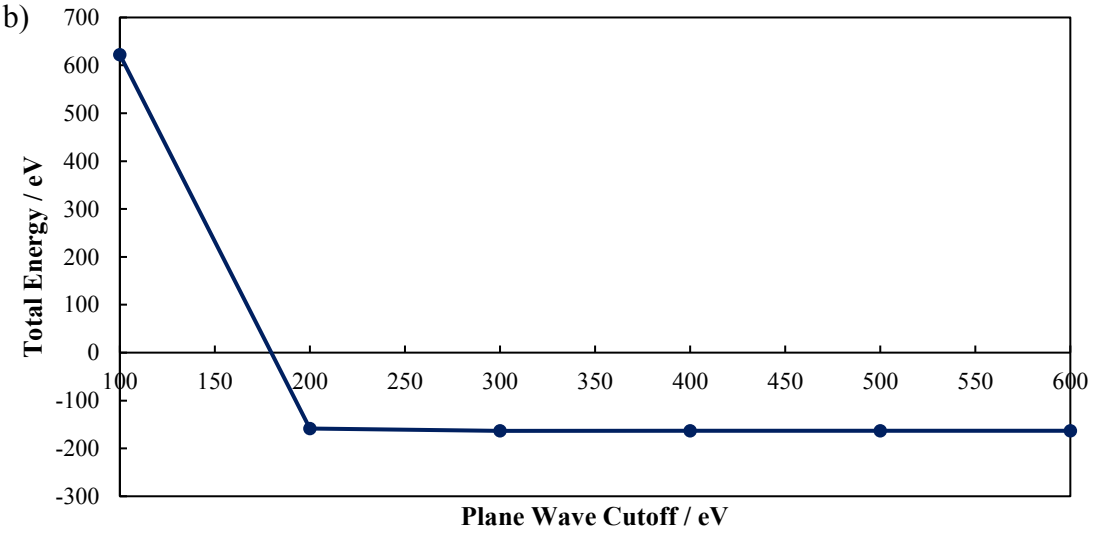
700
600
500
400
300
200
100
0
-100
-200
-300
Total Energy / eV
100
150
200
250
300
350
400
450
500
550
600
Plane Wave Cutoff / eV

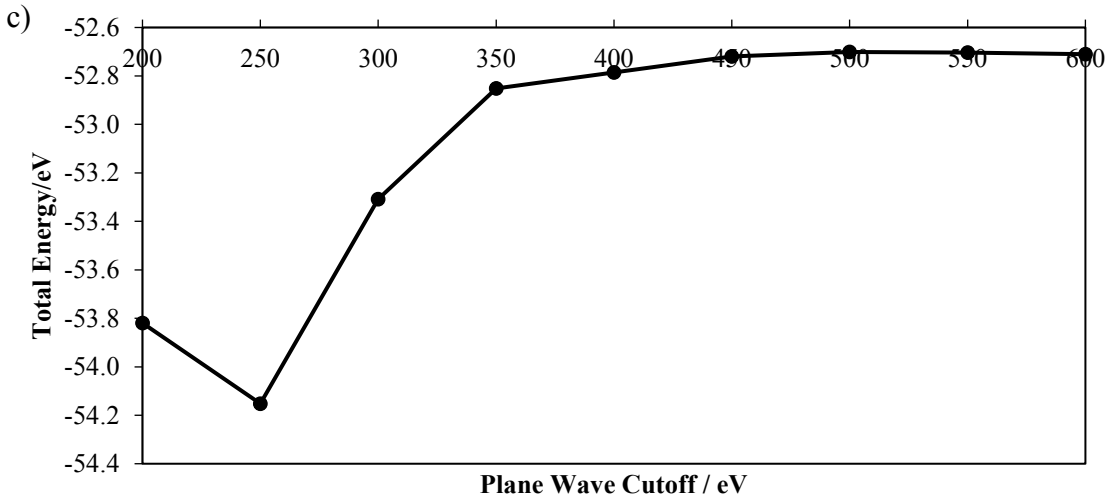

Figure 4.1: Total energy vs plane wave cut-off for: a) Au_{38}, b) Pd_{38} and bulk Rutile (c).

Data presented in 4.1 clearly indicates a plane wave cut off below 200 eV is unsuitable for both Au_{38} and Pd_{38} this is due to total energies of the system being positive and therefore indicates a larger value is required. For both metal particles fluctuation in total energies is minimal if a plane wave cut-off value is used greater than 400 eV. For bulk Rutile plane wave cut-off values below 350 eV are considerably lower in energy than higher energy cut-off values. From 350 – 500 eV total energies fluctuate by 0.2 eV and stabilise at 500 eV where increasing the cut-off value only affects total energies by 0.01 eV. The results of these calculations confirm a plane wave cut-off value of 500 eV is suitable for rutile and in order to ensure consistency across all calculations we have decided to apply this cut-off to isolated molecules / metal particles to ensure calculation parameters are consistent when comparing properties.

4.1.3 k-Point Convergence

The number of k-points required for a calculation is determined by the accuracy required, system size and the type of system being modelled. VASP converts a periodic unit cell into reciprocal space and therefore a large unit cell will have a small reciprocal space. This property can be utilized for calculations of isolated particles / clusters in large unit cells as a computationally efficient sampling mesh can be used. Using a small sample mesh also reduces the possibility of spurious self-interaction between isolated systems. For bulk materials a sampling sweep is required in order to determine a suitable mesh size. This is detailed in 4.1.4

4.1.4 Preparation of Bulk Materials

Lattice parameters for bulk Rutile and Anatase unit cells were obtained from literature (references 10 and 11). Whilst these are experimental lattice parameters they may not correspond to minimal energy structures within a calculation. As a result the following procedure is required in order to obtain lattice parameters which correspond to energy minima using the PBE functional in VASP.

Experimentally obtained structures of Anatase and Rutile were taken from literature – these were used as starting points. The starting structures underwent a $\pm$ 5% unit cell expansion at 0.5% increments. For each of these expansion points the cell was geometry optimised under fixed volume conditions and energies obtained. Energies obtained were plotted against volume. This procedure is repeated over a range of k-point sampling meshes. Figures 4.3a and 4.3b contain a plot of energy vs volume using k-points for both bulk Anatase and Rutile respectively.

The R^2 value of the second order parabolic line of best fit presented in figure 4.3 indicate a suitable fit for Anatase (0.9909) however for Rutile the fit is 0.9876 therefore indicating the fit is not exact in this instance. In order to hone in on the minimum energy region this data was replotted this time centring on the minimum energy point and two points either side. This re-centred plot is presented in figure 4.4.

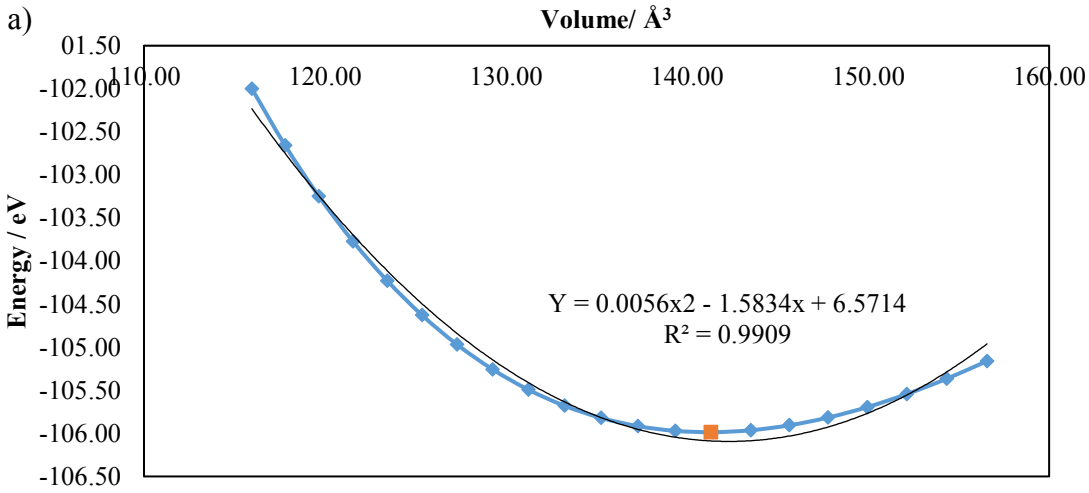

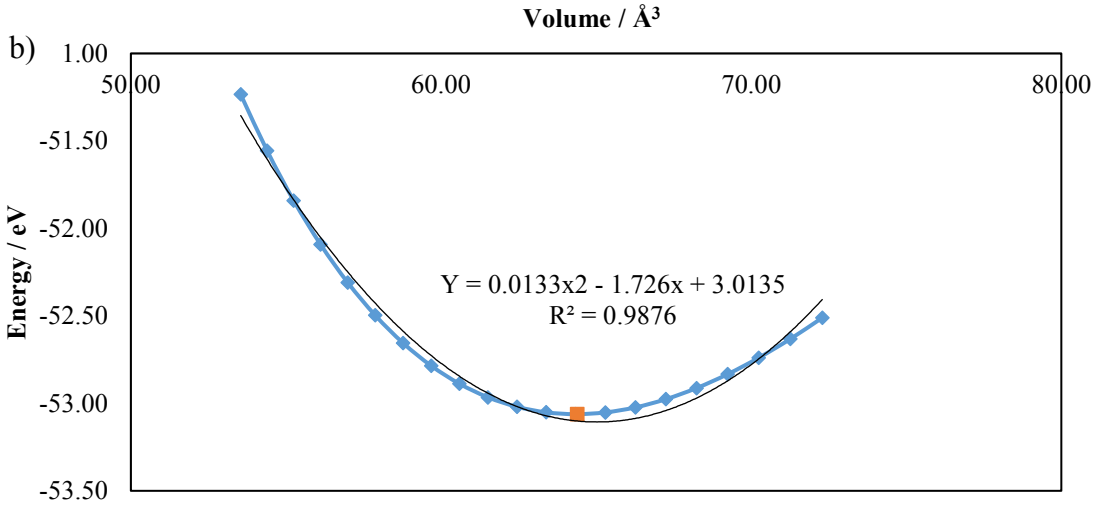

Figure 4.3: Volume vs energy for bulk Anatase (a) and Rutile (b) unit cell. Blue line represents actual data; black line is parabolic line of best fit. A red dot is used to indicate the lowest energy data point.

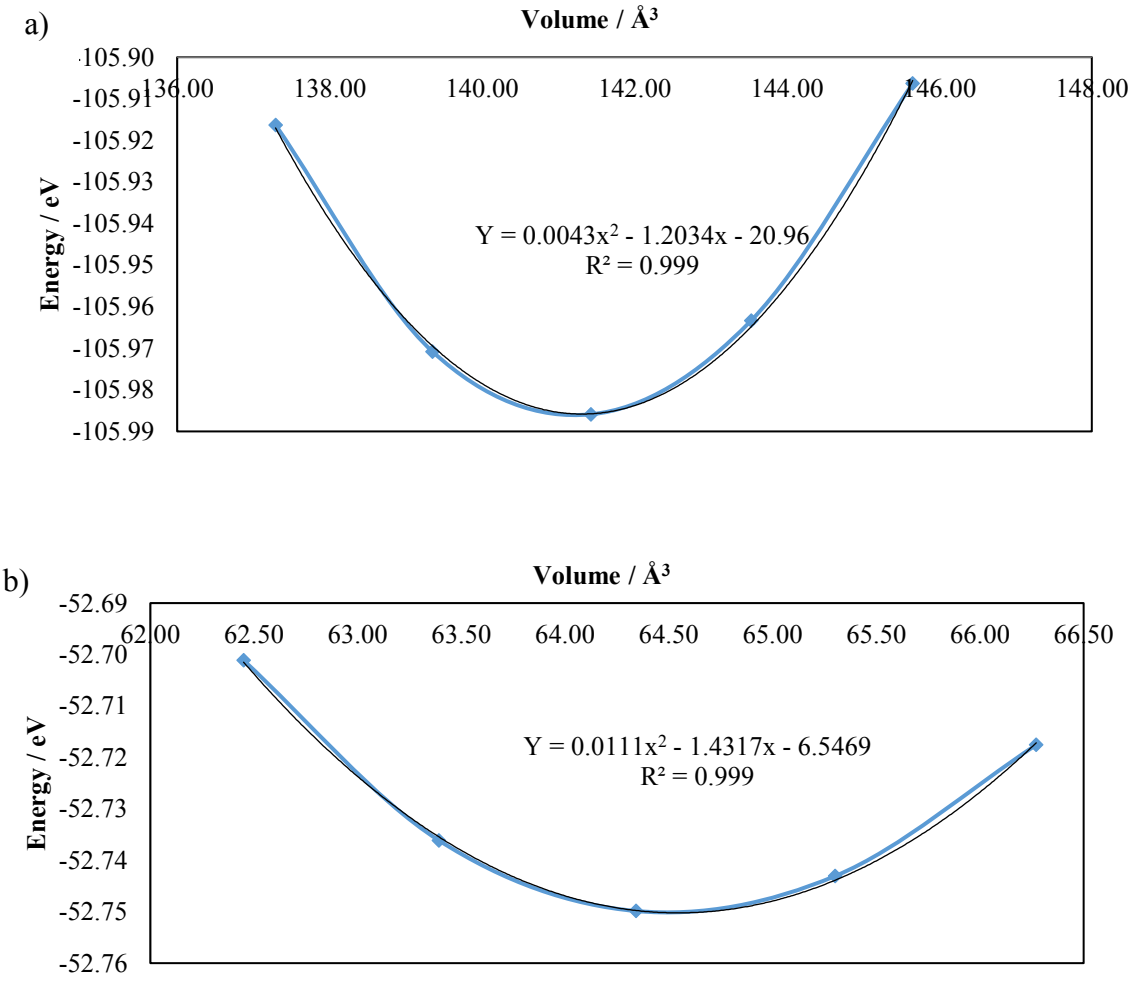

Figure 4.4: Volume vs energy for unit cell of Anatase (a) and Rutile (b). Blue line is actual data and black line is line of best fit.

Data presented in 4.4 clearly indicate a closer fit between the second order polynomial and the data using a re-centred plot. In both instances the R^2 value is 0.999 therefore for the purposes of further analysis the "minimum energy region" on the chart will be used.

The author of this work is aware of the Birch-Murnaghan method for determination of bulk moduli. The use of this method is beyond the scope of this thesis and we believe a parabolic fit around the minimum energy region provides a sufficiently accurate fit for calculation of bulk moduli.

The bulk modulus of an elastic material is given by equation 4.1. The bulk modulus (B_0) measures the resistance of a material to compression with a volume (V) at constant pressure (p)

—

Pressure is force over area. If a force (F) is applied evenly across all of the area the crystal will change a small distance ( ) (4.2).

—

This leads to equation 4.3 —

The second derivative of the energy with respect to volume is estimated from the second order polynomial line of best fit. The energy and volume corresponding to the lowest energy structure are taken and along with coefficients of the line of best fit bulk moduli are calculated for each k-point for both Anatase and Rutile. Figures 4.5a and 4.5b contain bulk moduli calculations vs k-point sampling mesh for Anatase and Rutile respectively.

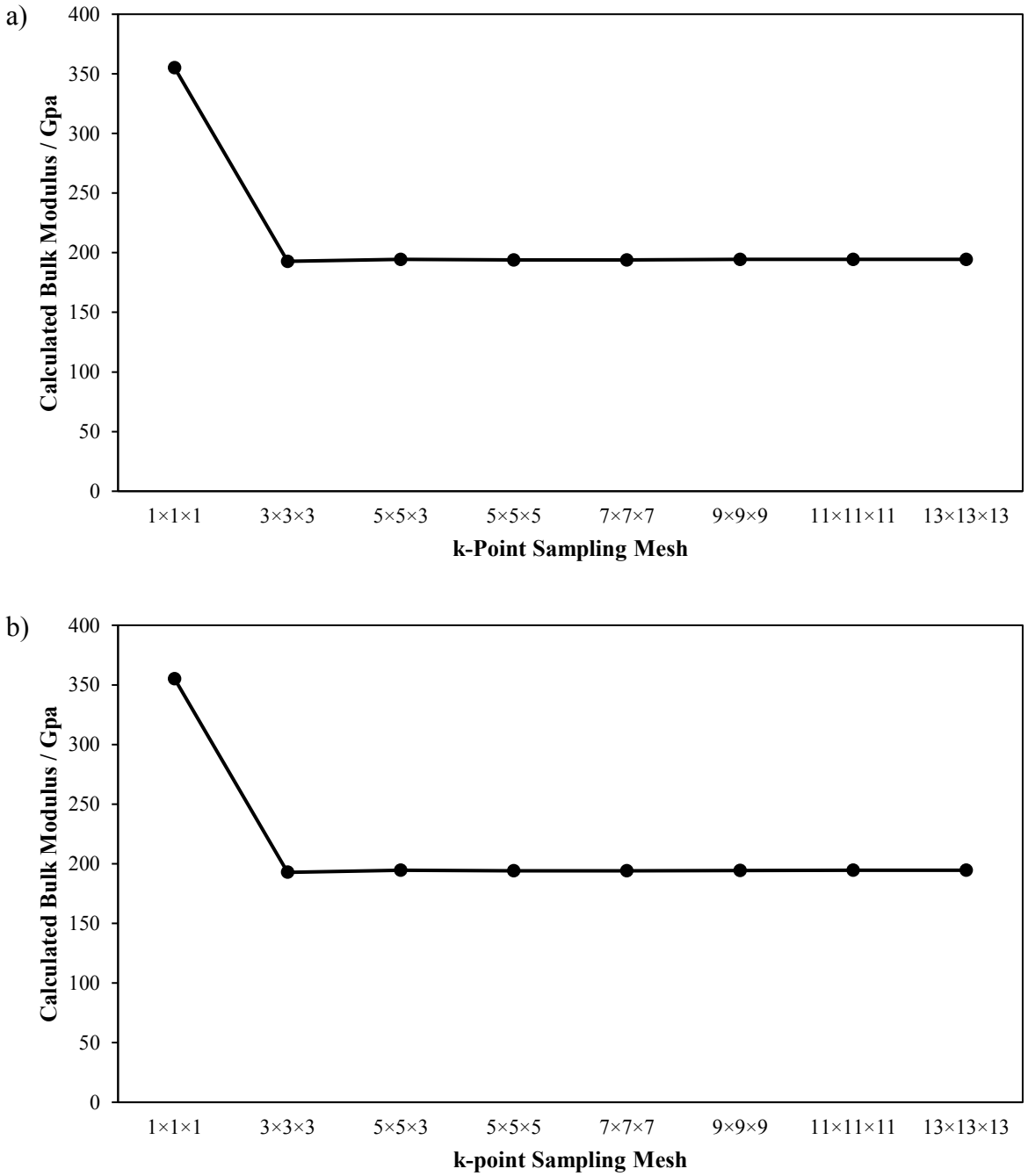

Figure 4.5: Bulk modulus vs k-point sampling mesh for bulk Anatase (a) and Rutile (b).

For both Anatase and Rutile the calculated bulk modulus values stabilise within 5 GPa of each other when a or higher k-point sampling mesh is used. The experimentally obtained bulk modulus for Anatase is 178 GPa[9]. At k-points a 192.81 GPa bulk modulus for Anatase has been calculated, as the k-point sampling mesh increases bulk modulus values converge to around 194 GPa and therefore a value of has been chosen. Using a smaller

sampling mesh in the z direction is appropriate due to the dimensions of the unit cell and therefore will reduce computational cost.

Similar analysis confirms is a suitable sampling mesh for Rutile. Using this value a bulk modulus of 227.7 GPa has been calculated which is in comparison to the experimentally obtained 210 GPa[8]. DFT will often produce errors of experimental properties around 10% therefore based upon this it can be concluded these errors are within an acceptable range. As this error is present in each calculation comparative properties such as adsorption and surface energies can be calculated with validity.

Once a k-point sampling mesh has been selected a final evaluation of the choice is performed by optimising the unit cell and comparing lattice parameters against experimentally determined ones. For Anatase and rutile these are presented in tables 4.2 and 4.3.

Table 4.2: Calculated lattice parameters for a unit cell of Anatase compared with literature.

	Calculated Lattice Parameter / Å	Literature Value[10] / Å
a	3.776	3.782
b	3.776	3.782
c	9.486	9.502

Table 4.3: Calculated lattice parameters for a unit cell of Rutile compared with literature.

	Calculated Lattice Parameter / Å	Literature Value[11] / Å
a	4.594	4.584
b	4.594	4.584
c	2.959	2.953

In both instances these are in excellent agreement with experiment (less than 1% deviation) therefore validation of the chosen k-point sampling mesh has been performed.

This procedure is repeated for any bulk material modelled in this thesis. Molecular and cluster calculations are always performed using a k-point sampling mesh due to the large unit cell these calculations are performed in (625 $Å^3$)

4.2 Modelling Surfaces

Planewave cut-off values along with an adequate k-point sampling mesh have been determined in 4.1. When constructing surfaces, the k-point in the z direction can be reduced to 1 due to the presence of a large vacuum gap. The vacuum gap used for all calculations in this chapter is 15 Å this is sufficiently large to prevent spurious self-interactions between slabs in this direction. Modelling a slab is a trade-off between accuracy and the computational costs of large slab models. Several methods can be employed to model a slab and these are presented here.

4.2.1 Surface Energies vs Slab Thickness

In order to compare stability and ascertain whether convergence criteria have been met surface energies can be determined at various slab thicknesses and used to indicate when these conditions have been met. Additional methods not presented in this chapter have been performed and are contained within the supplementary information.

Using Rutile (110) and Anatase (100) as test surfaces along with equation 4.4 surface energies were calculated at different slab thicknesses ranging from 3 to 13 layers (increments of two to ensure odd layer slab models). E_{surf} is the calculated surface energy in J m^{-2}, E_{slab} is the total energy of the slab in eV, n is the scaling factor of number of atoms within the slab divided by number of atoms within the unit cell, E_{bulk} is the energy of one-unit cell and S is the surface area in m^2. A factor of two is used in the denominator as these systems are fully relaxed and as a result have two exposed surfaces (top and bottom of the slab)

(4.4)

A plot of surface energy vs slab thickness for Anatase (100) and Rutile (110) is presented in figure 4.6.

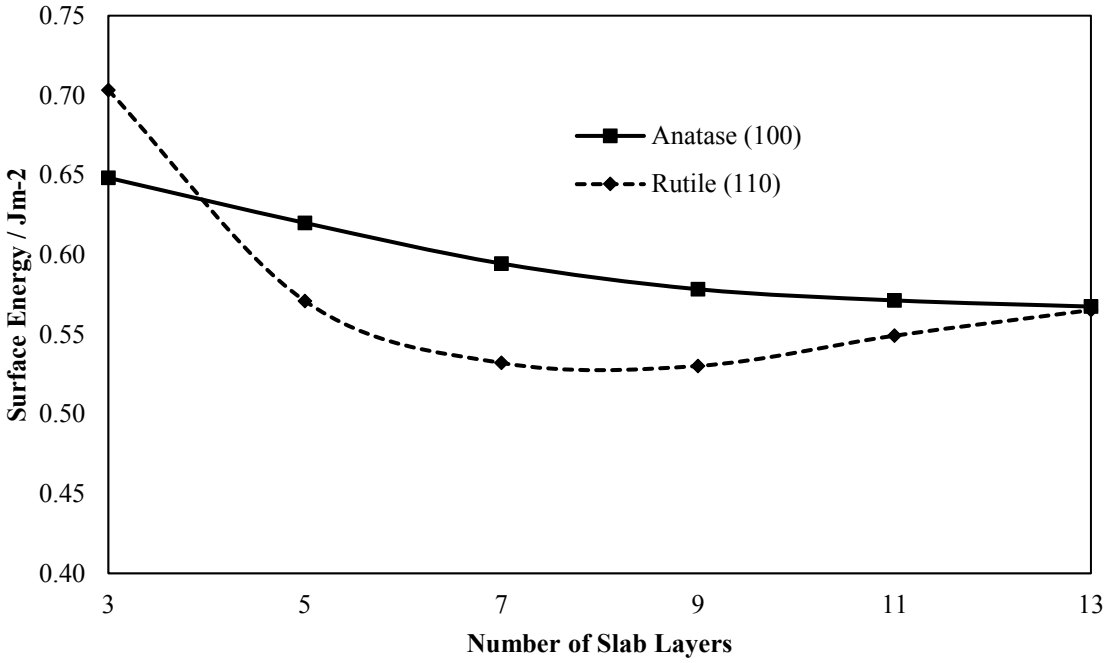

Figure 4.6: Calculated surface energies for Anatase (100) (solid line) and Rutile (110) (dashed line) for various slab thicknesses.

The surface energy for Anatase (100) appears to be steadily decreasing towards 0.57 J m^{-2} as the number of layers increases. It does not however converge to a consistent value indicating further layers are required in the model to obtain convergence. Due to computational cost this is not feasible and would greatly impede upon the ability to produce a sufficient quantity of calculations in order to conduct a feasible study. For Rutile (110) a "hockey stick" type plot is observed where surface energies decrease to a minimum of 0.53 J m^{-2} for 7 layers and then increase gradually to 0.57 J m^{-2} for 13 layers. Due to fluctuation of surface energy values it can't be said with any certainty which slab thickness to choose therefore another model is required.

Another method which fixes all but the top two layers of the slab can be utilized to obtain surface energies. This alternate method provides two advantages over calculations where each atom is allowed to relax:

1) Computational cost can be lowered as the total degree of freedom within the system is reduced.
2) Having all but the top two layers free allow for bulk properties to be mimicked through fixing of the bulk of the slab.

Using equation 4.5 surface energies were calculated for systems containing all but the top two layers fixed. is the surface energy in J m^{-2}, E_{slab} is the total energy of the slab in eV, n is the scaling factor which is obtained from the fraction of atoms within the slab to the bulk unit cell, E_{bulk} is the energy of the bulk unit cell, S is the surface area in m^2 of the slab surface which is free to relax and is the single point energy of the slab system. This method has previously been used by Howard *et al.* and produced reliable surface energies for α-Fe_2O_3[12].

(4.5)

Surface energies calculated using equation 4.5 are plotted in figure 4.7 where the data obtained using this method indicates a convergence for Anatase (100) surface energies. In this case surface energies converge at 0.64 J m^{-2} for 5 layer slabs and higher. For Rutile (110) there appears to be no clear convergence however the surface energy change which accompanies the increasing of slab layers is less pronounced than for the fully relaxed system. From this it is decided 5-layer slab thickness is appropriate for this system. Further surface treatment investigation has been conducted and will be presented in chapter 6.

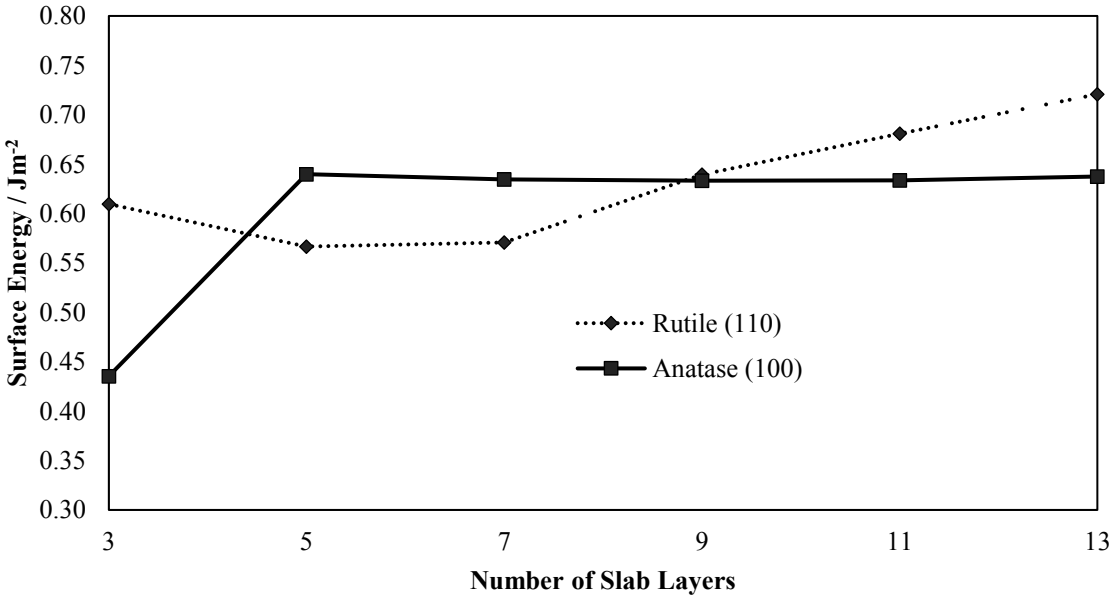

Figure 4.7: Calculated surface energies for Anatase (100) (solid line) and Rutile (110) (dashed line) for various slab thicknesses where the top two layers only are free to relax.

4.3 Determination of an Appropriate U Value for DFT+U Calculations

For strongly correlated systems such as the modelling of transition metal oxides, the DFT+U method of Dudarev[13] (discussed in chapter 3) has been used. Evaluation is required in order to determine a suitable U value for use in calculations. A common approach is to choose an experimentally measurable parameter of the system of interest and scan a range of U values to determine which value reproduces this experimentally observable property. Using TiO_2 and bulk Rutile as an example band gaps were calculated at a range of U values (from 0-7). Band gaps were obtained from performing a density of states (DOS) calculation in VASP using a k-point sampling mesh. This fine mesh was used as it is required when calculating electronic properties. DOS plots for each U value were used to determine the band gap and these are plotted vs U value used in figure 4.8.

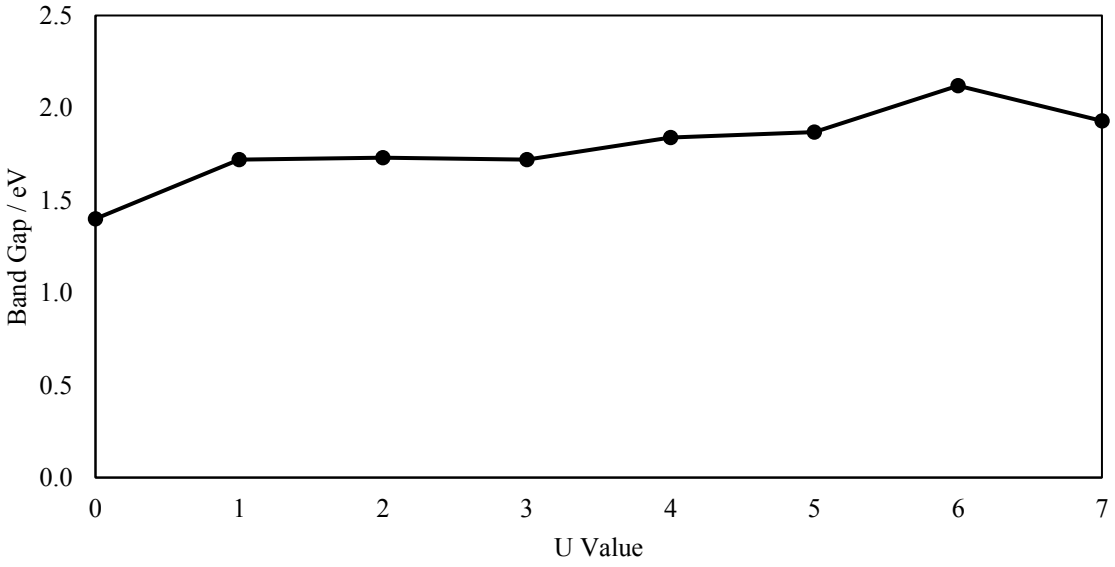

Figure 4.8: Band gap vs U value for bulk Rutile.

The experimentally determined band gap for Rutile is 3.0 eV[14]. If a U value of 6 is chosen, the calculated band gap is in the best agreement with experimental and therefore this will be used for calculations of Rutile systems. This methodology will be repeated for other strongly correlated systems modelled in this thesis unless stated otherwise.

4.4 Determination of Parameters for DFT-D2 Calculations

When the D2 method of Grimme is employed C_6 and R_0 values used to describe the long range dispersion interactions are automatically supplied through VASP 5.2.12 however for Au no such parameters exist. Instead a literature search was used to find parameters to input into the calculations[15]. Whilst evaluation of the suitability of these parameters is beyond the scope of this thesis there is one more variable within the INCAR file which needs evaluation. This is the cut-off distance for van der Waals interactions. In VASP 5.2.12, 30 Å is the default cut-off for vdW interactions when dispersion is activated. This may be unsuitable as unit cells to model cluster / molecules are 25 Å in length resulting in a spurious self-interaction stabilisation between periodic images. In order to ascertain a suitable cut-off two tests were performed which are detailed in 4.4.1.

4.4.1 Calculating Surface Energies of Rutile (110) and Anatase (100) with D2 Correction

Using methods detailed in 4.2 surface energies were calculated for both Anatase (100) and Rutile (110), each of these slabs were modelled to allow the top two layers freedom to relax. A 15 Å vacuum gap has been used in all cases along with a 500 eV planewave cut-off. For each system the vdW cut-off value was varied from 5-30 Å with 5 Å increments. Figure 4.9 contains the surface energy vs slab layer thickness results over all dispersion cut-off values used for Anatase (100).

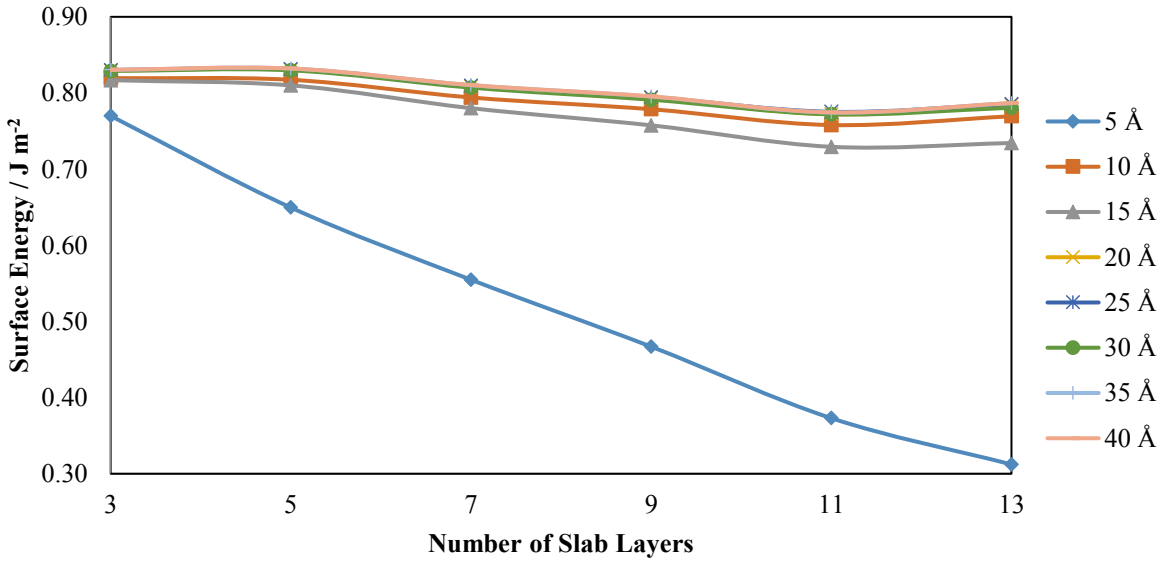

Figure 4.9: Surface energies for Anatase (100) for various slab thicknesses using a range of cut-off distances for dispersion interactions.

Data contained in figure 4.9 clearly indicate the surface energies obtained using a 5 Å cut-off for dispersion interactions produce values which steadily increase as the slab thickness increases, this is therefore discounted as a suitable a cut-off value. For higher values surface energies are in good agreement of each other (0.04 J m^{-2}). Figure 4.10 contains the results of calculations with Rutile (110).

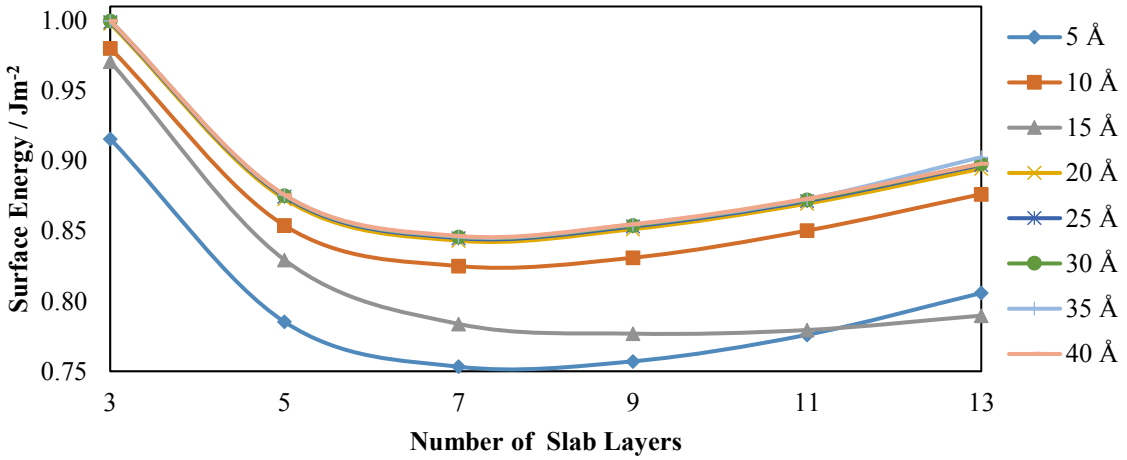

Figure 4.10: Surface energies for Rutile (110) for various slab thicknesses using a range of cut-off distances for dispersion interactions.

As in figure 4.7 the surface energies for Rutile (110) exhibit a "hockey stick" type trend. In both 4.9 and 4.10 surface energies are approximately 0.3 J m^{-2} higher with the D2 correction than without. The inclusion of dispersion stabilises the bulk structure and according to equation 4.5 will result in a higher surface energy as the bulk is more stable. As in 4.9 the use of a 5 Å cut-off is unsuitable as these values do not fit in with the other data sets. From 4.9 and 4.10 it is reasonable to suggest a 15 Å cutoff for vdW interactions in the treatment of surfaces.

4.4.2 Calculating Energies of Au_{13} with D2 Correction

As in 4.4.1 Au_{13} clusters of cuboctahedral geometry were placed in a 625 $Å^3$ box and geometry optimised using a range of cut off values for dispersion interactions. Figure 4.11 is a plot of total energies vs cutoff.

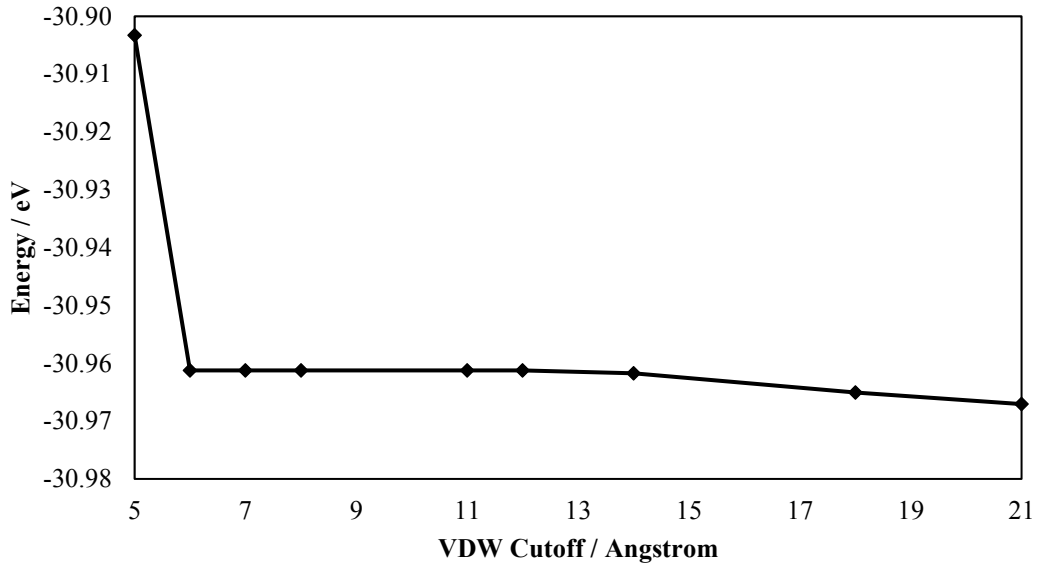

Figure 4.11: Total energies of Au_{13} cuboctahedral geometry vs D2 cut-off values.

As with the calculation of surface energies a value of 5 Å is unsuitable for modelling gold particles. It is interesting to observe the subtle change in energies when a vdW cut-off value of 18 Å or higher is used. In this instance the absolute energy decreases by 0.01 eV which corresponds to a spurious self-interaction between periodic images. Based upon this observation we view it necessary to always use a vdW cut-off value which will prevent such occurrence. In the case of surfaces a value of 15 Å was deemed suitable however adsorbates will eventually be placed onto the surface and may encroach upon distance between periodic images, therefore a value of 12 Å will be used as vdW cut-off for all calculations including the D2 correction.

4.5 Transition State Searches

Calculating transition states of a chemical reaction is a powerful tool available to computational chemists. Whilst a powerful tool it is often a complex process to ascertain a transition state due to the different pathways to reaction completion coupled with degrees of freedom in the system. As discussed in chapter 3 the NEB[16,17] and IDM[18] are available in VASP and have been used to determine transition states in this thesis. The nudged elastic band method requires knowledge of both start and end structures in which a linear interpolation is performed to obtain a reaction profile.This often can be computationally

demanding and require reruns to obtain a suitable transition state geometry / energy. The improved dimer method requires a reasonable suggestion of a transition state which is then optimised under special conditions to maximise the most unstable direction whilst minimising all others.

4.5.1 Improved Dimer Method

Using cuboctahedral Au_{13} as a test system, the adsorption and dissociation of molecular oxygen was investigated using the IDM following the below procedure:

1) Start geometry used was O_2 optimised on a (100) facet on Au_{13}.
2) End point taken as molecular oxygen dissociated into two (111) facets adjacent to the (100) facet.
3) A preliminary linear interpolation was used to obtain a 'rudimentary structure' of the transition state – this was taken by analysing the interpolation run and locating the mid-point.
4) This structure was inputted into an IDM calculation to optimise and obtain a suitable energy.

Initial calculations indicate the barrier to dissociation for the first molecular oxygen is 100 kJ mol^{-1} and in good agreement with a test NEB on the same system. The improved dimer method however appears to fail when determining the barrier for the second dissociation of molecular oxygen. In this case a barrier of 800 kJ mol^{-1} is produced by the IDM optimiser corresponding to 500 geometric iterations. A test NEB produces energies of 140 kJ mol^{-1} which indicates a failure of the IDM method. Further evaluation as to why this method has failed in this instance is beyond the scope of this thesis however from this test system it is decided all reaction barriers will be estimated using the Nudged Elastic Band method.

4.5.2 The Nudged Elastic Band Method

Using dissociation of O_2 on Au_{38} as a test example the following procedure is performed in order to determine a barrier using the NEB method:

1) Start and end points were obtained from geometry optimised structures of O_2 intact and dissociated on the cluster respectively.

2) A 24 step linear interpolation was performed – this is to ensure smooth reaction profile modelling. Initially 10 steps were chosen however it is found the reaction profile can be jagged and increases the likelihood of bypassing the barrier.
3) The NEB optimiser relaxes each image employing a spring constant of -5 to prevent fall-back to minima geometries. Each run of the NEB comprises of 10 geometric steps therefore several runs are required to minimise geometry. Image number vs energy relative to start structure for this test system are plotted in figure 4.12.

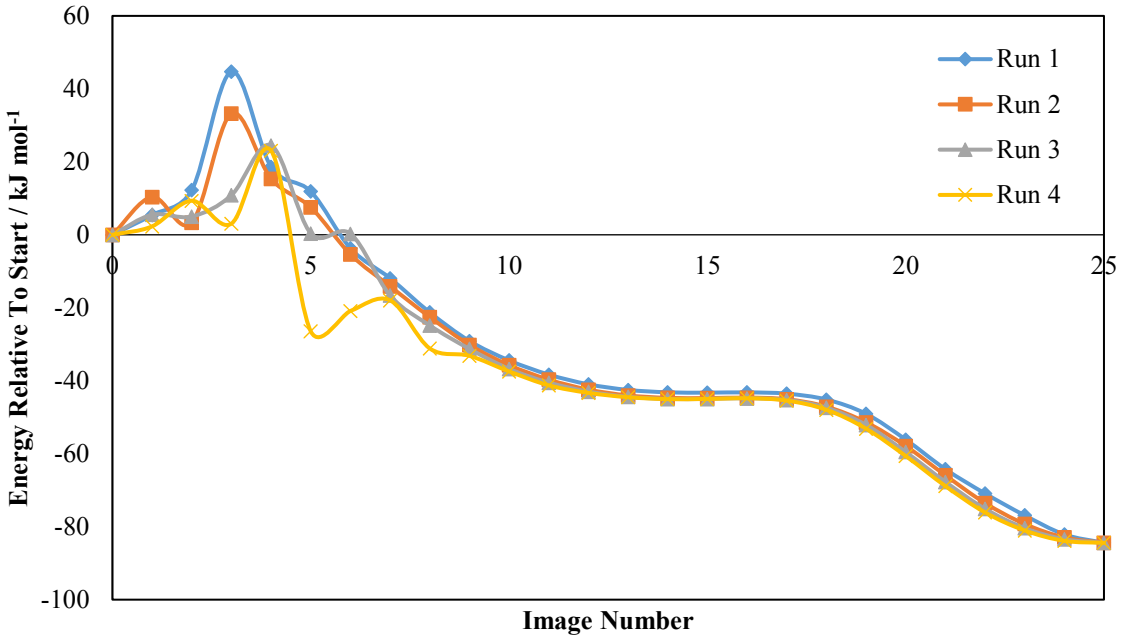

Figure 4.12: NEB runs for Au_{38} O_2 dissociation test system. Energies are set relative to the start structure.

Barrier data presented in figure 4.12 suggests an early transition state which has geometry closer to the start structure than the end point. This indicates further refinement of the barrier is required and therefore a new NEB was formed with image 0 and 6 being start and end points respectively. The results of this NEB are presented in 4.13.

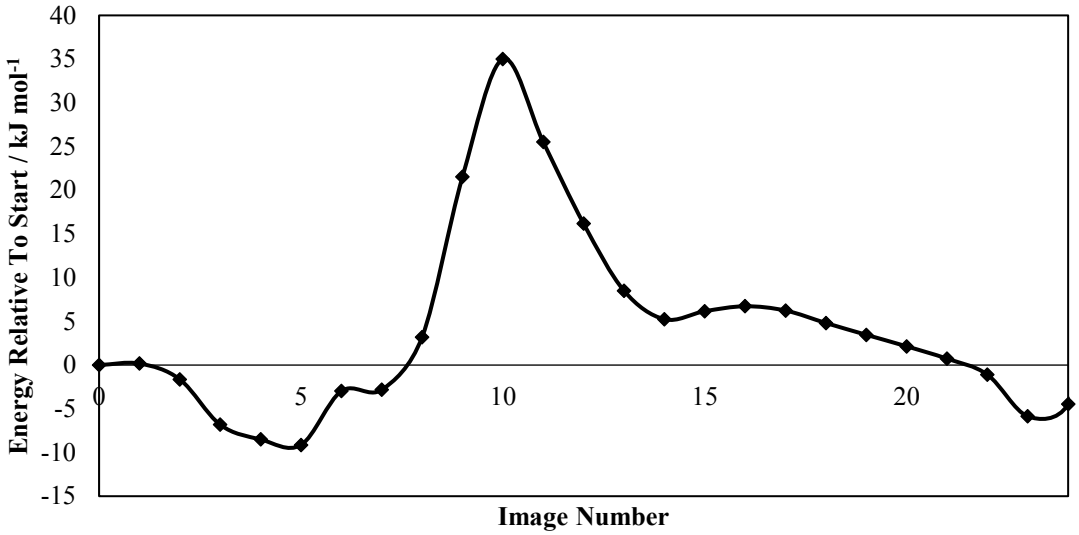

Figure 4.13: Refined NEB on Au_{38} O_2 dissociation test system. Energies are set relative to the start structure.

This refined barrier is considerably more symmetrical and centres on the tranistion state. The highest energy structure is taken and subject to a frequency analysis calculation in order to evaluate whether it is a transition state (location of a single imaginary mode). Unless otherwise specified this proceedure is used for all barrier calculations presented in this thesis.

4.6 Bader Charge Analysis

As discussed in chapter 3 Bader charge analysis has been performed to investigate the distribution of charge in systems where adsorption occurs. Bader charge analysis is sensitive to grid point spacing and therefore evaluation of suitable spacing is required. Previous work by Zeinalipour-Yazdi *et al.*[19] has concluded a grid spacing of 0.023 Å per sample point is required in order to have sufficient accuracy. For a periodic box size of Å this corresponds to 1087 sample points per dimension of the box. Due to processor and memory requirements of such a detailed analysis this may not be feasible and therefore an evaluation of a smaller grid density is performed. Using O_2 adsorbed on cuboctahedral Au_{13} as a test system in a symmetric box of 625 $Å^3$ a range of sampling points per dimension ranging from 300 to 700 were evaluated. This is presented in figure 4.14 where change in charge is reported against sampling point mesh.

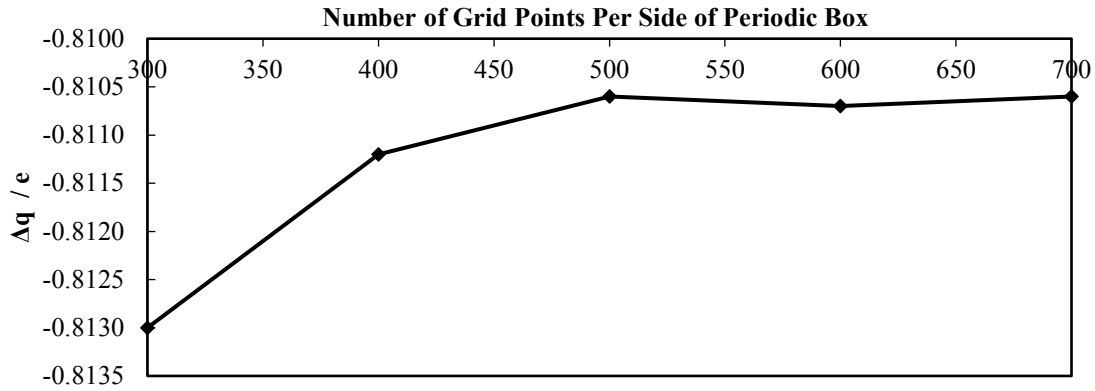

Figure 4.14: Number of grid points sampled per dimension of the periodic box vs total charge on O_2 molecule adsorbed on Au_{13} cluster.

The total charge on O_2 is displayed on the Y axis, it is clear it does not converge until 500 grid points per dimension of the box are used. This corresponds to 0.05 Å spacing. From this it can be concluded this is sufficient spacing and therefore the computational cost of finer sampling can be circumvented.

All Bader charge calculations performed in this thesis are subject to these conditions. Within the INCAR a spacing of 0.05 Å can be achieved by setting the NGZX, NGZY and NGZZ tag to the dimension size divided by 0.05.

References

1. Perdew, J. P., Burke, K. & Ernzerhof, M. Generalized Gradient Approximation Made Simple. *Phys. Rev. Lett.* **77,** 3865 (1996)

2. Perdew, J. P., Burke, K. & Ernzerhof, M. Generalized Gradient Approximation Made Simple [Phys. Rev. Lett. 77, 3865 (1996)]. *Phys. Rev. Lett.* **78,** 1396 (1997)

3. Rappoport, D., Crawford, N. R. M., Furche, F. & Burke, K. Which functional should I choose? (2008)

4. Perdew, J. P. *et al.* Atoms, molecules, solids, and surfaces: Applications of the generalized gradient approximation for exchange and correlation. *Phys. Rev. B* **46,** 6671 (1992)

5. Duan, Z. & Henkelman, G. CO Oxidation on the Pd(111) Surface. *ACS Catal.* **4,** 3435 (2014)

6. Grimme, S. Semiempirical GGA-type density functional constructed with a long-range dispersion correction. *J. Comput. Chem.* **27,** 1787 (2006)

7. Arlt, T. *et al.* High-pressure polymorphs of anatase TiO2. *Phys. Rev. B* **61,** 14414 (2000)

8. Ming, L. & Manghnani, M. H. Isothermal compression of TiO 2 (Rutile) under hydrostatic pressure to 106 kbar. *J. Geophys. Res.* **84,** 4777 (1979)

9. Swamy, V. & Dubrovinsky, L. S. Bulk modulus of anatase. *J. Phys. Chem. Solids* **62,** 673 (2001)

10. Jaćimović, J. *et al.* High-Pressure Study of Anatase TiO2. *Materials (Basel).* **3,** 1509 (2010)

11. Diebold, U. The surface science of titanium dioxide. *Surf. Sci. Rep.* **48,** 53 (2003)

12. Howard, K. L. *et al.* A periodic DFT study of the activation of O2 by Au nanoparticles on α-Fe2O3. *Faraday Discuss.* **152,** 135 (2011)

13. Dudarev, S. L., Savrasov, S. Y., Humphreys, C. J. & Sutton, A. P. Electron-energy-loss spectra and the structural stability of nickel oxide: An LSDA+U study. *Phys. Rev. B* **57,** 1505 (1998)

14. Luttrell, T. *et al.* Why is anatase a better photocatalyst than rutile? - Model studies on epitaxial TiO2 films. *Sci. Rep.* **4,** (2014)

15. Amft, M., Lebègue, S., Eriksson, O. & Skorodumova, N. V. Adsorption of Cu, Ag, and Au atoms on graphene including van der Waals interactions. (2010). at <http://arxiv.org/abs/1011.1113>

16. Sheppard, D. & Henkelman, G. Paths to which the Nudged Elastic Band Converges. *J Comput Chem* **32,** 1769 (2011)

17. Sheppard, D., Xiao, P., Chemelewski, W., Johnson, D. D. & Henkelman, G. A generalized solid-state nudged elastic band method. *J. Chem. Phys.* **136,** 74103 (2012)

18. Henkelman, G. & Jónsson, H. A dimer method for finding saddle points on high dimensional potential surfaces using only first derivatives. *J. Chem. Phys.* **111,** 7010 (1999)

19. Zeinalipour-Yazdi, C. D., Willock, D. J., Machado, A., Wilson, K. & Lee, A. F. Impact of co-adsorbed oxygen on crotonaldehyde adsorption over gold nanoclusters: a computational study. *Phys. Chem. Chem. Phys.* **16,** 11236 (2014)

Chapter 5

Oxygen Adsorption and Dissociation on Metal Particles

This chapter details the interaction of molecular oxygen with metal particles. Particular focus is directed towards the ability for metal particles to adsorb and dissociate oxygen. After both introduction and computational details, the results will be presented for nanoparticles which are both pure gold, pure palladium and alloys of these metals.

5.1 Introduction

Many of the reactions which gold nanoparticles can catalyse are oxidation. In these reactions a critical step is the adsorption and dissociation of O_2, an example being the low temperature oxidation of CO in which the adsorption of O_2 on the gold particles supported on TiO_2 may be the rate limiting step.[1] The mechanistic role of O_2 in such oxidation reactions has been the subject of much debate within the literature as in the case of CO oxidation it has been reported that the active species may be atomic[2] or molecular oxygen present in a peroxo or superoxo form[3]. Liu *et al.* report molecular oxygen and CO interacting together is favoured over CO reacting with atomically adsorbed oxygen[4], perhaps indicating that this is the mechanism for oxidation of CO. Furthermore, experimental studies by Salisbury *et al.* report only adsorption of molecular oxygen on negatively charged 2-22 atom Au clusters if there is an odd number of electrons.[5] The reasoning for this limitation of adsorption was suggested to be the requirement of an easy electron transfer from the cluster to molecular oxygen therefore making secondary adsorption unfeasible. However computational studies by Mills *et al.* demonstrated Au clusters which were both neutral and negatively charged were able to bind two oxygen molecules[6]. Density functional theory (DFT) calculations performed by Roldan *et al.*[7] investigated the adsorption and dissociation of molecular oxygen on gold nanoparticles. Nudged elastic band (NEB) calculations were used to investigate the pathway to dissociation on the particles. Strong adsorption of molecular oxygen on the nanoparticle is reported to be necessary but not the sole condition for dissociation. It is interesting to note it is reported that dissociated oxygen bound to the cluster is thermodynamically more stable than molecular oxygen, therefore indicating dissociation can be thermodynamically favourable under certain conditions. Whilst a consensus appears to indicate the thermodynamic favourability of

molecular oxygen to be dissociated onto the particles, there appears to be a lack of any kinetic data to confirm whether such dissociation is possible. Therefore, we decided to conduct further research into the adsorption and dissociation of oxygen on these particles. In this chapter a DFT investigation is presented discussing the interaction of molecular oxygen with gold particles, an extension of this study is to investigate the contrasting the behaviour with that of palladium particles and also bimetallic clusters containing a mixture of both Pd and Au. The aim of this work is to determine whether adsorption and dissociation of molecular oxygen is both kinetically and thermodynamically possible.

5.2 Computational Details

All calculations were performed using the Vienna Ab initio Simulation Package (VASP)[8,9,10,11]. The metal particles investigated here contain pure gold, pure palladium and their alloys. It is important to determine a suitable value for plane wave cut-off (E_{ncut}) within VASP which is suitable for all metals studied. For this two separate tests were performed with a cuboctahedral metal particle of both pure Au and pure Pd containing 38 atoms were separately placed within a cubic periodic box of 25 Å, total energy was plotted against plane wave cut-off. Figure 5.1 gives the resulting plot of total energy as a function of planewave cutoff.

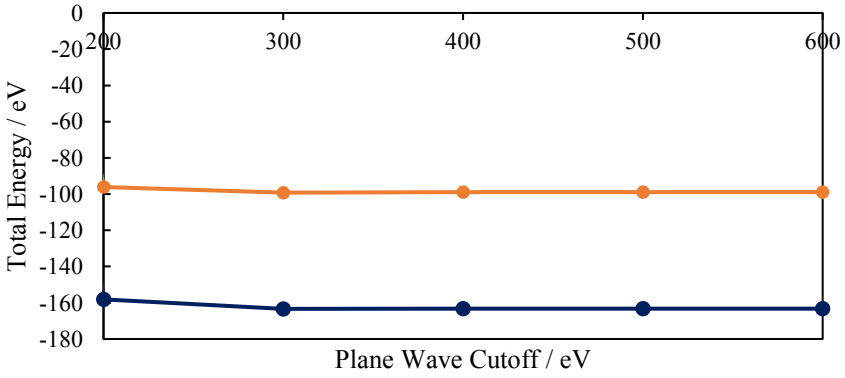

Figure 5.1: Total energy (eV) vs plane wave cut-off (eV) for Pd_{38} and Au_{38} particles. Gold is Au_{38}, blue is Pd_{38}.

Figure 5.1 clearly demonstrates a plane wave cut-off of 500 eV is suitable for treatment of both Pd and Au particles, this is because total energy has converged at this point. Further expansion of the plane wave cut off produces total energies which are a maximum of 0.008 eV different to the values obtained using 500 eV cut off therefore confirming this value is suitable. This value will be used for all further calculations. All calculations are performed using the generalized gradient approximation (GGA) using the functional of Perdew, Burke and Ernzerhof (PBE)[12,13]. PW91 was not chosen as a suitable functional as it is widely reported this functional can overestimate the binding energy of small molecules to metal surfaces[14,15] therefore exaggerating any calculated adsorption energies. All calculations are spin unrestricted with Projector Augmented Wave method (PAW) pseudopotentials used[16,17]. Explicit treatment of all electrons is unfeasible therefore a core valence system is employed which for gold contains 60 core and 19 valence electrons and for Pd 36 core, 10 valence electrons. For modelling of isolated systems/molecules in a large (625 $Å^3$) periodic box Monkhorst-Pack[18] *k*-point grid density was set to a mesh of . A small sample mesh along with adequately sized periodic box prevents any spurious self-interaction between periodic images. As these particles differ from bulk metal it is assumed they contain discrete orbital energies as opposed to continuous bands observed within bulk metals therefore Gaussian smearing with a very small width of 0.001 was employed within VASP to ensure electronic smearing does not occur at the Fermi level. All geometry relaxations were performed with electronic and force convergence criteria set to 10^{-4} eV and -0.05 eV $Å^{-1}$ respectively.

The PBE functional within VASP provides an option to include long range dispersion interactions using the D2 method of Grimme[19]. Parameters used to treat dispersion interactions are not supplied for gold and instead were obtained from literature[20]. Discussion of the inclusion of this D2 correction will be provided later within chapter 6.

Bader charge analysis was performed to deduce atomic charges on adsorption, this method was developed by Henkelman *et al.*[21–23] Grid spacing for Bader charge analysis was determined through investigation of a test system in which O_2 was adsorbed onto an Au_{13} cluster. Total charge transfer to/from the O_2 molecule was determined by subtracting the calculated Bader charge from the valence charge of oxygen. A negative value indicates oxygen has gained electron density whilst a positive value indicates O_2 has donated a degree of electron density to the metal particle. Interaction of O_2 with these particles has a degree of charge transfer from O_2 towards the cluster followed by back donation into the π^* orbital on O_2. Figure 5.2 indicates

total charge transfer to O_2 as a function of grid sample points. It is clear that 500 grid point sampling the charge transfer has converged. This equates to a sample point within the grid being taken every 0.05 Å. Within literature fine grid spacing is reported as a requirement for many systems with 0.023 Å reported a suitable spacing for gold particles[24]. The large system sizes used in this work made it difficult to achieve 0.023 grid spacing but these convergence tests show a 0.05 Å grid spacing is sufficient and therefore was chosen for all Bader charge analysis calculations discussed in this chapter. 0.05 Å grid spacing corresponds to NGXX = 500, NGXY and NGXZ = 500 within the VASP INCAR file.

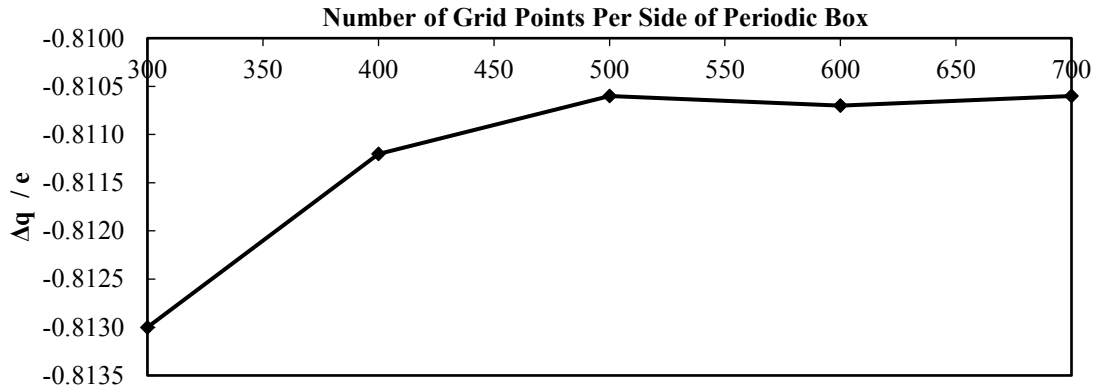

Figure 5.2: Number of grid points sampled per side of periodic box vs total charge on O_2 molecule adsorbed on Au_{13} cluster.

NEB calculations as discussed within the computational details section were used in order to determine transition states for O_2 dissociation. The transition states were verified by performing a frequency calculation on the proposed transition state system in order to locate a single imaginary frequency mode.

5.3 Oxygen Interaction with Metal Particles

Metal particles containing 38 atoms with the cuboctahedral geometry were chosen to investigate the adsorption of molecular oxygen. These clusters exhibit both square (100) and trigonal (111) facets. Bimetallic particles have been identified as demonstrating catalytic properties different to their pure metal counterparts. An example of contrasting behaviour is the alloy of Au/Pd which markedly increases the rate of H_2O_2 synthesis[25] in comparison to pure metal counterparts. Whilst these alloys have been characterised with a homogeneous distribution of both metals the alternative in which a core-shell comprising of gold with a palladium shell have also been successfully synthesized[26]. Core-shell particles have been identified and active for glycerol oxidation catalysis[27] therefore the author of this work believes the unique nature of such core-shell alloys warrants an investigation into their interaction with molecular oxygen. Au_6Pd_{32} has been chosen as this geometry enables a simple core / shell system to be modelled. A 50:50 homogeneous mixture contains a large amount of possible configurations therefore a simpler core / shell system was chosen for computational cost reasons.

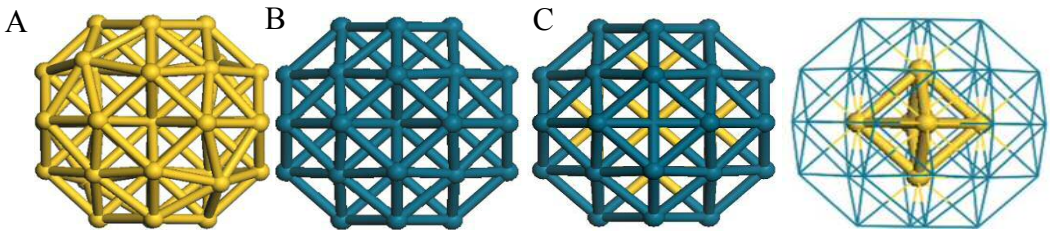

Figure 5.3: Metal particles investigated for adsorption with O_2. A) Au_{38}, B) Pd_{38}, C) Au_6Pd_{32} with separate image highlighting octahedron core.

Figure 5.3 details the metal particles investigated within this chapter. The particles are highly symmetrical and contain a mixture of (100) and (111) facets (squares and triangles respectively). These facets have previously been identified as sites of interest in which reactant molecules can adsorb and potentially react at. Corma *et al.* identified the junction of (100) and (111) facet as a site at which molecular oxygen binds most preferentially on an Au_{38} cluster[28].

Using VASP these 3 structures were fully relaxed and energies obtained which are denoted $E_{cluster}$. Molecular oxygen with a triplet ground state was placed within a periodic cell of the same size (625 $Å^3$) and fully relaxed. The energy of molecular oxygen is denoted E_{oxygen}. In order to deduce the most favourable mode of adsorption three distinct sites were investigated;

site A, site B and site C (Figure 3). Adsorption onto site A is one in which oxygen is adsorbed at the junction of two (111) facets. Adsorption site B is adsorption at the junction of a (100) and (111) facet and finally adsorption site C is one in which molecular oxygen is parallel and centred over the (100) facet. As adsorption followed by dissociation is of interest within this work, adsorption sites in which molecular oxygen are perpendicular to the facet have been discounted solely because the orientation of such adsorption prohibits a possibility of computationally investigating a mechanism for dissociation.

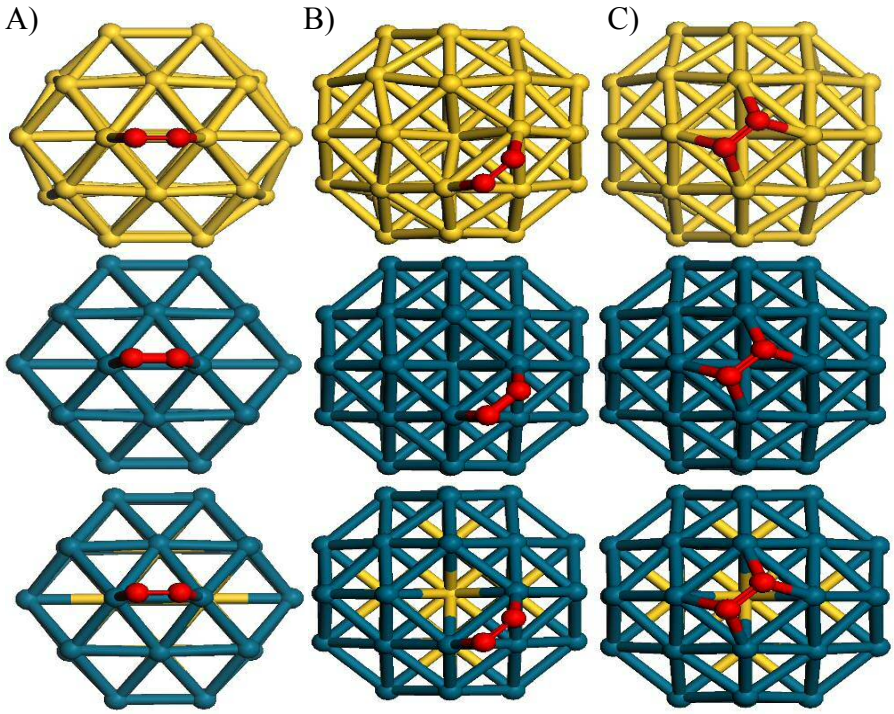

Figure 3: Molecular oxygen adsorbed onto site A, B and C for all three metal particle compositions studied.

Once molecular oxygen is adsorbed geometry relaxations produced an energy denoted $E_{cluster+oxygen.}$ Using equation 5.1 adsorption energies (E_{ads}) were determined with favourable adsorption indicated by a negative calculated value.

(5.1)

Table 5.1 displays calculated adsorption energies for molecular oxygen onto the three metal particles investigated.

Table 5.1: Adsorption energies calculated for oxygen adsorbed in three different positions onto the clusters studied.

	E_{ads} / eV		
	A	B	C
Au_{38}	-0.67	-0.72	-0.60
Pd_{38}	-1.28	-1.26	-1.59
Au_6Pd_{32}	-1.44	-1.47	-1.76

The calculated adsorption energies in Table 5.1 clearly indicate adsorption of molecular oxygen into all three sites is favourable as each value calculated is negative with increasing negativity corresponding to a stronger interaction. It is interesting to observe adsorption site C is the preferred mode of adsorption for molecular oxygen for Pd_{38} and the Au_6Pd_{32} clusters however this preference is shifted towards site B for the Au_{38} cluster. The data clearly indicates adsorption is greatly enhanced on Pd_{38} and Au_6Pd_{32} clusters compared to gold. Data obtained for Au_{38} is in excellent agreement with previous calculations performed by Corma *et al*. In their work adsorption energies were determined as -0.99 eV, -1.04 eV and -0.98 eV[28] for sites A, B and C respectively. Whilst these values differ from literature the ordering is consistent and validates data obtained here.

To quantify the changes in adsorption energies Bader charge analysis was performed. In order to maintain grid spacing appropriate to the tests performed and demonstrated in Figure 5.2, the periodic box was rescaled to 600 $Å^3$. Rescaling the box ensured memory requirements were not computationally exceeded.

Table 5.2 highlights the result of this charge analysis which focussed on determining the partial charges on the oxygen atoms. A negative value indicates the oxygen atoms have received electron density upon adsorption.

Table 5.2: Calculated Bader charge analysis for O_2 once adsorbed onto the three different clusters on all adsorption sites.

	q(O_2) / e		
	A	B	C
Au_{38}	-0.57	-0.59	-0.81
Pd_{38}	-0.53	-0.51	-0.73
Au_6Pd_{32}	-0.51	-0.52	-0.73

Bader charge analysis of O_2 adsorbed on all metal cluster indicate there is a greater degree of charge transfer which accompanies an adsorption onto site C. Both Pd_{38} and Au_6Pd_{32} have almost identical values for charge transfer to O_2 indicating electronically both adsorption modes are similar due to the predominating Pd shell present within the bimetallic cluster. As the shell is Pd it is reasonable to expect properties to be very similar to the pure Pd cluster. Adsorption is a balance between donation of electron density from O_2 to the metal particle followed by back donation to the π^* orbitals present on the O_2 molecule. As Bader charge analysis has indicated O_2 has received electron density it is reasonable to assume the back donation component of the adsorption is predominant here. Back donation will cause a decrease in the overall bond order of O_2 as electron density in the anti-bonding π orbital is increased, therefore weakening and increasing the bond distance within O_2. Table 5.3 details the O-O bond length upon adsorption at all three sites and the change in equilibrium bond distance.

Table 5.3: O-O distance upon adsorption onto sites A, B and C for all cluster compositions studied. These values are tabulated against the change in equilibrum bond distance where a positive value indicates an elongation of the O-O bond.

	r_{o-o} Upon Adsorption / Å			Δr_{o-o} Equilibrium / Å		
	A	B	C	A	B	C
Au_{38}	1.352	1.354	1.453	0.125	0.127	0.226
Pd_{38}	1.355	1.338	1.446	0.128	0.111	0.219
Au_6Pd_{32}	1.346	1.338	1.442	0.119	0.111	0.215

The changes in equilibrium bond distances observed in Table 5.3 clearly demonstrate a substantial elongation of the O-O bond once adsorbed into site C. This elongation is approximately a 20% increase therefore molecular oxygen can be considered adsorbed in a superoxo state this is supported through charge analysis indicating a negatively charged adsorbed O_2 species. DFT calculations performed by Landman *et al.* indicate the mechanism to dissociation of molecular oxygen on gold clusters is facilitated by adsorption of molecular oxygen in this superoxo state[29]. Figure 5.4 details the relationship between charge transfer and elongation in bond length in O_2 upon adsorption. It clearly demonstrates a correlation between the two confirming back donation and subsequent elongation of the O_2 bond distance upon adsorption. If adsorbed in site C, molecular oxygen is bound with the highest coordination number in comparison to the other sites studied. This suggests morphology of the particle may influence interactions within a catalytic process.

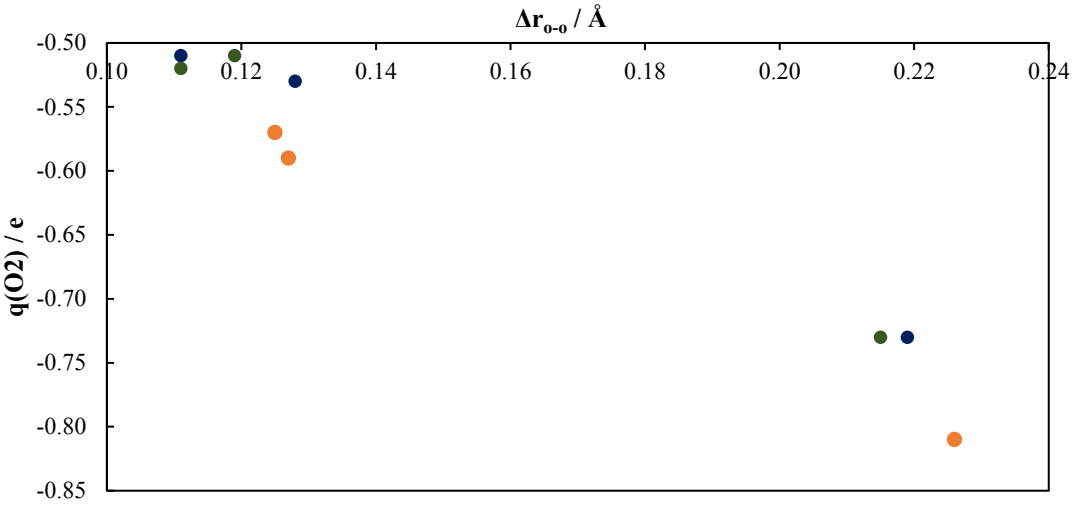

Figure 5.4: Change in equilibrium bond distance for O_2 upon adsorption vs charge transfer onto it. Gold colour indicates Au_{38}, blue colour Pd_{38} and green colour is Au_6Pd_{32}.

All three sites for adsorption are energetically feasible however as oxygen adsorption and dissociation are of interest here only adsorption via site C will be investigated for subsequent molecular oxygen molecules.

5.4 Multiple Molecular Oxygen Adsorption

To investigate how the presence of pre-adsorbed molecular oxygen influences subsequent O_2 adsorptions on each metal particle with molecular oxygen pre-adsorbed in site C was taken as a starting point to which another oxygen molecule was adsorbed. Each particle has 6 (100) facets which accompanied by the high symmetry allow for all other adsorption sites to be considered through sampling of each site. At each adsorption configuration stage E_{ads} was determined and Figure 5.5 details adsorption energies as a function of coverage. Figure 5.5 indicates distinctly different trends in adsorption across the particles studied, Au_{38} demonstrates a nonlinear plot which adsorption energy becomes less favourable and in some instances becomes positive at the 3rd molecular oxygen and then adsorption energies become favourable until all sites are covered. Pd_{38} and Au_6Pd_{32} together show a different pattern in which adsorption energies are largely favourable (E_{ads} ~-1.6 eV) until each (100) facet is saturated with molecular oxygen.

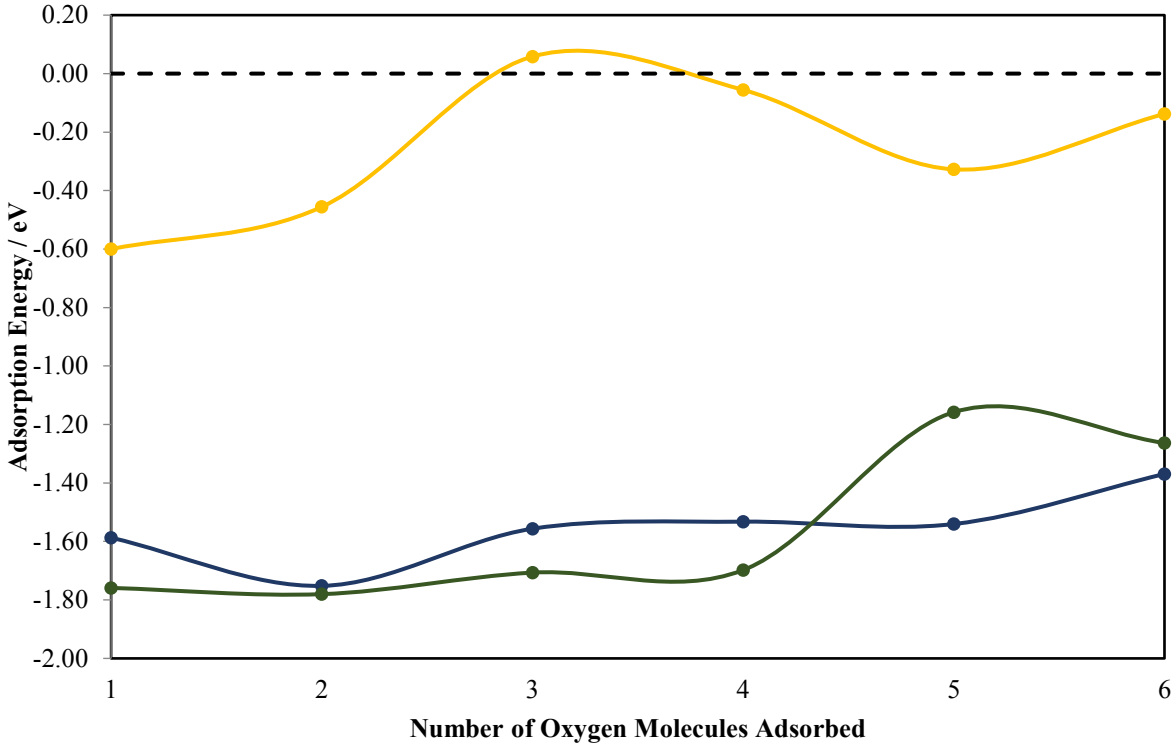

Figure 5.5: Adsorption energy vs number of oxygen molecules pre-adsorbed onto site C for all clusters. Gold colour represents Au_{38}, blue Pd_{38} and green Au_6Pd_{32}.

Based upon this data it would be reasonable to assume no more than two oxygen molecules can adsorb favourably onto Au_{38} whereas 6 can adsorb onto the other metal particles studied. With regards to dissociation it already has been ascertained charge transfer to the O_2 molecule facilitates dissociation through weakening and elongation of the O-O bond. Due to this requirement Bader charge analysis was again performed at each coverage point to deduce how charge transfer to the incoming adsorbate varies as a function of coverage. This is illustrated in Figure 5.6.

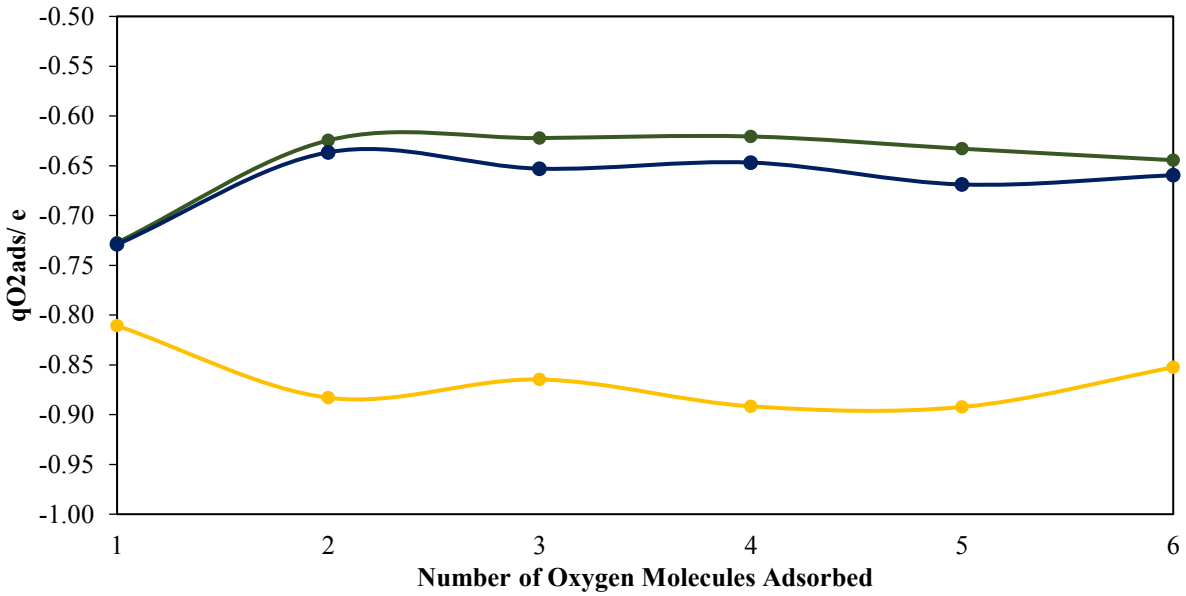

Figure 5.6: Bader charge analysis indicating charge transfer from metal particle to incoming O_2 molecule vs number of molecules adsorbed onto particles. Gold is Au_{38}, blue is Pd_{38} and green is Au_6Pd_{32}.

Substantial donation of electron density to O_2 is observed for all molecular oxygen adsorptions on Au_{38} with almost one electron transferred to each adsorbed O_2 species. Both Pd_{38} and Au_6Pd_{32} are similar in trends with a decrease in charge transfer which accompanies the second adsorbed O_2 molecule. This charge transfer data is accompanied by elongation of the O-O bond in the case of Au_{38}.

Observations made in this chapter clearly indicate gold exhibits a weaker interaction for molecular oxygen compared to palladium and its alloys. Charge transfer into the π^* orbitals may explain the origin of weaker adsorption energies as the Bader charge analysis indicates gold donates more electron density towards O_2 than the other metal particles studied, therefore destabilizing it. Another reason for weakened adsorption may be geometric, due to the size mismatch between O_2 and the (100) facet it is adsorbed on. Table 5.3 details measurements of the facet in which O_2 is adsorbed onto. As this facet is not a perfect square (minor geometric differences of the particle facet) the average of both sides were taken and denoted x. The equilibrium bond length for O_2 is calculated at 1.227Å and the biggest size mismatch between this and x occurs with Au_{38}, upon adsorption into this facet the O_2 molecule must undergo an elongation which inevitably requires energy and therefore may explain the weakened adsorption energies reported for O_2 adsorbed onto Au_{38}.

Table 5.3: Measurements of the (100) facets obtained for all three clusters in Å.

	Au_{38}	Pd_{38}	Au_6Pd_{32}
a	2.89	2.69	2.74
b	2.76	2.69	2.74
$x = \frac{a+b}{2}$	2.83	2.69	2.74

A breakdown of the different energy contributions to the adsorption can aid understanding as to whether elongation of the double bond within O_2 as it adsorbs onto the (100) facet destabilises the interaction between it and the Au_{38} particle. To perform this breakdown single point energy calculations were taken of the following; molecular oxygen within its adsorbed geometry and the metal particle geometry once O_2 is adsorbed. These single point calculations allow for the following to be determined; $\Delta E_{cluster}$ – the energy change in the cluster from starting geometry and ΔE_{o2} – the energy change in adsorbed molecular oxygen compared to isolated equilibrium geometry. Positive values for both calculated values indicate once adsorbed the species (cluster or O_2) are in a higher energy than their respective start points. Table 5.4 details the results of these calculations.

The calculated ΔE_{o2} values demonstrate upon adsorption onto Au_{38} molecular oxygen is significantly higher in energy compared to its equilibrium geometry. This energy is highest once adsorbed onto Au_{38} therefore offers explanation for the weakened adsorption energies observed when oxygen interacts with pure gold particles.

Table 5.4: Calculated cluster and oxygen rearrangements energies in eV.

	Au_{38}	Pd_{38}	Au_6Pd_{32}
$\Delta E_{cluster}$	0.356	0.184	0.150
ΔE_{o2}	1.112	1.058	1.033

These observations made in this section and also by Landman *et al.*[30] allow for a reasonable hypothesis that in order to dissociate molecular oxygen should adsorb via site C.

5.5 Dissociation of Molecular Oxygen

It has been ascertained that oxygen adsorbs favourably in all positions investigated onto all the metal particles studied within this work. Calculations performed allow for a prediction that dissociation via site C will be preferred. This hypothesis will now be confirmed through a systematic study of all dissociation pathways on the metal clusters. These three adsorption sites (A,B and C) give rise to 5 different dissociation routes. These routes are detailed in Figure 5.7. Dissociation pathway A occurs via adsorption position A, in this instance dissociated oxygen atoms occupy two (111) trigonal facets adjacent to each other. Dissociation pathways B, C and D occur via adsorption onto site B. Dissociation pathway B has two adjacent oxygen atoms present within a "linear bridge" type arrangement, dissociation site C has oxygen atoms in two (111) facets with a (100) facet in between. Dissociation pathway D has oxygen atoms in the (111) facets adjacent to the (100) facet which is an identical end point to pathway E.

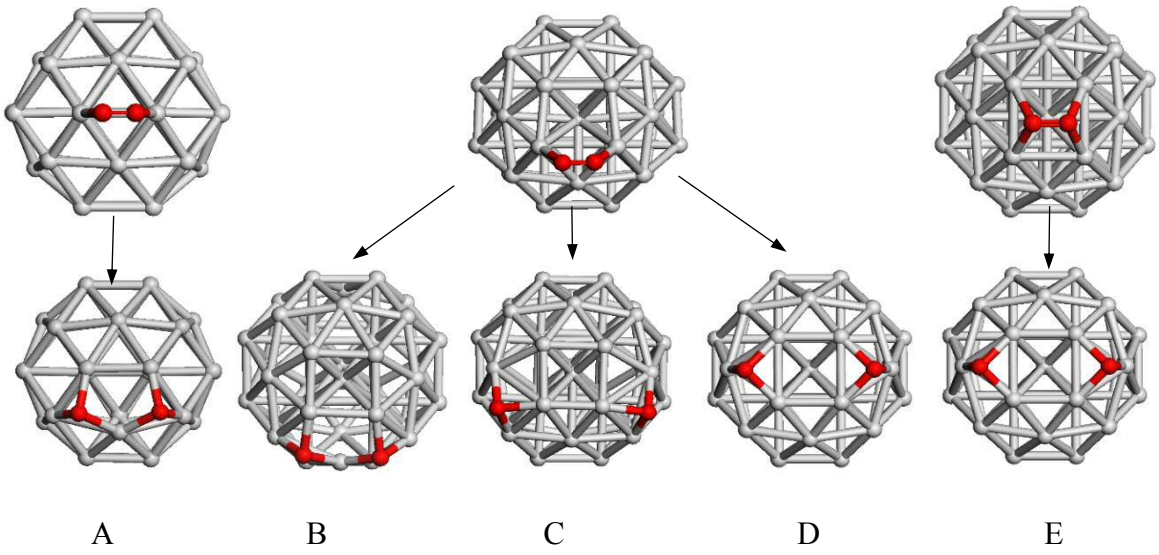

Figure 5.7: Dissociation pathways for molecular oxygen once adsorbed at the three different sites. Here a grey cluster is used to represent all metal clusters studied.

Each of these dissociated end points (A-E) were geometry optimised within VASP and used as termination points for the NEB calculations. The end point energies are presented in Table 5.5. These values are total energy output values and are reported as a comparison of different end point values indicate thermodynamic stability across a cluster composition. In order to cross a reaction barrier and overcome the energy required for dissociation the barrier calculated should

not be substantially larger than the adsorption energy of molecular oxygen. NEB calculations with 24 intermediate images were performed to determine these barriers. 24 images were found to be necessary as they produce a smooth profile and allow for effective sampling of the barrier. The dissociation barriers for O_2 adsorbed on Au_{38} are detailed in figures 5.9-5.11.

Table 5.5: End point energies in eV for each dissociation pathway.

	A	B	C	D	E
Au_{38}	-110.396	-110.382	-110.634	-110.563	-110.563
Pd_{38}	-175.276	-175.918	-175.721	-175.502	-175.508
Au_6Pd_{32}	-163.148	-163.722	-163.519	-163.432	-163.432

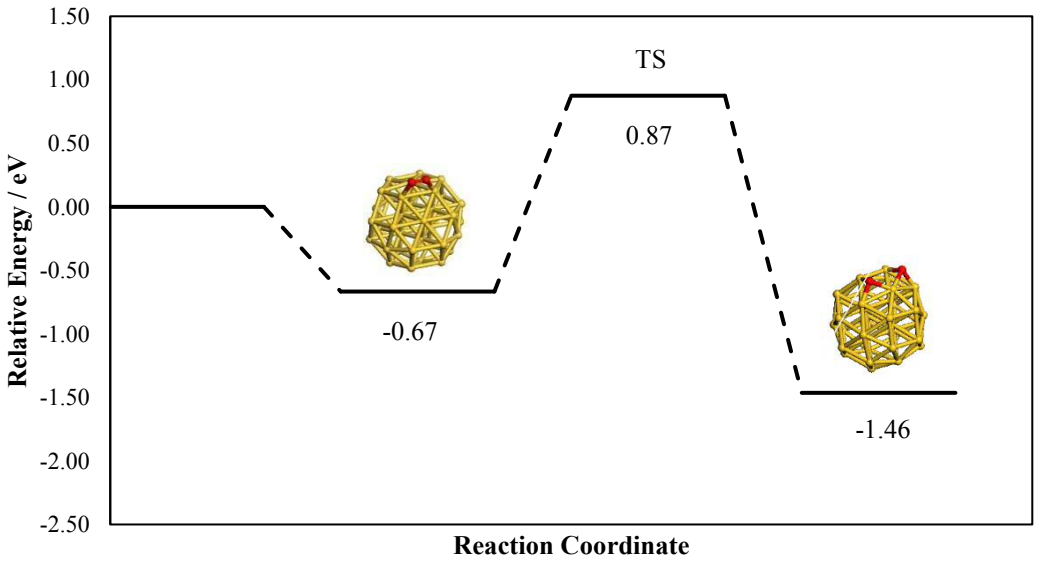

Figure 5.8: Reaction pathway for dissociation of O_2 on Au_{38} via pathway A**.** Zero energy is set relative to isolated gold cluster and isolated molecular oxygen. TS corresponds to transition state energy.

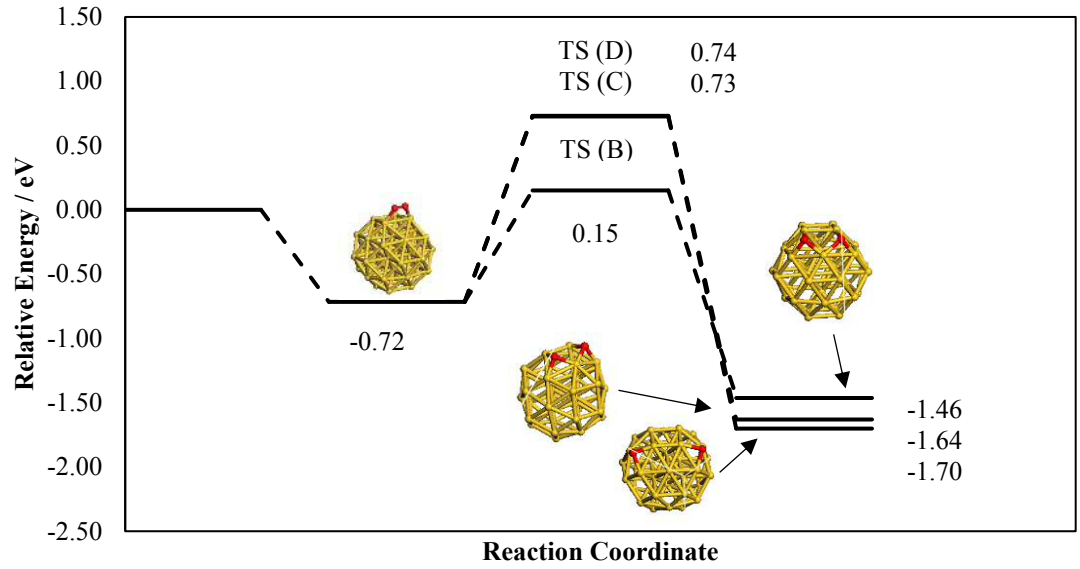

Figure 5.9: Reaction pathway for dissociation of O_2 on Au_{38} via pathways B, C and D. Zero energy is set relative to isolated gold cluster and isolated molecular oxygen. TS corresponds to transition state energy.

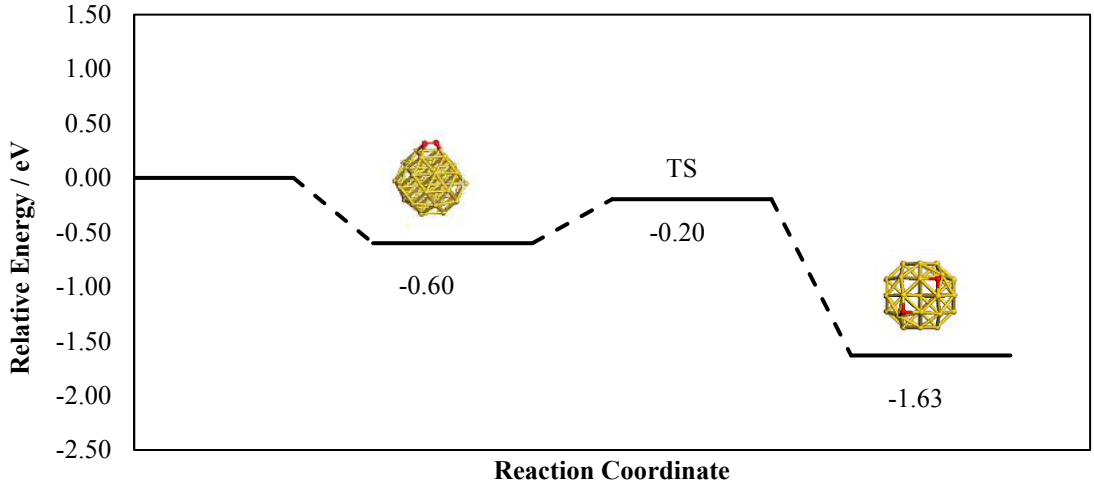

Figure 5.10: Reaction pathway for dissociation of O_2 on Au_{38} via pathway E. Zero energy is set relative to isolated gold cluster and isolated molecular oxygen. TS corresponds to transition state energy.

Figures 5.8-5.10 detail a large difference in the barrier to dissociation of O_2 depending upon which dissociation pathway was taken. For gold all barriers to dissociation are greater than the adsorption energy except via pathway E in which the barrier is 0.4 eV corresponding to a molecular adsorption energy of -0.6 eV therefore ensuring enough excess energy is present upon adsorption to initiate dissociation. For all other configurations it is reasonable to assume molecular adsorption only. Figures 5.11-5.13 are the calculated barriers to dissociation of molecular oxygen this time adsorbed on Pd_{38}.

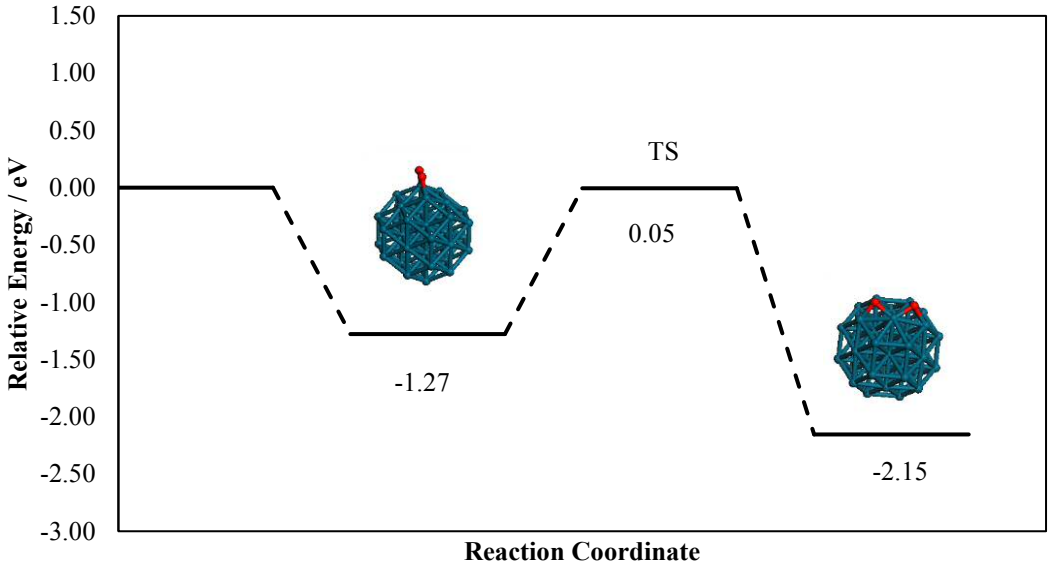

Figure 5.11: Reaction pathway for dissociation of O_2 on Pd_{38} via pathway A. Zero energy is set relative to isolated palladium cluster and isolated molecular oxygen. TS corresponds to transition state energy.

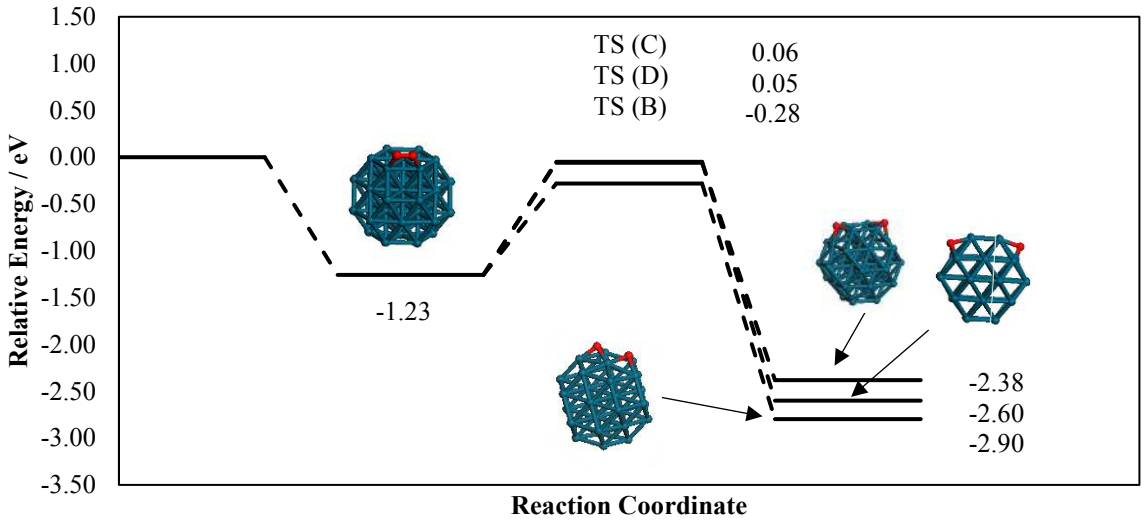

Figure 5.12: Reaction pathway for dissociation of O_2 on Pd_{38} via pathways B, C and D. Zero energy is set relative to isolated palladium cluster and isolated molecular oxygen. TS corresponds to transition state energy.

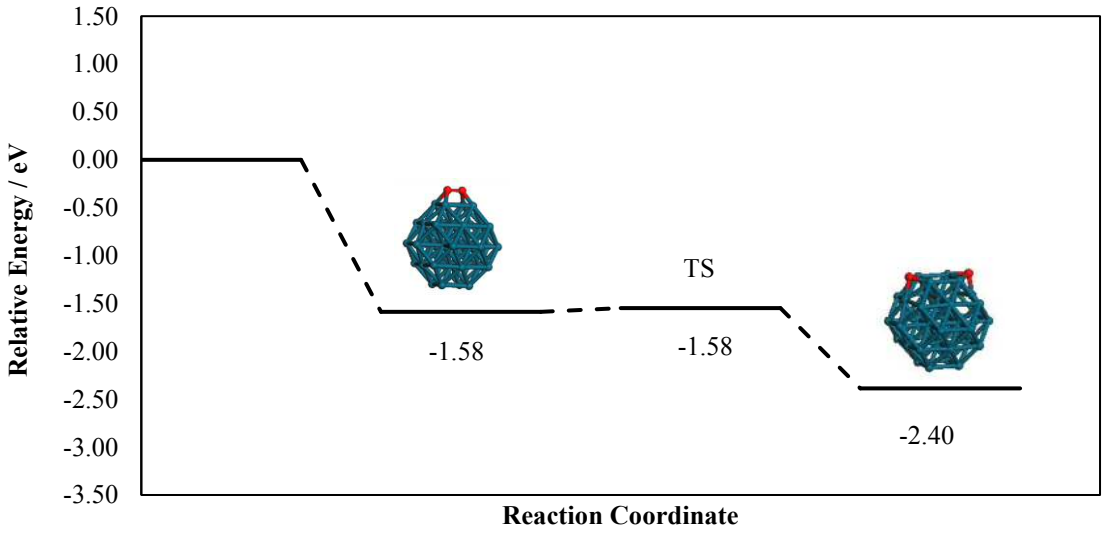

Figure 5.13: Reaction pathway for dissociation of O_2 on Pd_{38} via pathway E**.** Zero energy is set relative to isolated palladium cluster and isolated molecular oxygen. TS corresponds to transition state energy

Figures 5.11-5.13 demonstrate dissociation via pathway A-E is energetically feasible due to adsorption energies being higher than calculated barriers to dissociation. Figure 5.13

demonstrates however there is a clear preference for dissociation pathway E in which a barrier has been determined to be 0.04 eV relative to the adsorbed state which is substantially lower than any other route. Whilst adsorption energies exceed all other calculated barriers, dissociation pathway E is dramatically lower and as a result this will be studied as it is most feasible and will reduce computational cost to solely focus on this route.

Figures 5.14-5.16 are the calculated reaction barriers for pathways A-E for Au_6Pd_{32}.

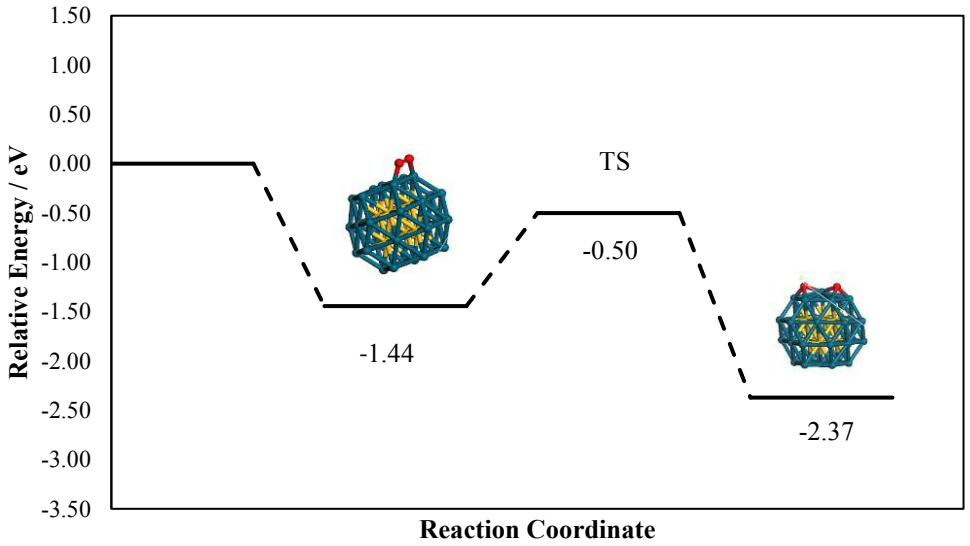

Figure 5.14: Reaction pathway for dissociation of O_2 on Au_6Pd32 via pathway A**.** Zero energy is set relative to isolated palladium cluster and isolated molecular oxygen. TS corresponds to transition state energy.

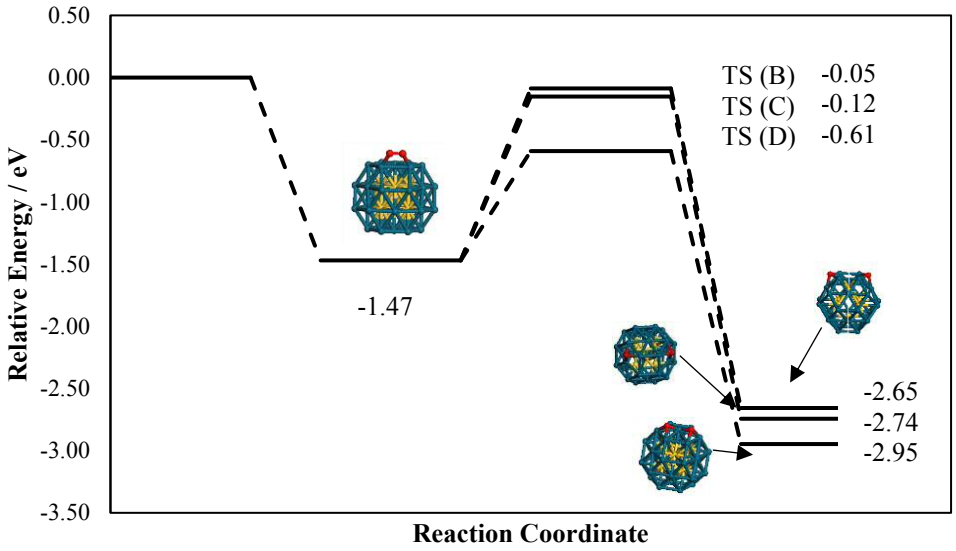

Figure 5.15: Reaction pathway for dissociation of O_2 on Au_6Pd_{32} via pathways B, C and D. Zero energy is set relative to isolated palladium cluster and isolated molecular oxygen. TS corresponds to transition state energy.

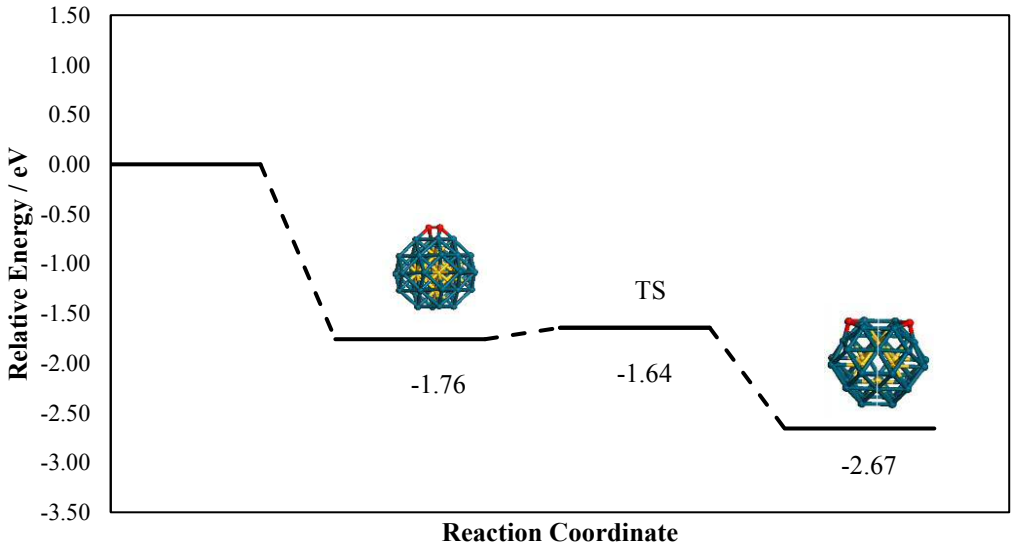

Figure 5.16: Reaction pathway for dissociation of O_2 on Au_6Pd_{32} via pathway E**.** Zero energy is set relative to isolated bimetallic cluster and isolated molecular oxygen. TS corresponds to transition state energy.

Figures 5.14-5.16 demonstrate dissociation via pathway E is the most energetically favourable route. In this instance the barrier to dissociation is 0.12 eV relative to the adsorption energy which is substantially lower than the other barriers computed. In all instances dissociation is possible however kinetically route E is the most likely.

5.6 Migration of Adsorbed Oxygen Species

For Au_{38} the adsorption which is most energetically favourable is site B however dissociation via this pathway has been demonstrated to be less probable due to the relatively high barrier in comparison to the adsorption energy calculated. We view it necessary to investigate the possibility of a two-step mechanism for dissociation in which molecular oxygen adsorbs onto site B and migrates to site C followed by a dissociation.

Figure **5.17** details this pathway for Au_{38}.

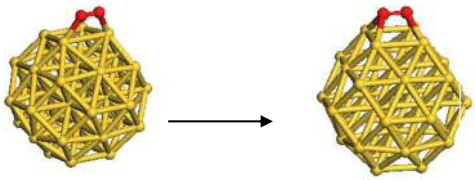

Figure 5.17: Migration pathway for molecular oxygen from site B to site C on Au_{38}.

Using the NEB method this migration pathway was investigated for all three compositions of cluster. Figure 5.18 details the reaction profile for this migration route.

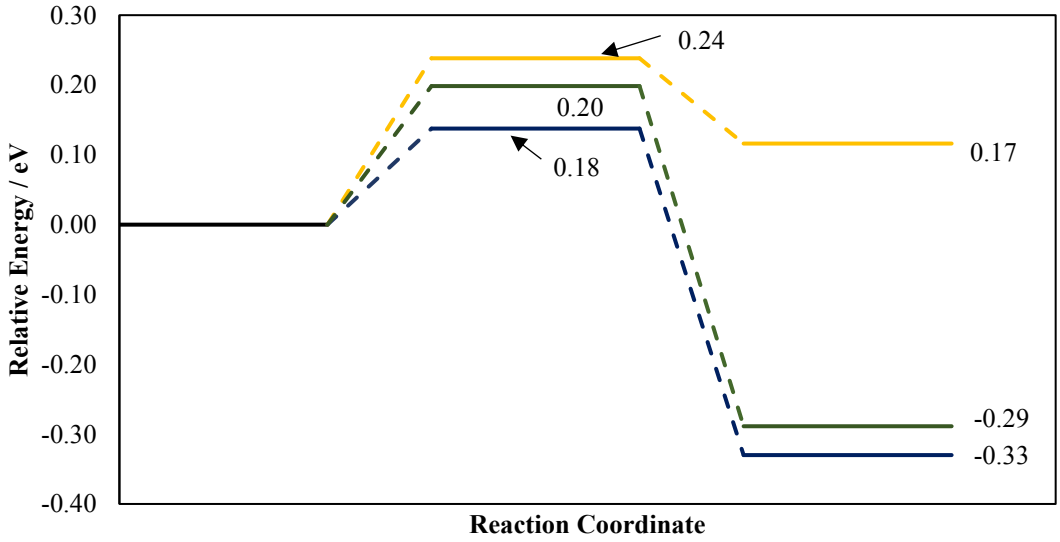

Figure 5.18: Calculated barriers for migration from site B to site C for all clusters studied. Energies are set to oxygen adsorbed into site B. Gold line is Au_{38}, blue is Pd_{38} and green is Au_6Pd_{32}. Energies are reported in eV.

The barrier to migration in all cases is no greater than 0.22 eV therefore it is reasonable to assume the movement of molecular oxygen into the (100) facet is a facile process and propose this is an alternate mechanism for a dissociation pathway.

5.7 Multiple Oxygen Adsorption and Dissociation

Within the literature there is clear debate regarding the ability of metal particles particularly gold to adsorb and dissociate multiple oxygen species. Whetten *et al.*[5] report multiple adsorption of molecular oxygen is unfavourable whereas Mills and Gordon[31] report multiple adsorption.

To deduce whether there is a capability to adsorb and dissociate multiple molecular oxygen species a systematic study was performed which determined the feasibility of such processes.

It has been deduced that molecular oxygen adsorbs and dissociates via the (100) facet (site C), the dissociated oxygen atoms occupy the (111) facet. This study has been extended by taking a metal particle with oxygen pre dissociated and adsorbing another molecular oxygen. The metal particles studied with cuboctahedral geometry have 6 (100) facets, therefore symmetry along with this number helps reduce the number of subsequent sites for adsorption of molecular oxygen. Figure 19 details the preferred adsorption site along with calculated adsorption energies (eV) for the three cluster compositions.

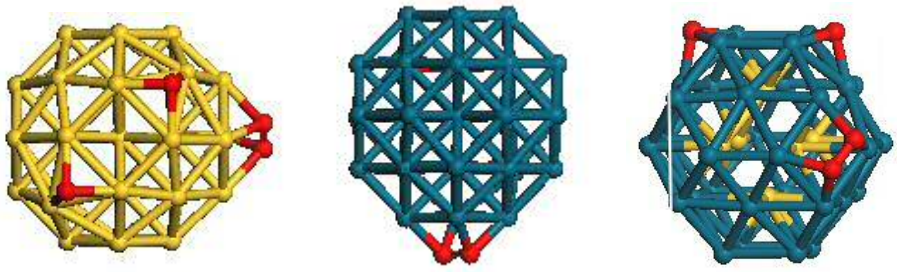

-0.083 -1.723 -1.798

Figure 5.19: Preferred adsorption site for second molecular oxygen on Au_{38}, Pd_{38} and Au_6Pd_{32}. This is accompanied by adsorption energies in eV.

Figure 5.19 demonstrates there is a marked reduction in adsorption energy for molecular oxygen adsorbing to a gold particle which contains pre-dissociated oxygen species. The

adsorption energy is almost negligible compared to the pure Pd and bimetallic clusters. For these three configuration there appears to be no trend in whether any particular site is favourable. This is due to no consistency in the most preferred adsorption site. In Au_{38} and Au_6Pd_{32} adjacent (100) facets are preferred whilst in Pd_{38} the (100) facet furthest from the occupied site is preferred.

Using the NEB method similar to that within 5.3.3 the barrier to dissociation was determined and is presented in figure 5.20.

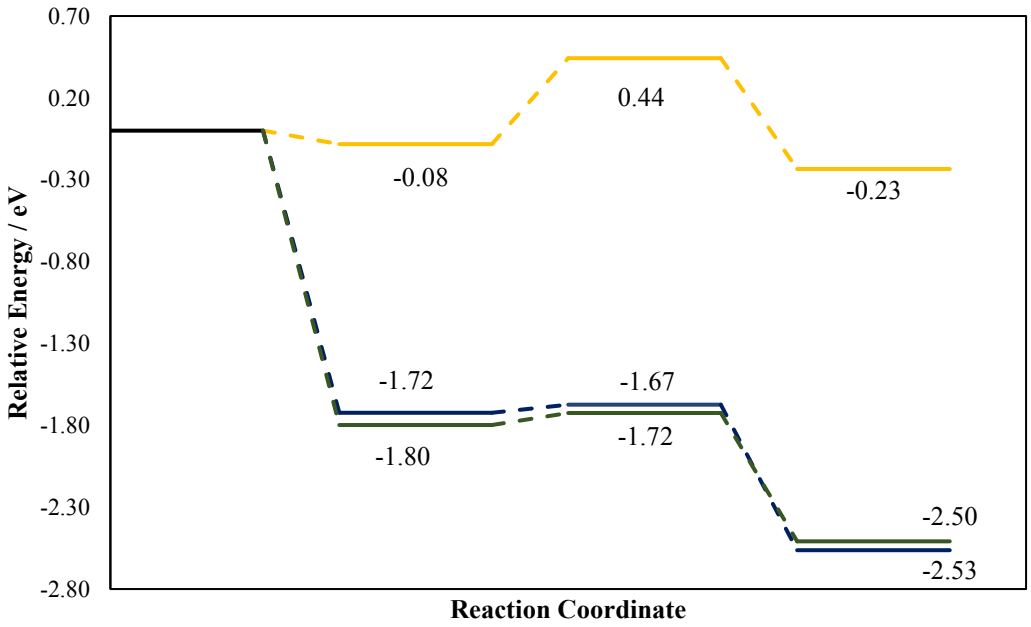

Figure 5.20: Energy profile for adsorption of secondary molecular oxygen species, followed by dissociation at site C (pathway E). Energies are set relative to the energy of isolated molecular oxygen and cluster with pre-dissociated oxygen present. Gold colour represents Au_{38}, blue Pd_{38} and green Au_6Pd_{32}. Energies are reported in eV

At this stage there is clearly a difference in properties between Au_{38} and Pd_{38} and Au_6Pd_{32}. The barrier to dissociation for Au_{38} is approximately 0.5 eV higher than the well it sits in following adsorption. There is however a minimal adsorption energy of molecular oxygen therefore it is assumed it is energetically unfeasible to adsorb and dissociate a second molecular oxygen species on Au_{38}. Based upon this observation it is reasonable to assume no dissociative adsorption occurs for this second species. Both Pd_{38} and Au_6Pd_{32} appear to have a similar reaction pathway. A large adsorption energy is accompanied by a small barrier ~0.1 eV therefore spontaneous dissociation following adsorption is likely.

To determine whether any further dissociation is possible on Au_{38} a third molecular oxygen was adsorbed to the metal particle which had 2 dissociated molecular oxygen species pre adsorbed. The most favourable adsorption site in this instance has a calculated adsorption energy of 0.15 eV therefore no favourable adsorption and by extension dissociation is possible on Au_{38}. It is concluded Au_{38} can adsorb and dissociate one molecular oxygen species, it is reasonable to assume at elevated temperatures and oxygen pressure that a second adsorption and dissociation is possible. Any further activity is hindered by positive adsorption energies.

The Pd_{38} and Au_6Pd_{32} oxygen adsorption and dissociation study was continued and figures 5.21 and 5.22 clearly indicate these particles can adsorb and dissociate molecular oxygen species with energetic ease whereas figure 5.23 indicates no more than one adsorption and dissociation of molecular oxygen is possible on Au_{38}. For Au_6Pd_{32} the dissociation study was terminated at 11 molecular oxygen dissociations, this is due to significant cluster distortion which prohibited a 12^{th} molecular oxygen from dissociating into trigonal (111) facets. Table 5.6 details the calculated barriers (TS) for each metal particle / oxygen system investigated.

Table 5.6: Calculated reaction barriers relative to adsorption well for O_2 dissociation in eV for each metal particle system investigated.

Transition State	Au_{38}	Pd_{38}	Au_6Pd_{32}
1	0.40	0.04	0.12
2	0.50	0.05	0.07
3	-	0.06	0.07
4	-	0.09	0.11
5	-	0.18	0.11
6	-	0.16	0.20
7	-	0.22	0.23
8	-	0.26	0.18
9	-	0.27	0.26
10	-	0.28	0.26
11	-	0.29	0.19
12	-	0.41	-

Table 5.6 indicates the barriers to dissociation experience a gradual increase in the barrier to O_2 dissociation for all particles studied. These barriers however are not insurmountable due to the sufficiently large adsorption energies (reported in table 5.7) for each configuration on the Pd_{38} and Au_6Pd_{32} particles.

Table 5.7: Oxygen adsorption energies for the most favourable bridge-bridge configuration on Pd_{38} and Au_6Pd_{32}

Molecular Oxygen Adsorption Number	O_2 E_{ads} on Pd_{38} / eV	O_2 E_{ads} on Au_6Pd_{32} / eV
1	**-1.59**	**-1.76**
2	**-1.72**	**-1.80**
3	**-1.77**	**-2.00**
4	**-1.83**	**-1.84**
5	**-1.47**	**-1.70**
6	**-1.60**	**-1.37**
7	**-1.43**	**-1.25**
8	**-1.31**	**-0.98**
9	**-1.03**	**-1.32**
10	**-0.39**	**-0.91**
11	**-0.75**	**-0.89**
12	**-0.22**	**-1.00**

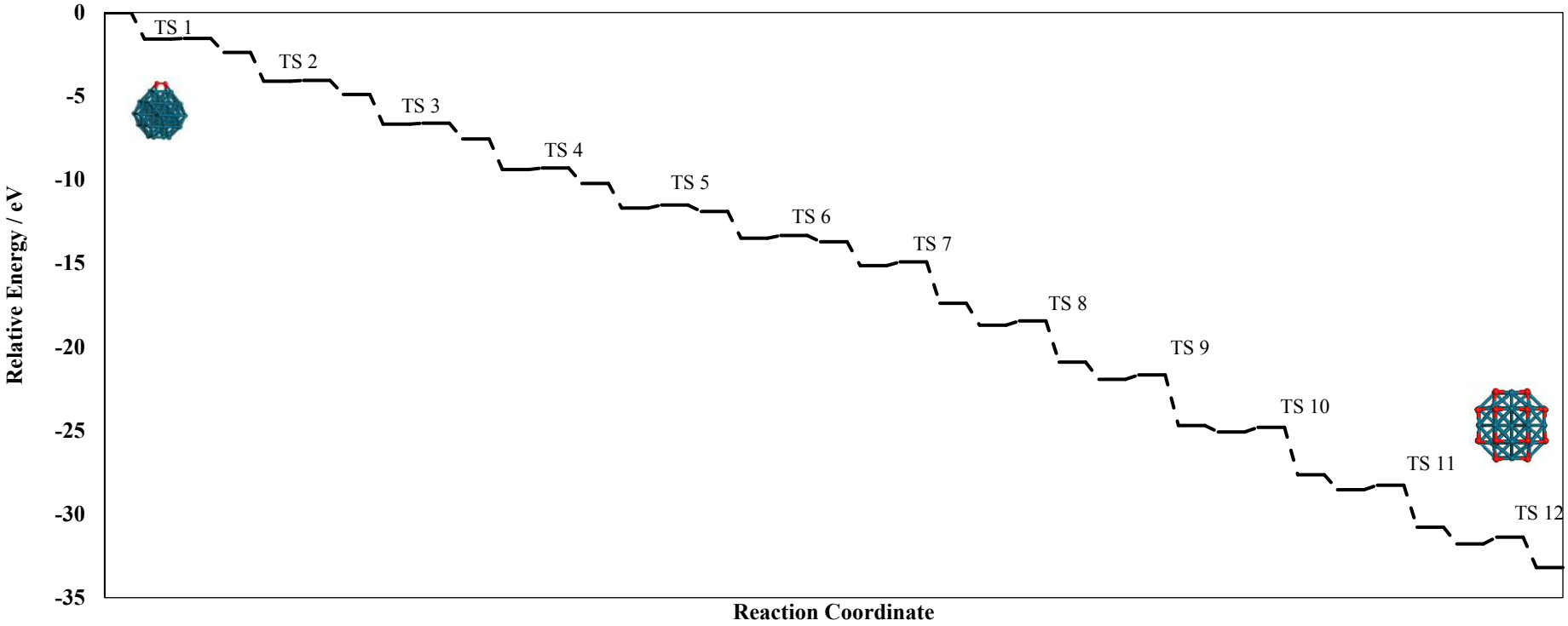

Figure 5.21: Reaction profile for adsorption and dissociation of molecular oxygen on Pd_{38}. Zero energy corresponds to the energy of isolated Pd_{38} + isolated $12O_2$. TS corresponds to the energies of each transition state (table 5.6).

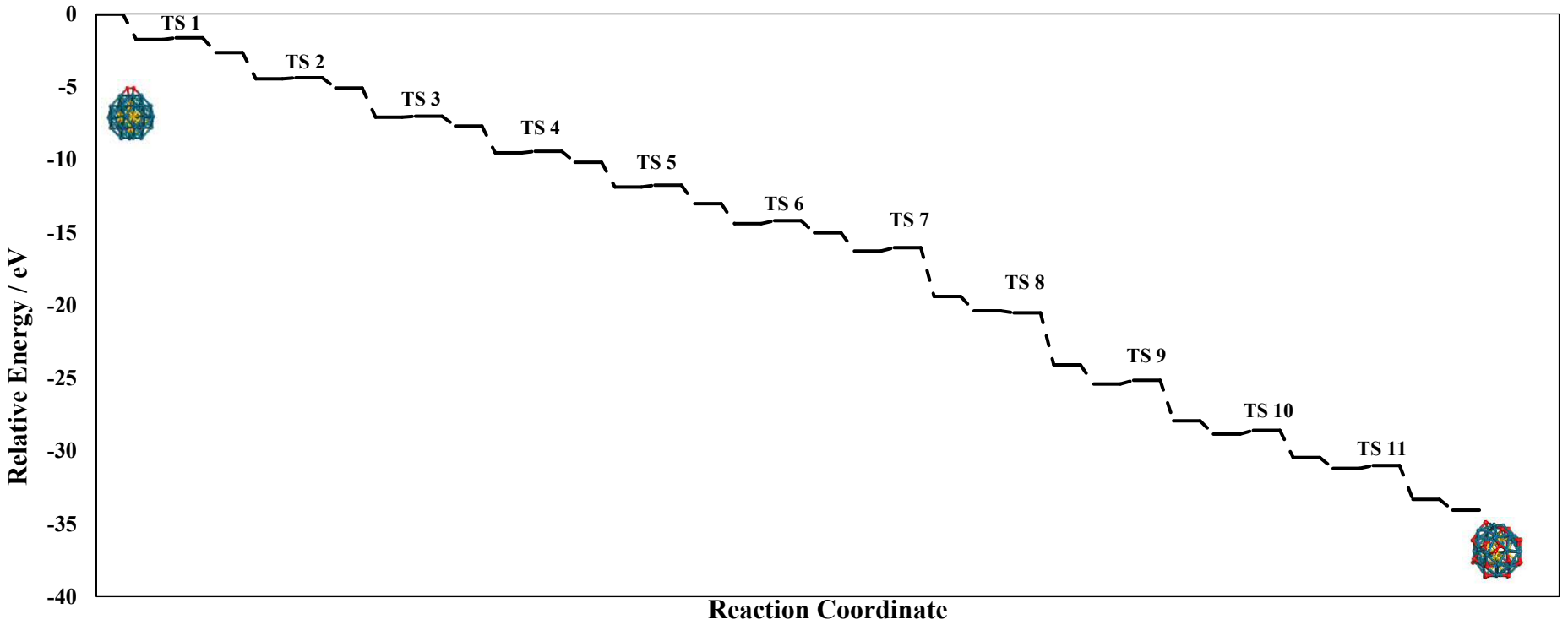

Figure 5.22: Reaction profile for adsorption and dissociation of molecular oxygen on Au_6Pd_{32}. Zero energy corresponds to the energy of isolated Au_6Pd_{32} + isolated $12O_2$. TS corresponds to the energies of each transition state (table 5.6).

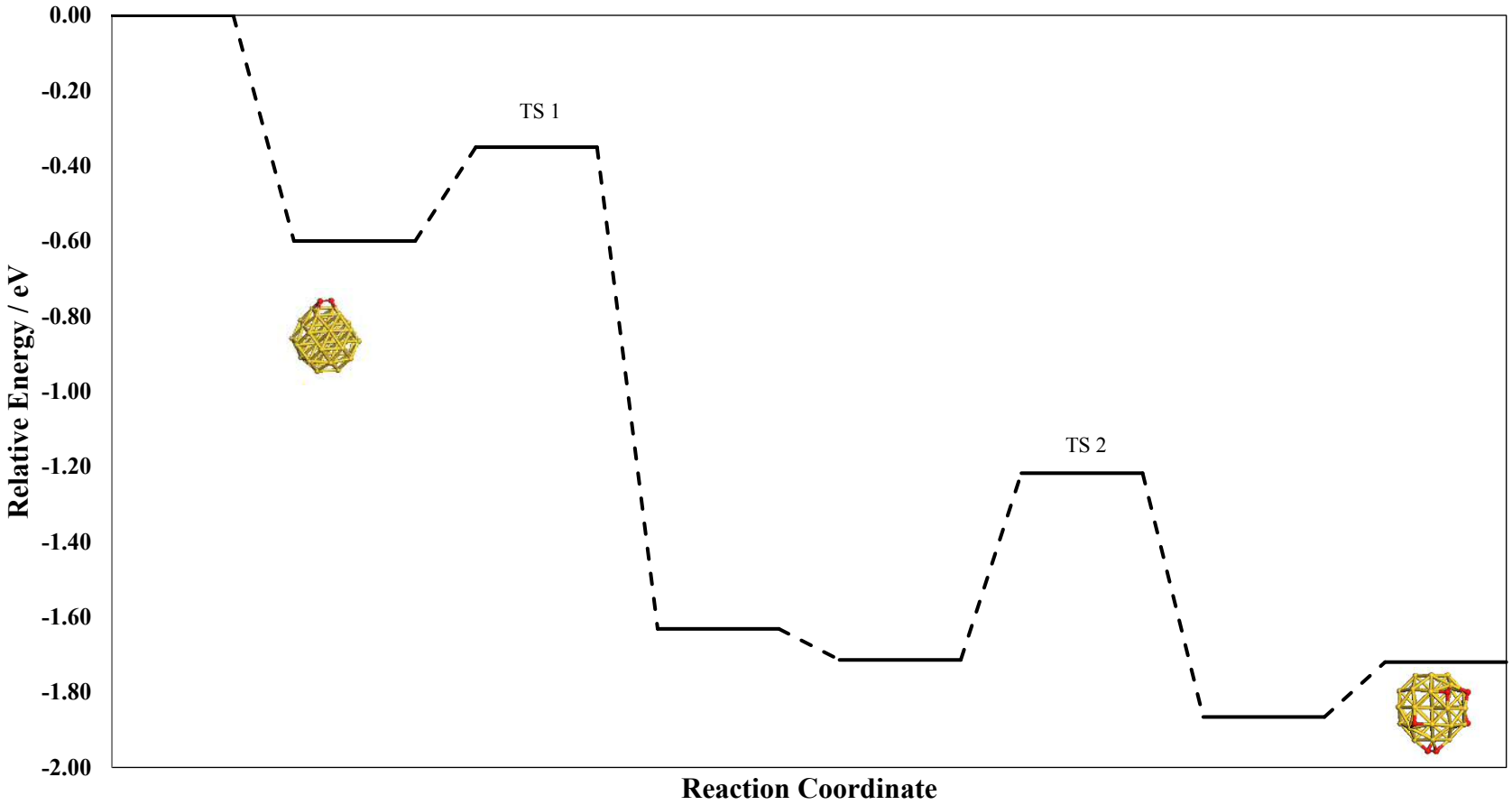

Figure 5.23: Reaction profile for adsorption and dissociation of molecular oxygen on Au_{38}. Zero energy corresponds to the energy of isolated Au_{38} + isolated $3O_2$. TS corresponds to the energies of each transition state (table 5.6).

5.8 Implications for H_2O_2 Production

Hydrogen peroxide is a major commodity chemical with uses as an antiseptic and bleach. The current industrial route for manufacture of H_2O_2 is through the anthraquinone process developed by BASF. This process has several environmental disadvantages due to the energy intensive multistep nature of the synthesis route requiring the presence of several organic solvents[32]. A direct synthesis of H_2O_2 starting from combining both molecular oxygen and hydrogen has been of interest for a significant period however a significant barrier to overcome is the preference for these two species to combine and form water over H_2O_2. Experimental observations by Hutchings *et al.* indicate supported Au particles can catalyse the production of hydrogen peroxide at low temperatures[25] (2°C). It is reported the rate of H_2O_2 production can be markedly increased by the addition of palladium. This discovery cements the importance of bimetallic particles within this greener synthesis route. Hydrogen peroxide synthesis requires the hydrogenation of O_2 therefore any interaction with a particle which could facilitate an O_2 dissociation would be disadvantageous for the process. Therefore it is of interest to investigate interactions of O_2 with various bimetallic particles.

5.8.1 Characterisation of Metal Particles

Both core shell (Au core Pd shell) and homogeneous bimetallic particles have been identified and characterised as active catalysts for the production of H_2O_2[25]. Recent unpublished work by Wang *et al.* indicate for supported nanoparticles prepared using the modified impregnation method a ratio of Au/Pd in the particles of 1:1.85 is the most active catalyst. It is proposed continuous palladium sites (on the metal particle) are responsible for the dissociation of molecular oxygen however if these sites are interjected with an Au atom the dissociation is deactivated. These observations warrant a study of the interaction of molecular oxygen with bimetallic particles of this ideal composition.

5.8.2 Obtaining suitable cluster models

A ratio of 1:1.85 corresponds to 80 weight percent gold within a metal particle comprising of 38 atoms. The ratio is $Au_{26}Pd_{12}$, which presents a combinatorial total of 9657700 clusters which exhibit this ratio. This is computationally too expensive and time consuming to systematically study the interaction of oxygen with. Therefore 4 particles of this composition were chosen, each of these 24 particles exhibits distinctly different arrangements of the atoms within them. 4 details these particles.

Configuration 1 contains a mixture of both pure Pd and pure Au (100) facets, configuration 2 contains mixed (100) facets in which Pd atoms occupy diagonal corners of the square, configuration 3 contains mixed (100) facets in which Pd atoms occupy one side of the square and finally configuration 4 contains pure Au (100) facets. These are presented in figure 5.24 along with absolute energies in eV.

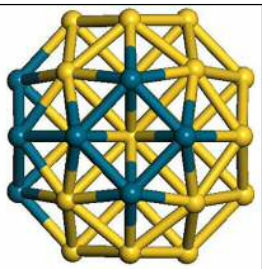	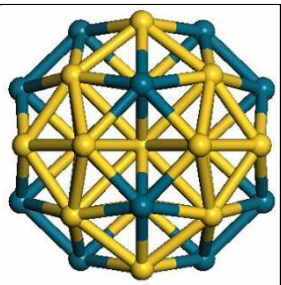	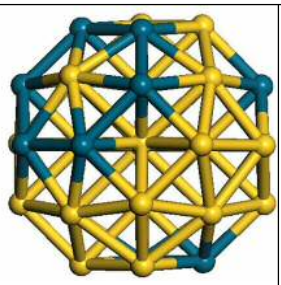	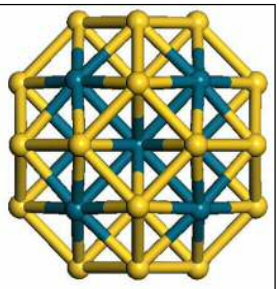
Configuration 1	Configuration 2	Configuration 3	Configuration 4
-119.80	-120.37	-119.98	-123.13

Figure 5.24: $Au_{26}Pd_{12}$ clusters studied with absolute energies in eV.

Adsorption of molecular oxygen followed by dissociation was investigated onto these four configurations. Due to time limitations only one adsorption and dissociation has been investigated. Table 5.8 details the optimised geometry of each adsorption accompanied by the calculated adsorption energies. Configuration 3 has two possibilities for O_2 adsorption – a in which O-O bond is parallel to Pd side of square and O-O bond parallel to mixed side of square.

Table 5.8: Optimised geometries of molecular oxygen adsorbed onto each cluster studied. Adsorption energies are reported in eV.

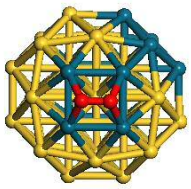	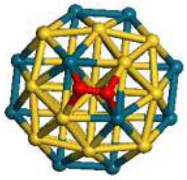	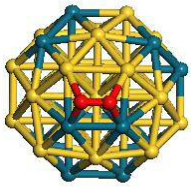	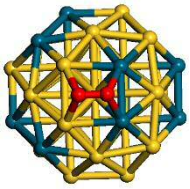	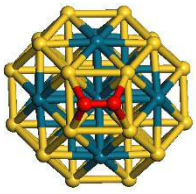
Configuration 1	Configuration 2	Configuration 3a	Configuration 3b	Configuration 4
-1.62	-0.35	-0.89	-0.69	0.09

The calculated adsorption energies indicate vastly different interactions between molecular oxygen and the metal particles. It is interesting to note adsorption onto the pure Pd facet is the most preferred by approximately 0.7 eV, this is followed by the mixed facets and finally the pure Au facet is indicating a positive adsorption energy. This observation is significant as it demonstrates a random distribution within an alloy of the same weight percentage ratio can give rise to distinctly different properties with regards to the interaction with molecular oxygen.

Using the NEB method barriers to dissociation of molecular oxygen were determined and figure 5.23 details the reaction profiles for dissociation. They demonstrate the varying properties in cluster interaction with molecular oxygen. Figure 5.19 demonstrates dissociation is energetically feasible in all cases except for configuration 4, in this instance a positive adsorption energy onto the Au (100) facet accompanied by a barrier to dissociation of approximately 0.5 eV warrant this route unfeasible.

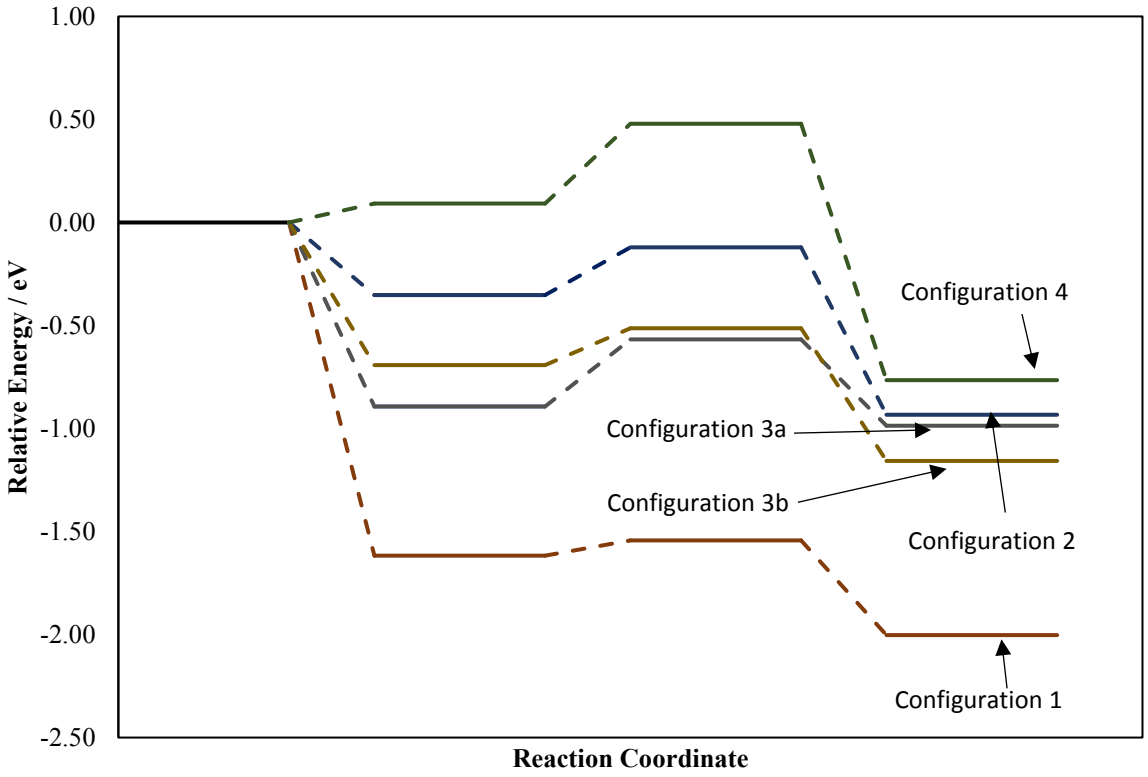

Figure 5.19: Reaction profile for adsorption a dissociation of molecular oxygen all four bimetallic cluster compositions. Energies are set relative to the energy of each isolated metal particle and isolated molecular oxygen. Green represents configuration 4, dark blue configuration 2, gold configuration 3b, lilac 3a and brown represents configuration 1.

5.9 Conclusions

Oxygen adsorption on Au_{38}, Pd_{38} and Au_6Pd_{32} was investigated by using VASP which employed the PBE functional. The NEB method was used to determine the barriers to dissociation of molecular oxygen adsorbed on these metal particles. Transition states were identified through a frequency calculation to identify one imaginary mode. The adsorption of molecular oxygen onto metal particles was investigated in more depth by performing a Bader charge analysis which indicates charge distribution once adsorbed. This study was extended to investigate other bimetallic particles of Au and Pd. Experimental observations indicated a weight percent of 80:20 (Au to Pd) was active for H_2O_2 synthesis and it was theorized this is due to the requirement of O_2 to not dissociate once adsorbed.

On all metal particles the adsorption of one molecular oxygen is feasible in the three distinct sites investigated. For Au_{38} the preferred site of adsorption corresponds to a calculated adsorption energy of -0.72 eV. This site is the junction of (100) and (111) facets. It is interesting to observe for Au_6Pd_{32} and Pd_{38} the most favourable site for adsorption is parallel to the (100) facet which corresponds to calculated adsorption energies of -1.59 eV and -1.76 eV.

Behaviour differences between gold, palladium and bimetallic particles were observed from an investigation of the interaction with a single molecular oxygen. Gold particles demonstrate a significantly weaker attraction for molecular oxygen than the palladium and bimetallic counterparts. The reasons for weaker adsorption energies have been investigated through Bader charge analysis and geometry analysis of the (100) facets. Au_{38} provides the greatest charge transfer to O_2 upon adsorption (0.81 eV) this back donation from the gold will fill the π^* orbital therefore increasing the antibonding character of the bond and destabilising it. Geometry analysis indicated the (100) facet has the biggest size mismatch between the equilibrium geometry of O_2 for Au_{38} therefore the O-O bond will stretch upon adsorption which is energetically unfavourable. This was confirmed by performing single point energy calculations of O_2 in its adsorbed state and comparing the energy of it to the equilibrium (isolated O_2) molecular energy.

Subsequent molecular oxygen were adsorbed onto site C and Au_{38} demonstrates a trend in which adsorption energies become increasingly positive and then decrease. Both Pd_{38} and Au_6Pd_{32} have a strong interaction with O_2 until each (100) site is saturated.

The three adsorption possibilities (which were studied) of molecular oxygen to these metal particles give rise to 5 different dissociation pathways. Each of these pathways had their barriers computed using the NEB method and for Au_{38} adsorption and dissociation via pathway E is the most preferred with a barrier computed of 0.40 eV. This pathway is also the most favourable for Pd_{38} and Au_6Pd_{32} with substantially lower barriers of 0.04 eV and 0.12 eV calculated respectively. Subsequent adsorption and dissociation of molecular oxygen has been found to be kinetically unfavourable on Au_{38} this is due to a weak adsorption energy in relation to the barrier which means no energy is available upon adsorption to cross the barrier. Therefore in conclusion Au_{38} has been determined to adsorb and dissociate no more than one molecular oxygen molecule.

Pd_{38} and Au_6Pd_{32} both fully oxidise due to the strong oxygen adsorption energies accompanied by relatively small barriers to O_2 dissociation, the computational investigation detailed within this chapter supports experimental observations by Salisbury *et al.*[5] who indicated one molecular oxygen was able to dissociated onto the gold particles they studied however contradicts the claim that multiple adsorption is prohibited asthis study indicates multiple molecular oxygen adsorption on gold is possible, supporting work by Gordon *et al*[6].

Bimetallic particles with 80wt% gold in palladium as a random alloy distribution were also studied. Particles containing 38 atoms at this composition produces a total number of configurations which is too computationally expensive to model therefore 4 distinct metal particles were investigated. These 4 particles demonstrated different properties with regards to their interaction with O_2. Particles containing a pure gold (100) facet showed the smallest calculated adsorption energy, this was followed by mixed facets and pure Pd demonstrating the highest affinity for molecular oxygen. The conclusion of this area of work is an interesting observation that whilst each of these metal particles have the same overall composition, the local arrangement within the cluster gives rise to vastly different properties and provides challenging experimental requirements which need to be met in synthesis of metal particles to exploit catalytic properties. For hydrogen peroxide synthesis it is proposed the best catalytic features are those where sufficient O_2 adsorption occurs without ease of dissociation. This ensures O_2 remains intact for hydrogenation.

References

1. Bondzie, V. A., Parker, S. C. & Campbell, C. T. The kinetics of CO oxidation by adsorbed oxygen on well defined gold particles on TiO2(110). *Catal. Letters* **63,** 143 (1999)

2. Kim, T. S., Stiehl, J. D., Reeves, C. T., Meyer, R. J. & Mullins, C. B. Cryogenic CO oxidation on TiO(2)-supported gold nanoclusters precovered with atomic oxygen. *J. Am. Chem. Soc.* **125,** 2018 (2003)

3. Boccuzzi, F. & Chiorino, A. FTIR Study of CO Oxidation on Au/TiO 2 at 90 K and Room Temperature. An Insight into the Nature of the Reaction Centers. *J. Phys. Chem. B* **104,** 5414 (2000)

4. Liu, Z.-P., Hu, P. & Alavi, A. Catalytic Role of Gold in Gold-Based Catalysts: A Density Functional Theory Study on the CO Oxidation on Gold. *J. Am. Chem. Soc.* **124,** 14770 (2002)

5. Salisbury, B. ., Wallace, W. . & Whetten, R. . Low-temperature activation of molecular oxygen by gold clusters: a stoichiometric process correlated to electron affinity. *Chem. Phys.* **262,** 131 (2000)

6. Mills, G., Gordon, M. S. & Metiu, H. The adsorption of molecular oxygen on neutral and negative Aun clusters (n=2–5). *Chem. Phys. Lett.* **359,** 493 (2002)

7. Roldán, A., González, S., Ricart, J. M. & Illas, F. Critical size for O(2) dissociation by au nanoparticles. *Chemphyschem* **10,** 348 (2009)

8. Kresse, G. & Hafner, J. Ab initio molecular dynamics for liquid metals. *Phys. Rev. B* **47,** 558 (1993)

9. Kresse, G. & Hafner, J. Ab initio molecular-dynamics simulation of the liquid-metal–amorphous-semiconductor transition in germanium. *Phys. Rev. B* **49,** 14251 (1994)

10. Kresse, G. & Furthmüller, J. Efficiency of ab-initio total energy calculations for metals and semiconductors using a plane-wave basis set. *Comput. Mater. Sci.* **6,** 15 (1996)

11. Kresse, G. Efficient iterative schemes for ab initio total-energy calculations using a plane-wave basis set. *Phys. Rev. B* **54,** 11169 (1996)

12. Perdew, J. P., Burke, K. & Ernzerhof, M. Generalized Gradient Approximation Made Simple. *Phys. Rev. Lett.* **77,** 3865 (1996)

13. Perdew, J. P., Burke, K. & Ernzerhof, M. Generalized Gradient Approximation Made Simple [Phys. Rev. Lett. 77, 3865 (1996)]. *Phys. Rev. Lett.* **78,** 1396 (1997)

14. Visart de Bocarmé, T. *et al.* Oxygen adsorption on gold nanofacets and model clusters. *J. Chem. Phys.* **125,** 54703 (2006)

15. Duan, Z. & Henkelman, G. CO Oxidation on the Pd(111) Surface. *ACS Catal.* **4,** 3435 (2014)

16. Blöchl, P. E. Projector augmented-wave method. *Phys. Rev. B* **50,** 17953 (1994)

17. Kresse, G. From ultrasoft pseudopotentials to the projector augmented-wave method. *Phys. Rev. B* **59,** 1758 (1999)

18. Monkhorst, H. J. & Pack, J. D. Special points for Brillouin-zone integrations. *Phys. Rev. B* **13,** 5188 (1976)

19. Grimme, S. Semiempirical GGA-type density functional constructed with a long-range dispersion correction. *J. Comput. Chem.* **27,** 1787 (2006)

20. Amft, M., Lebègue, S., Eriksson, O. & Skorodumova, N. V. Adsorption of Cu, Ag, and Au atoms on graphene including van der Waals interactions. (2010). at <http://arxiv.org/abs/1011.1113>

21. Tang, W., Sanville, E. & Henkelman, G. A grid-based Bader analysis algorithm without lattice bias. *J. Phys. Condens. Matter* **21,** 84204 (2009)

22. Sanville, E., Kenny, S. D., Smith, R. & Henkelman, G. Improved grid-based algorithm for Bader charge allocation. *J. Comput. Chem.* **28,** 899 (2007)

23. Henkelman, G., Arnaldsson, A. & Jónsson, H. A fast and robust algorithm for Bader decomposition of charge density. *Comput. Mater. Sci.* **36,** 354 (2006)

24. Zeinalipour-Yazdi, C. D., Willock, D. J., Machado, A., Wilson, K. & Lee, A. F. Impact of co-adsorbed oxygen on crotonaldehyde adsorption over gold nanoclusters: a computational study. *Phys. Chem. Chem. Phys.* **16,** 11236 (2014)

25. Landon, P., Collier, P. J., Papworth, A. J., Kiely, C. J. & Hutchings, G. J. Direct formation of hydrogen peroxide from H2/O2 using a gold catalyst. *Chem. Commun.* 2058 (2002)

26. Hsu, C., Huant, C., Liu., Fuqiang. Au/Pd core-shell nanoparticles for enhaced electrocatalytic activity and durability. *Elec. Chem. Comm,* **23,** 133 (2012)

27. Dimitratos, N. *et al.* Oxidation of glycerol using gold-palladium alloy-supported nanocrystals. *Phys. Chem. Chem. Phys.* **11,** 4952 (2009)

28. Boronat, M. & Corma, A. Oxygen activation on gold nanoparticles: separating the influence of particle size, particle shape and support interaction. *Dalton Trans.* **39,** 8538 (2010)

29. Yoon, B., Häkkinen, H. & Landman, U. Interaction of O_2 with Gold Clusters: Molecular and Dissociative Adsorption. *J. Phys. Chem. A* **107,** 4066 (2003)

30. Yoon, B., Ha, H. & Landman, U. Interaction of O 2 with Gold Clusters: Molecular and Dissociative Adsorption, *Journal of Physical Chemistry A,* **107,** 4066 (2002)

31. Mills, G., Gordon, M. S. & Metiu, H. *The adsorption of molecular oxygen on neutral and negative Aun clusters (n=2–5)*. *Chemical Physics Letters* **359,** 493 (2002)

32. Campos-Martin, J. M., Blanco-Brieva, G. & Fierro, J. L. G. Hydrogen peroxide synthesis: an outlook beyond the anthraquinone process. *Angew. Chem. Int. Ed. Engl.* **45,** 6962 (2006)

Chapter 6

The Interaction of Biomass Derived Molecules with Metal Particles

This chapter will present the results obtained for hydroxymethylfurfural (HMF) adsorption on metal particles of various sizes and compositions. The first two sections of this chapter contain a general overview of HMF focusing on its potential to replace traditional feedstocks, followed by computational details of the calculations performed. A preliminary mechanistic study of the conversion of HMF to 2,5-furandicarboxylic acid (FDCA) will be presented along with a discussion of the inclusion of dispersion interactions within the calculations. Due to the computational cost and time constraints a comprehensive mechanistic investigation is not possible however a preliminary investigation into modelling the rate limiting step for this interconversion will be presented. In keeping with the theme of biomass conversion discussion of the conversion of levulinic acid to γ-valerolactone will be briefly discussed along with theoretical calculations performed to correlate d-band centre with molecular hydrogen adsorption energies.

6.1 Introduction

Crude oil is currently the primary resource used for the production of fuels and plastics. Such a heavy dependence is problematic due to the non-renewable nature of this resource. In the UK approximately 38% of total plastics produced are used for the packaging industry[1]. Food and drinks packaging is a major component of this overall percentage and therefore it would be highly desirable to replace crude oil with a renewable alternative for food and drinks packaging.

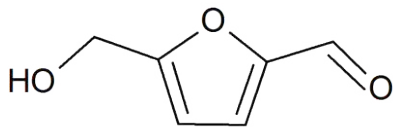

Figure 6.1: Hydroxymethylfurfural

Hydroxymethylfurfural (HMF) shown in Figure 6.1 is derived from the dehydration of glucose[2] (via fructose). It contains both an alcohol and aldehyde functional group attached to a furan

ring. HMF is a readily available biomass derived molecule which has attracted substantial interest as it has been labelled a "top 10" molecule by the United States Department of Energy[3]. This recognition is due to the variety of different molecules which can be formed via conversion of HMF. The high degree of versatility in the products which can be obtained from HMF has warranted labelling of it as a platform molecule which has potential to replace traditional feedstocks in vital industrial processes. Figure 2.11 (chapter 2) demonstrates HMF can be converted into the industrially used solvent and energy dense fuel additive DMF[5] and levulinic acid – a precursor for resin and plasticizers[6].

The desire to replace crude oils as a precursor for packaging material has led to the increased usage of biomass in this industry. Polylactic acid (PLA) is commonly used to manufacture disposable plastic cups however it has been demonstrated that PLA exhibits a low barrier to diffusion of both H_2O and CO_2[7], therefore making it unsuitable to be used for packaging of carbonated drinks.

The unsuitability of PLA for usage within certain food packaging has led research to investigate other suitable biomass derived materials. One such substitute for PLA is to use polymers derived from HMF. These polymers are first obtained by oxidising HMF to 2,5-Furandicarboxylic acid which itself undergoes polymerisation analogous to crude oil derived terephthalic acid (figure 6.2 – a simplified schematic of conversion route). These polyethylenefuranoate polymers demonstrate an improved barrier to both CO_2 and H_2O diffusion therefore confirming their suitability as a replacement to crude oil derived plastics[8].

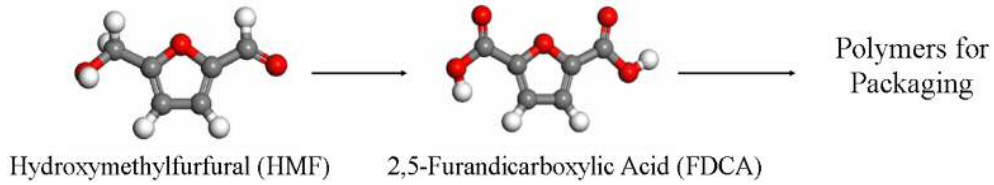

Figure 6.2: Conversion of HMF to Polymers for packaging via FDCA.

Often oxidation reactions performed industrially involve reagents such as dichromates or permanganates which can be of detriment to the environment. Instead of using these industrial oxidants it would be highly desirable to use greener alternatives. An ideal greener alternative would be to use a catalyst which could utilize atmospheric oxygen and work at low reaction temperatures and pressure. These requirements can be mostly met by using heterogeneous catalysts with gold particles reported to catalyse this oxidation reaction[9-10]. As detailed in

chapter 2 there is debate within the literature surrounding the mechanism of the oxidation route from HMF to FDCA. Davis *et al.* investigated the conversion of HMF to FDCA using high pH aqueous conditions and reported a rapid oxidation of the aldehyde side chain which was followed by O-H alcohol side chain activation[11]. The hypothesis of this order of oxidation is supported by Casanova *et al.* who determined the rate limiting step for this oxidation reaction catalysed by Au supported on TiO_2 is the oxidation of the alcohol group[12]. The literature debate leads to an overall consensus that oxidation of an aldehyde group in aqueous conditions is facile with an alcohol oxidation proving to be a rate limiting step. Due to this consensus this chapter will focus a study which solely investigates the kinetics of the cleavage of the O-H group which is preceded by adsorption of HMF to the metal particle. To the author's knowledge this is the first DFT study performed on adsorption and activation of the O-H group in HMF and will provide a fascinating insight into the kinetics of the mechanism. As no previous DFT studies on this oxidation have been found in the literature a model for the oxidation of an alcohol on a metal particle will be used as a base from which this study will be expanded. Previous DFT calculations performed by Corma *et al.* propose the mechanism for oxidation of ethanol adsorbed on Au particles occurs via adsorption of the molecule followed by cleavage of the O-H bond forming an alkoxy bound intermediate[13]. The previous work by Corma will provide a framework for the O-H activation study of HMF bound to a metal particle presented in this chapter. Any chemical interaction between organic molecules will no doubt contain an element of dispersion within the total interaction energy. Due to this a discussion of including dispersion interaction in metal particle – HMF adsorption calculations will be presented.

Levulinic acid (LA) derived from lignocellulose is an attractive molecule due to non-competition with food production. LA is the starting material for the production of γ-valerolactone (GVL), a promising biofuel[14]. The conversion of LA to GLV has been reported using a range of noble metal catalysts with ruthenium supported on carbon a commonly used system[15]. Often noble metals are rare resources and it is often the case certain countries may hold to the vast majority of a certain noble metal resource. The search for more abundant materials is necessary to ensure the sustainability of catalytic processes which currently use these rare resources. The novel use of catalytic Cu-ZrO_2 has demonstrated the hydrogenation of LA to GVL is both highly selective and produces an approximate yield of 80%[16]. Further modification of the catalyst can improve both selectivity and yield therefore suggesting the future potential of this novel catalyst.

Through internal discussion it has been suggested the rate limiting step in this catalytic hydrogenation is the adsorption and activation of molecular hydrogen. In the literature there is consensus that interactions of molecules with metals in their bulk form correlate to the d-band centre of the metal with positive correlation between d-band centre and adsorption energies[17]. d-band centre calculations obtained through DFT are presented for bulk Cu, Ni and Ru metal with brief discussion of how these results compare to adsorption energies of H_2 in the literature. Bulk metals are modelled in this chapter due to the established nature of the band structure. A novel investigation would be to extend d-band centre calculation to cluster systems and bulk alloys.

6.2 Computational Details

DFT calculations using projector augmented wave method (PAW)[18,19] pseudopotentials have been performed using the VASP program[20–23]. Calculations are performed within a generalized gradient approximation with an exchange-potential of Perdew, Burke and Ernzerhof (PBE)[24,25]. Pseudopotentials used here employ a valence / core model with 19 valence and 60 core electrons used to model Au. Relativistic effects such as core contraction are accounted for using these potentials however a crossing of core electrons into valence states is disallowed here. All isolated metal particle calculations are performed using a 625 $Å^3$ periodic box (each dimension of the box 25 Å). The reciprocal box size accompanied by use of 1 *k*-point sampling of the mesh prevents spurious periodic image self-interactions. As detailed in chapter 5 a plane wave cut-off of 500 eV is sufficient to model these metal particles. All calculations are spin unrestricted with Gaussian smearing employed with a width of 0.001 to ensure these metals are not treated as bulk like. These geometry relaxations have a convergence criteria set to 10^{-4} eV for electronic relaxation and -0.05 eV $Å^{-1}$ force convergence criteria for geometric relaxations respectively. Calculations including dispersion interactions will be presented later in this chapter. For these calculations the DFT-D2 method of Grimme[26] has been used with coefficients for Au obtained from the literature[27]. In order to obtain a suitable value for cut off distance for inclusion of dispersion interactions several test calculations have been performed by placing a cuboctahedral Au_{13} particle in a 625 $Å^3$ periodic box. Figure 6.3 presents data of these test calculations in which the cut off for dispersion interactions were varied and plotted against total energy to locate a convergence point.

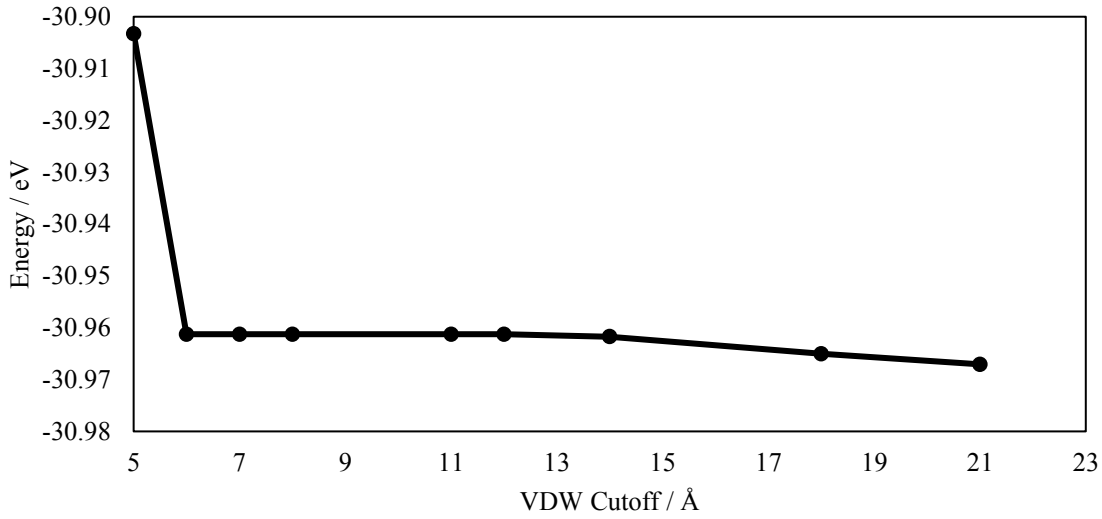

Figure 6.3: Total energy of an Au_{13} particle plotted against VDW cut-off distance in Angstrom.

From figure 6.3 a value of 12 Å was chosen as a cut off for accounting for VDW interactions in the calculations. This value was chosen as it corresponds to a convergence point in which three concordant results are obtained with a total energy of -30.96 eV reported. It is interesting to observe calculated total energy values decrease beyond a 15Å cut-off distance, it is hypothesized this is due to a spurious interaction occurring between periodic image units which produces a fictitious favourable interaction therefore lowering total energies. Using a 12Å cut off value prevents any such interactions occurring calculations which model metal particles.

Bader charge analysis was performed to deduce charges upon adsorption, this method was developed by Henkelman *et al.*[28–30] Grid spacing for Bader charge analysis has previously been investigated and in chapter 5 it has been concluded a 0.05 Å grid spacing corresponding to NGXX = 500, NGXY and NGXZ = 500 within the VASP INCAR file is sufficient.

Other molecular non periodic calculations to perform dihedral bond scans have been performed using Gaussian 09 along with localised basis sets. This will be discussed in more detail at appropriate points within the chapter. Calculations involving the activation of HMF are presented in kJ mol^{-1}, whereas adhesion energies of metal particles to the support are presented in eV.

6.3 Determining the Ground State Structure of HMF and Interaction with Metal Particles

HMF contains two functional groups attached to a furan ring. As these two functional groups are attached via a single bond it is reasonable to assume there is a degree of rotation and flexibility leading to a large number of possible conformers of HMF. Due to this plausible flexibility a dihedral angle scan was performed using Gaussian 09[31] and the 6-311G(d,p) basis set. These fully relaxed scans were performed using 75 steps which corresponds to a 5° scan interval. Figure 6.4 presents the scan performed on the hydroxymethyl group bond attached to the furan ring.

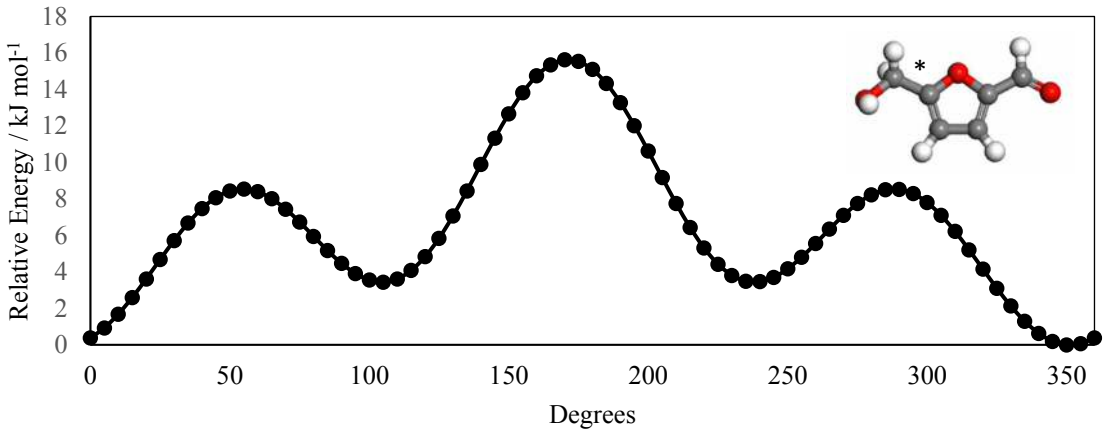

Figure 6.4: The dihedral scan performed (O-C-C-O) on the bond attaching the hydroxymethyl group to the furan ring within HMF. Energies are set relative to the lowest conformer in kJ mol^{-1}. An asterisk is used to denote which bond is scanned within the molecule.

Figure 6.4 indicates a large degree of flexibility of rotation of this bond within HMF. 18 kJ mol^{-1} is the highest relative energy difference between conformers visited during this dihedral scan. At room temperature it is reasonable to assume this bond is freely rotating. Factoring in zero point energy and 3/2 KT means free rotation of this bond is assumed. Figure 6.5 presents a dihedral scan of the bond attaching the aldehyde functional group attached to the furan ring.

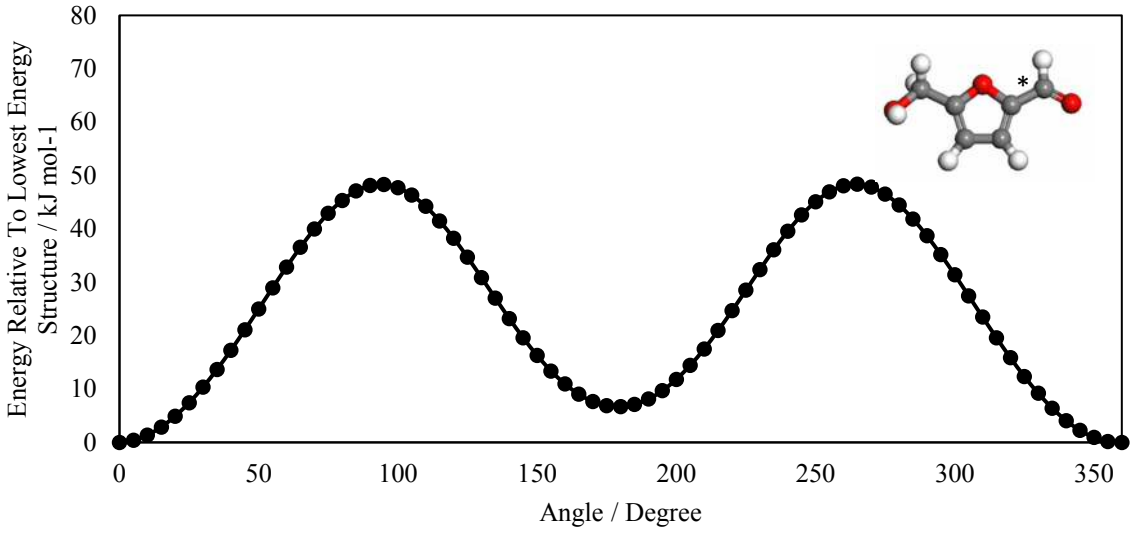

Figure 6.5: The dihedral scan (O-C-C-O) performed on the bond attaching the aldehyde group to the furan ring within HMF. Energies are set relative to the lowest conformer in kJ mol^{-1}. An asterisk is used to denote the bond undergoing dihedral scan.

The rotation of the bond attaching the aldehyde group to the furan ring is considerably more energetically difficult than the alcohol group counterpart. The two conformers exist which correspond to the aldehyde oxygen being either cis or trans to the oxygen atom in the furan ring. The energy difference between these conformers is approximately 8 kJ mol^{-1} however the barrier to interconversion is approximately 50 kJ mol^{-1}. This is perhaps due to conjugation between the furan ring and the carbon oxygen double bond which may need to be broken in order to rotate the bond. This indicates this bond is fairly fixed in comparison to the alcohol group bond attachment to the ring and would not be freely rotating at room temperatures.

A further dihedral scan was performed this time to investigate the energy differences between alcohol rotamers in HMF, this is presented in figure 6.6. The highest energy difference measured between each conformer is 14 kJ mol^{-1} indicating free rotation at room temperature.

All of the information obtained by these scans was pieced together and used to obtain a conformer of HMF which is lowest in energy in all rotatable bonds. This low energy conformer was geometry optimised and presented in figure 6.7 and is the structure of HMF used for all calculations presented in this chapter.

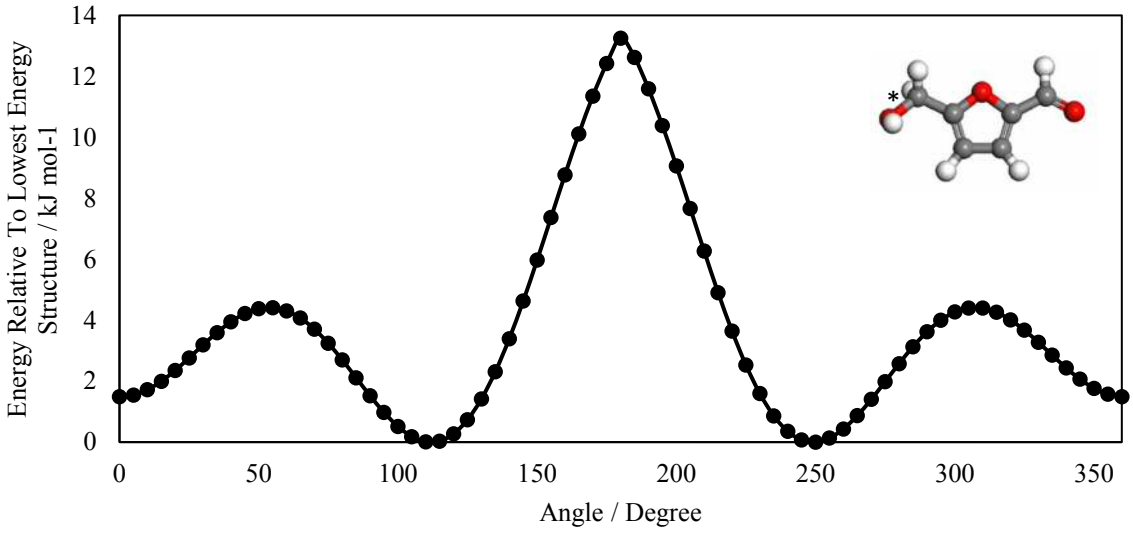

Figure 6.6: Alcohol rotamer dihedral scan (H-O-C-C) within HMF. Energies are set relative to lowest energy conformer in kJ mol^{-1}. An asterisk is used to denote the bond undergoing dihedral scan.

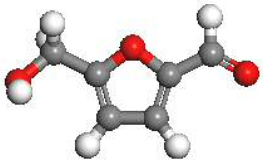

Figure 6.7*:* Optimised structure of HMF obtained through combination of the lowest energy conformers found through dihedral bond scans.

6.3.2 The interaction of Hydroxymethylfurfural with metal particles

As previously discussed in chapter 2, research presented by Corma *et al.* indicates the oxidation of an alcohol on a metal particle is one in which adsorption of reactant onto the metal particle occurs first which is followed by the cleavage of the alcohol group O-H bond forming a surface bound alkoxy intermediate. The primary aim of this chapter is to detail the energetics of such a process in HMF. The oxidation of an aldehyde functional group has been reported to occur with ease via a geminol diol intermediate[32] and therefore will not be computationally investigated in this chapter.

The first stage of the investigation is to determine how HMF adsorbs on a series of metal particles. The following metal particles; Au_{13}, Au_{38}, Pd_{13}, Pd_{38} and Au_6Pd_{32} (figure 6.8) were chosen to investigate adsorption of HMF. These particles are both nano and subnanometre

sized and an investigation into how particle size influences adsorption energies would provide an interesting insight into the relationship between size and adsorption energies and could provide suggestions for the target size for synthesis of metal particles which provide optimum adsorption properties.

6.3.3 Interaction of HMF with metal particles containing 13 atoms.

As numerous conformational possibilities exist for the adsorption of HMF on the metal particles detailed in figure 6.8 it was viewed that a systematic study of how each component of HMF interacted most favourably should be first obtained in order to deduce overall how HMF interacts most favourably. In order to perform a systematic adsorption study HMF was split into various components / functional groups. These were a furan ring, methanol, and formaldehyde. The purpose of such a breakdown was to determine how each of these isolated components interacted most favourably with a test metal particle system. The test particle in this instance is Au_{13} cuboctahedral geometry (figure 6.8 top left). By deducing the most favourable adsorption mode of each component the overall adsorption of HMF can be determined.

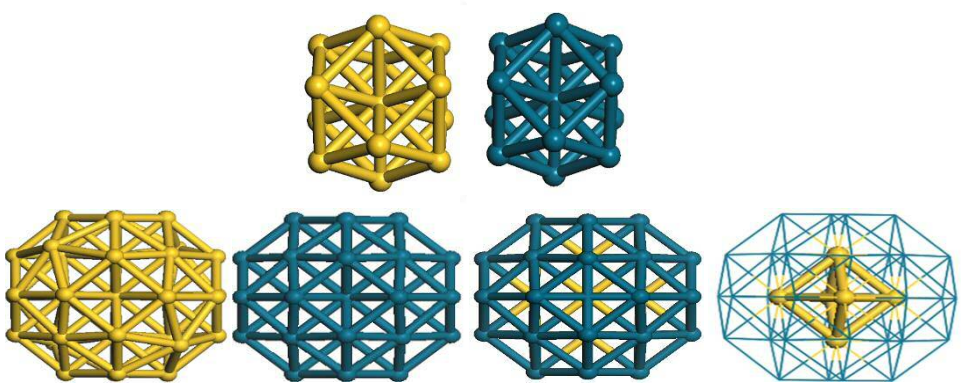

Figure 6.8: Metal particles used to investigate interaction of HMF.

Using equation 6.1 the adsorption energies of each of these molecules on Au_{13} were determined. E_{ads} is the calculated adsorption energy where a positive value indicates unfavourable adsorption and vice versa for a negative value. $E_{(Cluster+Molecule)}$ is the energy of the molecule adsorbed on the metal particle, $E_{Cluster}$ and $E_{Molecule}$ are the energies of isolated metal particles and molecules respectively.

(6.1)

The most favourable adsorption configurations for each molecule on Au_{13} are presented in figure 6.9 along with calculated adsorption energies in kJ mol^{-1}

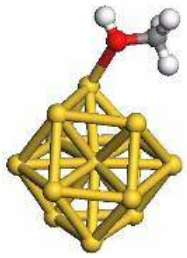	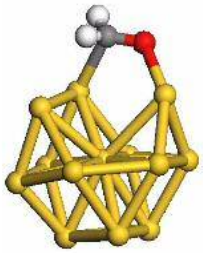	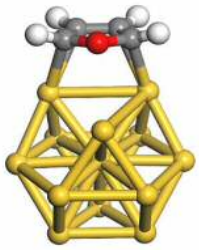
Methanol E_{ads} -21 kJ mol^{-1}	Formaldehyde E_{ads} -53 kJmol^{-1}	Furan E_{ads} -69 kJ mol^{-1}

Figure 6.9: Most favourable optimised geometries of methanol, formaldehyde and furan to cuboctahedral Au_{13} along with corresponding adsorption energies.

The predominant mode of adsorption of methanol is via an oxygen–gold atom interaction. For formaldehyde it is through both atoms of the C=O group along with an oxygen–gold atom interaction on the cluster. The preferred adsorption mode for the furan ring is one in which the ring is perpendicular to the edge site of the adjoining (100) and (111) facets. The strongest interaction energy is reported for furan therefore it is determined that this will be the predominant contribution of the interaction energy upon adsorption of HMF on metal particles.

The information contained in figure 6.9 has been pieced together to guide the search for the most favourable adsorption modes of HMF on the metal particles. Figures 6.10 and 6.11 report the two most favourable adsorption modes for HMF on Au_{13} and Pd_{13} respectively which are accompanied by the calculated interaction energies according to equation 6.1. A total of four interaction modes were modelled per cluster type. This was chosen due to pre-determination of favourable adsorption modes coupled with time constraints of modelling each configuration.

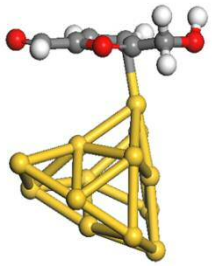	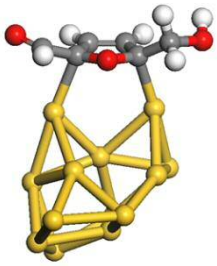
Adsorption 1: E_{ads} -118 kJ mol^{-1}. Au1 is directly interacting with C1 on the furan ring.	Adsorption 2: E_{ads} -128 kJ mol^{-1}. From left to right Au1 is directly interacting with C1 and Au2 is directly interacting with C2

Figure 6.10: The optimised two most favourable adsorption modes for HMF on Au_{13}. Adsorption energies are reported in kJ mol^{-1}.

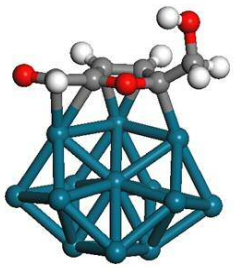	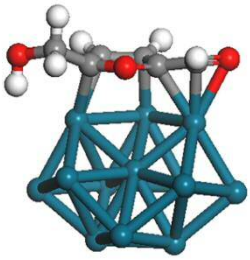
Adsorption 1: E_{ads} -233 kJ mol^{-1}. From left to right Pd1 is directly interacting with C1 and C2, Pd2 is directly interacting with C2 and C3 and Pd3 is directly interacting with C3.	Adsorption 2: E_{ads} -235 kJ mol^{-1}. From left to right Pd1 is directly interacting with C1 and C2, Pd2 is interacting with C3 and Pd3 is interacting with C4 and C5.

Figure 6.11: The optimised two most favourable adsorption modes for HMF on Pd_{13}. Adsorption energies are reported in kJ mol^{-1}

It is interesting to observe Pd_{13} exhibits a substantially greater interaction energy of -235 kJ mol^{-1} compared to -128 kJ mol^{-1} for Au_{13}. This trend is similar to that observed for adsorption of molecular oxygen presented in chapter 5. A degree of distortion of the metal particle is observed for both Au_{13} and Pd_{13}. These small particles are highly flexible in their nature and distort upon adsorption of molecules similar to that observed within chapter 5.

To account for distortions between adsorption state geometry and pre adsorption geometry a breakdown of the different components of adsorption has been performed. Using single point energy calculations, the change in energy of the cluster from pre-adsorption to adsorption geometry has been determined and denoted $\Delta E_{cluster}$ along with ΔE_{hmf} calculated to determine

any potential HMF distortion. Table 6.1 contains the results of these calculations for both Au_{13} and Pd_{13}.

Table 6.1: Calculated cluster and HMF rearrangements energies in kJ mol^{-1}. For the two most favourable adsorptions.

	Adsorption 1 Au_{13}	**Adsorption 2 Au_{13}**	**Adsorption 1 Pd_{13}**	**Adsorption 2 Pd_{13}**
$\Delta E_{cluster}$	-68	-78	-36	-35
ΔE_{hmf}	64	16	92	83

The calculated rearrangement energies for Au_{13} confirm rearrangement to a lower energy configuration occurs when HMF adsorbs on it. These values are significant and indicate the interaction energies calculated contain a strong component of the cluster rearrangement energy therefore exaggerating any adsorption energies determined. It is interesting to observe for Pd_{13} cluster rearrangement energies are approximately half of those calculated for Au_{13}. It is reasonable to assume Pd_{13} may be more rigid in nature and not distort when adsorbates are placed onto the cluster. This is supported by visualisation of the optimised geometries presented in figures 6.10 and 6.11 where it is clear distortion occurs to a lesser extent for Pd_{13} systems.

HMF undergoes an energetic change upon adsorption. The difference between equilibrium and adsorbed geometries has been calculated as positive indicating it rearranges to higher energy structure and therefore these values will counter the energetically favourable rearrangements of the metal particles. HMF in adsorption configuration 1 on Pd_{13} has the largest rearrangement energy. In this instance it is 92 kJ mol^{-1} higher in energy than equilibrium geometry. Visual inspection of the adsorption geometry reveals the alcohol group has rotated 180° in relation to adsorption 2 along with a C=C bond stretch when interacting with the cluster providing a reasonable explanation for the positive ΔE_{hmf} value calculated.

To investigate adsorption interactions in more detail a Bader charge analysis was performed in accordance with the conditions discussed in 6.2. In this analysis charge values are calculated in reference to neutral atoms therefore a calculated value which is negative indicates electron charge has moved onto the atom as a result of bonding interactions and electron charge has been removed from the atom upon bond formation for a value which is positive. For adsorption configuration 1 on Au_{13} there is a direct interaction between one carbon atom (labelled C1) on

the furan ring and one Au atom in the cluster (labelled Au1). For adsorption configuration 2 on Au_{13} two carbon atoms (C1 and C2) are directly interacting with two Au atoms (Au1 and Au2). Table 6.2 contains the Bader charge analysis calculation results for these atoms in the Au_{13} / HMF systems.

The Bader charge analysis in table 6.2 displays a clear trend where upon adsorption the carbon

Table 6.2: Calculated charge distribution obtained via Bader analysis atom numbering convention is detailed in figure 6.10, all values are reported in units of |e|.

	C1	C2	Au1	Au2
Adsorption 1 Au_{13}	-0.185	-	0.210	-
Adsorption 2 Au_{13}	-0.178	-0.387	0.165	0.120

atoms in HMF which are directly interacting with the metal particle are calculated to have an excess electronic density. For HMF atoms which are interacting directly with carbon atoms in the furan ring the opposite is observed where they are calculated to be electropositive. Both C1 and C2 in HMF form part of the furan ring and are double bonded to each other. The presence of both σ and π- electrons will create a region of high electron density therefore the Bader charge analysis obtained here is reasonable and in agreement with what is expected.

Similar Bader charge analysis has been performed for Pd_{13} which is presented in table 6.3. A higher degree of coordination is observed for HMF bound to Pd_{13} compared to Au_{13}. In these instances, all four carbon atoms in the furan ring are coordinated to the Pd_{13} particle. These four carbon atoms are denoted (C1-C4) and are coordinated to the palladium particle via 3 atoms (Pd1-Pd3). Further interaction occurs between the particle and the carbon belonging to the aldehyde functional group (C5).

Due to the nature of the furan ring and its conjugated system a non-uniform charge distribution is expected which is observed through the Bader charge analysis. C5 is double bonded to the oxygen atom forming the aldehyde functional group and therefore it is reasonable to expect

this carbon to be electropositive with respect to other carbon atoms as it is bonded to such an electronegative element.

Table 6.3: Calculated charge distribution |e| obtained via Bader analysis of HMF adsorbed on Pd_{13}. Labelling convention is detailed in figure 6.11.

	C1	C2	C3	C4	C5	Pd1	Pd2	Pd3
Adsorption 1 Pd_{13}	-0.193	1.194	0.211	-0.260	1.821	0.2857	0.1206	0.029
Adsorption 2 Pd_{13}	-0.207	1.173	0.245	-0.274	1.864	0.0784	0.2976	0.1072

Data reported in table 6.3 confirms as C5 is part of the electronegative aldehyde functional group side chain it has a charge distribution which is more electropositive in respect of all other C atoms part of the furan ring (due to being doubly bonded with electronegative O atom). All Pd atoms in direct interaction with HMF have an electropositive value indicating a deficiency in electron density. C1 and C4 both have a charge distribution indicating electron density is centred on them whilst C2 and C3 exhibit the opposite trend.

Bader charge analysis performed in tables 6.2 and 6.3 presents a snapshot of electronic distribution at the point of adsorption, whilst this is informative a comparative analysis of the charge distribution before and after would provide evidence for the type of interaction between HMF and the metal particles.

Bader charge analysis has been performed on HMF molecule and a sum of these charges indicates a neutral molecule. A sum of the partial atomic charges for all atoms in HMF once adsorbed on Au_{13} and Pd_{13} indicate striking differences between the interaction. For the Au_{13} / HMF system the partial charges on HMF decrease by 0.065 |e| indicating HMF has lost electron density to Au_{13}. The opposite is measured for Pd_{13} / HMF where an overall electron gain of 0.162 |e| is measured. This comparative Bader charge analysis suggests the HMF / Au_{13} interaction is predominately a σ interaction with no back donation and the HMF / Pd_{13} interaction has sufficient back donation to HMF.

6.3.4 Interaction of HMF with metal particles containing 38 atoms.

Figures 6.12, 6.13 and 6.14 present the two most favourable adsorption configurations for HMF on Au_{38}, Au_6Pd_{32} and Pd_{38} respectively accompanied by interaction energies calculated using equation 6.1.

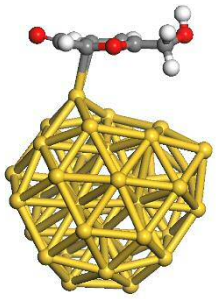	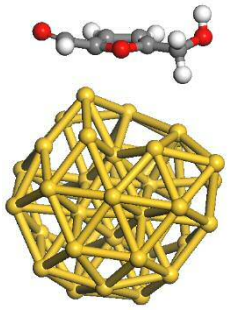
Adsorption 1: E_{ads} -75 kJ mol^{-1}	Adsorption 2: E_{ads} -73 kJ mol^{-1}

Figure 6.12: The optimised two most favourable adsorption modes for HMF on Au_{38}. Adsorption energies are reported in kJ mol^{-1}

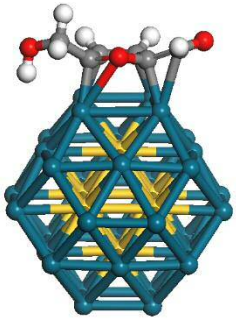	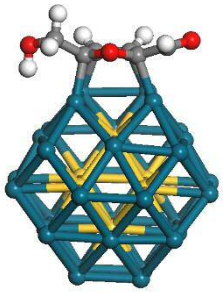
Adsorption 1: E_{ads} -151 kJ mol^{-1}	Adsorption 2: E_{ads} -119 kJ mol^{-1}

Figure 6.13: The optimised two most favourable adsorption modes for HMF on Au_6Pd_{32}. Adsorption energies are reported in kJ mol^{-1}.

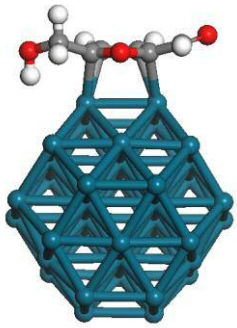	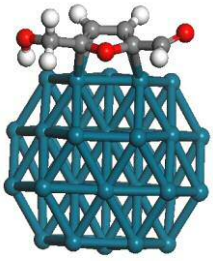
Adsorption 1: E_{ads} -106 kJ mol^{-1}	Adsorption 2: E_{ads} -100 kJ mol^{-1}

Figure 6.14: The optimised two most favourable adsorption modes for HMF on Pd_{38}.

Figures 6.12, 6.13 and 6.14 demonstrate two key differences between adsorption of HMF on 38 atom particles vs 13 atom particles. The first difference is HMF has significantly weaker

interaction energies on 38 atom particle vs 13 atom particles. The most favourable interaction between HMF and Au_{38} is calculated to be 55 kJ mol^{-1} weaker than the most favourable interaction with Au_{13}. The difference between calculated interaction energies between Pd_{13} and Pd_{38} is 133 kJ mol^{-1} which is significantly smaller indicating a greater affinity for HMF is present for sub nanometre particles vs larger ones.

The second difference between adsorption between 13 and 38 atom particles is distortion of the particle. Upon visual inspection the 38 atom particles appear to be much less distorted upon adsorption of HMF than the 13 atom particles. Such changes in distortion can be quantified by performing a breakdown of the components of adsorption analogous to that presented in table 6.1. These components are reported in table 6.4.

Calculated interaction energies between HMF and Au_6Pd_{32} lie between values calculated for Au_{38} and Pd_{38}. The addition of 6 gold atoms within the core increase the magnitude of calculated adsorption energies in comparison to pure Pd_{38} by approximately 50%. Such an increase in magnitude of adsorption energies could be due to a stretch of the Pd shell on the cluster. The lattice constant for Au is greater than Pd and therefore the presence of a 6 atom gold core can expand the periphery of the cluster. Measurements of the (100) facet confirm the Pd-Pd distance of the (100) facet is elongated by 0.05 Å in this bimetallic form. It would be of interest to investigate other alloy compositions and whether these influence interaction energies to the extent detailed here. Due to computational cost and time constraints an investigation of other alloy compositions is beyond the scope of this chapter.

Table 6.4: Calculated cluster and HMF rearrangement energies in kJ mol^{-1*}.

	Adsorption 1 Au_{38}	**Adsorption 2 Au_{38}**	**Adsorption 1 Au_6Pd_{32}**	**Adsorption 2 Au_6Pd_{32}**	**Adsorption 1 Pd_{38}**	**Adsorption 2 Pd_{38}**
$\Delta E_{cluster}$	-46	-48	16	8	10	24
ΔE_{hmf}	11	11	177	52	48	46

*Structures for adsorption mode 1 and 2 for all clusters can be seen in figures 6.12, 6.13 and 6.14 respectively.

Table 6.4 indicates the metal particles do not undergo a significant distortion upon adsorption of HMF therefore confirming they are more rigid in nature than metal particles containing 13

atoms. Both Au_6Pd_{32} and Pd_{38} geometries alter to become higher in energy than their starting structure upon adsorption of HMF. It is interesting to observe that for Au_{38} distortion to a lower energy structure occurs indicating the Au_{38} particle may exhibit more flexibility than the other metal particles of this size. This flexibility has been investigated in chapter 5 through molecular dynamics investigations with a conclusion that lower energy structures do exist for Au_{38} than the structure used in this chapter however significant energy barriers are required to be crossed in order to reach them.

HMF does not undergo significant distortion once it is adsorbed on Au_{38}, this is due to the relatively small differences in energy (11 kJ mol^{-1}) between pre-optimisation and adsorbed geometry HMF energies. The anomaly to this observation is the rearrangement energy of HMF once adsorbed via configuration 1 on Au_6Pd_{32}. This rearrangement energy is calculated at 177 kJ mol^{-1}. Figure 6.15 is an image of this structure, in which it is clear there is a significant distortion particularly around the furan ring which appears buckled. Such a distortion can break any conjugation present within the ring and may explain why this arrangement is in a significantly higher energetic state than the pre-optimised geometry. Upon adsorption these re-hybridised distorted carbon atoms are stabilised by the interaction with the metal particle.

Figure 6.15: Distorted structure of HMF which occurred via adsorption to Au_6Pd_{32} via adsorption site 1.

6.4 Activation of the O-H Bond within HMF

The consensus within the literature regarding the oxidation of HMF is that oxidation of the aldehyde group is facile and occurs via a germinal diol intermediate which is subsequently oxidised to the carboxylic acid functional group. The alcohol group oxidation is reported to occur at a slower kinetic rate which is a two stage process requiring conversion of alcohol to aldehyde followed by subsequent oxidation to carboxylic acid. Experimental observations discussed in the literature review (chapter 2) confirm this hypothesis. Due to this consensus

this chapter will solely focus on a computational oxidation study towards the conversion of the alcohol to gain an insight into kinetics of this mechanism.

Due to the computational expense of determining reaction barriers for all metal particles and adsorption modes, only the most favourable adsorption of HMF on Au_{13} and Pd_{13} will be chosen to perform an investigation into the cleavage of the O-H bond. A further study of larger particles would have provided a fascinating insight, however it is beyond the scope of this thesis.

To investigate O-H cleavage the geometry optimised structures of HMF bound to Au_{13} and Pd_{13} were taken as start points. The H atom belonging to the alcohol functional group was detached and bound to the nearest metal atom in the metal particle, this is for both thermodynamic feasibility and also to save the computational cost of modelling many abstraction positions on the metal particle. These structures were geometry optimised using standard conditions. Figure 6.16 presents the optimised structures along with their relative energies compared to starting structure in kJ mol^{-1}.

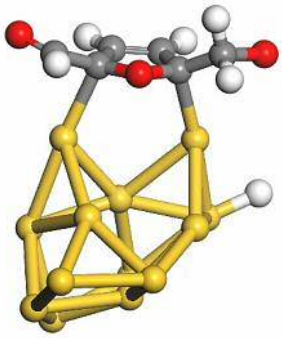	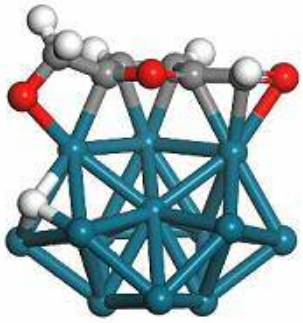
Relative Energy = 39 kJ mol^{-1}	Relative Energy = 33 kJ mol^{-1}

Figure 6.16: Geometry optimised structures of HMF adsorbed on Pd_{13} and Au_{13} particles with a H atom abstracted and placed on the nearest metal atom.

The thermodynamic preference is clearly to have HMF remain intact on the metal particle. With the H atom abstracted both Au_{13} and Pd_{13} systems are in a higher relative energy than the intact system. This indicates the formation of an alkoxy bound intermediate is thermodynamically unstable in comparison to the start structure.

As a comparison to metal particles containing 38 atoms the optimised geometries of structures with the H atom abstracted along with their relative energies for Pd_{38} and Au_6Pd_{32} are presented in figure 6.17.

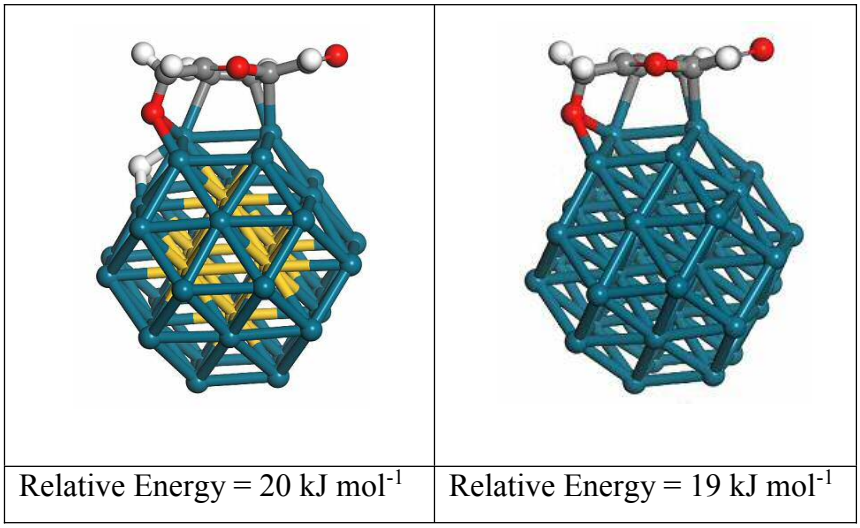

Relative Energy = 20 kJ mol^{-1}	Relative Energy = 19 kJ mol^{-1}

Figure 6.17: Geometry optimised structures of HMF adsorbed on Au_6Pd_{32} and Pd_{38} metal particles with a H atom abstracted and placed on the nearest metal atom in the metal particle.

The alkoxy intermediates presented in figure 6.17 have relative energies higher than their starting structures however the relative energy difference is at least 13 kJ mol^{-1} smaller than for the particles containing 13 atoms. This observation indicates forming the alkoxy bound intermediate is more thermodynamically favourable on the larger particles.

The structures discussed in figure 6.16 were taken as end points for nudged elastic band calculations (NEB)[33,34]. The NEB calculations comprised of a linear interpolation between the start and end structures which generated 24 intermediate structures. This fine sampling ensures generation of a smooth energy / reaction coordinate profile. Each image obtained through the interpolation was constrained optimised with a spring constant setting of -5 within VASP. Transition states were confirmed through performing a frequency analysis which identified one imaginary mode.

Figure 6.18 details the reaction profile for cleavage of the O-H bond on both Au_{13} and Pd_{13} respectively. Energies are set relative to the energy of the isolated metal particle and HMF.

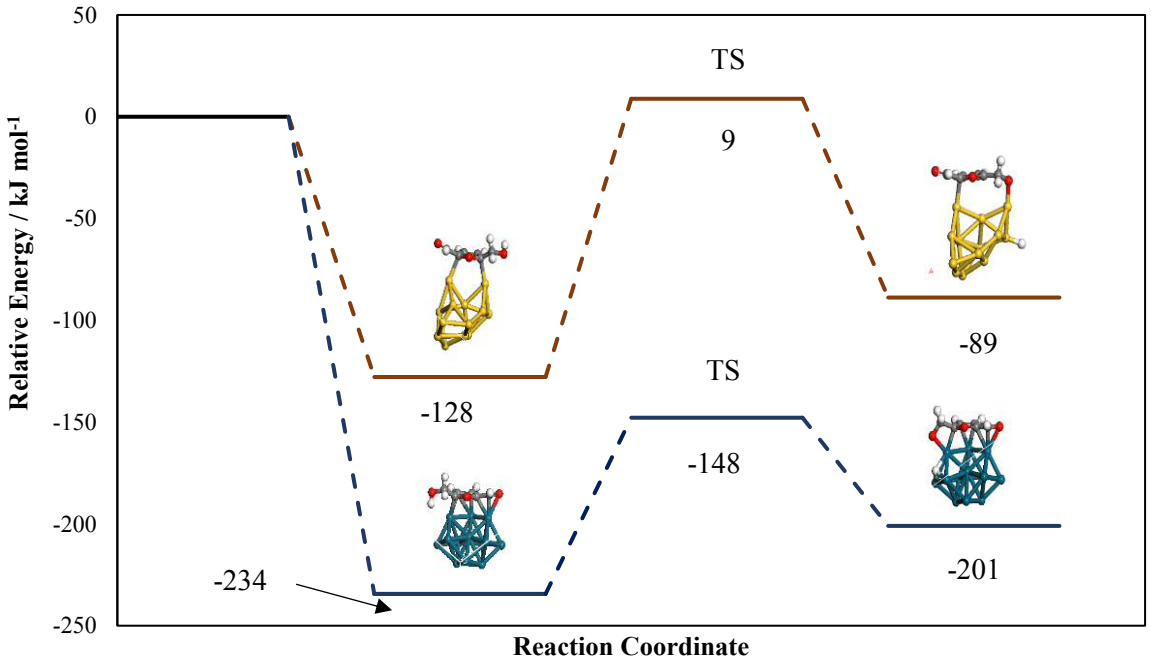

Figure 6.18: Calculated barriers for the adsorption and cleavage of the O-H bond in the HMF alcohol group. Energies are set relative to isolated metal particle and HMF. Gold line indicates O-H cleavage taking part on Au_{13} and blue line indicates the same process occurring on Pd_{13}. TS is used to indicate transition state.

The reaction scheme presented in figure 6.18 demonstrates a noticeable difference in the reaction profile gold and palladium clusters. Au_{13} exhibits an initial adsorption energy approximately 106 kJ mol^{-1} higher in energy than that for Pd_{13}. For Au_{13} the calculated barrier to dissociation exceeds the adsorption energy by 9 kJ mol^{-1} indicating at elevated reaction temperatures this may occur with ease and a completion between desorption vs dissociation occurs. For Pd_{13} a greater adsorption energy coupled with a calculated barrier lower in energy than the initial adsorption energy clearly indicate adsorption and dissociation is favourable on this Pd_{13} particle. In both instances the end point (alkoxy bound intermediate) is in a thermodynamically higher energy state than the intact adsorbate / metal particle system. This indicates at equilibrium it is expected a higher proportion of molecules with O-H intact will exist than the dissociated species.

Adsorption energies for metal particles containing 38 atoms were calculated to be lower than for Au_{13} and Pd_{13} therefore it is predicted if the barrier to O-H cleavage remains similar that dissociation of O-H on larger particles will not be preferred. Figure 6.19 presents calculated reaction barriers for cleavage of the O-H bond on Au_6Pd_{32} and Pd_{38}. Due to time constraints it

has not been possible to determine the barrier for O-H cleavage on Au_{38} however it would be of interest for future investigation.

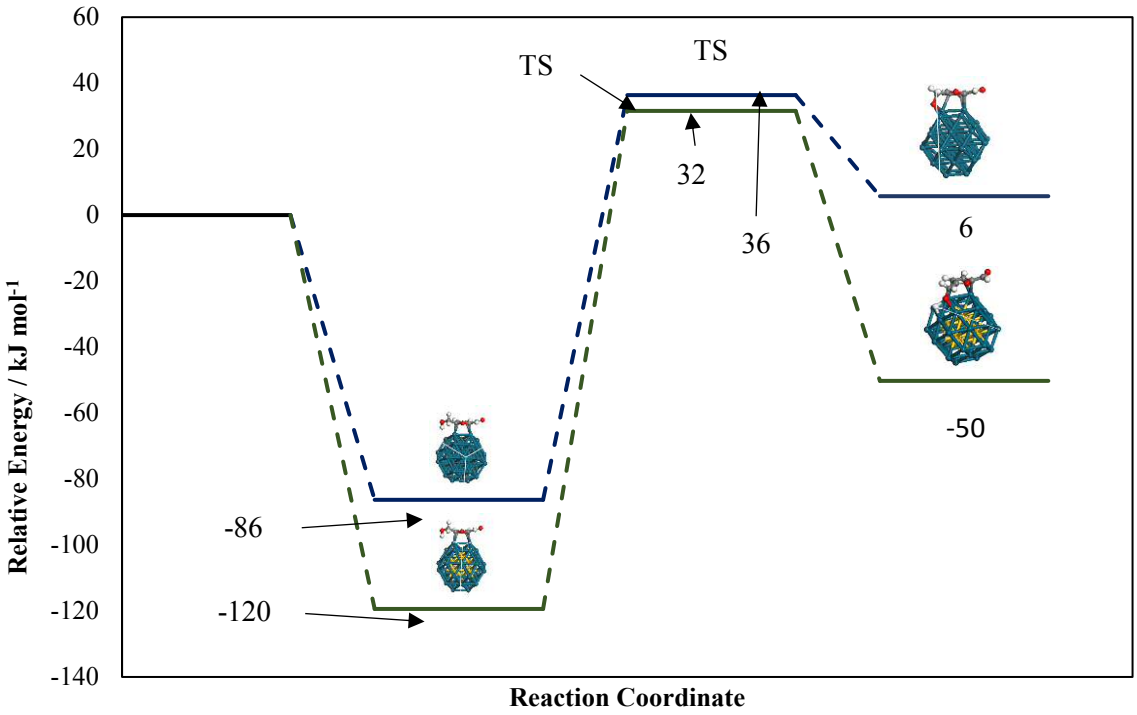

Figure 6.19: Calculated barriers for the adsorption and cleavage of the O-H bond in the HMF alcohol group. Energies are set relative to isolated metal particle and HMF. Green line indicates O-H cleavage taking part on Au_6Pd_{32} and blue line indicates the same process occurring on Pd_{38}. TS is used to indicate transition state.

Reaction barriers calculated for both Pd_{38} and Au_6Pd_{32} indicate the barrier exceeds adsorption energy for both cases and therefore it is reasonable to assume adsorption followed by dissociation of the O-H group will not occur spontaneously on these metal particles. For Pd_{38} an adsorption energy of -96 kJ mol^{-1} is followed by a barrier to dissociation of 36 kJ mol^{-1} (122 kJ mol^{-1} higher in energy than the minima in which it sits in following adsorption). Such a high barrier to dissociation suggests it is unlikely it will occur spontaneously. For Au_6Pd_{32} adsorption of -120 kJ mol^{-1} occurs with a barrier to O-H cleavage determined at 32 kJ mol^{-1} which at 152 kJ mol^{-1} higher than the energy minima well which makes this dissociation unlikely to occur spontaneously. For all of the 38 atom particles investigated Au_{38} has the lowest calculated adsorption energy of HMF (-75 kJ mol^{-1}). It can be speculated if the barrier height remains similar to that obtained for the other 38 atom particles a cleavage of the O-H bond within HMF would be least favourable on Au_{38}. Such speculation requires further barrier calculations which due to computational cost and time are beyond the scope of this chapter.

6.5 Adsorption of HMF to oxidised metal particles

Calculations performed in chapter 5 confirm it is energetically feasible to adsorb and dissociate at least one molecule of oxygen on each of the metal particles investigated in this chapter. Oxidation chemistry by its very nature occurs within an oxygen rich environment and therefore it is reasonable to assume under such conditions all the metal particles investigated here will contain adsorbed and dissociated oxygen species. It is of particular interest to investigate what effect if any the presence of this oxygen will have with regards to adsorption of HMF and activation of the O-H bond. In this section a systematic study of the adsorption of HMF with oxidised particles will be presented along with a discussion of the influence oxidised metal particles may have on the barrier to dissociation of the O-H group.

As previously determined oxygen adsorbs and dissociates most favourably via a (100) facet, this (100) facet is also the most preferential adsorption mode for HMF which occurs via a furan ring interaction over the (100)-(111) metal particle junction. Prior knowledge of the preferred adsorption site accompanied by the highly symmetric nature of the particles studied here makes a systematic study of HMF adsorption on oxidised metal particles possible and computationally efficient.

To initiate this study one molecular oxygen was adsorbed and dissociated at a (100) facet, this optimised structure was taken as reference for both energy and structure in which HMF will be adsorbed on. Each particle contains 6 (100) facets. Within these facets HMF can align with two possibilities (figure 6.20) therefore there are 12 adsorption modes per metal particle which will be investigated.

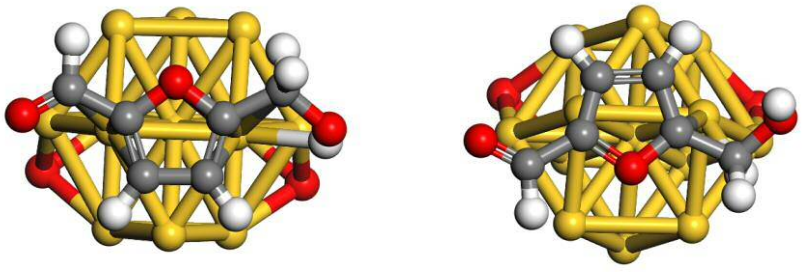

Figure 6.20: The orientation of two adsorption sites on the (100) facet on Au_{13}.

Due to the fully relaxed nature of the optimisations the geometry of the metal particle / adsorbate system alters during relaxation therefore breaking symmetry. In order to determine

and correlate how adsorption energies of HMF are influenced by proximity adsorbed oxygen atoms on the metal particle a centroid dummy atom was created in the furan ring. This dummy atom was used to measure distance from it to the two adsorbed and dissociated oxygen atoms on the particle. An average of these two values were taken and adsorption energies plotted against this distance are reported for each cluster composition in figure 6.21, 6.22, 6.23, 6.24 and 6.25.

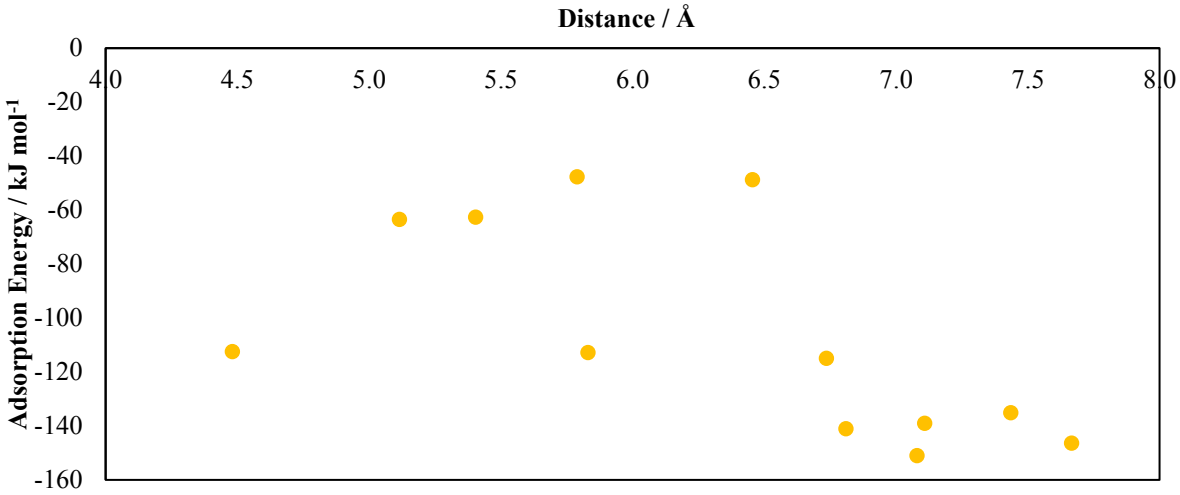

Figure 6.21: Average distance between the centroid of the furan ring and dissociated oxygen atoms on Au_{13} particle plotted against calculated adsorption energies.

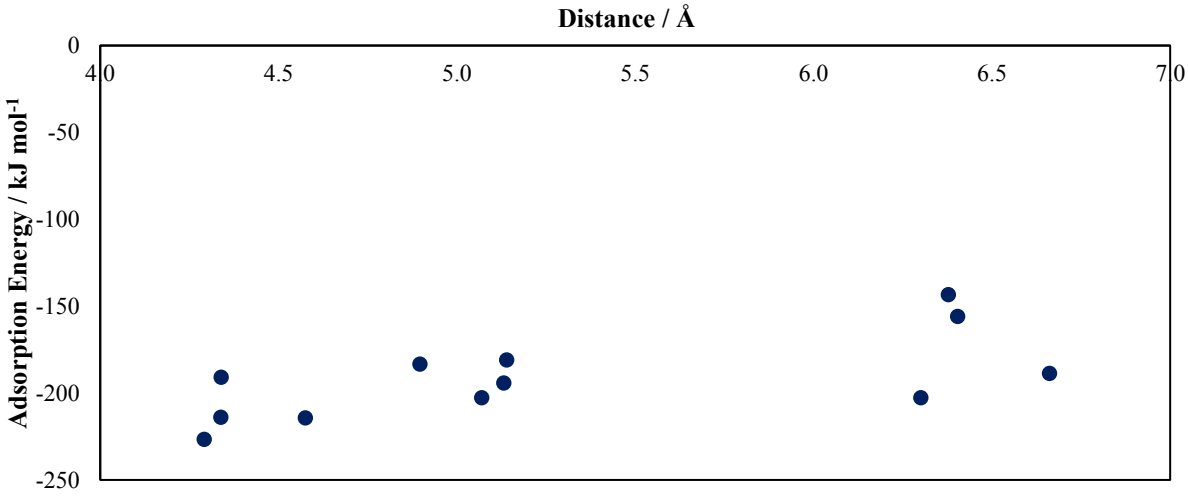

Figure 6.22: Average distance between the centroid of the furan ring and dissociated oxygen atoms on Pd_{13} particle plotted against calculated adsorption energies.

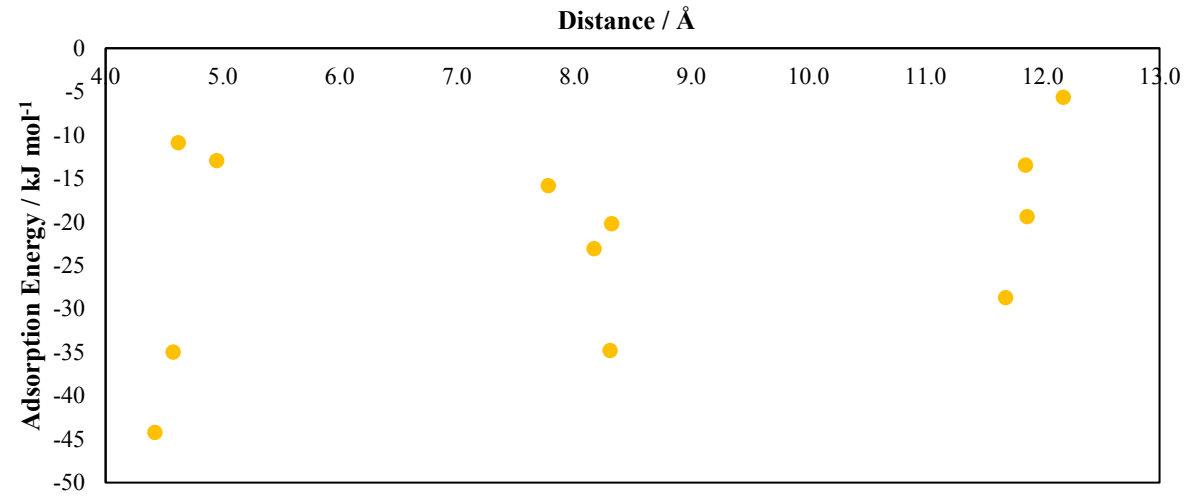

Figure 6.23: Average distance between the centroid of the furan ring and dissociated oxygen atoms on Au_{38} particle plotted against calculated adsorption energies.

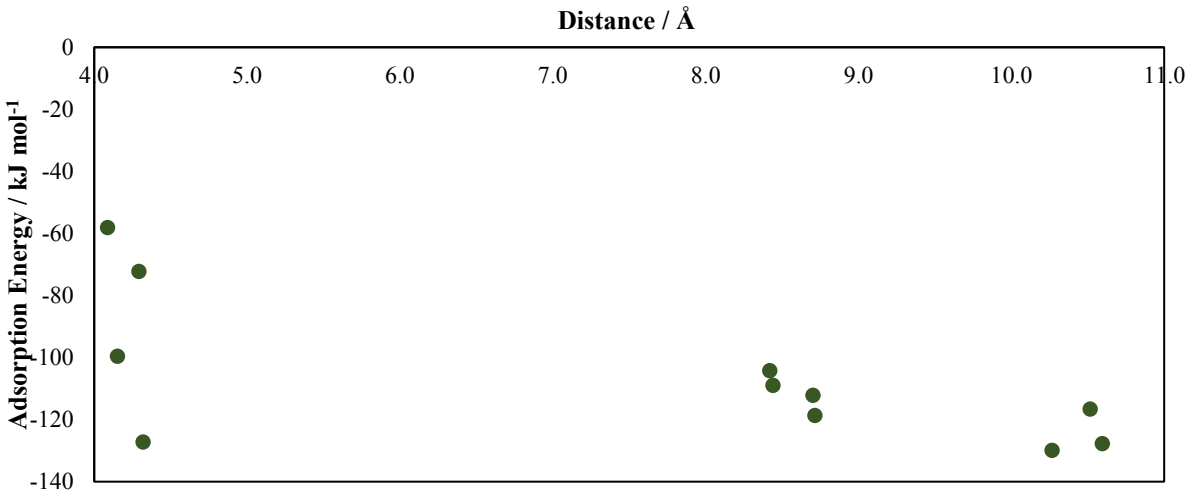

Figure 6.24: Average distance between the centroid of the furan ring and dissociated oxygen atoms on Au_6Pd_{32} particle plotted against calculated adsorption energies.

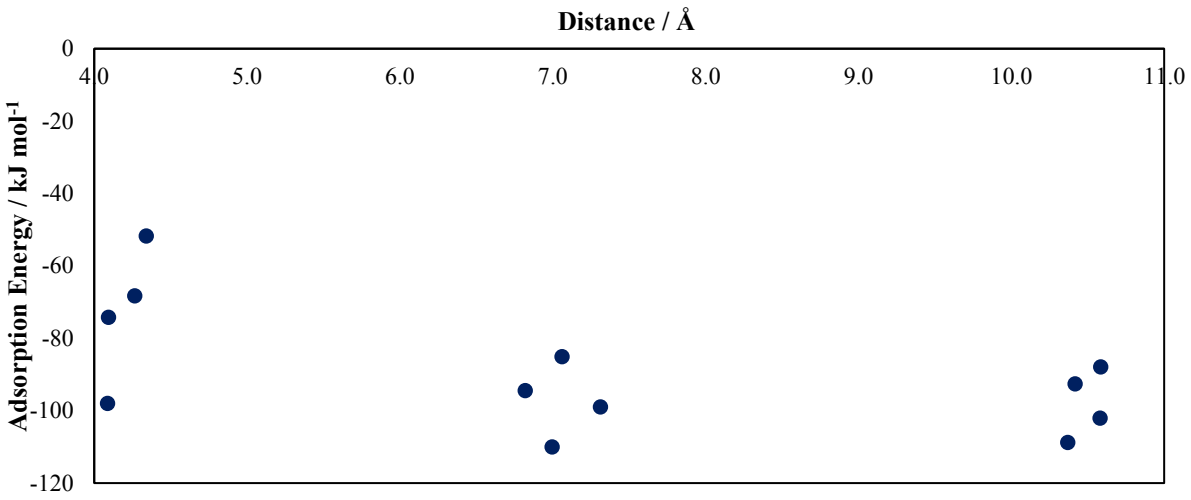

Figure 6.25: Average distance between the centroid of the furan ring and dissociated oxygen atoms on Pd_{38} particle plotted against adsorption energies.

The centroid distance / adsorption energy data plotted in figure 6.21 highlights a trend in which the highest adsorption energies occur at the largest distance from the adsorbed oxygen species on $Au_{13}O_2$. The trend however is not linear with the least favourable adsorption energies reported at 5.8 and 6.5 Å. For $Pd_{13}O_2$ the opposite trend occurs, here the most favourable adsorption energies correspond to those in a position closest to the oxygen atoms. This interesting observation suggests there is not a substantial steric influence of the oxygen atoms if they are dissociated into the (111) facets adjoining the HMF adsorption site. The same observation is made for $Au_{38}O_2$ and $Au_6Pd_{32}O_2$, however $Pd_{38}O_2$ exhibits the trend seen for $Pd_{13}O_2$. The relationship between adsorption energies and distance between the furan ring centroid and dissociated oxygen atoms on the whole does not cause detrimental adsorption properties therefore it is reasonable to assume favourable adsorption will occur for oxidised metal particles. It is however interesting to note stiffer clusters (containing 38 atoms) show data points closer together (more bunched) than the more flexible clusters containing 13 atoms. It is reasonable to assume greater cluster flexibility mean a broader range of O-centroid distances are observed vs the more fixed geometries of the stiffer metal particles.

6.5.1 O-H Cleavage of HMF on Oxidised Metal Particles

Due to computational cost only the barrier for O-H cleavage on HMF has been investigated on the $Pd_{13}O_2$ cluster. The structure chosen to perform this NEB analysis on is presented in figure 6.26. This structure has been chosen as the H atom in the alcohol group is in close alignment to one of the dissociated oxygen atoms on the particle. It is envisaged the cleavage of the O-H bond will be kinetically more favourable in this instance.

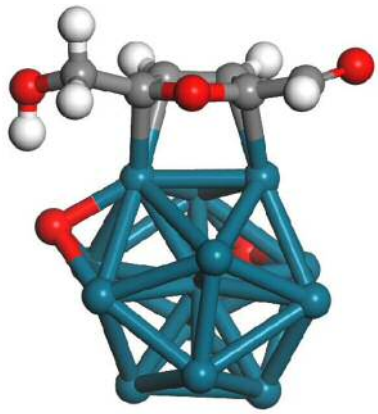

Figure 6.26: Configuration chosen to investigate cleavage of O-H bond in HMF on $Pd_{13}O_2$.

The barrier to O-H dissociation presented in figure 6.27 has not met final convergence requirements and as a result it is reported as preliminary. It however is an upper estimate of the barrier which makes it all the more striking as it is significantly lower than that observed for pure metal clusters investigated in this chapter. The barrier to dissociation of the O-H group in HMF has been preliminary calculated as 54 kJ mol^{-1} higher in energy than the energy minima well it is in following adsorption to the metal particle. For the bare cluster it is calculated to be 86 kJ mol^{-1} higher in energy which clearly indicates that the presence of dissociated oxygen species facilitates the cleavage of the O-H bond in HMF.

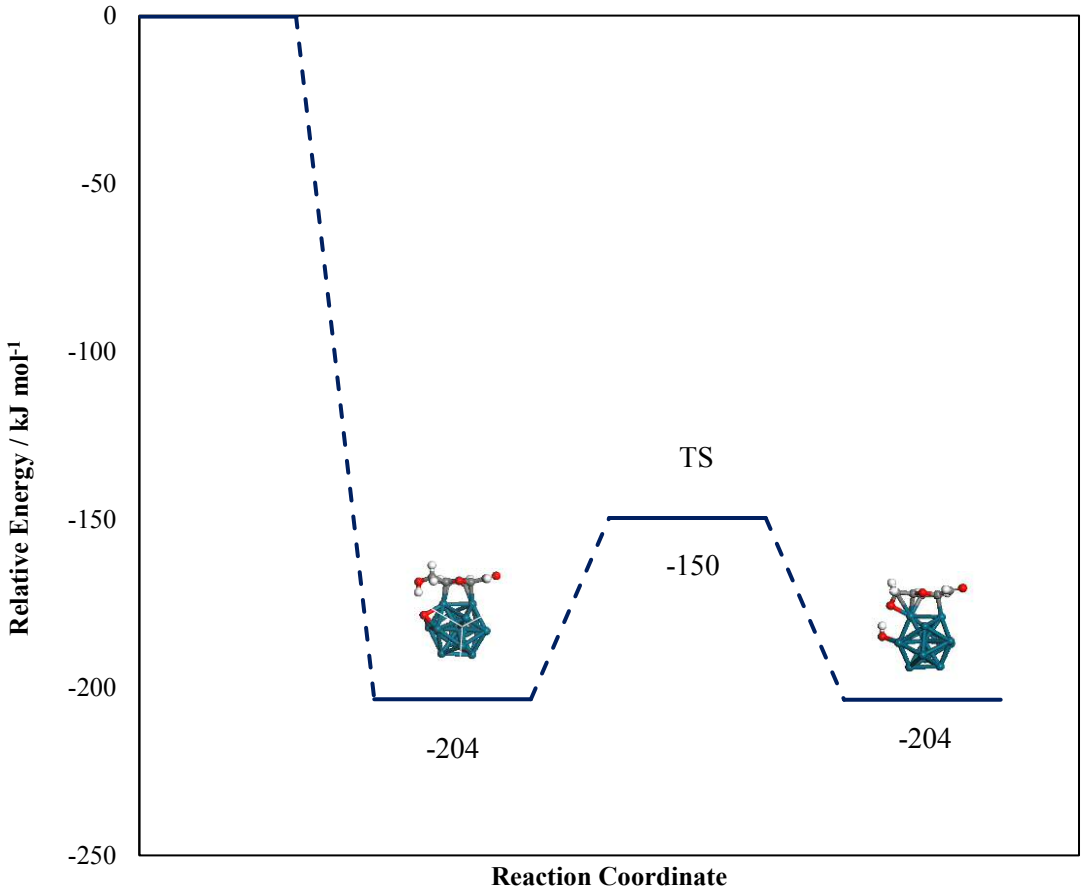

Figure 6.27: Calculated barriers for the adsorption and cleavage of the O-H bond in the HMF alcohol group. TS is used to indicate transition state. Energies are reported relative to isolated HMF and $Pd_{13}O_2$.

6.6 Calculations Performed with Dispersion Corrections

The DFT-D2 method of Grimme has been utilised in VASP to evaluate the component of dispersion in calculated interaction energies. No default parameters which can model dispersion interactions in systems containing gold atoms are available in VASP version 5.2.12. Because of this a literature search was used to obtain coefficients to describe Au dispersion interactions[27]. The coefficients used by Eriksson *et al.* were used to model bulk gold surfaces. Evaluation of whether these coefficients are suitable to model gold within particle form has not been performed and will be required in order to validate this data. As in 6.3.3 and 6.3.4 HMF was adsorbed on metal particles and interaction energies determined according to equation 6.1. Using DFT-D2 the most favourable adsorption energy for each metal particle are presented in

figure 6.28 along with a comparison with the most favourable adsorption energy for calculations performed without the D2 correction.

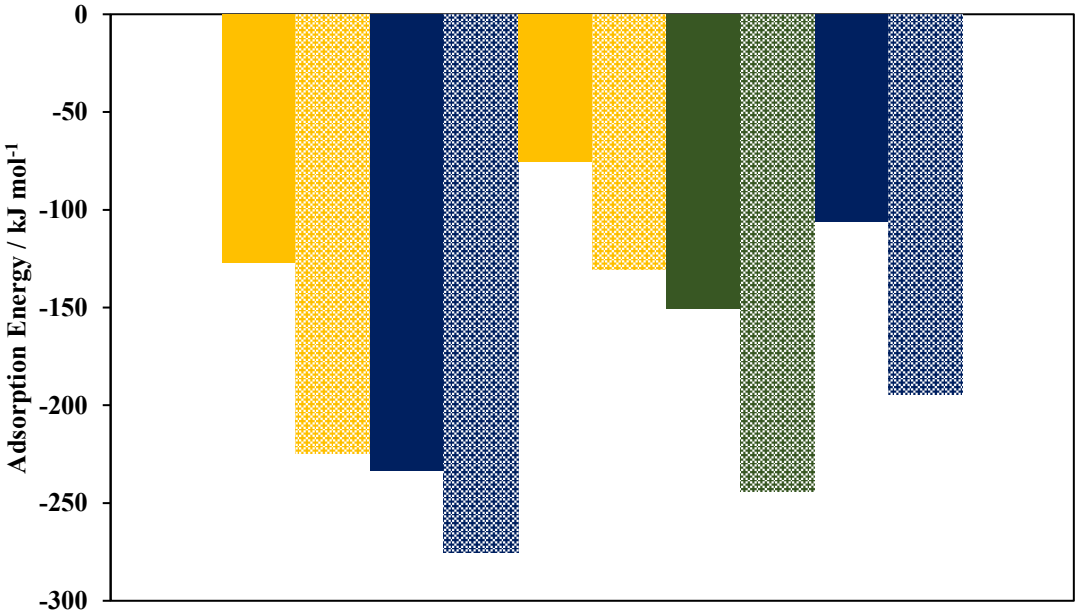

Figure 6.28: Most favourable adsorption configuration for each metal particle calculated with and without D2 correction. From left to right: Au_{13}, Pd_{13}, Au_{38}, Au_6Pd_{32} and Pd_{38}. Solid filled bars are calculations without D2 correction and partially filled bars are calculations performed using the D2 method of Grimme.

The inclusion of dispersion in calculations enhances the adsorption energies for all metal particles investigated. For Au_{13} the most favourable adsorption configuration with the D2 correction is calculated to be 97 kJ mol^{-1} more favourable than for Au_{13} without this correction. For Pd_{13} the energy difference is 42 kJ mol^{-1}, Au_{38} 55 kJ mol^{-1}, Au_6Pd_{32} 94 kJ mol^{-1} and for Pd_{38} the energy difference between most favourable configurations with and without the D2 correction is 88 kJ mol^{-1}. Inclusion of dispersion interactions has a greater influence on adsorption energies for gold and bimetallic particles. Gold is a highly polarisable metal and as a result it is expected a dispersion component of interactions would be greater for species containing high percentages of it. As adsorption energies are enhanced in all cases by inclusion of the D2 correction, it is reasonable to assume cleavage of the O-H bond would be more feasible as initial adsorption energies are larger and more likely to overcome the barrier. Investigation into the barrier of O-H dissociation including the D2 correction is beyond the scope of this thesis however would make an interesting future investigation and an accurate

inclusion of dispersion interactions would provide barrier data in better agreement with experiment.

6.7 Adhesion of Metal Particles to Surfaces

Using expansion of the lattice along with a sweep of *k*-point sampling detailed in the methodology section (chapter 4), various surfaces were prepared in order to support metal particles on. These surfaces were Fe_2O_3 (0001), Rutile (110) and MgO (100). Each of these slabs has the top two layers free to relax and were chosen as they contain examples of both reducible and irreducible supports. To each of these supports cuboctahedral geometry Au_{13} and Pd_{13} were placed directly in the centre point on the surface and then geometry optimised. Adhesion energies of these particles have been calculated using equation 6.2 where $E_{adhesion}$ is the calculated adhesion energy, E_{slab} is the energy of the slab and $E_{cluster}$ is the energy of the isolated metal cluster.

(6.2)

Adhesion energies have been calculated without the D2 correction. With the exception of Fe_2O_3 (0001) which has adhesion energies calculated with and without D2. Table 5 contains calculated adhesion energies.

Table 5: Adhesion energies calculated using equation 6.2. Energies are reported in eV.

	Au_{13}	**Pd_{13}**	**Au_{13} - D2**	**Pd_{13} – D2**
Fe_2O_3 (0001)	-5.015	-5.649	-8.821	-8.770
Rutile (110)	-3.405	-3.276	-	-
MgO (100)	-1.687	-3.387	-	-

In all systems investigated these metal particles adsorb favourably to the surface. The highest adhesion energy is reported for the iron oxide surface which has a calculated adsorption of -5.015 eV and -5.649 eV for Au_{13} and Pd_{13} respectively. Inclusion of D2 within these calculations increases adsorption energies by at least 3 eV in both cases which indicates a large degree of dispersion is prevalent within these interactions. An extension of this study would be of great interest to ascertain how HMF interacts with supported metal particles. Unfortunately, due to time constraints it is beyond the scope of this thesis however these preliminary calculations may be used for future studies to elucidate how the support influences adsorption energies and barriers to dissociation of the O-H bond in HMF. Upon adsorption metal particles

may alter geometry and therefore it is necessary to account for any particle rearrangement and determine the contribution of this to the interaction energy. Cluster rearrangement energies for both Au_{13} and Pd_{13} are reported in table 6.

Table 6: Calculated cluster rearrangement energies in eV, when they are adsorbed on various surfaces.

	Fe_2O_3 (0001)	**Fe_2O_3 (0001) D2**	**TiO_2 (110)**	**MgO (100)**
$\Delta E_{cluster}$ Au_{13}	-0.55	-1.38	-1.67	0.10
$\Delta E_{cluster}$ Pd_{13}	0.15	0.80	0.18	0.15

Rearrangement energies of the metal particles once again confirm Au_{13} is considerably flexible and in all cases except for MgO rearranges to a configuration which is lower in energy than the cuboctahedral geometry upon adsorption to the surface. It is interesting to observe Pd_{13} does not adsorb in a geometry which is lower in energy than the cuboctahedral structure. In all instances particles rearrange the least on MgO (100), visual inspection of these optimised systems confirms the particle remains in a very similar geometry to the start structure. Data obtained here confirms using Au_{13} with cuboctahedral geometry is suitable for investigating systems in which it is adsorbed on MgO (110) however this geometry can alter and distort once adsorbed onto the reducible supports TiO_2 (110) and Fe_2O_3 (0001) indicating a different start geometry may be required if comparisons between HMF interactions with and without a support are to be used for future calculations.

6.8 Conversion of Levulinic Acid to γ-Valerolactone

As previously discussed in chapter 2 the conversion of LA to gVL is of environmental and industrial significance. Conversion of levulinic acid requires a hydrogenation catalyst with Ru supported on carbon reported to produce > 90 % conversion at 100 ^oC using 5 bar H_2. Through classification purposes of the NOVACAM project, Ru is designated a metal which is either rare or not abundant in multiple countries, therefore there is potential restriction if current demands for this metal are maintained. An alternative would be to use metals which are more abundant with copper suggested as an alternative.

Internal unpublished research reports a Cu-ZrO_2 system prepared through oxalate gel precipitation converts 100% of LA to gVL at 200 ºC. Whilst promising activity is observed for this catalyst H_2 pressures of 35 bar are required for this conversion compared to 5 bar for the Ru / C system. This high H_2 pressure requirement is undesirable for environmental and cost reasons.

Through internal discussion of the experimental data it is proposed the rate limiting step of the conversion of LA to gVL is the adsorption of molecular hydrogen to the supported particle followed by dissociation. As a result of this discussion an investigation into electronic properties of bulk Ru, Ni and Cu has been performed through d-band centre analysis.

In the literature there is a consensus that the higher the d-band centre the stronger the bonding of the adsorbate to the metal will be[35]. As a result of this a study, determination of bulk metal d-band centre has been performed. This data has been obtained via a density of states (DOS) analysis within VASP with d-band centre calculated based upon a centre point determination of the DOS plot. All DOS calculations utilized ( ) KPOINT sampling mesh.

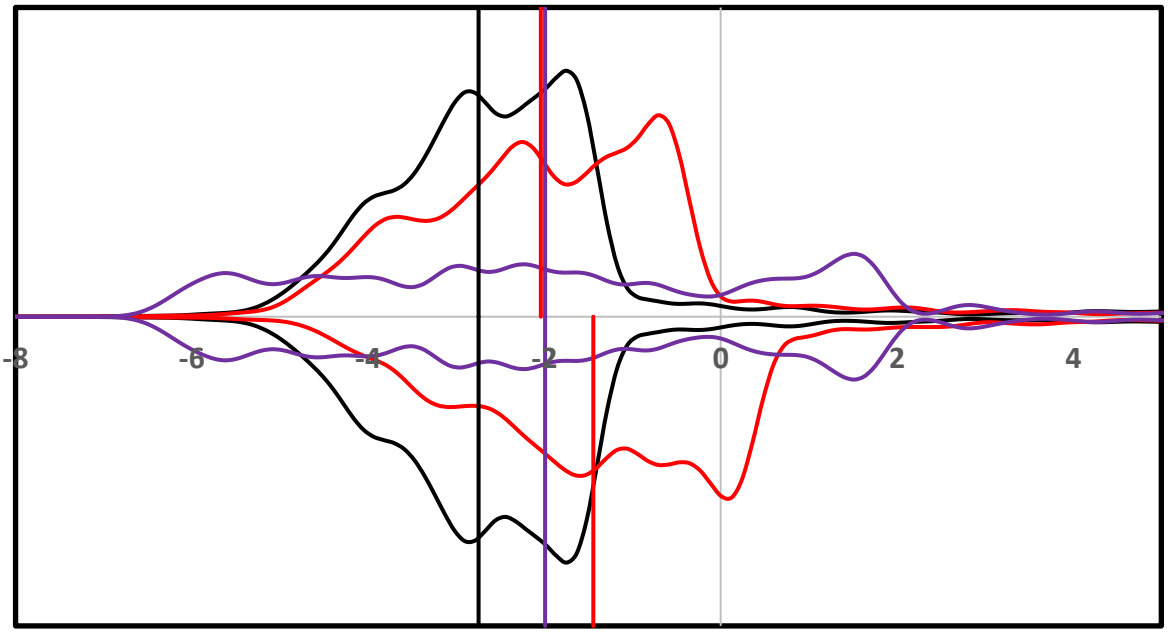

Figure 6.29: DOS plots for bulk Ni (red line), Ru (purple line), and Cu (black line). Calculated d-band centres (in eV) are solid lines along the Y-axis (arbitrary units).

DOS plots for bulk Ru, Ni and Cu are presented in figure 6.29. The result of this d-band centre analysis indicates bulk copper has the lowest d-band centre followed by Ru and Ni.

The magnetism of Ni is correctly accounted for as the up and down spin d-band centres are of different energies – all calculations are performed spin unrestricted which correctly accounts for this behaviour. This interesting observation may explain the different adsorption behaviours between the metals. For Cu (110) Campbell *et al.* report an experimentally determined activation energy for dissociative adsorption of hydrogen to be 59.83 $\pm$ 5.85 kJ mol^{-1} [36], whilst theoretical calculations by Yang *et al.* determined the lowest barrier to dissociation of H_2 on various sites on Ni (111) to be 6.69 kJ mol^{-1} [37]. These vastly different activation energies correlate to the d-band centres determined through this DOS analysis. Whilst the correlation is promising and indicates a relationship between the adsorption energies and d-band centres, this alone is not sufficient in conclusively proving the relationship.

This data suggests d-band centre calculations may provide insight into experimental observations and pose an interesting question regarding how the d-band centre may be altered by adding dopants to bulk metals. If experimentally a higher d-band centre is desired as it gives rise to enhanced adsorption of H_2, a computational investigation into loading of dopants in bulk metals could be performed and an ideal ratio proposed to experimenters. An example of computing d-band centre as a function of addition of dopant is presented in figure 6.30 where Ni atoms are added to a 2 1 supercell of bulk Cu and at each doping stage the d-band centre calculated. This data can enable experimental teams to "fine tune" bimetallic catalysts to enable desirable properties to be obtained.

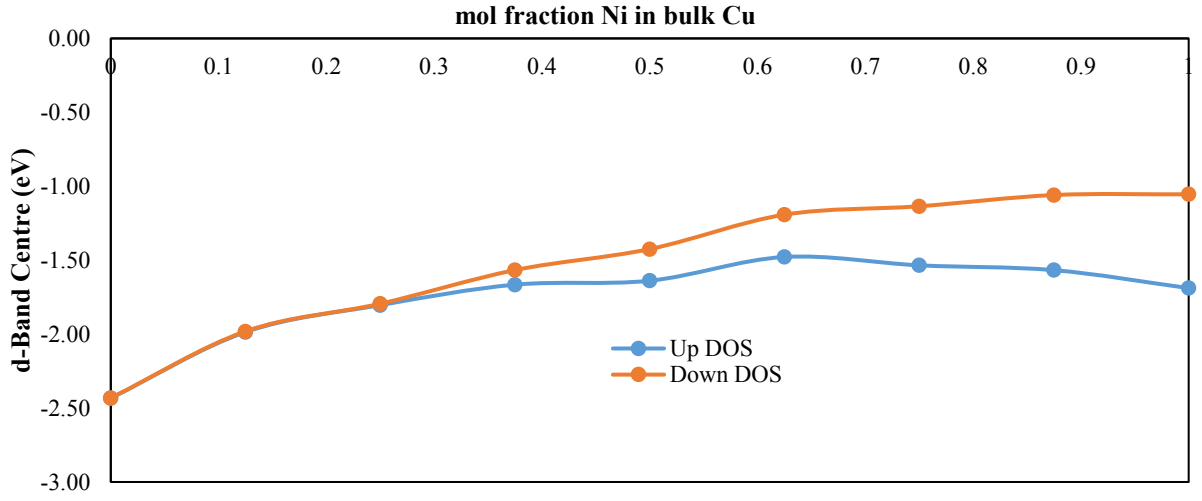

Figure 6.30: d-band centre calculation for adding Ni in a 2 1 supercell of bulk Cu. Asymmetry between d-band centres becomes more pronounces as the mole fraction of Ni is increased.

6.9 Conclusions

Using GGA DFT along with the PBE functional it has been demonstrated HMF interacts favourably with Au_{13}, Pd_{13}, Au_{38}, Pd_{38} and Au_6Pd_{32} particles. Adsorption energies confirm HMF interacts more favourably with sub nanometre particles with adsorption energies calculated to be 55 kJ mol^{-1} stronger on Au_{13} than Au_{38} and 135 kJ mol^{-1} stronger on Pd_{13} than Pd_{38}. A breakdown of the various components of these adsorptions reveal significant cluster rearrangement for Au_{13} which alters geometry to adopt a structure which is 75 kJ mol^{-1} lower in energy than the cuboctahedral starting geometry. The structure for the global minimum of Au_{13} has been the subject of much debate in the literature. This debate centres on whether Au_{13} adopts a 2D or 3D geometry[38–40]. Calculations performed here indicate Au_{13} is indeed highly flexible and further research presented in chapter 7 supports this hypothesis.

It is interesting to observe how the bimetallic particle Au_6Pd_{32} exhibits the greatest affinity for HMF of the 38 atom metal particles investigated. Doping Au into Pd particles in a 1:4 ratio have previously been reported to enhance catalytic activity of hydrogenation of 4-pentenoic acid in comparison to monometallic equivalents[41]. Experimental work by Enache *et al.* report solvent free oxidation of primary alcohols to aldehydes using Au / Pd bimetallic catalysts[42]. As HMF contains a primary alcohol group it is reasonable to suggest this composition may assist with the rate limiting oxidation of the alcohol group. This is however computational speculation and heterogeneous catalyst design is a balance between obtaining significant adsorption levels to facilitate the reaction but not too strong an interaction to prevent any desorption. Data presented here confirm both sub nanometre (Au_{13} and Pd_{13}) and Au_6Pd_{32} particles have significant interaction energies with HMF and therefore future experimental testing is required in order to deduce whether such a strong interaction inhibits or improves the efficiency of a catalyst. From the data presented here the bimetallic Au_6Pd_{32} is the composition proposed as the most suitable catalyst for initial adsorption of HMF.

The preliminary investigation which focussed on the cleavage of the O-H bond proves it is energetically unfeasible for all bare particles investigated. This supports experimental observations from both Davis *et al.*[10] and Gorbanev *et al.* [43] who reported the oxidation of HMF proceeds via oxidation of the aldehyde group then alcohol group. Such a high barrier to cleavage of the O-H group indicates it will not occur with ease on a metal particle and therefore

future studies focusing on the role of the metal / support interface are required in order to determine how these calculated barriers are influenced by the support.

Both Au_{13} and Pd_{13} have been shown to anchor on both reducible (Rutile (110) and Fe_2O_3 (0001)) and reducible (MgO (100)) surfaces. Visual geometry analysis coupled with calculation of cluster rearrangement energies confirm Pd_{13} does not alter geometry to the extent of Au_{13} therefore adding weight to the argument that Au_{13} is highly flexible in nature.

The confirmation of the relative rigidity of Pd_{13} support the use of this cluster geometry in future calculations. The geometry of this particle remains similar upon interaction of HMF and various support materials. In contract Au_{13} significantly alters geometry and therefore the highly ordered Au_{13} cuboctahedral particle may not be a representative model of its true geometry.

The presence of adsorbed oxygen atoms on the metal particle has a destabilising effect on the interaction with HMF. Proximity of the adsorbed HMF to these oxygen atoms does not influence the strength of interaction energies confirming steric factors do not contribute significantly to interaction energies.

Whilst our study is incomplete, the presence of oxygen facilitates the cleavage of the O-H bond by reducing the calculated barrier by 33 kJ mol^{-1} when HMF is adsorbed on the Pd_{13} particle. This significant reduction in barrier height suggests atmospheric oxygen assists with the conversion of HMF to FDCA. There is debate in the literature regarding the role molecular oxygen has with regards to this oxidation[44,45]. The author of this work suggests these preliminary calculations confirm the energetic difficulty of the activation of the O-H bond and any catalyst which can facilitate an energetically viable cleavage would be of great significance for green chemistry. The author of this work also suggests whilst not directly incorporated within the FDCA product, atmospheric oxygen is required to adsorb and dissociate on the particle surface to facilitate proton abstraction and may assist with further C-H cleavage in order to form the aldehyde. To the authors knowledge this is the first suggestion of this type in the literature.

Electronic properties of systems can directly influence catalytic properties. As adsorption is a key requirement in nearly every catalytic process correlation between it and d-band centre has been performed. Using the requirements of the NOVACAM project it is suggested Cu may be a suitable replacement for the Ru / C system for conversion of LA to GVL. Internal discussion suggests the rate limiting step in this conversion is hydrogenation which requires hydrogen to

dissociate. In order to aid dissociation a strong adsorption energy is required and it is well accepted d-band centre levels correlate to adsorption energies. Ru and Ni have a calculated d-band centre higher than copper however it is shown that doping of Ni into bulk Cu can raise this level. This research raises the tantalising possibility of using DFT to fine tune catalyst properties which can aid experimentalists achieve the desired outcome.

References

1. British Plastics Federation. at www.bpf.co.uk last checked July 2016

2. Chheda, J. N., Roman-Leshkov, Y. & Dumesic, J. A. Production of 5-hydroxymethylfurfural and furfural by dehydration of biomass-derived mono-and poly-saccharides. *Green Chem.* **9,** 342 (2007)

3. Bozell, J. J. & Petersen, G. R. Technology development for the production of biobased products from biorefinery carbohydrates—the US Department of Energy's 'Top 10' revisited. *Green Chem.* **12,** 539 (2010)

4. Rosatella, A. A., Simeonov, S. P., Frade, R. F. M. & Afonso, C. A. M. 5-Hydroxymethylfurfural (HMF) as a building block platform: Biological properties, synthesis and synthetic applications. *Green Chem.* **13,** 754 (2011)

5. Wyman, C. E. *Aqueous Pretreatment of Plant Biomass for Biological and Chemical Conversion to Fuels and Chemicals*. (Wiley, 2013). at <https://books.google.co.uk/books?id=XR9MM3zauLUC>

6. Ghorpade, V. & Hanna, M. *Industrial Applications for Levulinic Acid, Cereals.* 49 (1997)

7. *Biofoams: Science and Applications of Bio-Based Cellular and Porous Materials*. (CRC Press, 2015). at <https://books.google.com/books?id=AHe9CgAAQBAJ&pgis=1>

8. Brolly, J. B., Bower, D. I. & Ward, I. M. Diffusion and sorption of CO2 in poly(ethylene terephthalate) and poly(ethylene naphthalate). *J. Polym. Sci. Part B Polym. Phys.* **34,** 769 (1996)

9. Casanova, O., Iborra, S. & Corma, A. Biomass into chemicals: aerobic oxidation of 5-hydroxymethyl-2-furfural into 2,5-furandicarboxylic acid with gold nanoparticle catalysts. *ChemSusChem* **2,** 1138 (2009)

10. DAVIS, S. E., ZOPE, B. N. & DAVIS, R. J. On the mechanism of selective oxidation of 5-hydroxymethylfurfural to 2,5-furandicarboxylic acid over supported Pt and Au catalysts. *Green Chem.* **14,** 143 (2013)

11. Davis, S. E., Zope, B. N. & Davis, R. J. On the mechanism of selective oxidation of 5-hydroxymethylfurfural to 2,5-furandicarboxylic acid over supported Pt and Au catalysts. *Green Chem.* **14,** 143 (2012)

12. Casanova, O., Iborra, S. & Corma, A. Biomass into chemicals: aerobic oxidation of 5-hydroxymethyl-2-furfural into 2,5-furandicarboxylic acid with gold nanoparticle catalysts. *ChemSusChem* **2,** 1138 (2009)

13. Boronat, M. *et al.* Mechanism of selective alcohol oxidation to aldehydes on gold catalysts: Influence of surface roughness on reactivity. *J. Catal.* **278,** 50 (2011)

14. Alonso, D. M., Wettstein, S. G. & Dumesic, J. A. Gamma-valerolactone, a sustainable platform molecule derived from lignocellulosic biomass. *Green Chem.* **15,** 584 (2013)

15. Cao, S., Monnier, J. R., Williams, C. T., Diao, W. & Regalbuto, J. R. Rational nanoparticle synthesis to determine the effects of size, support, and K dopant on Ru activity for levulinic acid hydrogenation to γ-valerolactone. *J. Catal.* **326,** 69 (2015)

16. Jones, D. R. *et al.* The conversion of levulinic acid into γ-valerolactone using Cu–ZrO 2 catalysts. *Catal. Sci. Technol.* **6,** 6022 (2016)

17. Spivey, J. J. *et al. Catalysis*. (Royal Society of Chemistry, 2012). at <https://books.google.co.uk/books?id=ThuA8aT8D-IC>

18. Blöchl, P. E. Projector augmented-wave method. *Phys. Rev. B* **50,** 17953 (1994)

19. Kresse, G. From ultrasoft pseudopotentials to the projector augmented-wave method. *Phys. Rev. B* **59,** 1758 (1999)

20. Kresse, G. & Hafner, J. Ab initio molecular dynamics for liquid metals. *Phys. Rev. B* **47,** 558 (1993)

21. Kresse, G. & Hafner, J. Ab initio molecular-dynamics simulation of the liquid-metal–amorphous-semiconductor transition in germanium. *Phys. Rev. B* **49,** 14251 (1994)

22. Kresse, G. & Furthmüller, J. Efficiency of ab-initio total energy calculations for metals and semiconductors using a plane-wave basis set. *Comput. Mater. Sci.* **6,** 15 (1996)

23. Kresse, G. Efficient iterative schemes for ab initio total-energy calculations using a plane-wave basis set. *Phys. Rev. B* **54,** 11169 (1996)

24. Perdew, J. P., Burke, K. & Ernzerhof, M. Generalized Gradient Approximation Made Simple. *Phys. Rev. Lett.* **77,** 3865 (1996)

25. Perdew, J. P., Burke, K. & Ernzerhof, M. Generalized Gradient Approximation Made Simple [Phys. Rev. Lett. 77, 3865 (1996)]. *Phys. Rev. Lett.* **78,** 1396–1396 (1997).

26. Grimme, S. Semiempirical GGA-type density functional constructed with a long-range dispersion correction. *J. Comput. Chem.* **27,** 1787 (2006)

27. Amft, M., Lebègue, S., Eriksson, O. & Skorodumova, N. V. Adsorption of Cu, Ag, and Au atoms on graphene including van der Waals interactions. (2010). at <http://arxiv.org/abs/1011.1113>

28. Tang, W., Sanville, E. & Henkelman, G. A grid-based Bader analysis algorithm without lattice bias. *J. Phys. Condens. Matter* **21,** 84204 (2009)

29. Sanville, E., Kenny, S. D., Smith, R. & Henkelman, G. Improved grid-based algorithm for Bader charge allocation. *J. Comput. Chem.* **28,** 899 (2007)

30. Henkelman, G., Arnaldsson, A. & Jónsson, H. A fast and robust algorithm for Bader decomposition of charge density. *Comput. Mater. Sci.* **36,** 354 (2006)

31. Gaussian 09 Citation. at <http://www.gaussian.com/g_tech/g_ur/m_citation.htm>

32. Rautiainen, S. Selective Oxidation Of Alcohols And Aldehydes With Gold Nanoparticle Catalysts (2016)

33. Mills, G., Jónsson, H. & Schenter, G. K. Reversible work transition state theory: application to dissociative adsorption of hydrogen. *Surf. Sci.* **324,** 305 (1995)

34. Hannes Jónsson, G. M. K. W. J. Nudged Elastic Band Method for Finding Minimum Energy Paths of Transitions Chapter 16.

35. Hammer, B. & Norskov, J. K. Why gold is the noblest of all the metals. *Nature* **376,** 238 (1995).

36. Campbell, J. M. & Campbell, C. T. The dissociative adsorption of H2 and D2 on Cu(110): activation barriers and dynamics. *Surf. Sci.* **259,** 1 (1991)

37. Yang, H. & Whitten, J. L. Dissociative adsorption of H2 on Ni(111). *J. Chem. Phys.* **98,** 5039 (1993)

38. Longo, R. & Gallego, L. Structures of 13-atom clusters of fcc transition metals by ab initio and semiempirical calculations. *Phys. Rev. B* **74,** 193409 (2006)

39. Wang, J., Wang, G. & Zhao, J. Density-functional study of Aun(n=2–20) clusters: Lowest-energy structures and electronic properties. *Phys. Rev. B* **66,** 35418 (2002)

40. Shafai, G., Hong, S., Bertino, M. & Rahman, T. S. Effect of Ligands on the Geometric and Electronic Structure of Au 13 Clusters. *J. Phys. Chem. C* **113,** 12072 (2009)

41. Yoshiteru Mizukoshi, Taku Fujimoto, Yoshio Nagata, Ryuichiro Oshima, and & Maeda, Y. Characterization and Catalytic Activity of Core−Shell Structured Gold/Palladium Bimetallic Nanoparticles Synthesized by the Sonochemical Method. (2000)

42. Enache, D. I. Edwards, J. K, Landon, P. Solsona-Espiriu, B. Carley, A.F. Herzing, A. Watanabe, M. Kiely, C.J. Knight, D.W, Hutchings, G. J. Solvent-free oxidation of primary alcohols to aldehydes using Au-Pd/TiO2 catalysts. *Science* **311,** 362 (2006)

43. Gorbanev, Y. Y., Klitgaard, S. K., Woodley, J. M., Christensen, C. H. & Riisager, A. Gold-catalyzed aerobic oxidation of 5-hydroxymethylfurfural in water at ambient temperature. *ChemSusChem* **2,** 672 (2009)

44. Zope, B. N., Hibbitts, D. D., Neurock, M. & Davis, R. J. Reactivity of the gold/water interface during selective oxidation catalysis. *Science* **330,** 74–8 (2010)

45. Mallat. T. & Baiker, A. Oxidation of Alcohols with Molecular Oxygen on Solid Catalysts, *Chem*. *Rev* **104,** 3037 (2004)

Chapter 7

Oxygen Vacancy Defects on Metal Particle Supported Fe_2O_3

This chapter presents an investigation of oxygen defects on both a pure (0001) α-Fe_2O_3 surface and one in which metal particles containing 10 atoms of various compositions have been supported. To perform this study a comprehensive discussion of the different methods of modelling support materials will be presented. As a follow up to the primary investigation a subsequent study into flexibility of small gold particles will be discussed along with implications of this flexibility within catalysis and computational modelling.

7.1 Introduction

Iron oxides have widespread industrial usage not limited to metal production. These oxides have usage in pigmentation[1], magnetic recording[2] and medicine[3]. In the catalysis industry Iron oxides are primarily used as support materials with gold supported on α-Fe_2O_3 reported to catalyse oxidation reactions[4]. One such oxidation reaction of vital importance to industry and the environment is the oxidation of CO to CO_2.

One of the functions of the three-way catalyst found in vehicle catalytic converters is to perform such an oxidation. These oxidations however have been plagued with a problem arising from the temperature in which these catalysts need to reach in order for this oxidation to occur. In order to reduce the temperature of these "light off" values, research has been performed on a variety of metal and metal support materials in order to deduce which combination can effectively lower the light off temperature making the catalyst more efficient and environmentally friendly.

Both gold and palladium nanoparticles have been reported to catalyse the low temperature oxidation of CO to CO_2. Whilst Au catalysts are excellent low temperature catalysts for this oxidation Pd catalysts are reported to have a higher turnover frequency therefore being of interest in industrial catalysis[5].

It is widely accepted for this low temperature CO oxidation to occur through gold particle catalysis a particle diameter of less than 5 nm is required for optimal activity[6]. Recent advances within characterisation techniques however have deduced it is likely much smaller particles within the sub-nanometre region are the active species for this low temperature CO oxidation when supported on Fe_2O_3[7]. These active particles contain approximately 10 gold atoms corresponding to a diameter of 0.5 nm. DFT studies performed by Hutchings and co workers[7] support this observation confirming the ability of subnanometre supported Au_{10} to catalyse this oxidation reaction.

The role of the support in these catalysed oxidation reactions has been the subject of much discussion within the literature and is presented in more detail in chapter 2.

Fe_2O_3 is classed as an active support and demonstrated to adsorb large quantities of O_2 during CO oxidation reactions[8]. Studies by Norskov *et al* suggest the surface of the support may encourage nucleation of Au particles through oxygen vacancy defects[9]. For CO oxidation it has been proposed surface bound lattice oxygen on CeO_2 may be incorporated within CO to form CO_2, this mechanism has been proposed by Henklemen *et al*[10] and raises the possibility of other oxidation mechanisms using different supports to follow a similar route. Further studies by Illas *et al* indicate surface oxygen defects on CeO_2 are facilitated by supported Pt_8[11]. These observations have generated interest in pursuing these mechanisms further and therefore a detailed study of the energetics of removal of surface bound oxygen on a Fe_2O_3 (0001) surface are presented on both a bare surface and one in which a metal particle containing 10 palladium atoms. To investigate other compositions of metal particle this palladium cluster was sequentially doped to Au_{10} with oxygen vacancy defect energies in the surface of the Fe_2O_3 support calculated at each composition. To the authors knowledge these are novel calculations and provide insight into bimetallic influence on surface oxygen defect energies. These calculations provided an interesting observation in which it became apparent that supported Au rich particles exhibit a high degree of flexibility once a defect site is created on the surface of the iron oxide. This observation initiated subsequent investigation of geometric preference for gold particles which is discussed later in this chapter.

The geometry and global minimum of subnanometre particles such as Au_{10} which are presented in this chapter have been subject to substantial debate within the literature. Through DFT studies neutral Au_n particles are reported to adopt a planar structure up until n=11[12]. This

proposal however is subject to debate as Au_{13} has also been proposed as having a 2D structure as its minimum energy structure[13]. Further literature investigation leads to the conclusion that no such consensus exists regarding the global minima energy structure of Au_{13}. To date it is proposed it can adopt an icosahedral[14], buckled biplaner[12] and cuboctahedral geometries[15]. In this work we will add to the literature debate regarding flexibility of these nanometre particles and believe the evidence obtained demonstrating flexibility of supported Au_{10} justifies further research, which is presented via a comprehensive molecular dynamics confirmation search.

7.2 Computational Details

All calculations were performed using the Vienna Ab initio Simulation Package (VASP)[16–19]. As detailed in chapters 5 and 6 a plane wave cutoff (E_{ncut}) of 500 eV has been used for all calculations. For calculations solely containing metal particles a 25Å^3 periodic box along with (Monkhorst-Pack KPOINT sampling mesh was used to prevent spurious self-interactions between images. Calculations were performed using the generalized gradient approximation (GGA) using Perdew, Burke and Erzerhof (PBE) functional[20,21]. Projector Augmented Wave method (PAW)[22,23] pseudopotentials were used to treat all atoms. Due to the strongly correlated d-states in iron DFT+U was used following Dudarev's method ($U_{eff} = U - J$)[24]. Previous work by Willock *et al*[25] has deduced a value of U = 4.0 produces calculated values of bulk moduli, lattice parameters and band gap in good agreement with their experimentally determined counterparts. To model the Fe_2O_3 surface a four-layer slab was obtained via a supercell of bulk Fe_2O_3 cleaved to form a (0001) surface. The bottom 2 layers of the slab were fixed to represent bulk rigidity leaving the top layer fully relaxed. Having two layers fully relaxed greatly reduces computational expense and allows for a systematic study of defect energies. Discussion of the modelling of surfaces will be presented in 7.2.1. In bulk Fe_2O_3 iron formally is Fe^{3+} which corresponds to a d^5 configuration. This high spin state has been accounted for by initially setting a magnetic moment (using the MAGMOM feature of VASP) to which is in an alternating sequence of +--++--+ for the iron layers. Such an ordering ensures the overall magnetic moment across the slab is zero. A dipole correction has been applied perpendicular to the surface along with a vacuum gap of 25Å ensuring no self-interaction energies occur in the z direction. Such a large vacuum gap is required as these surfaces will have metal particles supported on them. As the unit cell is large it is deemed KPOINT sampling is sufficient as the reciprocal lattice sufficiently

small. The Pd_{10} particle used here is obtained from a face centred cubic bulk lattice gold and is a (7,3) bilayer structure with atoms substituted to Pd. Upon adsorption and geometry relaxation this geometry chances significantly.

Oxygen defect energies are calculated using equation 7.1. E_{defect} is the oxygen vacancy defect energy, $E(Pd_{10}/Fe_{72}O_{108})$ is the calculated energy of the Pd_{10} in contact with the non-defect iron oxide slab system, $E(Pd_{10}/Fe_{72}O_{107})$ is the energy of the slab system with one oxygen atom removed from the surface and $E-O_2$ is half the energy of triplet O_2 calculated in a periodic box the same size as the Fe_2O_3 slab.

$$E_{defect} = E(Pd_{10}/Fe_{72}O_{107}) - E(Pd_{10}/Fe_{72}O_{108}) - E-O_2 \quad (7.1)$$

As the Pd_{10} particle was sequentially doped *x* has been used to denote the number of palladium atoms present in the particle with 10-*x* being the number of Au atoms in the 10 atom particle.

Bader charge analysis was performed to deduce charges upon adsorption, this method was developed by Henkelman *et al*[26–28]. The sampling mesh for this analysis is spaced at 0.033 Å per sample point in each direction corresponding to NGXF = 458, NGYF = 458, NGZF = 1010 in the VASP INCAR parameter file.

All molecular dynamics calculations were performed using the VASP program which utilises Born-Oppenheimer dynamics in which each geometric movement of the atoms is accompanied by instantaneous electronic relaxation. Each geometric movement is accompanied by an electronic relaxation comprising of 30 iterations. The total simulation time is 30 picoseconds with a 3 femtosecond time step. This time step was chosen as a frequency characterisation calculation confirmed a typical Au-Au stretch in the cuboctahedral Au_{13} particle occurs at approximately 230 fs therefore a 3 femtosecond time step enables for a molecular dynamics run accounting for all vibrational modes. All simulations were performed at 500K using the Nosé-Hoover thermostat. Calculations were performed in a periodic box as described above with Gaussian smearing of 0.05. Analysis of the molecular dynamics calculations was performed using the in-house developed analyse_hist and inter_vasp codes.

7.2.1 DFT Modelling of Surfaces

In heterogeneous catalysis a multitude of different surfaces are often employed to support metal particles. These surfaces can act as more than a mere support. It is reported a surface can aid catalysis through charge transfer between support and metal particle[29] or through a Mars van Krevelen type mechanism[10]. Accurate modelling of a support is vital to ensure calculated properties / reaction pathways are an accurate reflection of a catalytic process.

The computational modelling of such surfaces can be of great expense due to the many degrees of geometric freedom present with full slab relaxations coupled with the multitude or electronic states that have to be simulated if a cell containing several hundred atoms is used. As a result, compromises are made within the calculation. One such method commonly employed in the DFT modelling of surfaces is the fixing of layers of the model slab. This is discussed in more depth in chapter 4. Fixing of all but a few layers can dramatically reduce computational cost and also mimic bulk behaviour observed experimentally. The relatively small particle size usually means the surface is a termination of a large amount of the bulk support material therefore fixing the fixing of layers mimics bulk behaviour. In order to determine a suitable method to model the slab preliminary calculations were performed on a model TiO_2 system which was chosen due to its highly prevalent usage within catalysis along with substantial literature available as a comparison.

7.2.2 Preparation of Bulk Anatase

Using an initial (1 KPOINT sampling mesh coupled with the PBE functional a unit cell of Anatase and Rutile were taken and geometry optimised over a $\pm$ 5% expansion range at 0.5% increments. This resulted in 20 structures generated at within this range. From these calculations both volume and total energy in eV were obtained and plotted against each other.

As discussed in chapter 4 a $\pm$ 5% expansion of the unit cell can be used to calculate a bulk modulus. This is achieved by obtaining the coefficients from plotting a quadratic curve to the energy vs volume plot. This procedure has been repeated over a KPOINT sampling sweep and is used to determine suitable sampling for these bulk systems. Figure 7.1 reports bulk modulus plotted against KPOINT sampling for the bulk Anatase cell.

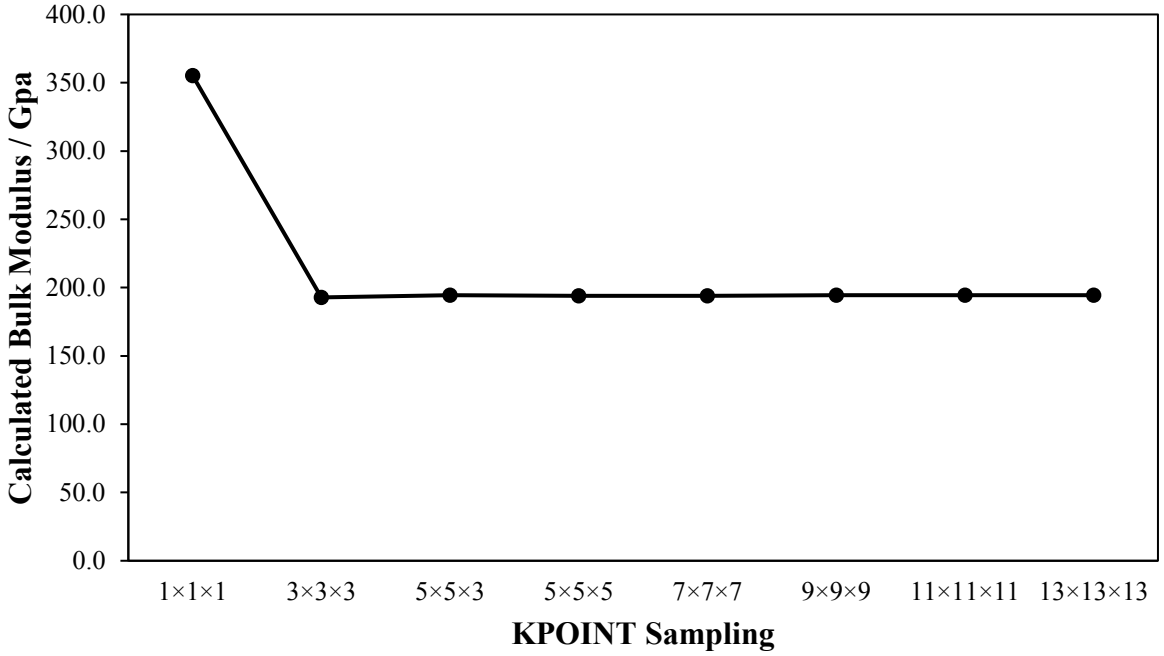

Figure 7.1: KPOINT sampling vs calculated bulk modulus for a bulk Anatase unit cell.

The experimentally determined bulk modulus for Anatase is 178 $\pm$ 1 GPa[30]. Figure 7.1 clearly indicates bulk modulus converges to 2.5 GPa range from using a sampling mesh of KPOINTS or larger. Using a KPOINT sampling mesh the bulk modulus calculated is within 16 GPa of the experimentally determined value and is computationally more efficient as the sampling mesh has been reduced in the Z direction corresponding to the larger size along this axis. Along with bulk modulus comparison, the lattice parameters can be compared to literature and are presented in table 7.1. This data is within good experimental agreement with a 1% deviation from experimentally determined values.

Table 7.1: Calculated lattice parameters for a unit cell of Anatase compared with literature.

	Calculated Lattice Parameter / Å	Literature Value[31] / Å
a	3.776	3.782
b	3.776	3.782
c	9.486	9.502

The data obtained and presented in figure 7.1 and table 7.1 confirm a sampling mesh of is suitable for the investigation of Anatase and this will be used for all surface modelling calculations.

7.2.3 Preparation of Bulk Rutile

Using the same method described in 7.2.2 a cell of bulk rutile has been subject to a ± 5% expansion to determine the bulk modulus at each KPOINT sampling mesh. Figure 7.2 contains calculated bulk modulus plotted against KPOINT sampling.

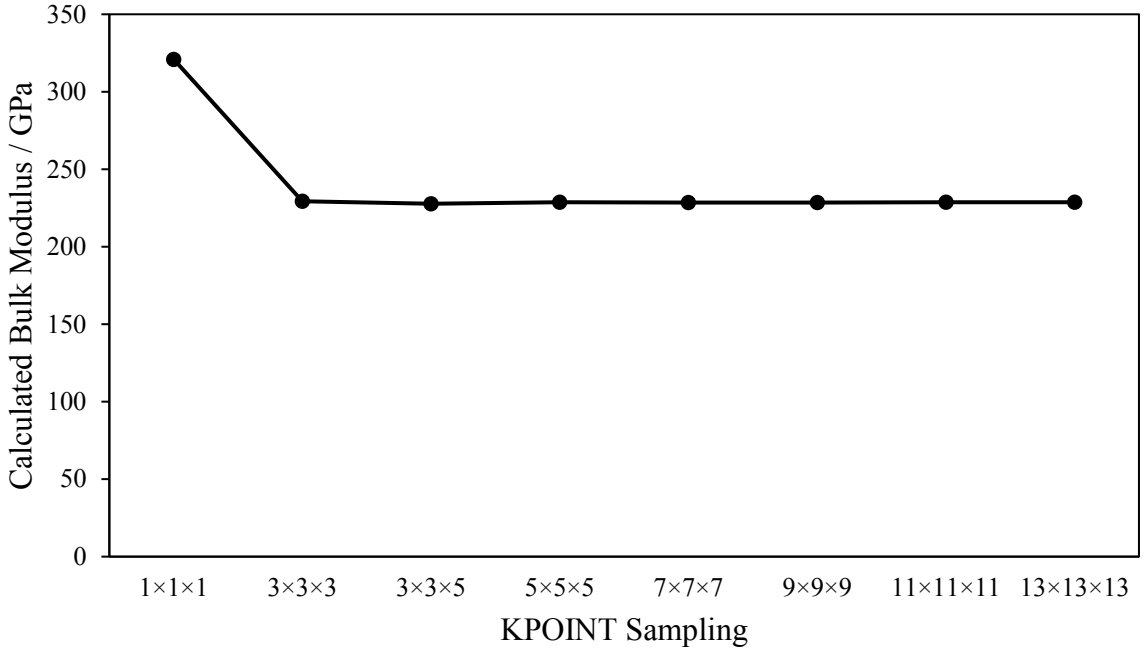

Figure 7.2: KPOINT sampling vs calculated bulk modulus for bulk Rutile unit cell.

The experimentally determined bulk modulus for Rutile is 210 GPa[32] The data presented in figure 7.2 indicates bulk modulus does not fluctuate more than 2 GPa using a KPOINT sampling mesh of and higher. As both X and Y lattice parameters within bulk rutile are larger than the Z parameter the KPOINT sampling has been adjusting accordingly to which produces a bulk modulus of 227 GPa. Whilst this is 17 GPa higher than experimentally determined values it is within a 10% error which is determined to be permissible for these calculations as DFT often will produce physical properties within this range of error compared to experimentally determined values. The calculated bulk modulus is in excellent agreement with previous DFT GGA calculations performed by Perron *et al* who

have a calculated GGA (PAW10) bulk modulus to be 217 GPa[33]. The lattice parameters calculated from this optimised bulk Rutile system are presented in table 7.2 along with an experimental comparison.

Table 7.2: Calculated lattice parameters for a unit cell of Rutile compared with literature.

	Calculated Lattice Parameter / Å	Literature Value[34] / Å
a	4.594	4.584
b	4.594	4.584
c	2.959	2.953

Whilst the calculated bulk modulus lies within an experimental error of approximately 10% the lattice parameters calculated are in excellent agreement with experimentally determined values of less than 1% deviation. This data indicates KPOINT sampling is appropriate for modelling bulk Rutile and will be used for all calculations performed in this chapter.

7.2.4 Surface Energies for Anatase (100)

A supercell of bulk Anatase was obtained by taking the optimised unit cell and scaling up accordingly. This supercell was used to cleave a (100) surface (figure 7.3) with various slab thicknesses.

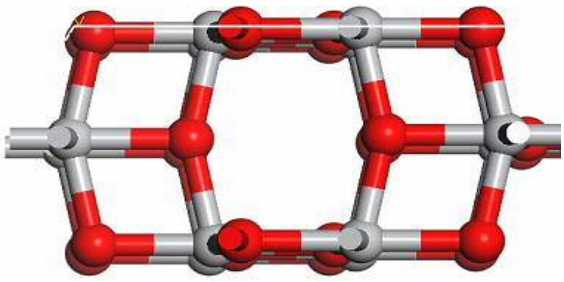

Figure 7.3: Surface termination of a 3 layer (100) Anatase slab. Red atoms are used to represent Oxygen and grey atoms represent Titanium.

Each slab of various thickness was created with a 15 Å vacuum gap to ensure no spurious self-interactions occur between periodic images along the Z direction. As KPOINTS operate in

reciprocal space the Z direction KPOINT was reduced to 1 in all calculations. Using equation 7.2 surface energies were calculated at each slab thickness. E_{surf} is the calculated surface energy in J m^{-2}, E_{slab} is the total energy of the slab in eV, n is the scaling factor of number of atoms within the slab divided by number of atoms within the unit cell, E_{bulk} is the energy of one-unit cell and S is the surface area in m^2.

(7.2)

Figure 7.4 contains calculated surface energies for (100) Anatase of various slab thicknesses. Contained within figure 7.4 a comparison of the below three distinct methods of optimisation are presented:

1) Full relaxation of the slab – every atom within the slab system is free to move during optimisation.
2) Middle layer fixed – For modelling of odd number layered slabs in which the middle layer only is fixed and every other atom is free to relax during optimisation.
3) Top 2 layers free to relax only.

Both methods 1 and 2 have a surface on the top and bottom of the slab which is free to relax and therefore only equation 7.2 is applicable as it accounts for two relaxed surfaces in the denominator. By fixing all but the top two layers within method 3 only one surface is free to relax and therefore must be accounted for whilst calculating surface energies. Equation 7.3 details the method for surface energy calculation for systems using method 3. is the surface energy in J m^{-2}, E_{slab} is the total energy of the slab in eV, n is the scaling factor which is obtained from the fraction of atoms within the slab to the bulk unit cell, E_{bulk} is the energy of the bulk unit cell, S is the surface area in m^2 of the slab surface which is free to relax and is the single point energy of the slab system.

(7.3)

Calculated surface energies using these three methods are presented in figure 7.4.

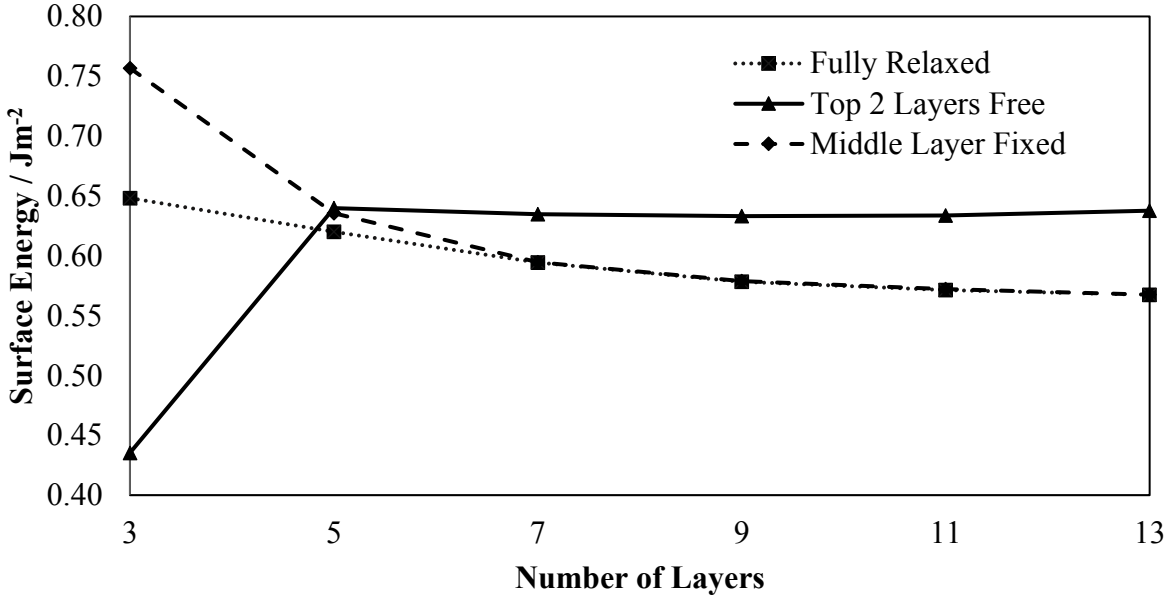

Figure 7.4: Surface energies for Anatase (100) obtained through three different methods.

Calculated surface energies detailed in figure 7.4 present an interesting observation in which having a middle layer fixed does not affect calculated surface energies with respect to fully relaxed systems with more than 3 layers. A middle layer which is fixed within a three-layer slab produces surface energies 0.10 Jm^{-2} higher than fully relaxed structures. As the slab thickness increases surface energies reduce and converge with fully relaxed values. At 13 layers for both middle layer fixed and fully relaxed systems the surface energies calculated indicate convergence is not yet met. This is due to slowly decreasing values calculated however they do not appear to have reached stable flat line level indicating convergence. For the systems in which the top two layers are free to relax it is interesting to observe an opposite trend in which converge after the slab reaches five layers. In this case convergence is deemed to have been met as surface energies calculated beyond 5 slab layers do not fluctuate in value more than 0.02 J m^{-2}. The converged surface energies calculated using the method of top two layers free to relax deviate from fully relaxed values with a maximum of 0.07 J m^{-2}, indicating suitability of this method.

Previous work by Pastrello *et al* employing a DFT/B3LYP hybrid functional using CRYSTAL06 obtained a surface energy of 0.55 J m^{-2} for Anatase (100)[35]. This is in good agreement with all three methods employed here.

Whilst accuracy is paramount within any DFT calculation it often has to be balanced with computational expense. For each of the methods presented in figure 7.4 the CPU time has been

obtained and is plotted in figure 7.5. This plot clearly indicates adopting a method in which the middle layer only is fixed will cause CPU time to be greater than the other two methods. At its greatest CPU time is 10000 seconds higher using this method confirming it is computationally more expensive than the other methods used. It is interesting to observe very similar CPU times are required using a fully relaxed and top two layers free method. At its maximum using a fully relaxed method will require 5000 seconds more CPU time than the top two layers free method.

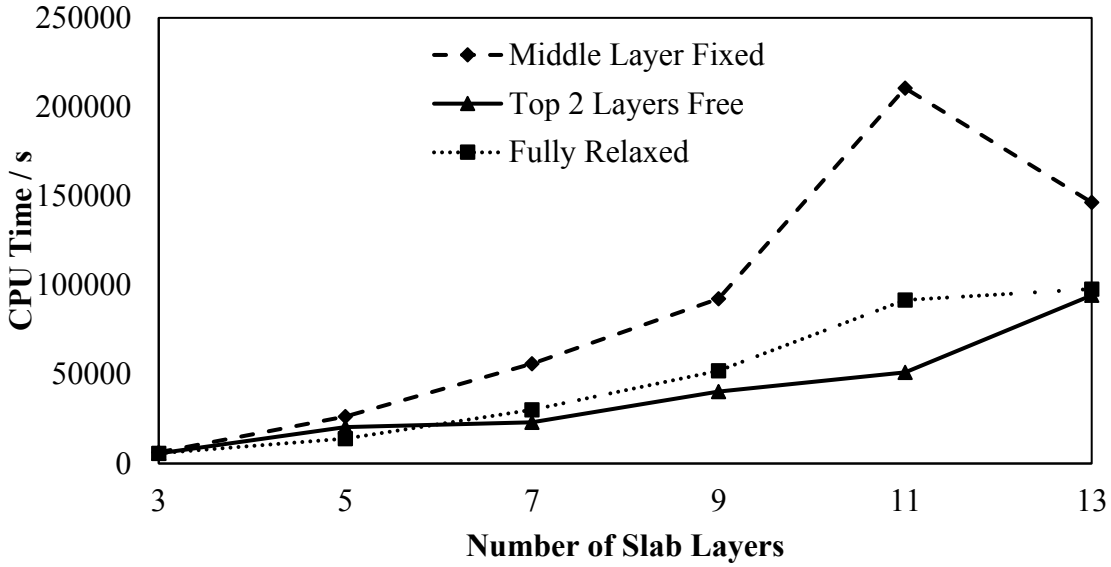

Figure 7.5: Comparison of CPU times for slab calculations using the three different methods.

7.2.5 Surface Energies for Rutile (110)

A supercell of bulk Rutile was obtained by taking the optimised unit cell and scaling up accordingly. This supercell was used to cleave a (110) surface (figure 7.6) with various bridging oxygen terminated tri-layer slab thicknesses.

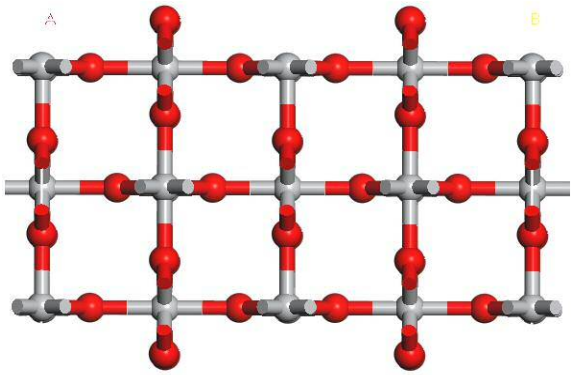

Figure 7.6: Surface termination of a 3 layer (110) Rutile slab. Red atoms are used to represent Oxygen and grey atoms represent Titanium.

Using KPOINT sampling along with a 15 Å vacuum gap, the surface energies for (110) Rutile were computed using methods 2 and 3 described in 7.2.4. The results are contained in figure 7.6.

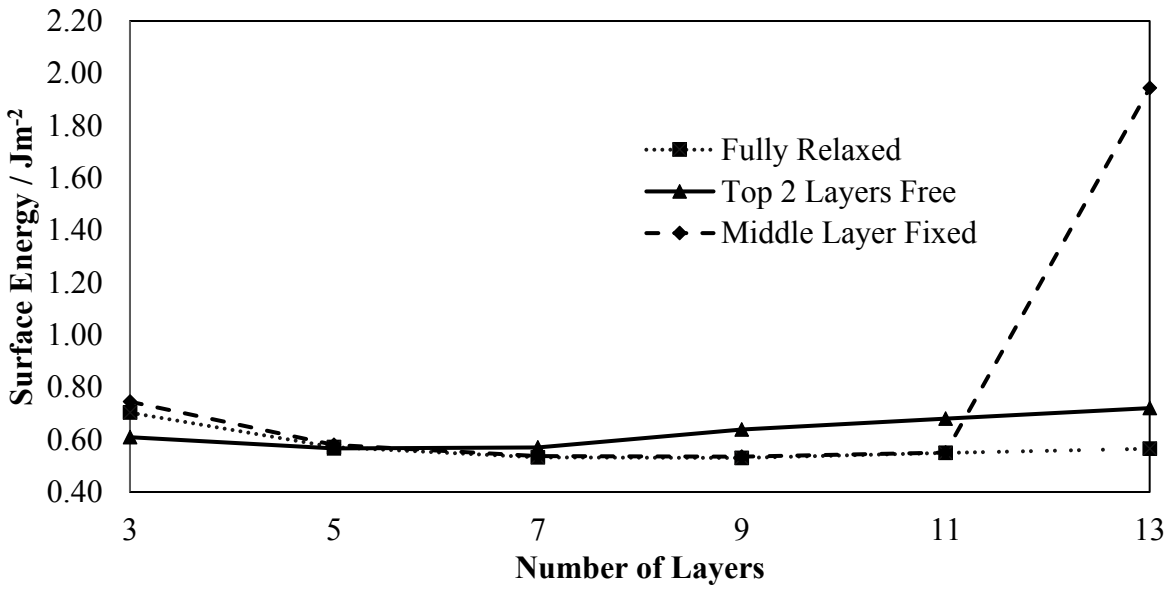

Figure 7.6: Surface energies for Rutile (110) obtained through three different methods.

The calculated surface energies presented in figure 7.6 confirm up to an 11-layer slab thickness the three methods produce surface energies within 0.18 Jm^{-2} of each therefore. For a 13 layered slab with a middle layer fixed a surface energy 1.2 J m^{-2} is produced which is higher than the other methods indicating either an error within the VASP calculation or this method is unsuitable for use in modelling rutile (110). Further replication of this data point is required in order to ascertain the reason for such an anomaly, however due to time constraints has not been performed and therefore is not presented in this chapter. Similar to the data presented in figure 7.5 the top two layers fixed and fully relaxed methodologies produce calculated surface energies with a maximum deviation of 0.02 Jm^{-2} at all thicknesses clearly indicating little deviation in calculation outcome using these different methods.

DFT investigations by Perron *et al* conclude surface energies for Rutile (110) depend on the number of layers used in the slab. Internal constraints were added and through these restrictions surface energies stabilised[33]. Using GGA (PAW4) a surface energy of 0.60 J m^{-2} is reported which is in excellent agreement with values obtained using method two.

CPU times were obtained from each calculation method (figure 7.7). This data indicates similar CPU times for all three methods however this diverges at 13 slab layers where having the top two layers free drastically reduces CPU time from 120000 seconds in the fully relaxed system to 51000 seconds which conclusively determines this method is the most computationally efficient for modelling rutile (110). These calculations were performed using HPC Wales Swansea Sandy Bridge centre. All calculations were performed in parallel using 6 computing nodes comprising of 16 cores per node.

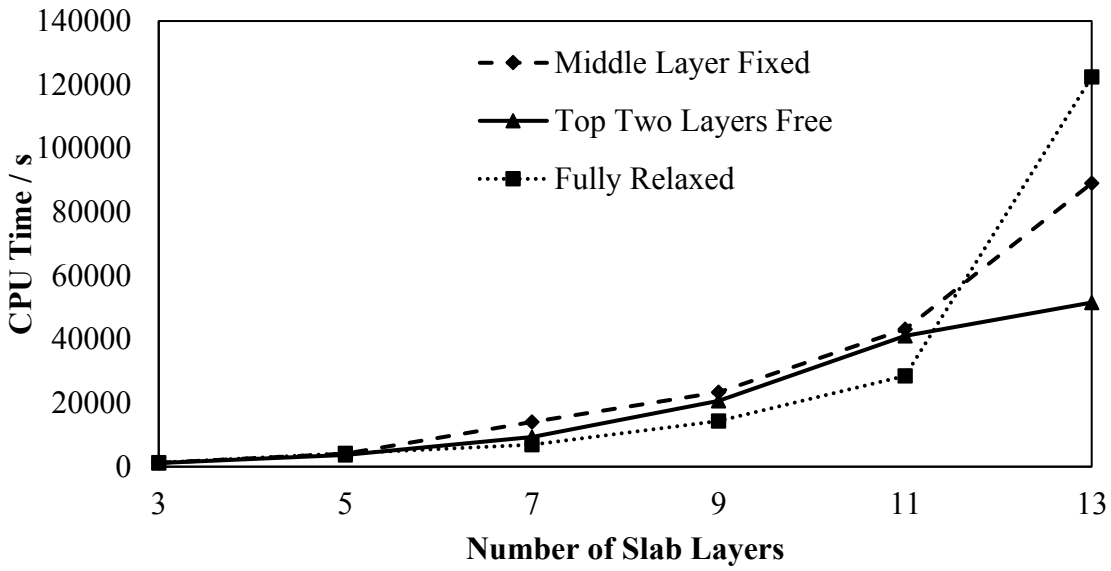

Figure 7.7: Comparison of CPU times for slab calculations using the three different methods

For Anatase (100) and Rutile (110) it is concluded that adopting a method in which the top two layers are free and every other layer fixed is the best trade-off between computational cost and accuracy in calculated surface energies. This method will be used for all calculations presented in this chapter unless otherwise specified.

7.3 Surface Oxygen Defect Energies

Pd_{10} was placed over the centre point on the surface of the Fe_2O_3 (0001) slab with an initial placement at a vertical distance of 2 Å from the surface. A multitude of initial adsorption positions are possible however due to computational cost only this initial adsorption mode has been modelled for this work. The system was then geometry optimised (figure 7.8) using conditions described in 7.2. Once this base structure was optimised surface bound oxygen atom in each location in Fe_2O_3 was removed and the newly defected system optimised to allow for a calculation of oxygen vacancy defect energies (according to equation 7.1). Before removal of this oxygen atom a measurement was taken between it and the nearest atom in the metal particle. Figure 7.9 details calculated defect energies for this Pd_{10}/Fe_2O_3 system accompanied by distance measurements.

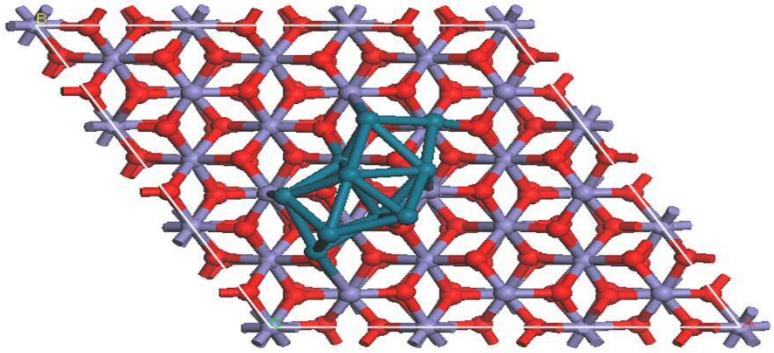

Figure 7.8: Geometry optimised Pd_{10}/Fe_2O_3 system. Iron atoms are represented in purple, oxygen red and palladium blue.

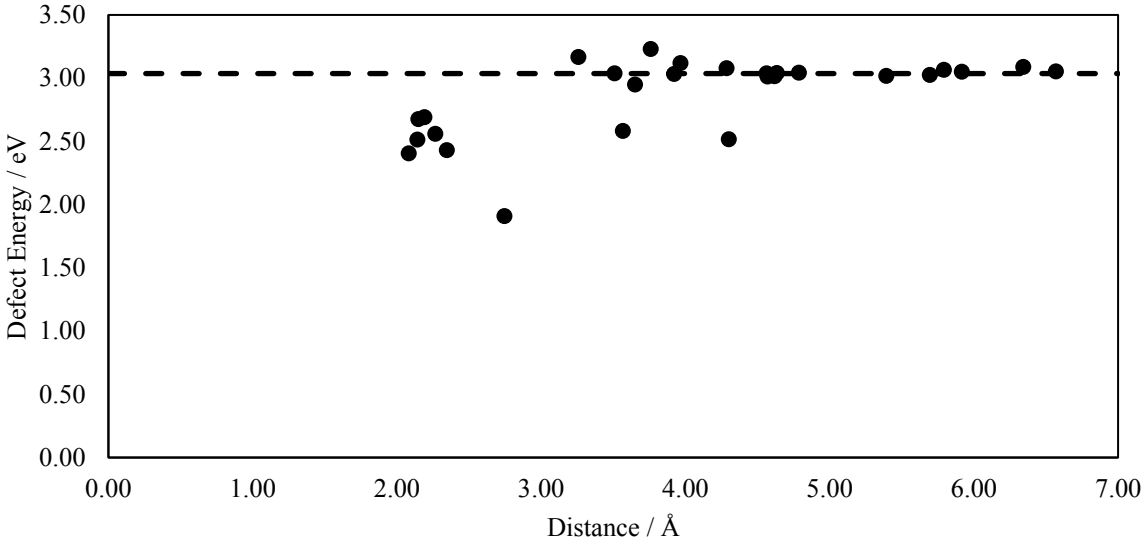

Figure 7.9: Oxygen vacancy defect energy in eV plotted against the defect site distance from the nearest atom in the metal particle. The dashed line indicates defect energy on a bare (0001) Fe_2O_3 surface which is determined to be 3.02 eV.

It should be noted the calculated reference energy is in excellent agreement previous unpublished calculations by Hoh *et* al. Figure 7.9 indicates that at a distance greater than 4.1 Å from the metal particle the presence of supported Pd_{10} has no influence on calculated defect energies. At these sufficiently large distances calculated defect energies are within 0.1 eV of the reference defect energy therefore indicating particle influence is negligible. It is interesting to observe at closer distances (<3.0 Å) defect energies decrease to less than the reference defect

energy clearly indicating the presence of the supported particle decreases the energy required to remove a surface bound oxygen atom. The implications of such an observation is certainly of interest within mechanisms where the support may act as a supply of oxygen.

Palladium particles are often alloyed with gold to tune and enhance catalytic properties. For example alloys are reported to be more active in 1,3-cyclooctadiene hydrogenation compared to either pure gold or palladium[36]. Similarly DFT studies by Peng *et al* also suggest alloying gold with palladium may enhance catalytic activity for CO oxidation[37]. The difference in catalytic properties between pure and bimetallic particles is often attributed to electronic differences between metals. Whilst these electronic differences have been investigated in depth, the influence of such bimetallic particles if any on surface oxygen defect energies is less understood. It is therefore of catalytic interest to investigate how these alloys influence oxygen vacancy defect energies on the (0001) surface of α-Fe_2O_3.

7.3.1 Sequential doping of Pd_{10} to Au_{10}

Taking the optimised structure of Pd_{10}/Fe_2O_3 as a start structure an Au atom was exchanged with one Pd atom in the particle. As symmetry is broken there are 10 possible substitution positions. Each of these substitutions was geometry optimised with energies used to determine the thermodynamic preference for substitution position. The most thermodynamically favourable substitution was taken and as a new structure for investigation of iron oxide surface oxygen removal. This process was repeated until Pd_{10} was sequentially doped to Au_{10}. Figure 7.10 highlights the total energy change from Pd_{10} to Au_{10} via the lowest energy pathway.

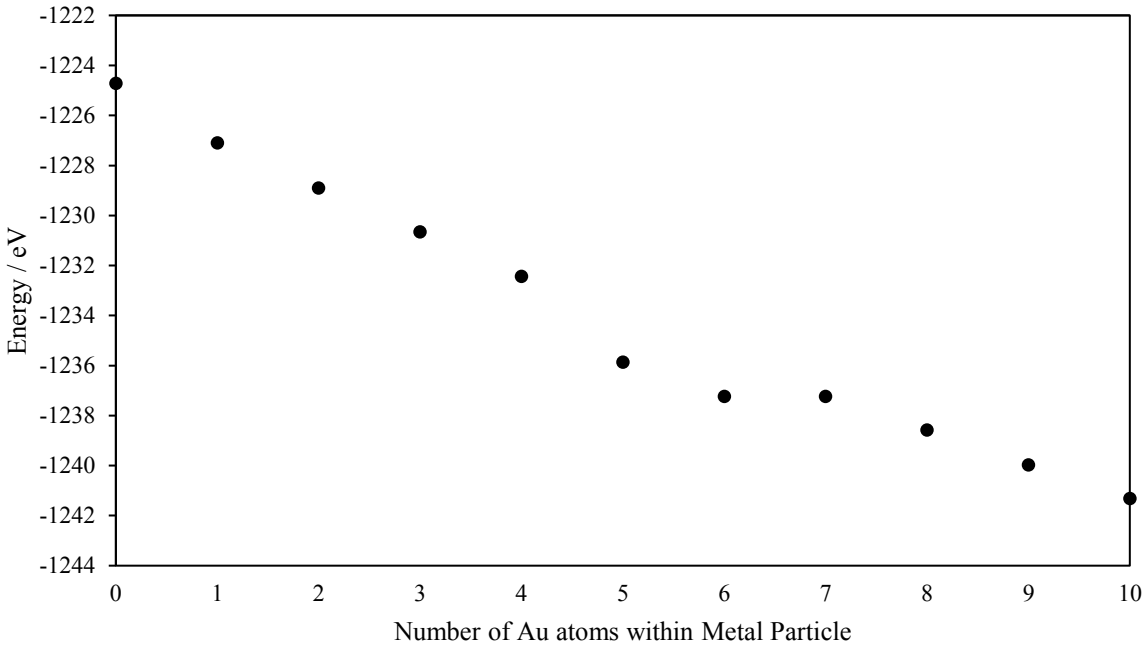

Figure 7.10: Total energies of cluster + slab system vs number of Au atoms in metal particle. Zero Au atoms corresponds to Pd_{10} and ten Au atoms corresponds to full substitution (Au_{10})

The thermodynamic route to complete substitution presented in figure 7.10 is not suitable for comparative analysis due to the different compositions of the metal particle. Instead the difference between calculated energies and the bare slab + (nAu + mPd) have been performed, n is the number of Au atoms in the supported particle subtracted from 10 and multiplied by the energy of an isolated Au atom in a periodic box of the same size and m is the same but for Pd.

A worked example is the Au_1Pd_9 supported metal particle:

Using this method all systems are referenced to the energy of both 10 Au and Pd atoms. Data from this analysis is presented in figure 7.11.

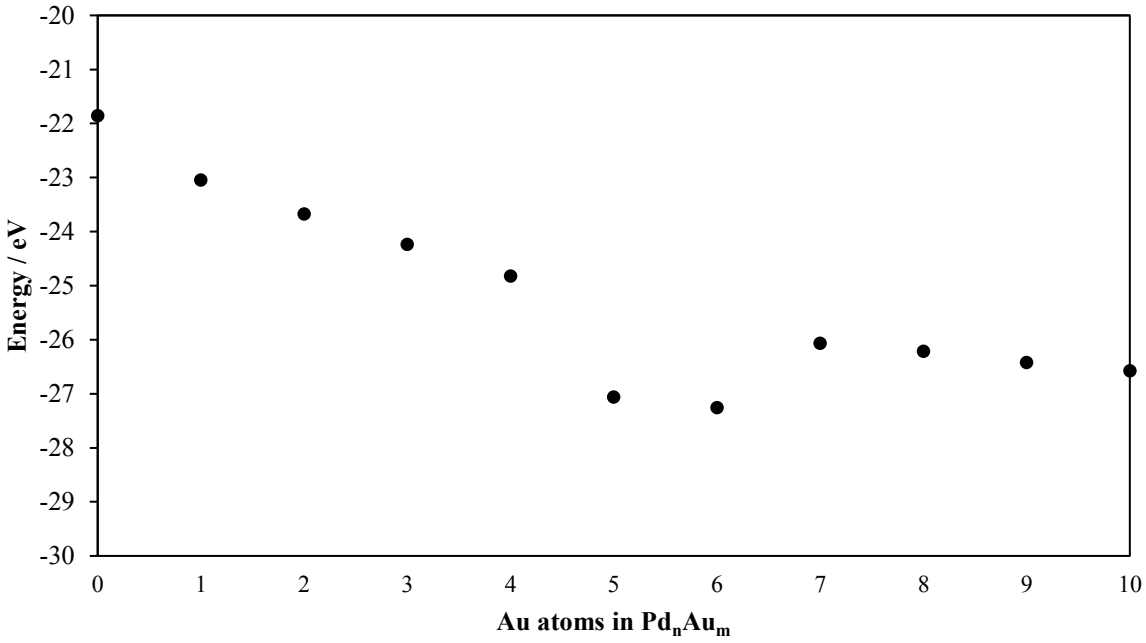

Figure 7.11: The difference between energies of the cluster slab system and the isolated components of the system (slab, nAu + mPd). A negative sign on the energy indicates it is thermodynamically preferred for the system to be in a combined state than isolated components.

Data contained in figure 7.11 clearly indicate it is thermodynamically more preferable to have a metal particle adsorbed on the Fe_2O_3 surface than isolated components. This is due to the large difference in energy (at least 22 eV) between adsorbed state and isolated components. It is interesting to observe this energy gap increases to a maximum at the Au_6Pd_4 composition where the system is 27.3 eV lower in energy than the isolated components. Data obtained above suggests this composition is particularly stable and may be a significantly important ratio for catalysis.

Substitution of an Au atom into Pd_{10} has numerous possibilities with the thermodynamically most favourable substitution reported in figure 7.10. Figure 7.12 depicts the range in total energies of the system which can arise per substitution. It reports the highest energy calculated per cluster composition which is set relative to the thermodynamically most favourable particle within the set cluster composition.

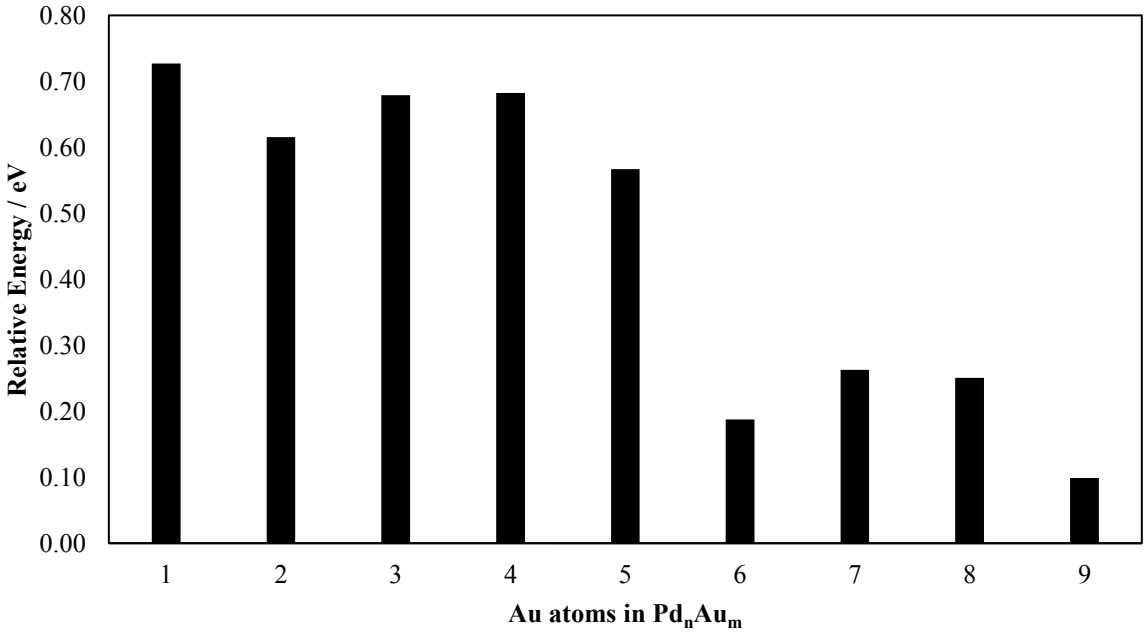

Figure 7.12: Range of total energies obtained at each substitution position. Only one configuration exists for both Pd_{10} and Au_{10} therefore no range is present here. Energies are reported relative to the lowest energy configuration for the combination.

The energy differences between each configuration is clearly significantly large (~0.7 eV) for substitution of one Au atom within Pd_{10}, this clearly indicates clearly there exists a favoured thermodynamic substitution position of Au within clusters containing high percentage Pd atoms. As the cluster becomes more substituted less substitution positions exist and therefore the range in energies observed decreases indicating at higher Au content the preference for substitution decreases.

In order to account for the differences in energy which are dependent upon the substitution preference, a thorough analysis has been performed to ascertain the makeup of the configurations of the substituted metal particles and deduce whether a trend exists between this and the relative energies of the system. For each configuration the number of Au-Au, Au-Pd and Pd-Pd interactions below 3 Å were counted and this data is presented per cluster composition in figure 7.13. For Au_1Pd_9 there are 10 configurations and 10 sets of measurements, as the substitution to Au_{10} increases the number of data sets decreases accordingly.

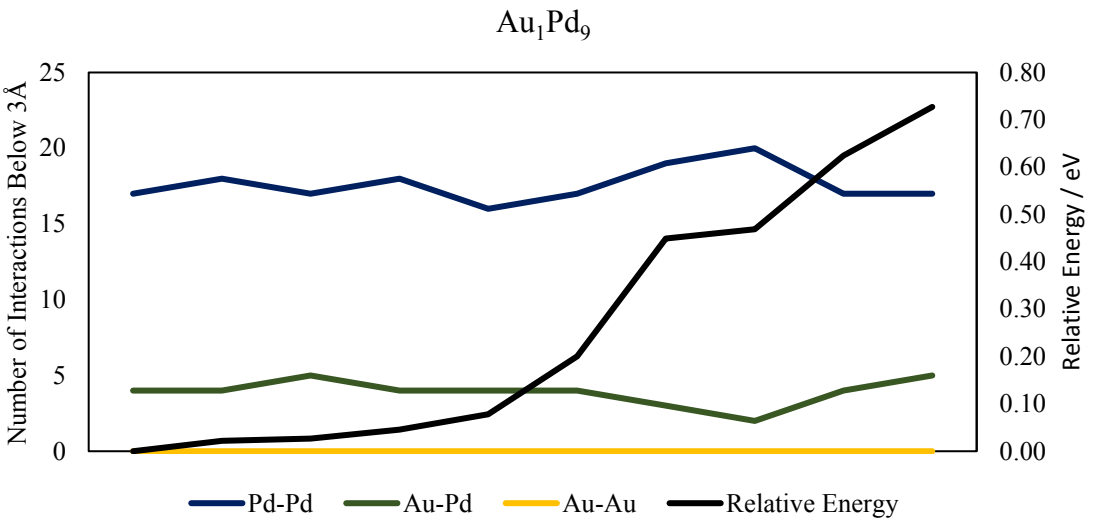
Au1Pd9
Number of Interactions Below 3Å
Relative Energy / eV
0
5
10
15
20
25
0.00
0.10
0.20
0.30
0.40
0.50
0.60
0.70
0.80
Pd-Pd
Au-Pd
Au-Au
Relative Energy

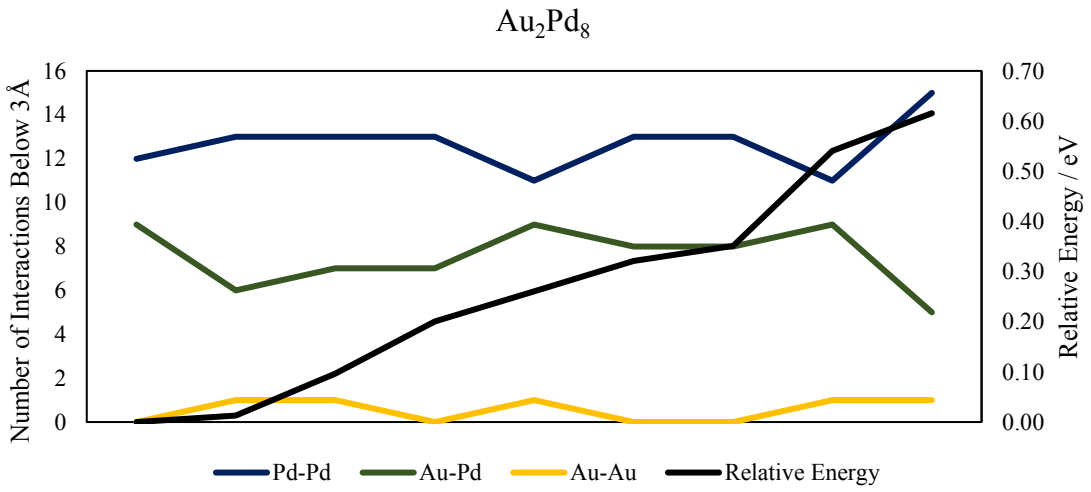
Au2Pd8
Number of Interactions Below 3Å
Relative Energy / eV
0
2
4
6
8
10
12
14
16
0.00
0.10
0.20
0.30
0.40
0.50
0.60
0.70
Pd-Pd
Au-Pd
Au-Au
Relative Energy

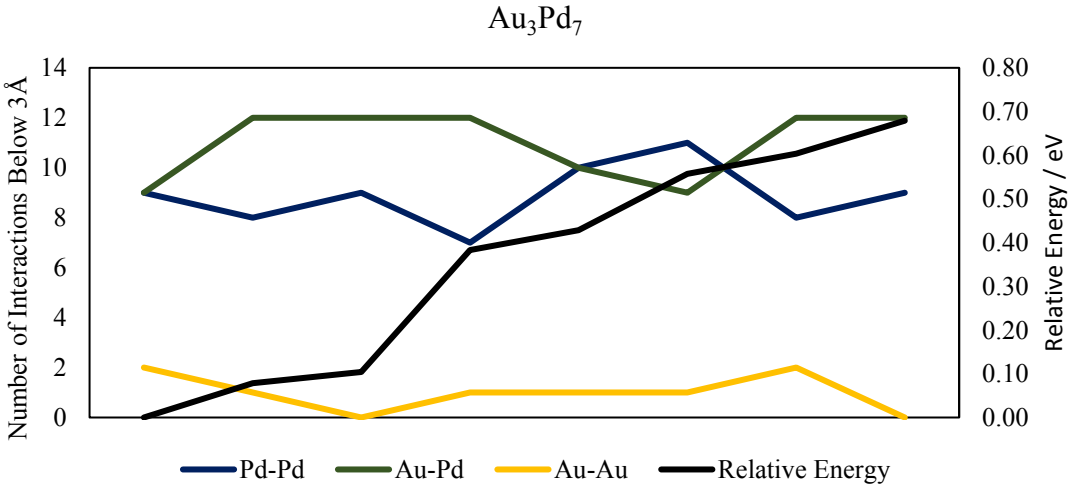
Au3Pd7
Number of Interactions Below 3Å
Relative Energy / eV
0
2
4
6
8
10
12
14
0.00
0.10
0.20
0.30
0.40
0.50
0.60
0.70
0.80
Pd-Pd
Au-Pd
Au-Au
Relative Energy

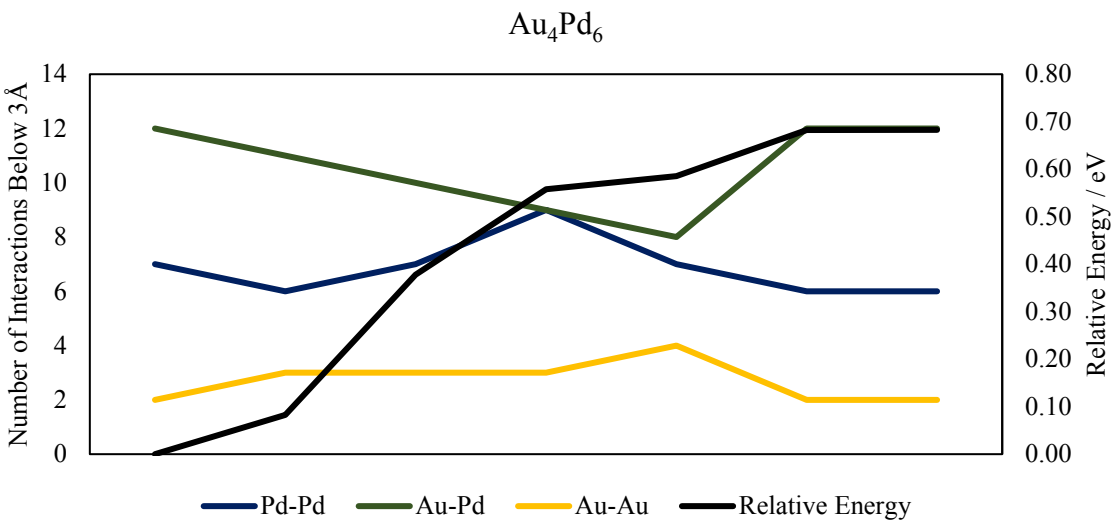
Au4Pd6
Number of Interactions Below 3Å
Relative Energy / eV
0
2
4
6
8
10
12
14
0.00
0.10
0.20
0.30
0.40
0.50
0.60
0.70
0.80
Pd-Pd
Au-Pd
Au-Au
Relative Energy

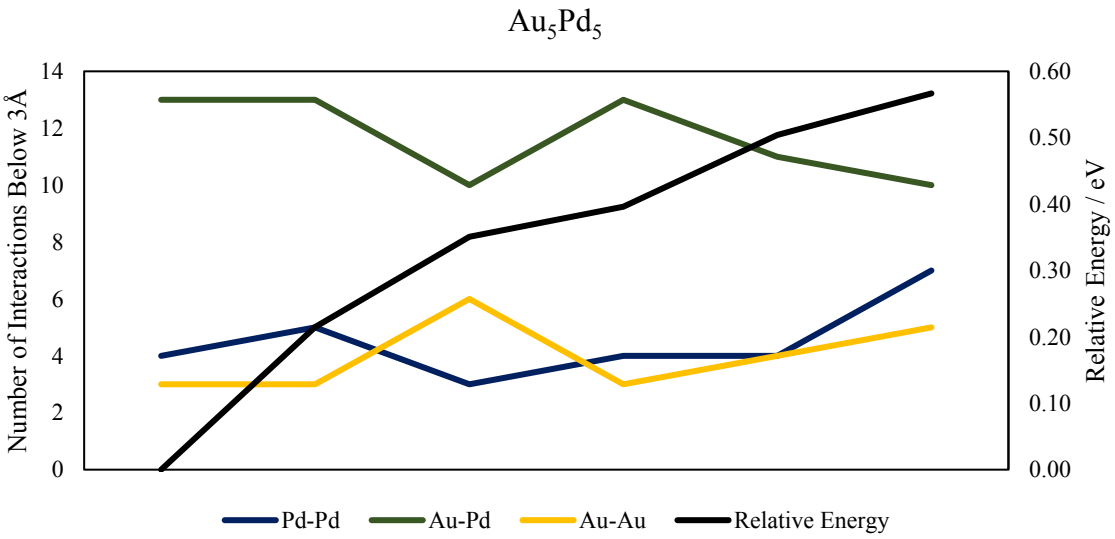
Au5Pd5
Number of Interactions Below 3Å
Relative Energy / eV
0
2
4
6
8
10
12
14
0.00
0.10
0.20
0.30
0.40
0.50
0.60
Pd-Pd
Au-Pd
Au-Au
Relative Energy

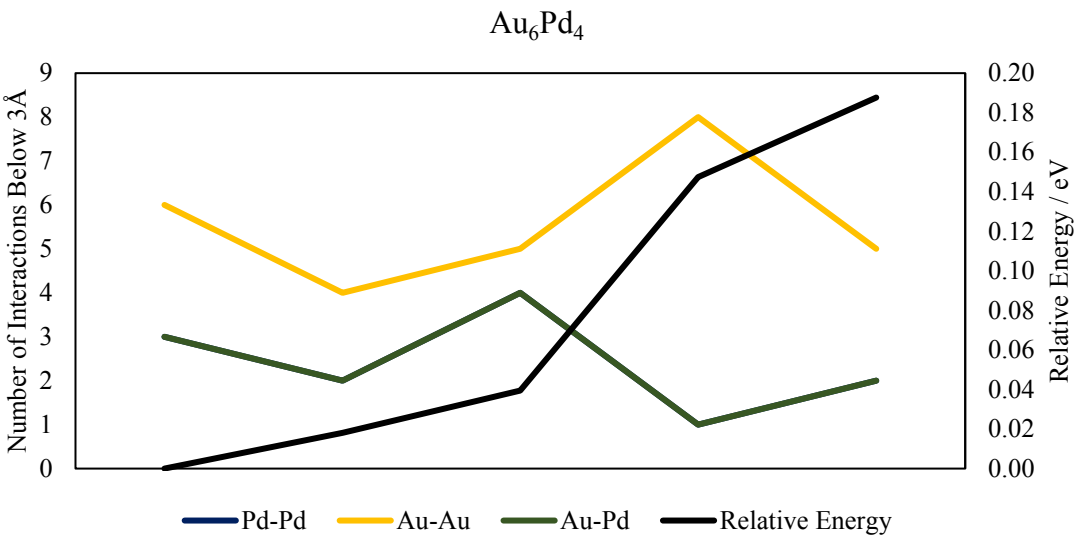
Au6Pd4
Number of Interactions Below 3Å
Relative Energy / eV
0
1
2
3
4
5
6
7
8
9
0.00
0.02
0.04
0.06
0.08
0.10
0.12
0.14
0.16
0.18
0.20
Pd-Pd
Au-Au
Au-Pd
Relative Energy

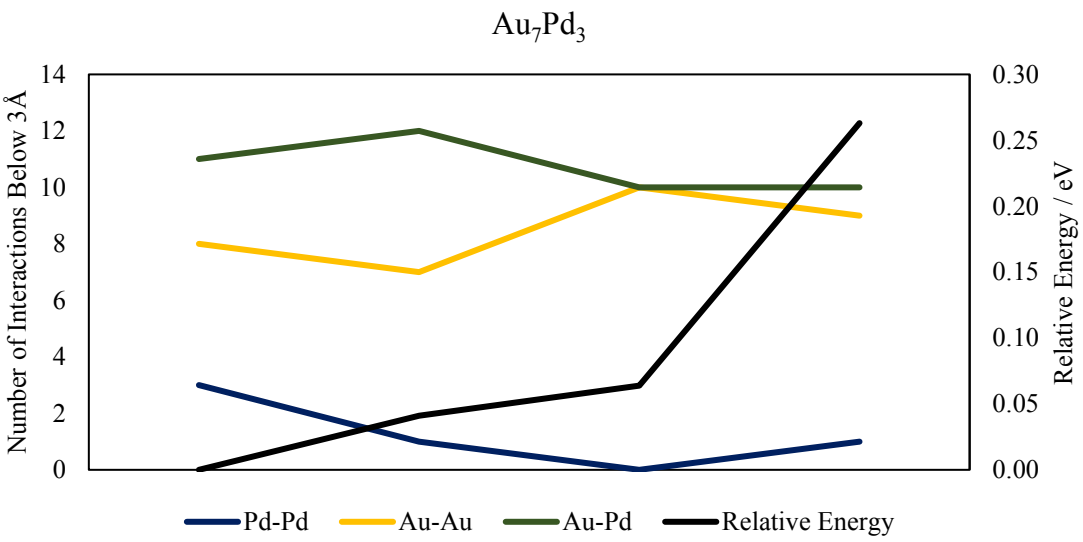
Au7Pd3
Number of Interactions Below 3Å
Relative Energy / eV
0
2
4
6
8
10
12
14
0.00
0.05
0.10
0.15
0.20
0.25
0.30
Pd-Pd
Au-Au
Au-Pd
Relative Energy

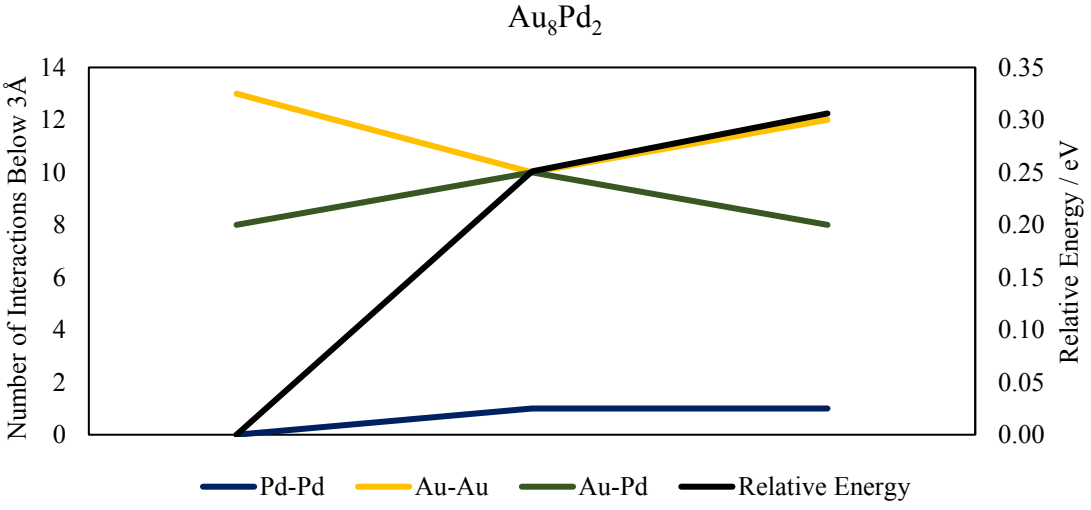
Au8Pd2
Number of Interactions Below 3Å
Relative Energy / eV
0
2
4
6
8
10
12
14
0.00
0.05
0.10
0.15
0.20
0.25
0.30
0.35
Pd-Pd
Au-Au
Au-Pd
Relative Energy

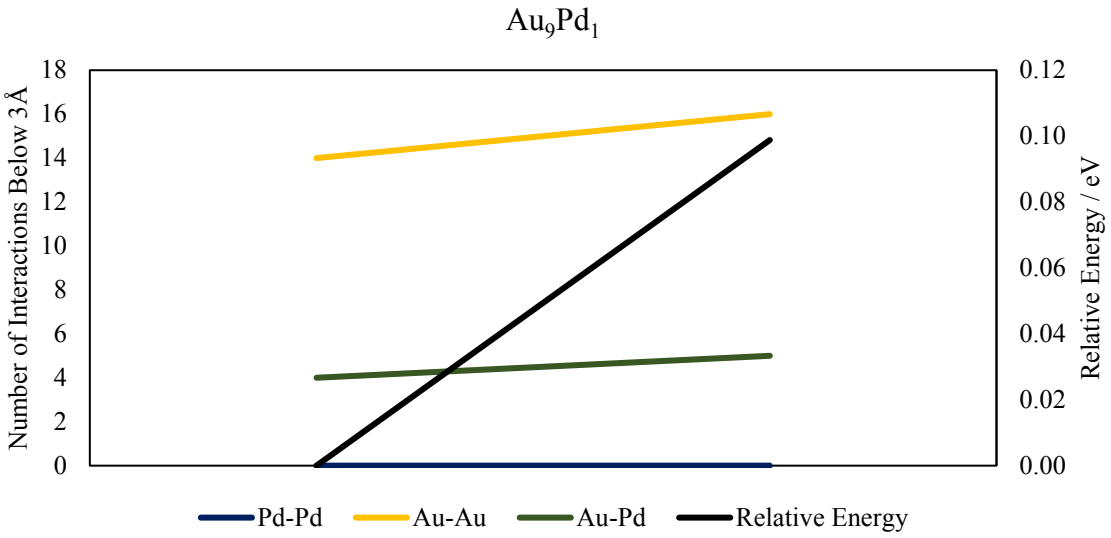

Figure 7.13: From top to bottom Au_1Pd_9 being substituted to Au_9Pd_1. For each configuration the number of Au-Au, Pd-Pd and Au-Pd interactions below 3 Å were tallied and plotted against relative energy of the supported metal particle in eV. Primary axis is the tally of interactions whilst secondary axis is relative energy.

In figure 7.13 data for Au_1Pd_9 indicates the number of Pd-Pd interactions in each cluster configuration remains stable and no correlation between these values and relative energy occurs. A similar observation occurs for when accounting for Au-Pd interactions. No Au-Au interactions occur within these particles as only 1 Au atom is present in this composition of particle. For Au_2Pd_8 more variety is observed with regards to the number of interactions. It is interesting to observe the lowest energy configuration has the highest number of Au-Pd interactions (9) and the highest energy system corresponds to the highest number of Pd-Pd interactions. For Au_3Pd_7 the highest energy particle corresponds to the highest number of Au-Pd interactions which is the reverse to that observed for the Au_2Pd_8 configuration therefore confirming that maximising these interactions is not a prerequisite for a low energy metal / support system. Throughout the substitution to Au_9Pd_1 similar contrasting observations are reported therefore it can be concluded the relative energies of the systems investigated are not dependent on the types of interaction occurring within the metal particle itself.

A graphical route of the sequential substitution of Pd_{10}/Fe_2O_3 to Au_{10}/Fe_2O_3 is presented in figure 7.14.

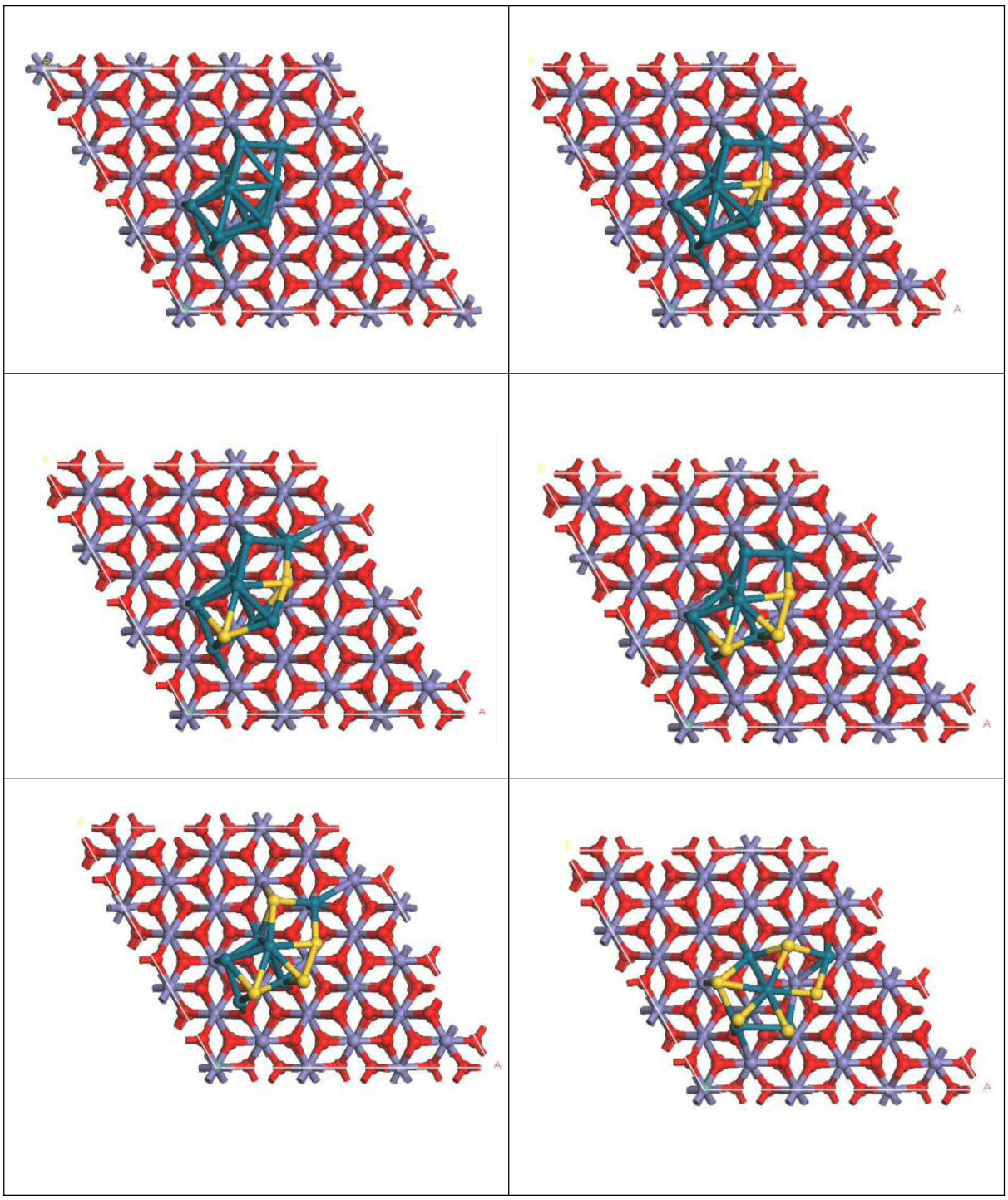

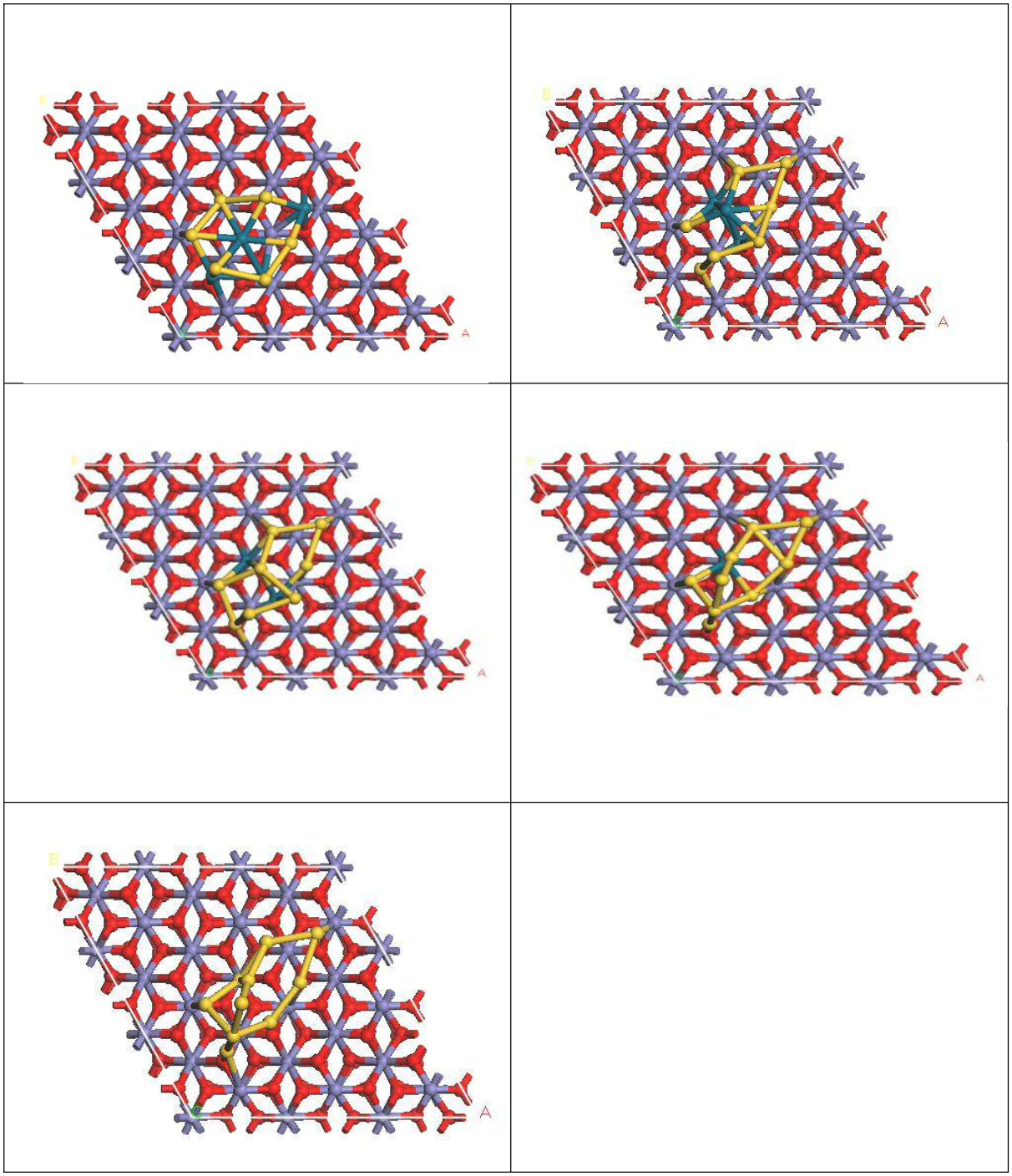

Figure 7.14: Graphical representation of the thermodynamically lowest energy substitution route from Pd_{10} to Au_{10} whilst supported on Fe_2O_3.

Visual inspection of this graphical route suggests Pd atoms are interacting with surface bound Fe atoms. It is possible these interactions may be the thermodynamic driving force for cluster stability and therefore further analysis of these configurations is required.

Using methods similar to that presented in figure 7.14 the number of Au-$Fe_{surface}$ and Pd-$Fe_{surface}$ interactions of 3 Å or less have been counted per cluster composition and this data is plotted against relative energy for each composition in figure 7.15.

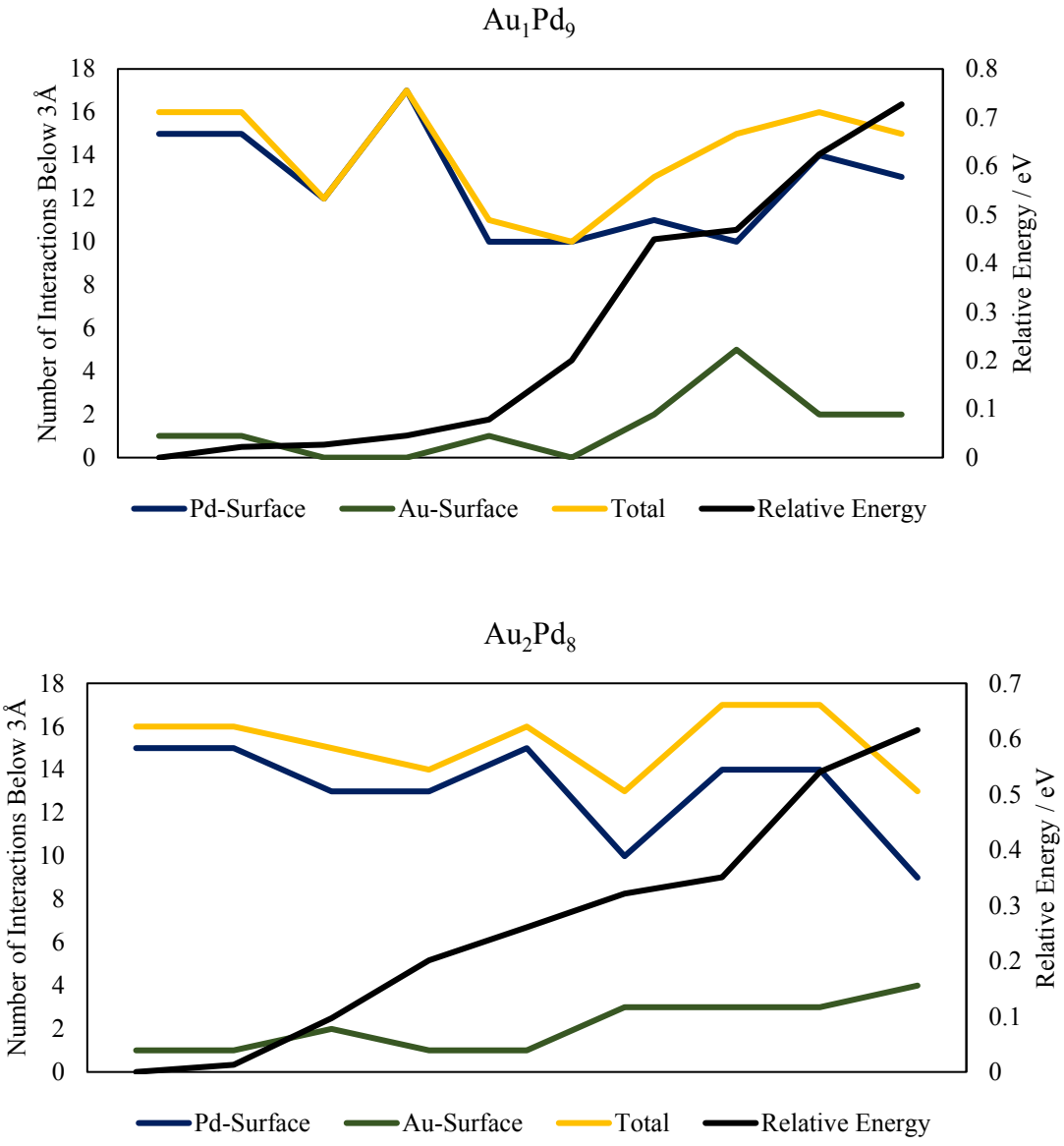

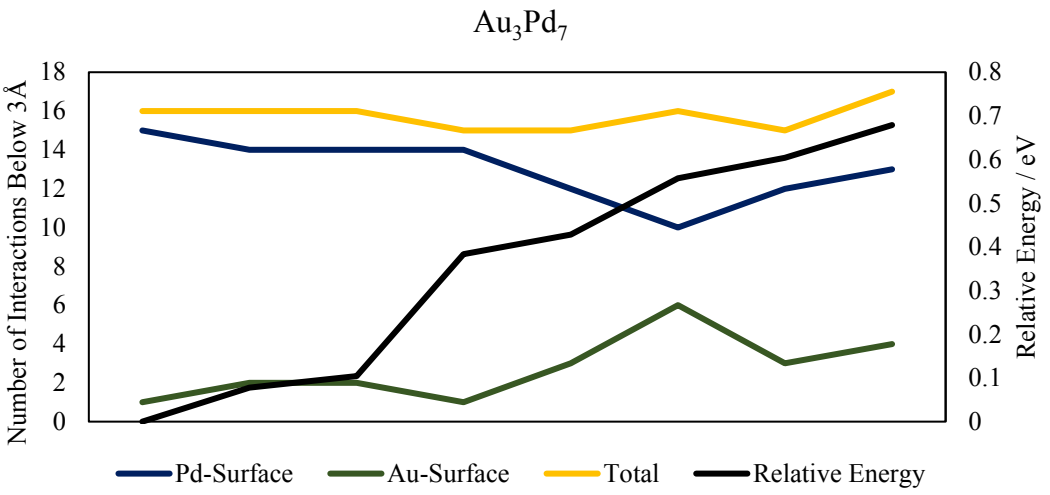
Au3Pd7
Number of Interactions Below 3Å
Relative Energy / eV
0
2
4
6
8
10
12
14
16
18
0
0.1
0.2
0.3
0.4
0.5
0.6
0.7
0.8
Pd-Surface
Au-Surface
Total
Relative Energy

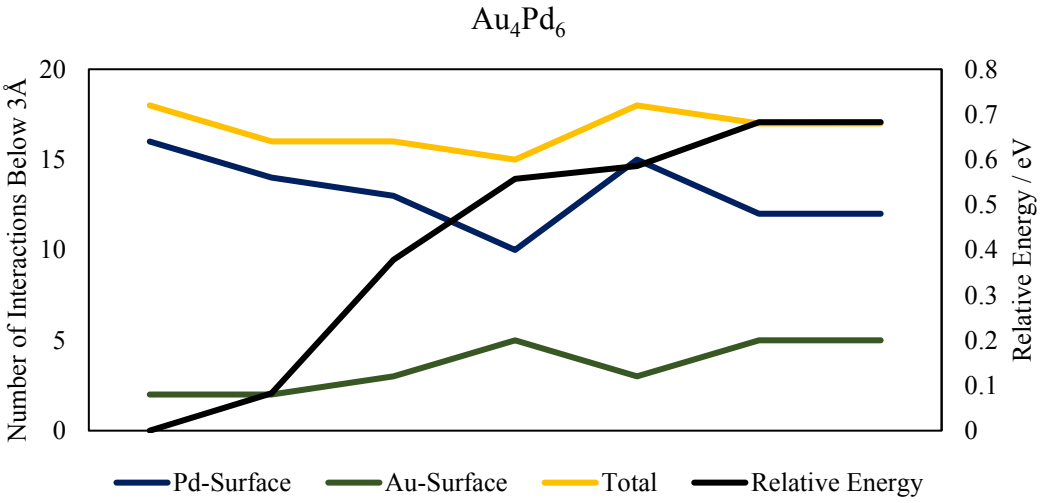
Au4Pd6
Number of Interactions Below 3Å
Relative Energy / eV
0
5
10
15
20
0
0.1
0.2
0.3
0.4
0.5
0.6
0.7
0.8
Pd-Surface
Au-Surface
Total
Relative Energy

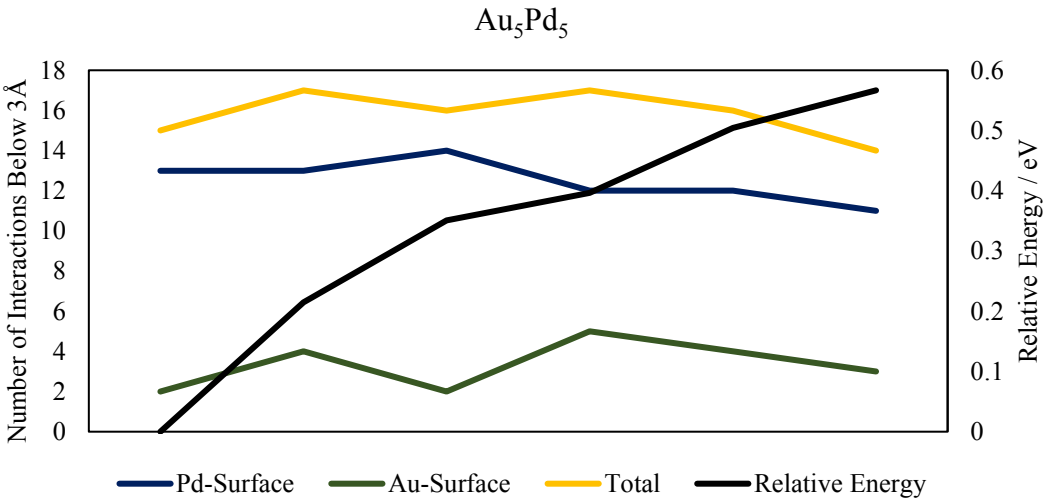
Au5Pd5
Number of Interactions Below 3Å
Relative Energy / eV
0
2
4
6
8
10
12
14
16
18
0
0.1
0.2
0.3
0.4
0.5
0.6
Pd-Surface
Au-Surface
Total
Relative Energy

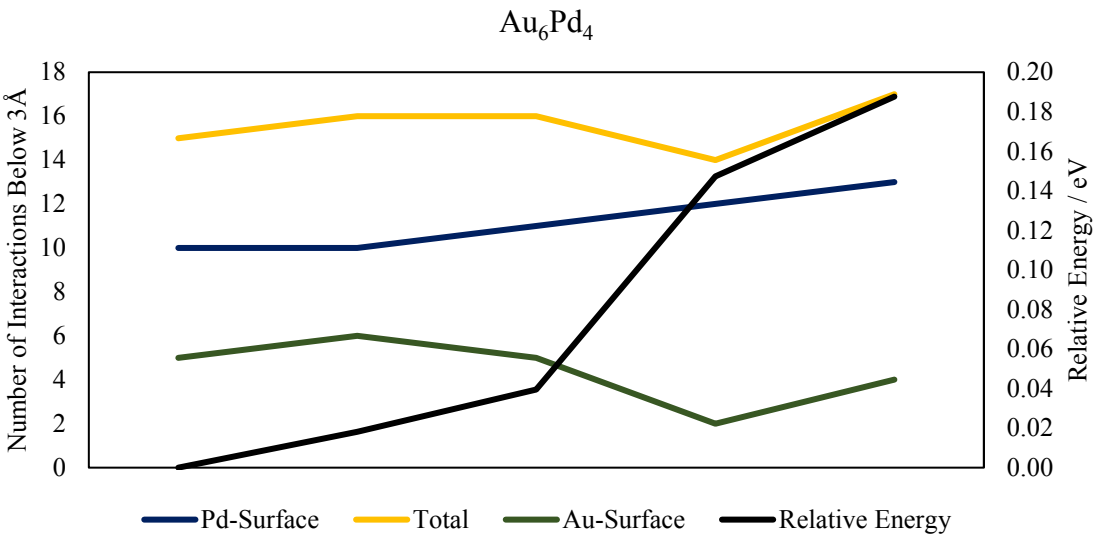
Au6Pd4
Number of Interactions Below 3Å
Relative Energy / eV
0
2
4
6
8
10
12
14
16
18
0.00
0.02
0.04
0.06
0.08
0.10
0.12
0.14
0.16
0.18
0.20
Pd-Surface
Total
Au-Surface
Relative Energy

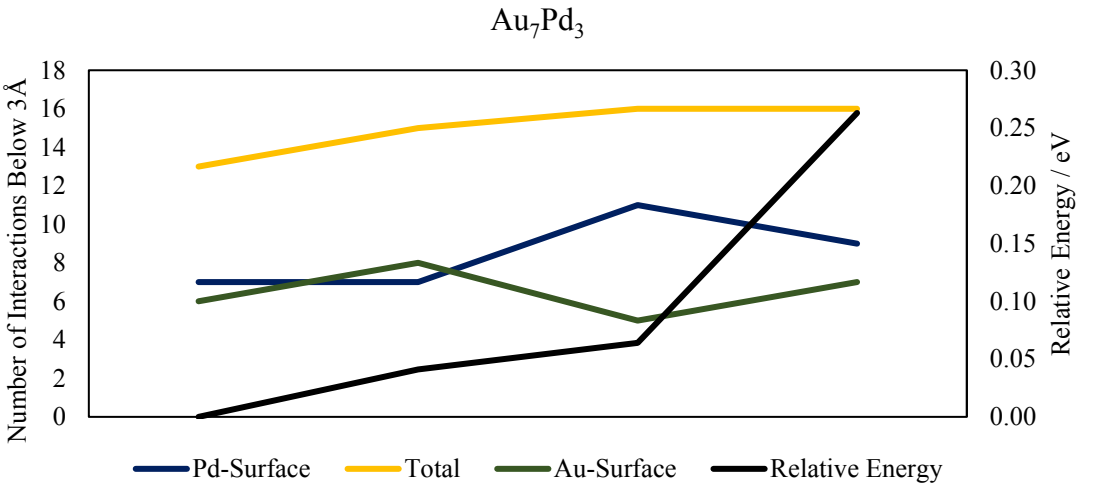
Au7Pd3
Number of Interactions Below 3Å
Relative Energy / eV
0
2
4
6
8
10
12
14
16
18
0.00
0.05
0.10
0.15
0.20
0.25
0.30
Pd-Surface
Total
Au-Surface
Relative Energy

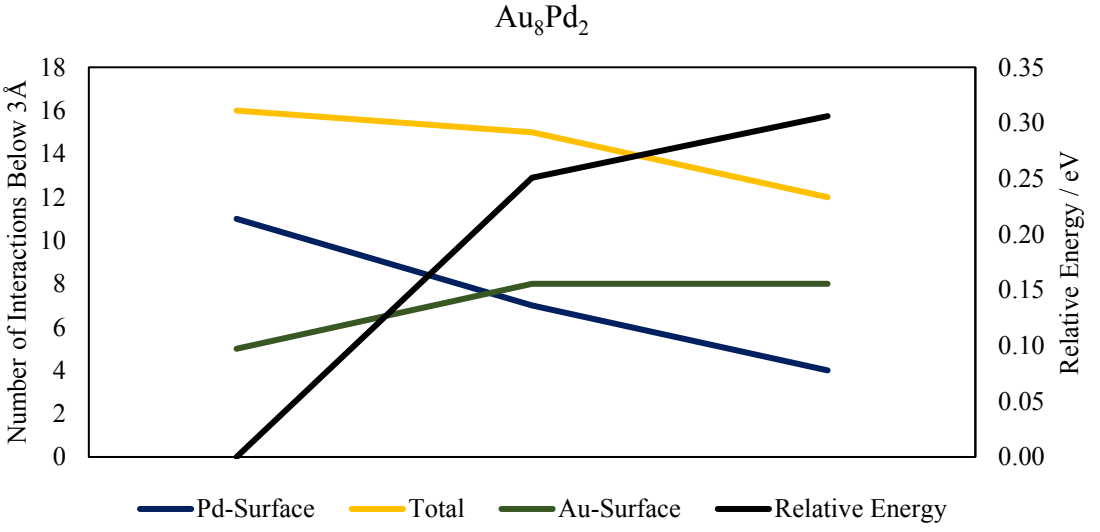
Au8Pd2
Number of Interactions Below 3Å
Relative Energy / eV
0
2
4
6
8
10
12
14
16
18
0.00
0.05
0.10
0.15
0.20
0.25
0.30
0.35
Pd-Surface
Total
Au-Surface
Relative Energy

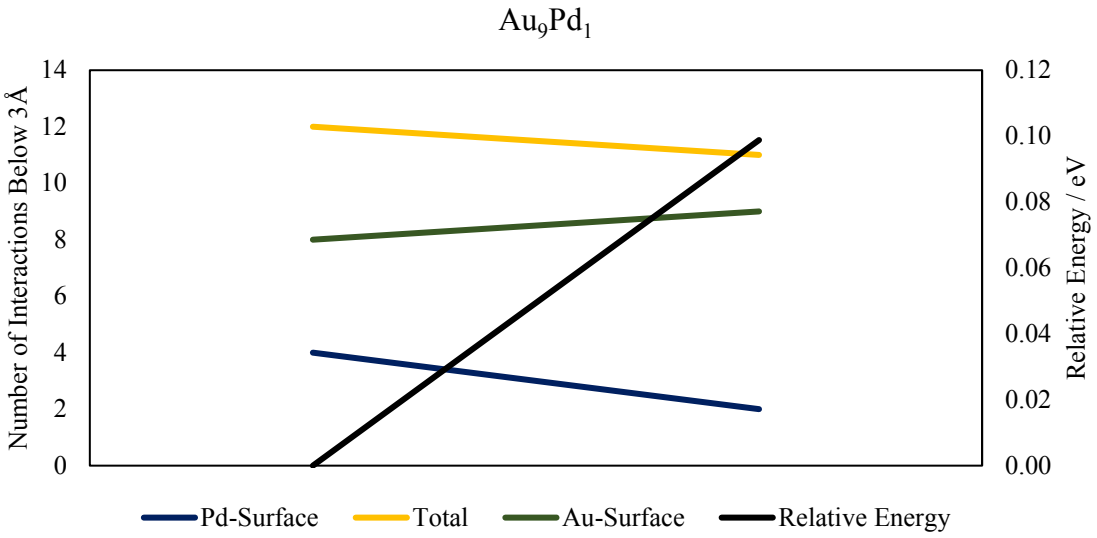

Figure 7.15: From top to bottom Au_1Pd_9 being substituted to Au_9Pd_1. For each configuration the number of Au-$Fe_{surface}$ and Pd-$Fe_{surface}$ interactions below 3 Å were tallied and plotted against relative energy of the supported metal particle in eV. Primary axis is the tally of interactions whilst secondary axis is relative energy.

Data presented in figure 7.15 provides a fascinating insight into the link between cluster conformation and their relative energies. For Au_1Pd_9 the number of surface – Au interactions is minimal however it is of interest to note the lowest energy configuration comprises of the highest number of Pd - surface interactions. For Au_2Pd_8 the highest energy configuration has the maximum number of Au-surface interactions and the lowest configuration has the highest number of Pd-surface interactions as in Au_1Pd_8. This trend continues until Au_5Pd_5 indicating the lowest energy configurations correspond to the maximum number of Pd-surface interactions. Beyond this the gap between energies of the different configurations lowers to a negligible amount (0.10 eV) therefore thermodynamic preference decreases as these higher percentage gold particles.

The above evidence indicates the driving force between configurational preference is the requirement to maximise the number of Pd-surface interactions and minimise Au interactions.

7.3.2 Surface Oxygen Defect Energies with Bimetallic Particles

At each configuration presented in figure 7.14 a single surface oxygen atom on Fe_2O_3 has been removed and the oxygen vacancy defect energy calculated according to equation 7.1. In total 26 surface oxygen atoms have been removed per configuration resulting in 286 separate computational calculations. Figure 7.16 contains the result of these calculations. A sliding colour scale is used to represent cluster compositions where dark blue indicates Pd_{10} and orange is used to represent Au_{10}. For clusters containing majority Pd atoms there is a similar trend to what has been reported within figure 7.9 in which at distance above 3.2 Å the presence of the supported metal particle is negligible with respect to the oxygen vacancy defect energies. This trend however does not apply to metal particles containing high percentages of Au. In the case of Au_8Pd_2, Au_9Pd_1 and Au_{10} there is a dramatic difference in calculated defect energies. Here at large distance from the defect site (> 3.5Å) the defect energies calculated are approximately 1.1 eV lower than the reference defect energy (without a supported metal particle), this observation indicates high percentage gold particles influence oxygen vacancy defect energies differently to their palladium counterparts. This noticeable observation presents an interesting question as to what is the origin of the contrasting behaviour.

All surface oxygen defect energies have been plotted against the distance from the defect site to the metal particle. This measurement has been obtained before optimisation of the cluster / slab system therefore as the metal particle and first two layers of the slab are free to relax some surface rearrangement is likely during the energy optimisation. In order to account for this a further measurement has been obtained which corresponds to the distance between the centre of the defect site and the nearest metal particle atom post optimisation. Defect energies obtained via equation 7.1 are now plotted against the nearest metal particle atom post optimisation which presented in figure 7.17.

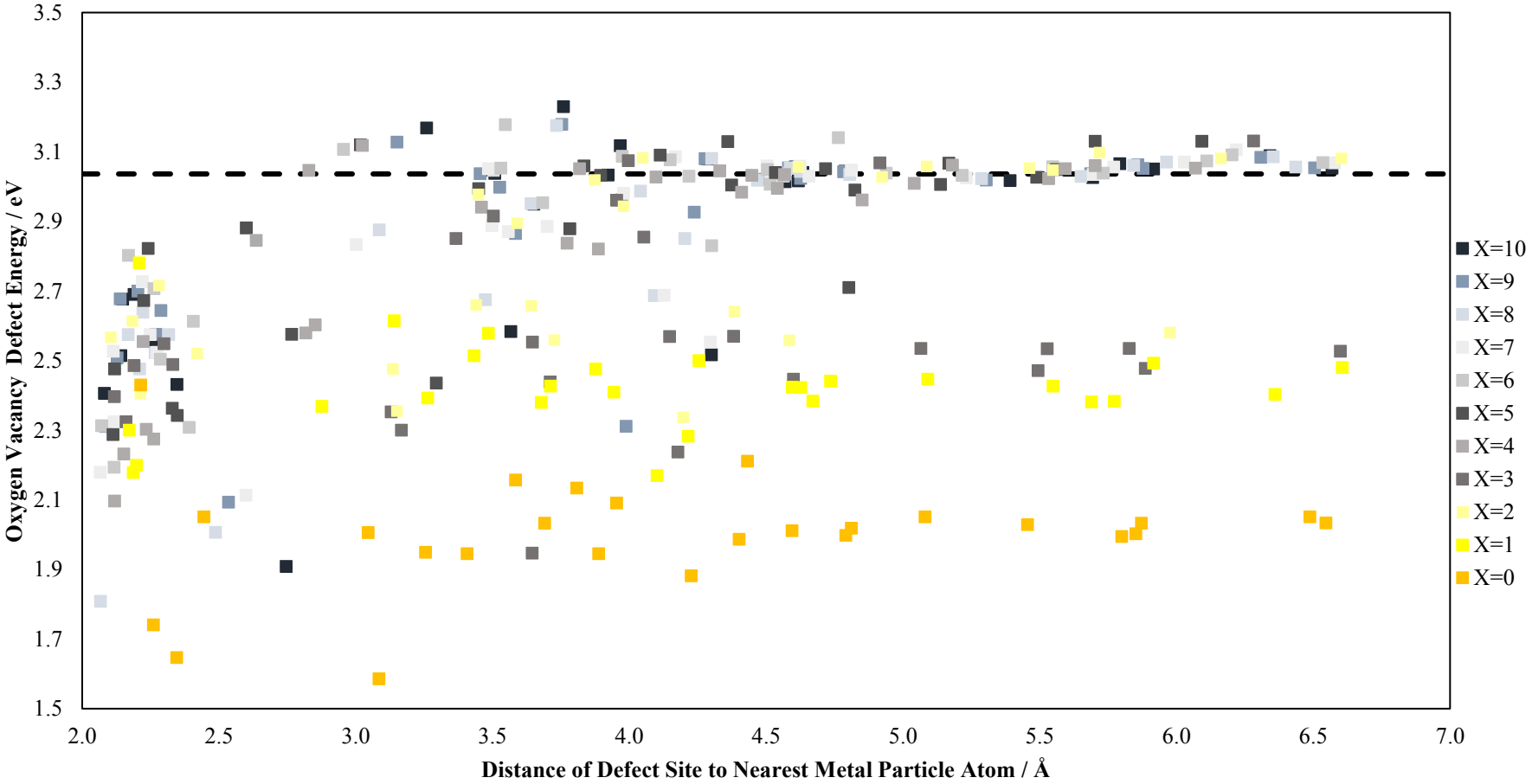

Figure 7.16: Calculated defect energies using equation 7.1 plotted against distance of oxygen atom to be removed from nearest metal cluster atom. X denotes the number of Palladium atoms in the cluster.

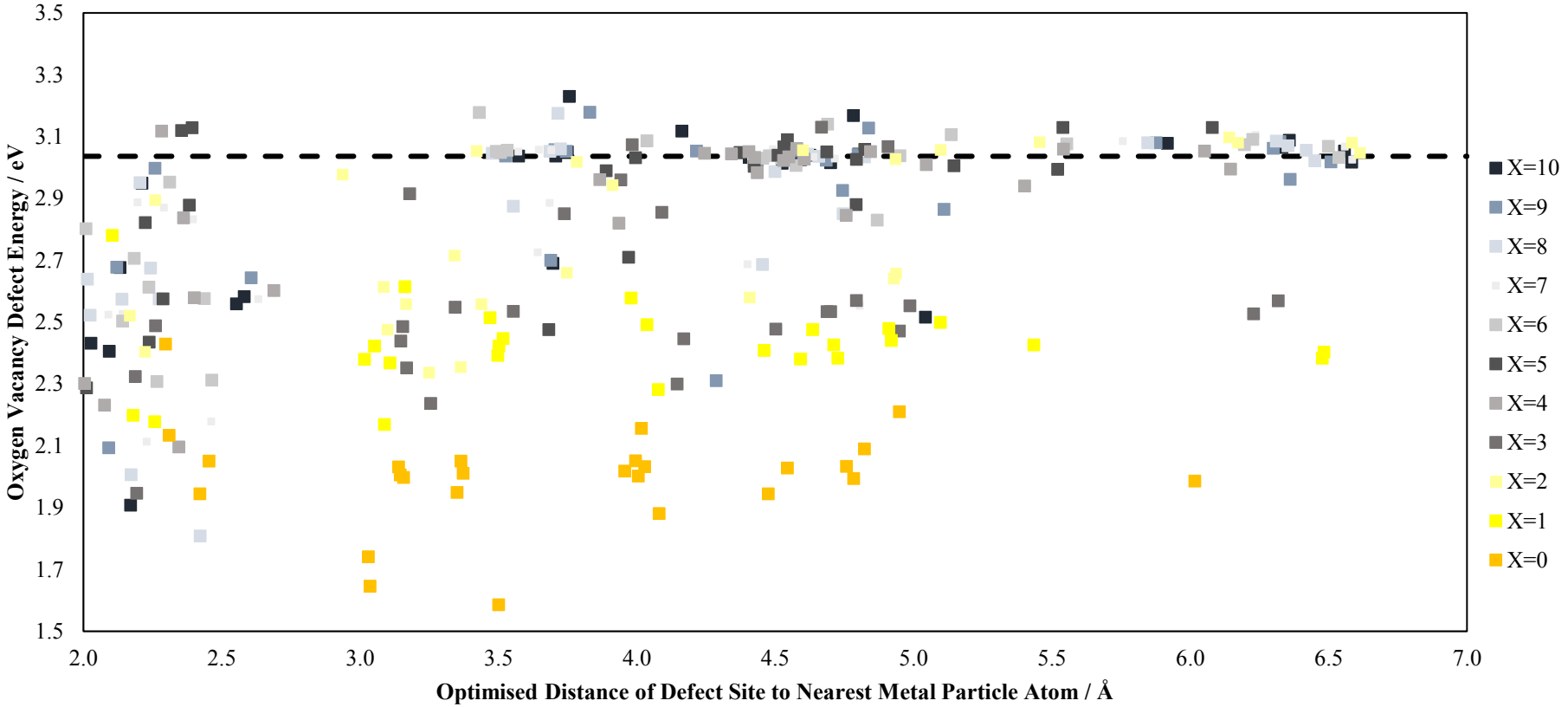

Figure 7.17: Calculated defect energies using equation 7.1 plotted against optimised distance of defect site to nearest metal particle atom. X denotes the number of Palladium atoms in the cluster.

Figure 7.17 provides an indication as to how the cluster / surface relaxes upon creation of a defect. For high palladium content clusters the trend in which defect energies decrease in comparison to the reference energy at distances below 2.5 Å is still observed in the post relaxation measurement. At larger distances the high content palladium particles do not have any influence over the calculated defect energies. For Au rich particles calculated defect energies are substantially lower (~1 eV) even at distances greater than 2.5 Å. In order to quantify geometric changes which occur to the metal particle the change (pre and post optimisation) in distance from metal particle atom to defect site has been determined and averaged out across all metal particles / defect systems for each Au/Pd composition. This data is presented in figure 7.18.

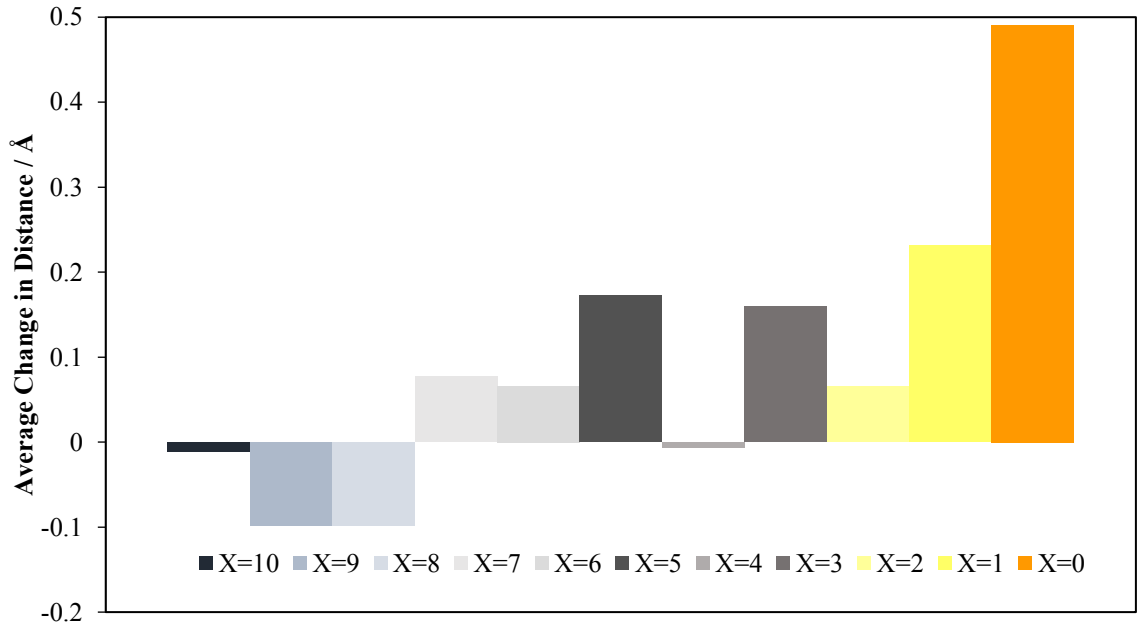

Figure 7.18: Change in distance between defect site pre optimisation and defect site post optimisation. These distances are measured per cluster configuration averaged out over all defect possibilities. X is used to denote the number of Pd atoms in the cluster (X=0 is Au_{10}). Positive values indicate the metal particle has shifted towards the defect site whereas negative values are used to denote movement away from the defect site.

The data presented in figure 7.18 clearly indicate for metal particles containing 6 to 10 palladium atoms there is relatively small cluster rearrangement upon creation of a surface oxygen defect. For these cluster configurations the average change in the distance from the nearest metal atom to the defect site is less than 0.1 Å therefore indicating negligible cluster

rearrangement occurs. This however is not the case for metal particles containing 9 and 10 gold atoms. For these configurations the distance between the closest metal particle atom and the defect site decreases indicating the metal particle shifts and almost acts as a plug to the defect site lowering the energy of the system overall which results in a calculated defect energy which is approximately 1 eV lower than for a system which does not contain a supported particle. This striking observation and its implications for catalysis are discussed in 7.3.5.

7.3.3 Electronic Adjustments upon Defect Creation

The data presented in 7.3.2 points towards geometric adjustment of the metal particle upon defect creation as a plausible explanation of lowered defect energies. Whilst this observation provides a significant step towards explanation of the differing behaviour upon creation of defect sites it may not alone provide a full explanation. A further possibility as to why this contrasting behaviour is observed may electronic effects. In Fe_2O_3 oxygen has a formal charge of 2^-. When a defect is created a neutral O atom is removed which will leave two electrons behind on the surface. It is possible these two electrons reduce adjacent Fe^{3+} or alternatively the electrons may be accommodated onto the metal particle reducing either Au or Pd. In order to test these two possibilities a Bader charge analysis investigation was performed using conditions detailed in 7.2. A full study was not conducted due to computational cost of performing charge analysis on each configuration but as a compromise appropriate selected configurations were chosen to perform the analysis on. Bader charge analysis was performed on the three nearest defect site – metal particle systems, the three at midpoint from the particle and finally the three farthest defect site – metal particle distances. This can be viewed as 3 concentric rings at increasing distance from the metal particle. For these configurations the charge distribution has been obtained for each metal particle atom and has been averaged out over all cluster metal atoms to produce a single value. A lower value for the calculated charge indicates the metal particle has received electron density upon defect creation whereas an increase indicates atoms in the metal particle have been oxidised.

This average Bader charge analysis is presented in figure 7.19. Block 1 is presented as the first data set. This block corresponds to defect sites closest to the metal particle. The average change in the Bader charge presented here conclusively indicates that at close proximity the metal particles of all Au/Pd atoms in the metal particle receive electron density upon creation of a defect. This indicates it is not local iron ions undergoing reduction at this close proximity distance. The distance data block does not present a trend as anomalous data indicates at Pd_5Au_5

(second data block) the charge transfer on the metal particle exceeds any other configuration studied. At the block furthest from the defect site charge transfer is effectively zero for high percentage Pd particles however an interesting observation occurs in which at Pd_1Au_9 and Au_{10} the particles appear to become reduced even at this large distance from the defect site. It can therefore be summarized that both flexibility and ability for the metal particle to accept electron density allow for a reduction in surface oxygen defect energies in the presence of a supported metal particle.

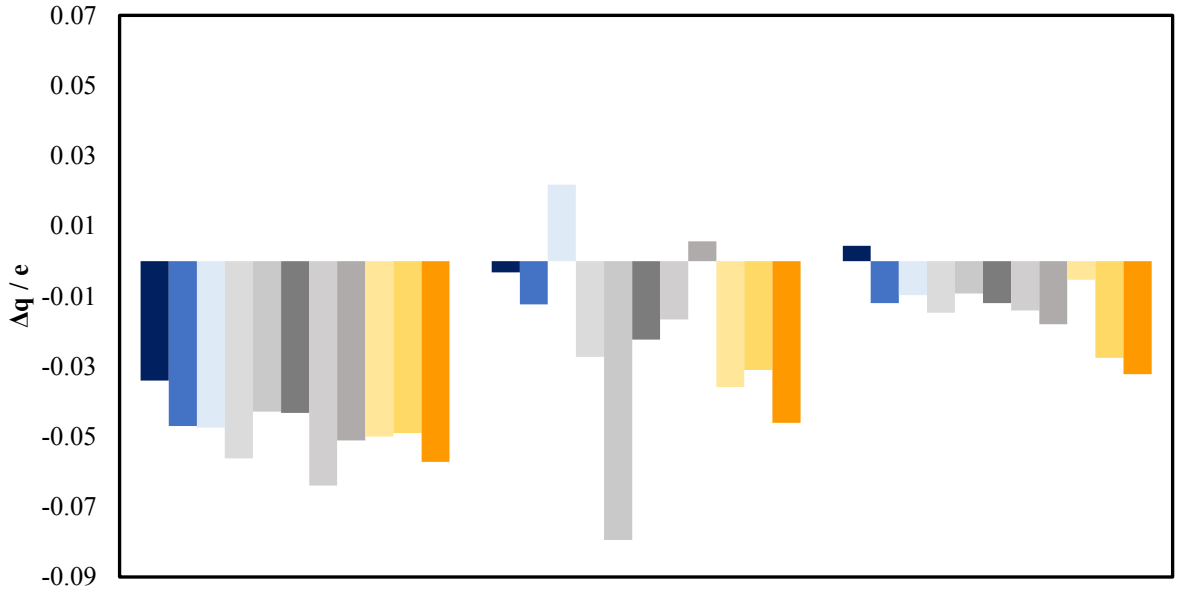

Figure 7.19: Average Bader charge for each metal particle composition divided across three blocks of increasing distance from the metal particle. A sliding colour scale is used to represent cluster compositon. Dark blue is Pd_{10} whereas gold colour is Au_{10}.

7.3.5 Implications for CO Oxidation

The data presented here poses an interesting question with regards to catalytic CO oxidation as to whether it is atmospheric oxygen incorporated within CO to form CO_2 or alternatively the surface may act as an oxygen supply which itself is replenished by atmospheric oxygen. Previous computational studies by Hoh *et al* indicate a supported Au_{10} (supported on Fe_2O_3) particle itself can readily adsorb and dissociate molecular oxygen at the periphery of the cluster / support[38]. Further study by Hoh *et al* indicate once dissociated into atomic form this oxygen is around 0.5 eV more energetically difficult to abstract than lattice oxygen on an α-Fe_2O_3 (0001) support. The findings presented here clearly indicate lattice oxygen is a viable source of oxygen during oxidation chemistry therefore presenting an interesting conclusion in which the composition of high percentage gold particles dramatically alter energetics of oxygen removal and make it more viable for it to be incorporated within reactants during oxidation chemistry.

Lattice oxygen has been reported to be incorporated within CO to form CO_2 using Pt / CeO_2 systems with atmospheric oxygen primarily used to replace abstracted lattice oxygen[39]. This observation raises an interesting question regarding what role the supported Pt particle plays in facilitating this abstraction.

DFT Studies performed by Lu *et al* for CO oxidation using SnO_2 also suggest it is energetically feasible for lattice oxygen to be incorporated in CO forming CO_2[40]. Whilst this research was performed on bare surfaces without the presence of a metal particle it raises the tantalising question as to whether the presence of such a particle would make abstraction of lattice oxygen more feasible.

Based upon the above evidence it is reasonable to state a supported metal particle aids abstraction of surface bound oxygen on Fe_2O_3 (0001). The Au rich particles in particular dramatically aid this abstraction. The author of this work theorizes oxygen rich supports in catalytic systems which contain a supported metal particle are more likely to undergo a Mars van Krevelen type mechanism and therefore the correct metal composition to aid such a mechanism is vital to ensuring efficient catalysis. Computational calculations may aid experimentalists to design particles to exploit this property.

7.4 Molecular Dynamics of Au Particles

The study of defect creation presented in the preceding section gave rise to an interesting observation in which gold particles demonstrated considerably higher flexibility than their palladium counterparts. This observation warrants further study to obtain quantifiable measurements of this property.

As previously discussed gold particles within the subnanometric region have a degree of uncertainty regarding their global minimum structure. Previous studies have reported Au_{13} can adopt both 2D and 3D structures as minima and this contrasting information would make a comprehensive study of the molecular dynamics of 2D vs 3D structures justified. Using VASP and its' inbuilt molecular dynamics function four gold particles of 13 atoms were chosen to perform a study of. These particles are presented in figure 7.20. Using a 625 $Å^3$ box and a 30 ps overall simulation time these particles underwent a molecular dynamics simulation at 500K. This temperature has been chosen to force and exaggerate any structural changes which may occur within the gold particles. In addition to particle geometries the absolute energies are reported in eV.

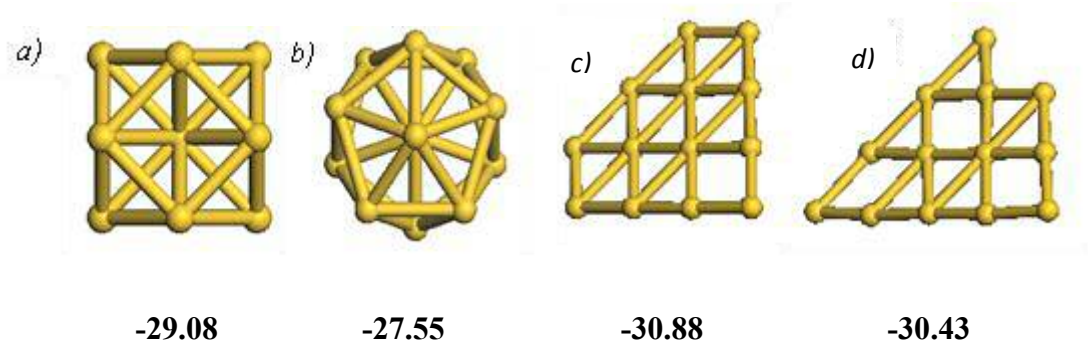

Figure 7.20: Au_{13} particles investigated, a) is cuboctahedral 3D structure, b) is icosahedral 3D structure, c) is a 2D structure denoted 2D(A) and d) is a 2D structure denoted 2D(B).

Analysis of the molecular dynamics calculations were made using the in-house developed inter_vasp and analyse_hist code. The output of this analysis is discussed in 7.4.1

7.4.1 Energetic Change over Time

In order to obtain a reference all energies of the molecular dynamics runs are plotted relative to the energies of 13 isolated Au atoms (unless otherwise stated). Figure 7.21 details how these relative energies change as a function of time during the MD simulation for the three dimensional Au_{13} particles studied whilst figure 7.22 details the same but for two dimensional Au_{13} clusters.

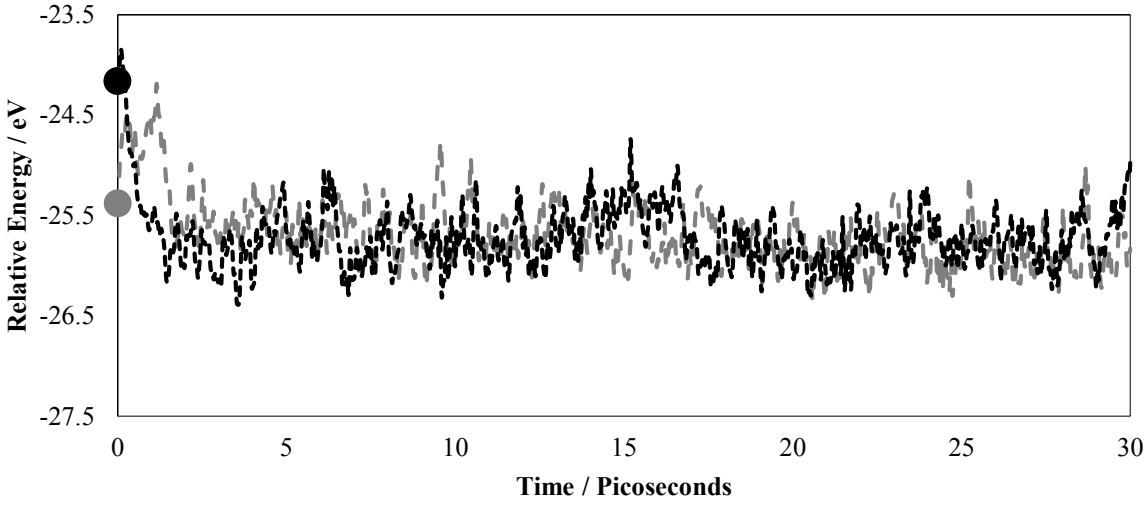

Figure 7.21: Energies of Au_{13} three dimensional clusters as a function of time. Energies are set relative to 13 x isolated Au atoms. Grey dashed lines represent the cuboctahedral structure whilst black dashed lines the icosahedral structures. Circles indicate the relative energies of the starting structure.

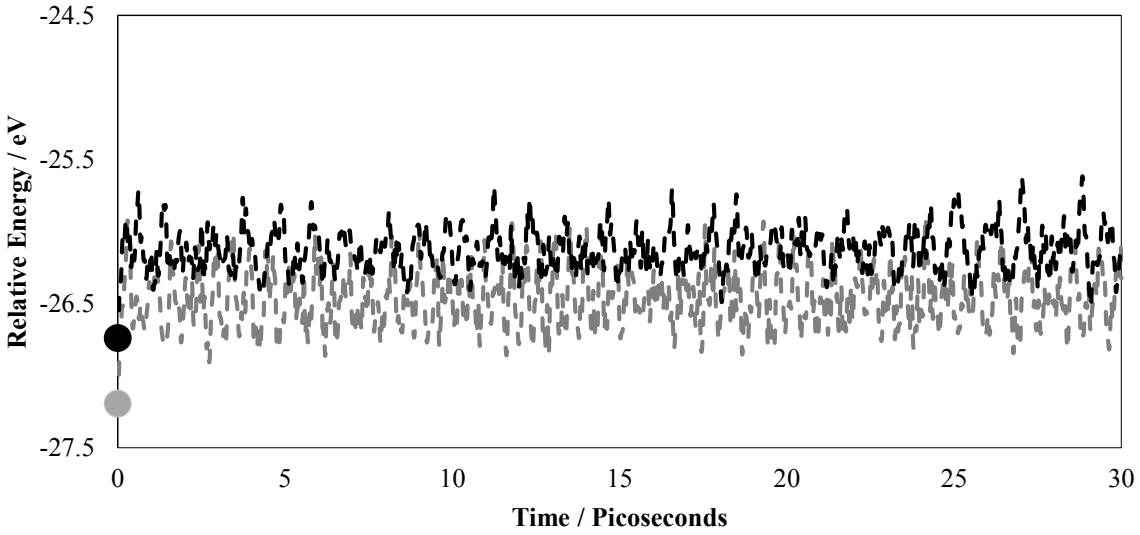

Figure 7.22: Energies of Au_{13} two dimensional clusters as a function of time. Energies are set relative to 13 x isolated Au atoms. Grey dashed lines represent 2D(1) structure whilst black dashed lines the 2D(2) structure. Circles indicate relative energies of the starting structure.

Figure 7.21 indicates both cuboctahedral and icosahedral clusters rearrange structures which are lower in energy during the simulation after an equilibration time of approximately 5ps is passed. The cuboctahedral structure adopts a structure which is approximately 0.8 eV in energy lower than the start structure whilst the icosahedral structure rearranges to a structure 1.3 eV lower in energy. These two rearrangements within the very short equilibration period clearly confirm that neither icosahedral or cuboctahedral structure is the energetic preference for a global minimum of Au_{13}. After 5 picoseconds of simulation relative energies of both simulations stabilise in what is deemed an "energy overlap" region where energies of both structures share a region of 0.3 eV.

Figure 7.22 demonstrates an opposite trend in which no structures are found during the simulation which are relatively lower in energy than their starting structures. These molecular dynamics confirmation searches have presented structures on average which are 0.7 eV higher in energy than the start structures. This data allows for the conclusion that 2D structures investigated here are substantially thermodynamically and kinetically more favourable than 3D structures.

Presented in chapters 5 and 6 multiple adsorptions of both HMF and O_2 on Au_{38} have been performed. Of interest would be a comparison of the relative flexibility of Au_{38} compared to Au_{13} and therefore a molecular dynamics investigation using Au_{38} (figure 7.23) has been performed using the same criteria detailed for Au_{13} particles.

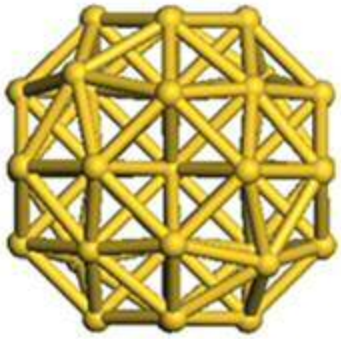

Figure 7.23: Cuboctahedral Au_{38} cluster

Over 30 picoseconds the molecular dynamics run was performed with relative energies compared to 38 isolated Au atoms obtained at each time step. The results of this run are contained within figure 7.24.

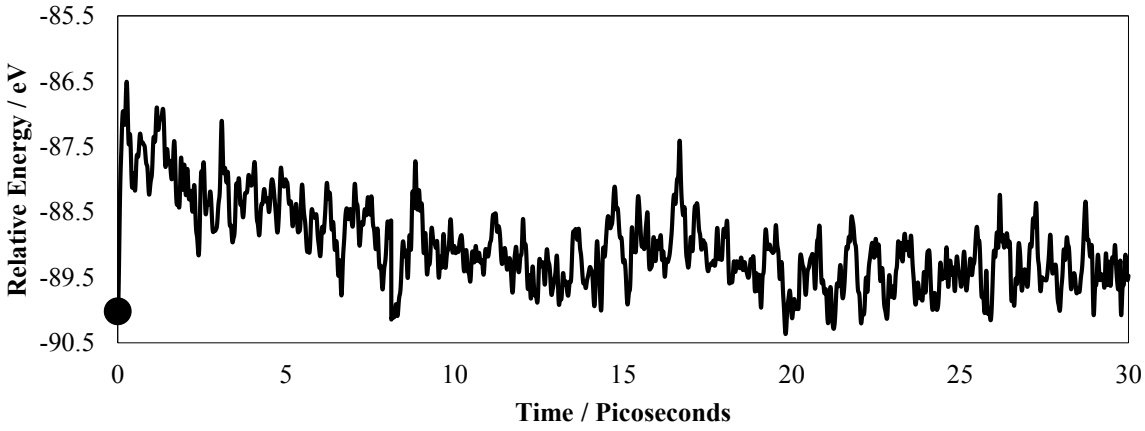

Figure 7.24: Energies of Au_{38} structure as a function of time. Energies are set relative to 38 x isolated Au atoms. The circle indicates relative energy at the start of the run.

Figure 7.24 confirms the majority of cluster configurations visited throughout the MD run are higher in energy than the highly ordered starting structure. Only 203 of the 10000 configurations visited throughout the MD run were lower in energy than the starting structure.

The lowest relative energy structure obtained is 0.31 eV lower in absolute energy than Au_{38} within the cuboctahedral geometry. In order to reach these structures, it is clear an energy barrier must be overcome first. This is indicated by the sharp rise in energy observed after 2 picoseconds which gradually decreases through the run. The MD energy profiles presented within figures 7.22, 7.23 and 7.24 indicate that Au_{13} with 3D starting geometrys are far more flexible than Au_{38}.

In order to further quantify structural changes throughout these calculations the radius of gyration for each configuration has been determined using the analyse_hist program. This value has been averaged over every configuration and is presented in table 7.3 along with the range and standard deviation.

Table 7.3: Radius of gyration presented for each metal particle investigated. Values are reported in nanometer.

Cluster	Average Radius of Gyration / nm	Range / nm	Standard Deviation / nm
Cuboctahedral	0.12	0.023	0.004
Icosahedral	0.12	0.022	0.003
2D(A)	0.15	0.008	0.001
2D(B)	0.15	0.008	0.001
Au_{38}	0.17	0.010	0.001

A large average radius of gyration is indicative of a cluster geometry which is more spread out. For 3D structures the average radius of gyration is smaller than for 2D structures confirming the 2D structures remain opened and flat within their configurations. The range in values along with standard deviation has also been determined with a clear observation both cuboctahedral and isocahedral 3D structures have an observed range of 0.015 and 0.014 angstrom respectively higher than the 2D structures. This measurement coupled with the larger standard deviation confirms 3D structures are structurally more flexible than 2D and adopt a range of different geometries throughout the MD run. For Au_{38} the range of radius of gyration values is 0.010 angstrom which is comparable to the 2D structures confirming this larger structure retains its geometry through the molecular dynamics run.

7.4.2 Shape Analysis Throughout Molecular Dynamics Calculations

To further quantify the geometries of the structures obtained throughout the MD run moment of inertia analysis was performed using the analyse_hist code. Highly ordered three dimensional clusters have an almost identical moment of inertia within the X, Y and Z axis due to their spherical nature. Two dimensional clusters will exhibit different moment of inertia as they are not spherical in shape. As already discussed in 7.4.1 icosahedral and cuboctahedral Au_{13} rearrange to geometries lower in energy than their starting structures. Using moment of inertia analysis this change in energy can be correlated shape analysis and a correlation between energies and shapes determined. Figures 7.25 and 7.26 present moment of inertia analysis for cuboctahedral and icosahedral Au_{13} respectively.

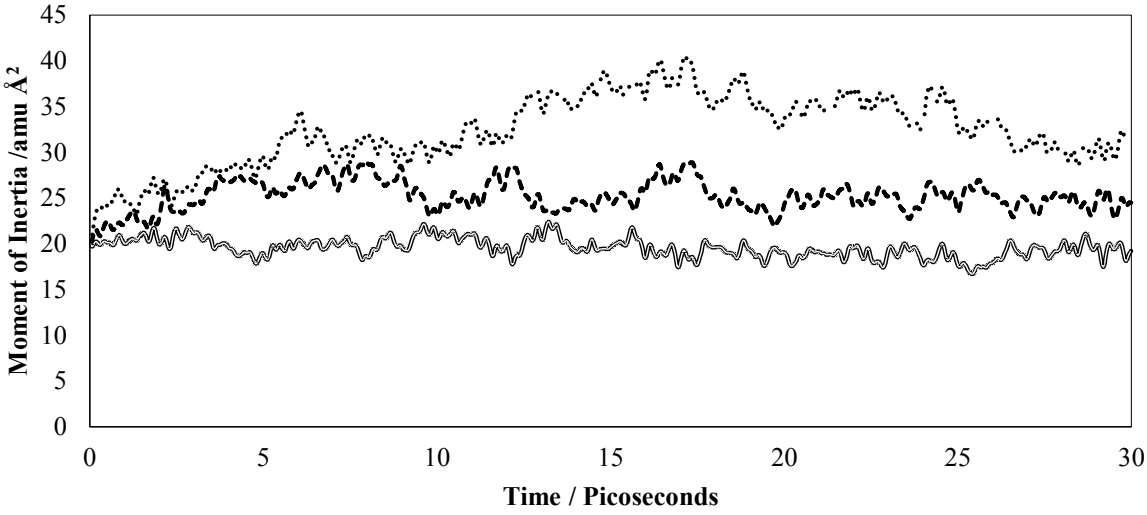

Figure 7.25: Moment of inertia analysis for Au_{13} cuboctahedral structure. Circle lines, double lines and dashed lines represent moment of inertia in X, Y and Z directions respectively.

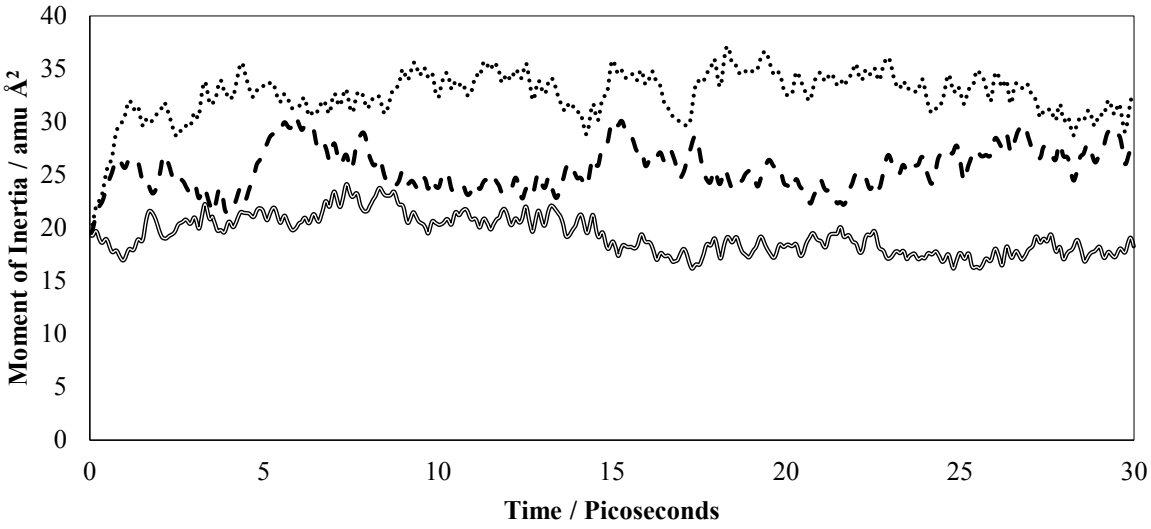

Figure 7.26: Moment of inertia analysis for Au_{13} icosahedral structure. Circle lines, double lines and dashed lines represent moment of inertia in X, Y and Z directions respectively.

The moment of inertia analysis displayed in figures 7.25 and 7.26 indicate a substantial change of moment of inertia throughout both runs within the X and Z directions. At it's the greatest the change in moment of inertia is calculated to be 0.18 amu $Å^2$ within these directions. Within the Y direction the moment of inertia remains stable which indicates the spreading of the cluster geometry in the X and Y directions forming an almost disc like shape. Figures 7.27 and 7.28 present moment of inertial analysis for 2D(A) and 2D(B) structures respectively.

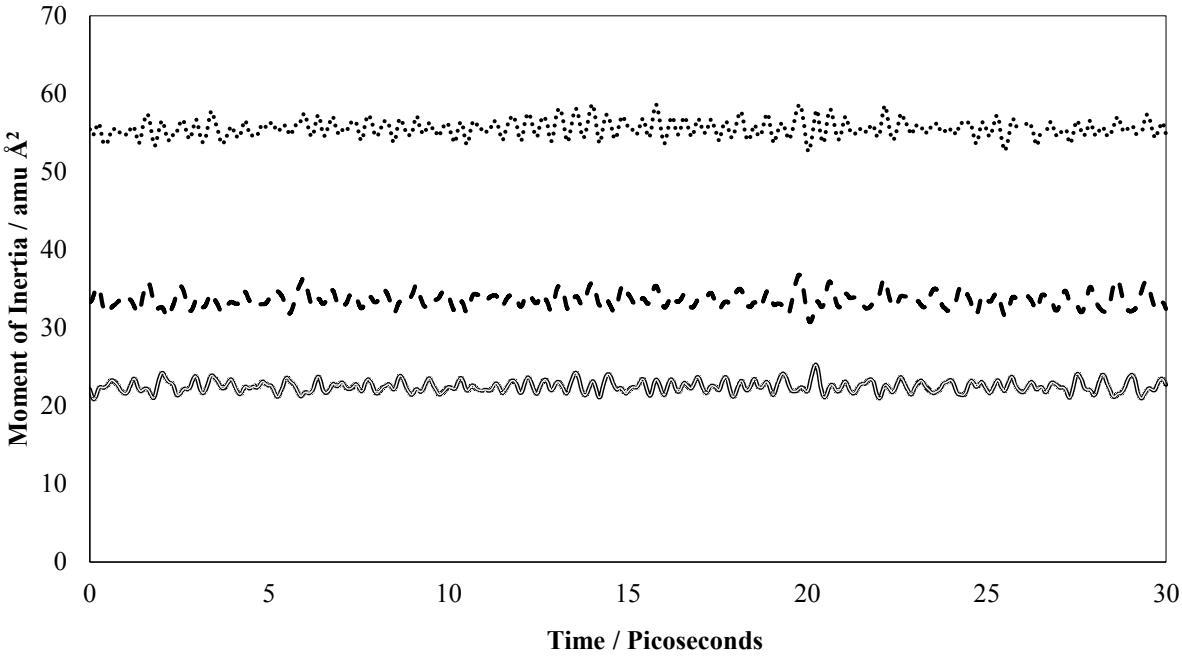

Figure 7.27: Moment of inertia analysis for Au_{13} 2D(1) structure. Circle lines, double lines and dashed lines represent moment of inertia in X, Y and Z directions respectively.

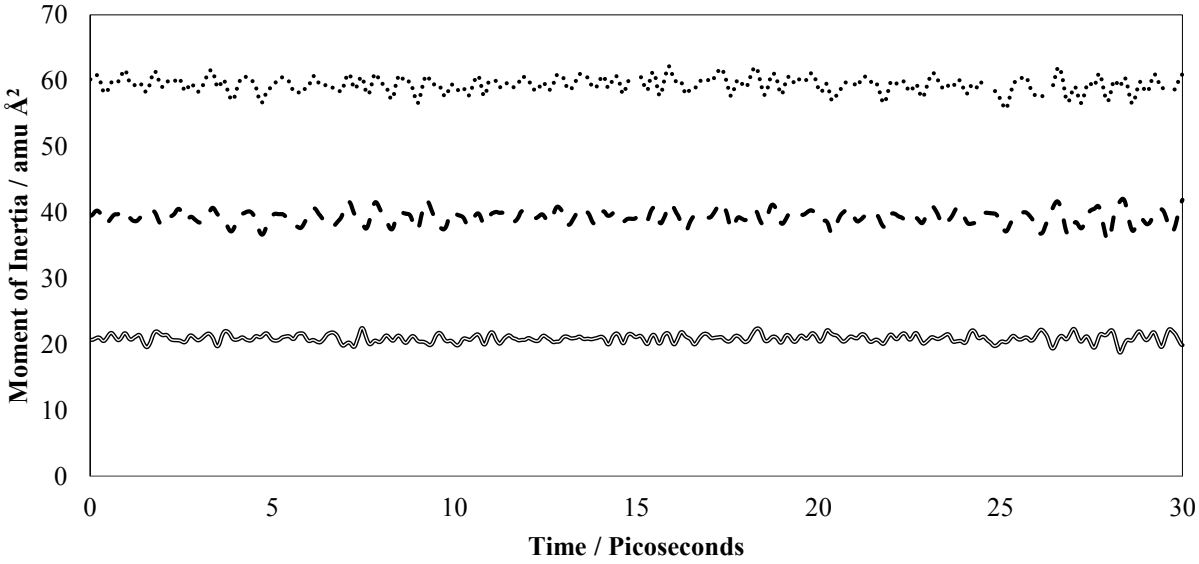

Figure 7.28: Moment of inertia analysis for Au_{13} 2D(2) structure. Circle lines, double lines and dashed lines represent moment of inertia in X, Y and Z directions respectively.

Moment of inertia analysis presented within figures 7.27 and 7.28 is in sharp contrast to that obtained for 3D structures of Au_{13}. Deviation of a maximum of 0.008 amu $Å^2$ is observed for these two dimensional clusters indicating their shape does not alter significantly through the molecular dynamics run in all directions. This data coupled with the observation that relative energies do not alter significantly through the calculations confirm 3D Au_{13} particles are considerably flexible in their nature compared to their 2D counterparts studied here making the two dimensional structures candidates for global minima Au_{13} structures.

7.4.3 The Influence of Oxygen on the stability of Au_{13}

As gold nanoparticles are commonly used as catalysts for oxidation reactions it is of importance to consider how the presence of oxygen atoms on the cluster affects the morphology of the cluster. As the 3D clusters of Au_{13} demonstrated the greatest flexibility in comparison to their 2D counterparts the highly ordered cuboctahedral cluster was chosen and fully saturated with oxygen in the trigonal (111) facets. In chapter 5 Au_{13} with cuboctahedral geometry has been determined to adsorb and dissociate one molecular oxygen via these facets. By theoretical extension full saturation of these facets would result in an $Au_{13}O_8$ structure which is presented in figure 7.29.

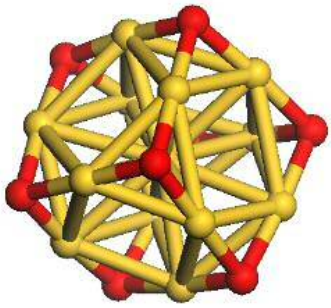

Figure 7.29: $Au_{13}O_8$ optimised geometry for cuboctahedral structure

A 30 picosecond MD run was performed on this oxidised cluster and relative energy (compared to its' starting structure) along with radius of gyration analysis performed is presented in table 7.5. Figure 7.30 confirms no low energy structures are found throughout the MD run relative to the starting structure. Cluster configurations visited throughout this MD run are spread across an energy range of 2.94 eV.

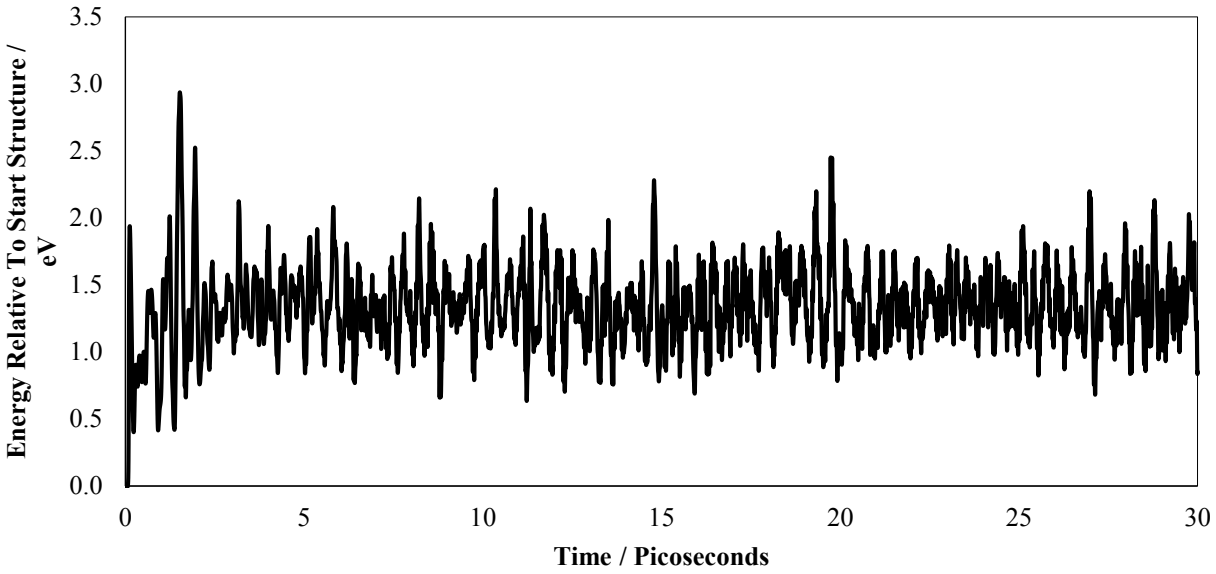

Figure 7.30: $Au_{13}O_8$ energies relative to the start structure throughout the 30 picosecond MD run.

Table 7.5: Radius of gyration data (nm) for $Au_{13}O_8$, as a comparison Au_{13} cuboctahedral geometry data is also presented.

Cluster	Average Radius of Gyration / nm	Range / nm	Standard Deviation / nm
$Au_{13}O_8$	0.12	0.01	0.0009
Au_{13}	0.12	0.02	0.0035

Radius if gyration data presented in table 7.5 provides an insight into the influence of adsorbed and dissociated oxygen species on the geometry of the cluster. The oxidised cuboctahedral structure has a range of radius of gyration half of that of its un-oxidised counterpart. Standard deviation data also confirms a much smaller deviation of 0.0009 for the oxidised particle vs un-oxidised (0.0035). In order to probe the geometry of $Au_{13}O_8$ further, moment of inertia analysis was performed in accordance with 7.4.2.

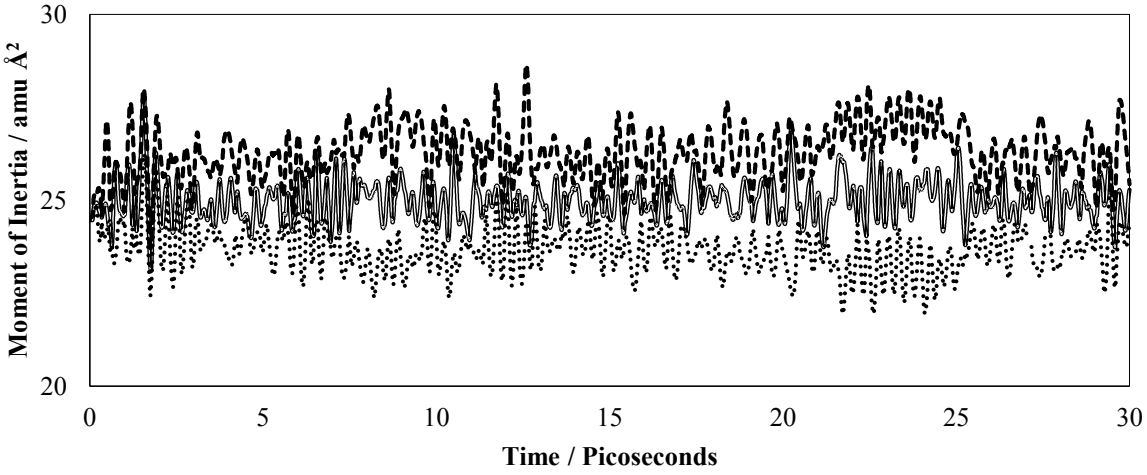

Figure 7.31: Moment of inertia analysis for $Au_{13}O_8$. Circle lines, double lines and dashed lines represent moment of inertia in X, Y and Z directions respectively.

The moment of inertia data plotted in figure 7.31 differs of that presented on the bare cluster (figure 7.25) as moment of inertia in all three directions overlaps with average values of approximately 25 amu $Å^2$ in all directions. For the bare Au_{13} octahedral particle moment of inertia values varied per axis with a deviation of 10 amu $Å^2$ observed between axis. This data confirms the presence of adsorbed and dissociated oxygen species has a stabilising effect on the cluster geometry. Of interest would be a future study which could determine the stabilising effect if any on smaller quantities of adsorbed oxygen species have on the cluster geometry however due to time constraints and computational cost this has not been explored further within this thesis.

7.5 Conclusions

Surface oxygen defect energies on the (0001) surface of α-Fe_2O_3 were investigated through a comprehensive DFT study, results of this confirm 3.02 eV is required to abstract a neutral oxygen atom from the surface. Energies obtained through these model calculations indicate abstraction is considerably difficult and would require the presence of atmospheric oxygen or migration from bulk material to stabilise the defected surface.

Supported Pd_{10} does not influence calculated defect energies at a distance greater than 3 Å from the nearest metal atom within the particle. At these distances defect energies are comparable to the reference energy. At closer proximity to Pd_{10} a dramatic reduction of defect energies is observed with defect energies of 1.3 eV lower than the reference energy possible at low proximity. Whilst a different metal particle composition this striking observation supports work by Illas *et al.*[11] where the presence of a Pt_8 particle reduces the barrier to surface oxygen removal on Cerea. It also raises the tantalising possibility these effects are not limited to Pt and Pd composition of particles with catalytic design influence guided by ease of surface oxygen removal in MvK mechanisms.

Sequential doping of Pd_{10} to Au_{10} indicate it is not internal interactions (Au-Pd, Au-Au or Pd-Pd) which correlate to the thermodynamic substitution preference but instead Au-Surface and Pd-Surface interactions which are the largest factor in doping preference Lowest energy configurations generally have maximum Pd-Surface and minimum Au-Surface interactions indicating the strength of these interactions.

Computing surface oxygen defect energies during sequential doping confirm high percentage gold particles dramatically influence defect energies even at distances above 3 Å. The differing behaviour between high percentage palladium and gold particles can be attributed to particle flexibility and electronic influences.

High percentage Au particles alter geometry upon creation of a surface oxygen defect to shift towards the defect site acting as a plug which stabilises the newly defected surface. High content Pd particles do not exhibit this property with average distances moved by the Pd particle upon creation of a defect site less than 0.1 Angstrom compared to 0.5 Angstrom for Au_{10}.

Electronic properties obtained via Bader charge analysis confirm high content Au particles receive electron density upon creation of an oxygen vacancy. This indicates the metal particle as opposed to neighbouring surface bound Fe are reduced when a defect is created. For high content Pd particles this is not the case instead charge analysis confirms the Pd particle is not reduced which leads to the conclusion it is neighbouring Fe becoming reduced upon defect creation.

Computational investigation by Henkelman *et al.*[10] indicate it is lattice oxygen incorporated in CO to form CO_2 for Au_{12} supported on Ceria. The author of this work proposes for reasons determined above it is the highly flexible nature coupled with reducibility potential which facilitate lattice oxygen incorporation in CO.

From a catalyst design perspective these results are significant as they indicate how catalyst composition can directly influence the support material. If a MvK mechanism utilising surface oxygen / defect sites are proposed for a catalytic cycle it is reasonable to suggest a supported gold subnanometre particle should be synthesized due to the dramatic reduction in surface oxygen defect energies observed. Computational calculations indicate how catalyst composition can be fine-tuned to deliver desired properties.

The discovery of greater flexibility of supported Au_{10} in comparison to the palladium counterpart led to a detailed investigation into the flexibility of Au_{13} and Au_{38} particles. Within the literature there is clear debate regarding the preferred structure of Au_{13}. From the DFT molecular dynamics calculations reported within this chapter it can be confirmed Au_{13} can adopt various structures of similar energies however a clear preference exists for two dimensional conformations supporting the work of Assadollahzadeh *et al.*[13] Through relative energy and radius of gyration analysis the Au_{38} particle investigated here is rigid in comparison to Au_{13} three dimensional structures confirming more bulk like behaviour with regards to flexibility is observed as particle size increases.

DFT molecular dynamics calculations validate the use of the cuboctahedral Au_{38} as a model particle, this is due to the rigidity it demonstrates throughout the run confirming its geometry does not alter significantly in comparison to Au_{13} structures. For Au_{13} calculations we suggest a breakdown of components of adsorption energy calculations (as performed in chapters 5 and 6) in order to fully account for cluster rearrangement which occurs due to flexibility.

The presence of oxygen greatly increases the stability of Au_{13} cuboctahedral structures with this theoretical study presenting a fascinating insight into the stabilising ability of adsorbed and dissociated molecular oxygen.

References

1. Gunter, Buxbaum, Gerhard, P. *Industrial Inorganic Pigments*. (2005)

2. Sugimoto, M. The Past, Present, and Future of Ferrites. *J. Am. Ceram. Soc.* **82,** 269 (2004)

3. Kim, E. C. The Oxidation of Magnetic Particles in Medicinal Ointment. *J. Magn.* **17,** 83 (2012)

4. Gupta, N. M. & Tripathi, A. K. The role of nanosized gold particles in adsorption and oxidation of carbon monoxide over Au/Fe2O3 Catalyst. *Gold Bull.* **34,** 120 (2001)

5. Zhou, Y. Wang, Z. Liu, C. Perspective on CO Oxidation over Pd-Based Catalysts. *Catal. Sci. Technol.* **5,** 69 (2015)

6. Lopez, N. On the origin of the catalytic activity of gold nanoparticles for low-temperature CO oxidation. *J. Catal.* **223,** 232 (2004)

7. Herzing, A. A., Kiely, C. J., Carley, A. F., Landon, P. & Hutchings, G. J. Identification of active gold nanoclusters on iron oxide supports for CO oxidation. *Science* **321,** 1331 (2008)

8. Schubert, M. CO Oxidation over Supported Gold Catalysts—'Inert' and 'Active' Support Materials and Their Role for the Oxygen Supply during Reaction. *J. Catal.* **197,** 113 (2001)

9. Wahlström, E. *et al.* Bonding of Gold Nanoclusters to Oxygen Vacancies on Rutile TiO2(110). *Phys. Rev. Lett.* **90,** 26101 (2003)

10. Kim, H. Y. & Henkelman, G. CO Oxidation at the Interface of Au Nanoclusters and the Stepped-CeO 2 (111) Surface by the Mars–van Krevelen Mechanism. *J. Phys. Chem. Lett.* **4,** 216 (2013)

11. Bruix, A. *et al.* Effects of deposited Pt particles on the reducibility of CeO2(111). *Phys. Chem. Chem. Phys.* **13,** 11384 (2011)

12. Longo, R. & Gallego, L. Structures of 13-atom clusters of fcc transition metals by ab initio and semiempirical calculations. *Phys. Rev. B* **74,** 193409 (2006)

13. Assadollahzadeh, B. & Schwerdtfeger, P. A systematic search for minimum structures of small gold clusters Au(n) (n=2-20) and their electronic properties. *J. Chem. Phys.* **131,** 64306 (2009)

14. Erkoç, Ş. Stability of gold clusters: molecular-dynamics simulations. *Phys. E Low-dimensional Syst. Nanostructures* **8,** 210 (2000)

15. Häberlen, O. D., Chung, S.-C., Stener, M. & Rösch, N. From clusters to bulk: A relativistic density functional investigation on a series of gold clusters Au[sub n], n=6,…,147. *J. Chem. Phys.* **106,** 5189 (1997)

16. Kresse, G. & Hafner, J. Ab initio molecular dynamics for liquid metals. *Phys. Rev. B* **47,** 558 (1993)

17. Kresse, G. & Hafner, J. Ab initio molecular-dynamics simulation of the liquid-metal–amorphous-semiconductor transition in germanium. *Phys. Rev. B* **49,** 14251 (1994)

18. Kresse, G. & Furthmüller, J. Efficiency of ab-initio total energy calculations for metals and semiconductors using a plane-wave basis set. *Comput. Mater. Sci.* **6,** 15 (1996)

19. Kresse, G. Efficient iterative schemes for ab initio total-energy calculations using a plane-wave basis set. *Phys. Rev. B* **54,** 11169 (1996)

20. Perdew, J. P., Burke, K. & Ernzerhof, M. Generalized Gradient Approximation Made Simple. *Phys. Rev. Lett.* **77,** 3865 (1996)

21. Perdew, J. P., Burke, K. & Ernzerhof, M. Generalized Gradient Approximation Made Simple [Phys. Rev. Lett. 77, 3865 (1996)]. *Phys. Rev. Lett.* **78,** 1396 (1997)

22. Blöchl, P. E. Projector augmented-wave method. *Phys. Rev. B* **50,** 17953 (1994)

23. Kresse, G. From ultrasoft pseudopotentials to the projector augmented-wave method. *Phys. Rev. B* **59,** 1758 (1999)

24. Dudarev, S. L., Savrasov, S. Y., Humphreys, C. J. & Sutton, A. P. Electron-energy-loss spectra and the structural stability of nickel oxide: An LSDA+U study. *Phys. Rev. B* **57,** 1505 (1998)

25. Hoh, S. W., Thomas, L., Jones, G. & Willock, D. J. A density functional study of oxygen vacancy formation on α-Fe2O3(0001) surface and the effect of supported Au nanoparticles. *Res. Chem. Intermed.* **41,** 9587 (2015)

26. Tang, W., Sanville, E. & Henkelman, G. A grid-based Bader analysis algorithm without lattice bias. *J. Phys. Condens. Matter* **21,** 84204 (2009)

27. Sanville, E., Kenny, S. D., Smith, R. & Henkelman, G. Improved grid-based algorithm for Bader charge allocation. *J. Comput. Chem.* **28,** 899 (2007)

28. Henkelman, G., Arnaldsson, A. & Jónsson, H. A fast and robust algorithm for Bader decomposition of charge density. *Comput. Mater. Sci.* **36,** 354 (2006)

29. Tauster, S. J., Fung, S. C., Baker, R. T. K. & Horsley, J. A. Strong interactions in supported-metal catalysts. *Science (80-.).* **211,** 1121 (1981)

30. Arlt, T. *et al.* High-pressure polymorphs of anatase TiO2. *Phys. Rev. B* **61,** 14414 (2000)

31. Jaćimović, J. *et al.* High-Pressure Study of Anatase TiO2. *Materials (Basel).* **3,** 1509 (2010)

32. Ming, L. & Manghnani, M. H. Isothermal compression of TiO 2 (Rutile) under hydrostatic pressure to 106 kbar. *J. Geophys. Res.* **84,** 4777 (1979)

33. Perron, H. *et al.* Optimisation of accurate rutile TiO2 (110), (100), (101) and (001) surface models from periodic DFT calculations. *Theor. Chem. Acc.* **117,** 565 (2007)

34. Diebold, U. The surface science of titanium dioxide. *Surf. Sci. Rep.* **48,** 53 (2003)

35. Pastrello, B., Beltran, A. & Sambrano, J. R. Surface structure and stability of TiO_2 anatase: DFT computational study.Surf Sci. **490,** 116 (2001)

36. Toshima, N. & Yonezawa, T. Bimetallic nanoparticles—novel materials for chemical and physical applications. *New J. Chem.* **22,** 1179 (1998)

37. Peng, S.-L., Gan, L.-Y., Tian, R.-Y. & Zhao, Y.-J. Theoretical study of CO adsorption and oxidation on the gold–palladium bimetal clusters. *Comput. Theor. Chem.* **977,** 62 (2011)

38. Hoh, S. W. Oxidation catalysis using transition metals and rare earth oxides. (2014). at <http://orca.cf.ac.uk/69756/2/Electronic Theses and Dissertations Publication Form_SWH-signed %282%29.pdf>

39. Andreeva, D. *et al.* Low-temperature water-gas shift reaction over Au/CeO2 catalysts. *Catal. Today* **72,** 51 (2002)

40. Lu, Z. *et al.* Direct CO oxidation by lattice oxygen on the SnO_2 (110) surface: a DFT study. *Phys. Chem. Chem. Phys.* **16,** 12488 (2014)

Chapter 8

General Conclusions and Suggested Further Work

Modern computational techniques which employ periodic DFT have proven to be a powerful tool to enable this investigation of the fundamental interactions of molecular oxygen and biomass derived products with metal particles of various sizes. Through the plane wave code of VASP and localised basis sets used in Gaussian09 a comprehensive study has been performed with conclusions presented in this section.

8.1 General Conclusions

Oxygen adsorption on the cuboctahedral geometry Au_{38}, Pd_{38} and Au_6Pd_{32} was investigated using the planewave code VASP with the PBE functional. For all metal particles studied the interaction of a single molecule of oxygen with the particle is energetically feasible. For Au_{38} the preferred mode of adsorption is the top-bridge-top site. This finding is in excellent agreement with computational work by Corma *et al.* where the interaction of oxygen with Au_{38} concluded this is the preferential binding mode[1]. Of particular interest is the contrasting observation for Au_6Pd_{32} and Pd_{38} where the preferred mode of adsorption is in a bridge-bridge configuration. Both Pd_{38} and Au_6Pd_{32} demonstrate a greater affinity for molecular oxygen than Au_{38} as adsorption energies are calculated to be of the order of 0.8-1 eV more favourable.

Charge transfer analysis performed through the code of Bader[2,3] indicate a greater degree of charge transfer to molecular oxygen when adsorbed in the bridge-bridge configuration, this is due to the greater degree of coordination (4 vs 2) with the metal particle and molecular oxygen when adsorbed in these sites.

Bader charge analysis confirms that of all particles studied Au_{38} provides the greatest charge transfer to O_2 when adsorbed in the bridge-bridge configuration (0.81 |e|). Transfer of electron density from the cluster to the oxygen molecule must populate the π^* orbital adding to the antibonding character of the bond and may destabilise the interaction therefore explaining why adsorption energies are weakest for Au_{38}. Another cause for weakened adsorption energies is the geometric differences of the (100) facets of the metal particles studied. For Au_{38} there is a greater size mismatch between facet size and equilibrium bond distance of O_2. It is proposed

that the O-O bond stretches the most on Au_{38} to fit on this facet and therefore can destabilise an interaction.

One of the aims of this work is to shed light on conflicting reports within the literature regarding the ability of gold nanoparticles to adsorb and dissociate molecular oxygen species. Through the nudged elastic band method (NEB)[4,5] a comprehensive study of dissociation pathways were investigated with the following conclusions:

- On all particles the preferred mode of dissociation is to adsorb on the bridge-bridge site and dissociate into two adjacent trigonal (111) facets. For Au_{38} the barrier to dissociation is 0.4 eV and is less than the 0.6 eV calculated adsorption energy therefore indicating this route is kinetically favourable.
- For Au_6Pd_{32} and Pd_{38} calculated barriers to dissociation are significantly lower in all cases. The calculated barrier to the most favourable dissociation pathway is at greatest 0.1 eV higher in energy than the energy well the system is in following molecular adsorption. Such observations indicate a spontaneous dissociation in contrast to Au_{38}.
- The behaviour of Au_{38} with regards to oxygen adsorption and dissociation diverges from Au_6Pd_{32} and Pd_{38} when a second molecular oxygen is adsorbed onto a partially oxidised cluster. For Au_{38} the second adsorption energy is calculated to be -0.08 eV however the barrier to dissociate is 0.5 eV. In this instance calculations confirm a second dissociation is ruled out for Au_{38} instead molecular adsorption occurs. For Au_6Pd_{32} and Pd_{38} the particles oxidise to saturation point in contrast to Au_{38}.

The summary of this comprehensive study clearly indicate a single adsorption and dissociation of O_2 is kinetically favourable however a secondary and tertiary dissociation are ruled out on Au_{38}. Whilst dissociation is unlikely we report multiple non dissociative adsorption is possible and therefore our findings disagree with work by Whetten *et al.*[6] and supports computational work by Mills and Gordon who report secondary oxygen interaction with a pre-oxidised gold particle is weaker in nature[7]. This study supports work by Corma *et al.*[1] where we confirm particle morphology (the need for (100) facets) plays a part in the activity of metal particles towards oxygen adsorption and dissociation. We believe our findings contribute significantly to the debate by providing detailed barriers to adsorption and dissociation which are not present within current literature.

Surface oxygen defect energies on a (0001) surface of α-Fe_2O_3 were investigated through a comprehensive DFT + U study. Results of this study confirm 3.02 eV is required to abstract a

neutral oxygen atom from the clean surface. Subsequent calculations were performed in order to investigate the effect of a supported metal particle on oxygen vacancy defect energies.

It is found Pd_{10} does not influence oxygen vacancy defect energies if the defect site is at a distance greater than 3 Å from the particle. There is a correlation between defect energies and distance from the particle. At a proximity of 2 Å defect energies are lowered by 1 eV clearly indicating the presence of the particle facilitates creation of a defect site.

Sequential doping of Pd_{10} to Au_{10} was performed and at each composition the thermodynamically favoured configuration was chosen to perform defect energy calculations. It is found no preference for internal composition of the metal particle exists as no trend between Pd-Pd, Au-Au and Au-Pd interactions and total energies is observed. Instead it is found that the lowest energy configurations generally have maximum Pd-surface and minimum Au-Surface interactions indicating a hierarchy in strength of these interactions.

In contrast to predominately palladium particles, high percentage gold particles dramatically influence defect energies even at distances above 3 Å. The differing behaviour between high percentage palladium and gold particles has been attributed to both particle flexibility and electronic properties as detailed below:

- Through Bader charge analysis Au_{10} is found to be charged upon creation of a surface oxygen vacancy. The removal of a neutral oxygen atom will leave behind two electrons with the possibility of either reducing local Fe^{3+} or metal particle atoms however for high gold content clusters the latter is proposed.
- Pd_{10} was found to not be charged even when surface oxygen defects were created in close proximity to the metal particle. This suggests local Fe^{3+} is reduced instead of Pd.
- Measurement of metal particles before and after oxygen vacancy defect creation indicate a higher degree of flexibility for high percentage gold particles than any other. In these instances, the metal particle shifts towards (average 0.5 Å for Au_{10}) the defect site acting almost as a plug to stabilise it. For Pd_{10} movement of 0.1 Å was observed.

Whilst the composition of metal particles studied in this work differs, the striking observation that high percentage gold particles lower defect energies support work by Illas *et al.*[8] where the presence of a Pt_8 particle reduces the barrier to surface oxygen removal on Ceria. Further supporting work is presented through a computational investigation by Henkelman *et al.*[9] In

this study it is suggested lattice oxygen is incorporated in CO to form CO_2 for Au_{12} supported on Ceria.

The author of this work proposes for Au particles and reasons detailed above that it is the highly flexible nature coupled with reducibility potential which facilitate lattice oxygen incorporation in CO to form CO_2. Calculations presented in this thesis raise the tantalising possibility of fine tuning metal particle composition in order to facilitate Mars van Krevelen mechanisms where surface oxygen removal is a component of the catalytic cycle. Adsorption and dissociation of reaction pathways proposed in chapter 5 indicate on Au_{38} the barrier to dissociation of O_2 is approximately 0.4 eV. This is significantly lower than the ~ 1 eV required to abstract neutral oxygen from the iron oxide support and therefore it is reasonable to assume atmospheric oxygen is the preferred source of oxygen in this instance. To confirm this hypothesis abstraction energies of oxygen from Au particles would be required however this is beyond the scope of this thesis.

Flexibility of gold particles was investigated in more depth through a comprehensive molecular dynamics study using VASP using constant volume and temperature (controlled through the Nose – Hoover thermostat). In this study Au_{13} in both cuboctahedral and icosahedral geometries were found to be considerably more flexible than Au_{38}. Radius of gyration along with moment of inertia analysis confirm Au_{13} has a thermodynamic preference for 2 dimensional shapes and as a result we propose this as a suitable catalytic model for Au_{13} instead of three dimensional geometries which are found to rearrange significantly upon adsorption of molecules.

Finally, the interaction of HMF with Au_{13}, Pd_{13}, Au_{38}, Pd_{38} and Au_6Pd_{32} was investigated and it is found favourable interaction occurs in all instances with a hierarchy of adsorption energies being $Au_{38} < Au_{13} < Pd_{38} < Au_6Pd_{32} < Pd_{13}$. It is interesting to observe how the bimetallic particle Au_6Pd_{32} exhibits the greatest affinity for HMF of the 38 atom metal particles investigated. Parallels can be drawn from the ranking of adsorption energies for 38 atom clusters with data obtained in chapter 5 as in both cases Au_{38} demonstrates the weakest affinity for the adsorbate. Doping Au into Pd particles in a 1:4 ratio have previously been reported to enhance catalytic activity of hydrogenation of 4-pentenoic acid in comparison to monometallic equivalents[10]. Experimental work by Enache *et al.* report solvent free oxidation of primary alcohols to aldehydes using Au / Pd bimetallic catalysts[11]. As HMF contains a primary alcohol

group it is reasonable to suggest this composition may assist with the rate limiting oxidation of the alcohol group.

Data obtained in this thesis confirm both sub nanometre (Au_{13} and Pd_{13}) and Au_6Pd_{32} particles have significant interaction energies with HMF and therefore future experimental testing is required in order to deduce whether such a strong interaction inhibits or improves the efficiency of a catalyst. From the data presented here the bimetallic Au_6Pd_{32} is the composition proposed as the most suitable catalyst for initial adsorption of HMF. This is due to the ability to adsorb HMF however not too strongly where it can irreversibly bind prohibiting reaction.

Experimental observations from both Davis *et al.*[12] and Gorbanev *et al.*[13] report the oxidation of HMF proceeds via oxidation of the aldehyde group then alcohol group. It is reported the rate limiting step is the oxidation of the alcohol group as this occurs after the aldehyde oxidation.

NEB calculations to obtained barriers to O-H cleavage suggest a high barrier exists which is greater than any adsorption energy calculated on the metal particles studied. This suggests oxidation of the alcohol side chain will not occur with ease on a metal particle and to the authors knowledge are the first such computational mechanistic study of HMF conversion in the literature. Our findings support the view that it is indeed the alcohol group oxidation which limits the rate of conversion of HMF to FDCA using gold particles.

A brief extension of this study was made to investigate whether pre-adsorbed and dissociated oxygen could facilitate an O-H cleavage on particles. For Pd_{13} the presence of oxygen was found to dramatically reduce the barrier to O-H cleavage by 80 kJ mol^{-1} through formation of a surface bound hydroxy species. This incomplete study provides a fascinating insight into how reactions can be assisted through atmospheric oxygen.

8.2 Suggested Further Work

The study of the interaction of molecular oxygen with metal particles provided a fascinating insight into the contrasting behaviours of different compositions and sizes of particles. The surprising ability of Au_6Pd_{32} to oxidise to saturation point generates speculation as to whether it is this property is composition or morphology dependent. A future study investigating other atomic configurations of this composition would provide insight into this property.

Data obtained in this work suggests high percentage gold particles facilitate oxygen vacancy formation on (0001) Fe_2O_3. A further study to determine whether this effect is transferred when particles are supported on other surfaces would confirm gold particles are ideal catalysts for surface oxygen facilitated mechanisms.

Molecular dynamics investigations of Au_{13} indicate two dimensional clusters are thermodynamically preferred. Clusters saturated with oxygen atoms in (111) facets are considerably more rigid, it would be interesting to extend this study of intermediate oxidised particles and also confirm the rigidity of Pd particles by performing molecular dynamics studies on these particles.

Finally, the HMF study performed in this work was on ideal gas phase systems without the presence of a solvent. Experimentally these reactions are performed using a variety of solvent and therefore an extension of this study including solvent would provide a fascinating insight into the mechanism.

Extension of the alcohol oxidation mechanism under gas phase conditions by secondary abstraction of H to form an aldehyde would complete the energy profile for conversion of alcohol to aldehyde and confirm with certainty through quantified barriers whether this is indeed the rate limiting step as proposed in the literature.

References

1. Boronat, M. & Corma, A. Oxygen activation on gold nanoparticles: separating the influence of particle size, particle shape and support interaction. *Dalton Trans.* **39,** 8538 (2010)

2. Tang, W., Sanville, E. & Henkelman, G. A grid-based Bader analysis algorithm without lattice bias. *J. Phys. Condens. Matter* **21,** 84204 (2009)

3. Sanville, E., Kenny, S. D., Smith, R. & Henkelman, G. Improved grid-based algorithm for Bader charge allocation. *J. Comput. Chem.* **28,** 899 (2007)

4. Sheppard, D. & Henkelman, G. Paths to which the Nudged Elastic Band Converges. *J Comput Chem* **32,** 1769 (2011)

5. Sheppard, D., Terrell, R. & Henkelman, G. Optimization methods for finding minimum energy paths. *J. Chem. Phys.* **128,** 134106 (2008)

6. Salisbury, B. ., Wallace, W. . & Whetten, R. . Low-temperature activation of molecular oxygen by gold clusters: a stoichiometric process correlated to electron affinity. *Chem. Phys.* **262,** 131 (2000)

7. Mills, G., Gordon, M. S. & Metiu, H. *The adsorption of molecular oxygen on neutral and negative Aun clusters (n=2–5)*. *Chemical Physics Letters* **359,** 493 (2002)

8. Bruix, A. *et al.* Effects of deposited Pt particles on the reducibility of CeO2(111). *Phys. Chem. Chem. Phys.* **13,** 11384 (2011)

9. Kim, H. Y. & Henkelman, G. CO Oxidation at the Interface of Au Nanoclusters and the Stepped-CeO 2 (111) Surface by the Mars–van Krevelen Mechanism. *J. Phys. Chem. Lett.* **4,** 216 (2013)

10. Yoshiteru Mizukoshi, *,†, Taku Fujimoto, ‡, Yoshio Nagata, ‡, Ryuichiro Oshima, ‡ and & Maeda†, Y. Characterization and Catalytic Activity of Core−Shell Structured Gold/Palladium Bimetallic Nanoparticles Synthesized by the Sonochemical Method.*J. Phys. B.* **104,** 6028 (2000)

11. Enache, D. I. *et al.* Solvent-free oxidation of primary alcohols to aldehydes using Au-Pd/TiO2 catalysts. *Science* **311,** 362 (2006)

12. DAVIS, S. E., ZOPE, B. N. & DAVIS, R. J. On the mechanism of selective oxidation of 5-hydroxymethylfurfural to 2,5-furandicarboxylic acid over supported Pt and Au catalysts. *Green Chem.* **14,** 143 (2013)

13. Gorbanev, Y. Y., Klitgaard, S. K., Woodley, J. M., Christensen, C. H. & Riisager, A. Gold-catalyzed aerobic oxidation of 5-hydroxymethylfurfural in water at ambient temperature. *ChemSusChem* **2,** 672 (2009)